University of Wuppertal

School of Electrical, Information and Media Engineering

BERGISCHE
UNIVERSITÄT
WUPPERTAL

PhD Thesis

Functional Layers and Interfaces for Perovskite Single- and Multi-Junction Solar Cells

Kai Oliver Brinkmann

Institute of Electronic Devices

First examiner: Prof. Dr. Thomas Riedl
Second examiner: Prof. Dr. Dieter Neher

Submission date: August 18, 2022

Preface

First I would like to express my deepest gratitude for the opportunity to conduct my doctoral work in the Institute of Electronic Devices at the University of Wuppertal. A very special thank I want to direct to the institute's head, Prof. Dr. Thomas Riedl, who was also my supervisor. I want to thank him for the time, patience and nerves that he invested in me and my work, not to mention all the things he enabled in his function as our head of institute. While still providing the freedom to pursue my own ideas and make my own mistakes, he was present and deeply invested, whenever matters got pressing, even if everyone's schedule was tight.

Next I want to thank my former as well as my present colleagues, who are substantially important for most of the achievements and insights presented in this work. Ever since my Master thesis I especially enjoyed our joint works, projects and eventually publications. Also I would like to thank deeply for the nerves, my sometimes exotic work stile during these intense years surely have cost. Namely I want to thank Tim Becker, Dr. Tobias Gahlmann, Dr. Lukas Hoffmann, Dr. Junjie He, Dr. Jie Zhao, Florian Zimmermann, Tobias Haeger, Cedric Kreusel, Manuel Theisen, Christian Tückmantel, Dr. Neda Pourdavoud, Dr. Ralf Heiderhoff, Dr. Detlef Theirich, Tim Hasselmann, Manuel Runkel, Dr. Ting Hu, Ahmed Kadid, Dr. Sara Trost, Dr. Andreas Behrend, Dr. Andreas Polywka, Dr. Andre Räupke and finally Dr. Kirill Zilberberg, who initially introduced me into the field and ignited my pursuit for firstly organic and later perovskite solar cells.

I also want to direct special thanks to our lab engineer Karsten Brennecke, without whom large portions of the work would not have been possible. Also I want to dedicatedly thank Eva Grimberg and her predecessor Kordula Kraus, in our office, as well as Felicitas Richert, Bärbel Jark from our dean's office, Wolfgang Alt from our caretaker service and Katrin Ködderitzsch from our purchasing department, whose flexibility and effort were outstanding and eventually enabled many things, that might have been impossible with a less involved administration.

During this work, I experienced great support by a number of students, who either conducted their bachelor or master thesis, or contributed as student workers to this endeavour. For their hard work and tireless effort, I want to thank Jessica Malerczyk, Felix Schubert, Fabian Göbelsmann, Tobias Stolz, Berhad Sammu, Batin Saydam, Dominik Pilichowski, Patrick Rehrmann, Manuel Günster, Henrik Weidner and finally Cedric Kreusel and Timo Maschwitz, who I am very delighted to call my colleagues nowadays.

While a lot of great collaborative work was done within our institute, many insides presented in this thesis were also enabled by close and highly fruitful collaborations with other institutes and research groups. Within the University of Wuppertal, special thanks goes to the group of Prof. Dr. Patrick Görrn, Prof. Dr. Ullrich Scherf and Prof. Dr. Stefan Kirsch, Dr. Andreas Kotthaus, Prof. Dr. Sebastian Weber and Prof. Dr. Dirk Lützenkirchen-Hecht and inside their groups Dr. Frederic van Gen Hassend, Dr. Andre Mayer, Dr. Markus Mühlinghaus, Dr. Tina Keller, Dr. Alex Palma, Dr. Venkata Suresh Mothika and Andreas Siebert.

Beyond the institution of our university, I want to direct my thanks to the groups of Dr. Selina Olthof, Dr. Martin Stolterfoht, Prof. Dr. Dieter Neher, Prof. Dr. Klaus Meerholz, Prof. Dr. Frank Schreiber, Prof. Dr. Sanjay Mathur, Prof. Dr. Henry Snaith, Prof. Dr. Steve Albrecht, Dr. Detlef Rogalla, Dr. Babtiste Gault and inside their groups dedicatedly Lena Merten, Dr. Alexander Hinderhofer, Dr. Feray Ünlü, Jarla Thiesbrummel, Dr. Emilio Gutierrez-Partida, Dr. Christian Wolff, Dr. Marco Jost, Francisco Pena-Camargo, Pietro Caprioglio, Dr. Fengjiu Yang, Dr. Amran Al-Ashouri, Lorena Perdigón Toro, Dr. Leonie Gomell, Dr. Siyuan Zhang, Dr. Dirk Hertel, Dr. Felix Lang, Dr. Christine Koch and Dr. Heidi Schwartz.

Additionally, I want to dedicatedly thank the PhD student community of the SPP-2196 joint program of the DFG. The monthly online discussions and in-depth insides into our respective fields and expertise gave me very diverse viewing angles and most intriguing approaches to tackle the topic of perovskites. I especially want to highlight the scientific exchange with Lena Merten, Clemens Baretzky, Dr. Artem Musiienko, Andrei Karabanov, Dr. Feray Ünlü, Jarla Thiesbrummel, Dr. Emilio Gutierrez-Partida and Dr. Clement Maheu, who each greatly participated in the wonderful discussions and overall connecting experience we had, despite the roadblocks, COVID-19 presented in the past years.

Last, but not least I want to express my deep gratitude to my loving wife Natascha Brinkmann, my friends and my family, who carried me over these very intense past years. All of which occasionally put their own needs on hold, during times of very high pressure and I am sincerely grateful for all the support and the safety net, I had the pleasure of experiencing.

Thank you all, for making this work possible and the past years to such an outstanding experience for me!

Contents

Abbreviations, Symbols and Constants

Abbreviations

abbreviation	meaning	abbreviation	meaning
2D	two dimensional	EEL	electron extraction layer
2T	two terminal	EL	electroluminescence
3D	three dimensional	ESL	electron selective layer
4T	four terminal	ETL	electron transport layer
A	acceptor	FA	formamidinium
a.u.	arbitrary units	GISAXS	grazing incidence small angle
ABF	annular bright-field		X-ray scattering
ABo	anti-bonding	GIWAXS	grazing incidence wide angle
AFM	atomic force microscope		X-ray scattering
ALD	atomic layer deposition	HAADF	high angle annular dark-field
AM	air mass	HEL	hole extraction layer
AZO	aluminium doped zinc	HOMO	highest occupied molecular
	oxide		orbital
BHJ	bulk heterojunction	HSL	hole selective layer
Bo	bonding	HTL	hole transport layer
CB	conduction band	Im	imaginary
CIGS	copper indium gallium	IPES	inverse photoelectron
	selenide		spectroscopy
D	donor	ITO	indium tin oxide
diel	dielectricum	LED	light emitting diode
DMF	dimethyl formamide	LUMO	lowest unoccupied
DMSO	dimethyl sulfoxide		molecular orbital
EDS	energy-dispersive X-ray	MA	methylammonium
	spectroscopy	MPP	maximum power point

abbreviation	meaning	abbreviation	meaning
NFA	non fullerene acceptor	SAM	self assembled
NIR	near infrared		monolayer
NMP	n-methyl pyrrolidone	SCN	thiocyanate
NMR	nuclear molecular	SD	standard deviation
	resonance	SEM	scanning electron
NP	nanoparticle		microscope
NW	nanowires	SQ	Shockley-Queisser
OSC	organic solar cell	STEM	scanning transmission
OSJ	organic single junction		electron microscopy
PL	photoluminescence	TEM	transmission electron
PLQY	photoluminescence		microscopy
	quantum yield	UPS	ultraviolet photoelectron
PSC	perovskite solar cell		spectroscopy
PSJ	perovskite single junction	VB	valence band
RBS	Rutherford backscattering	VIS	visible
Re	real	XPS	X-ray photoelectron
S-ALD	spatial atomic layer		spectroscopy
	deposition	XRD	X-ray diffraction
		XRR	X-ray reflectivity

Symbols and Constants

symbol / constant	meaning	unit / value
ϵ_r	relative permittivity	unitless
λ	wavelength	nm
ν	frequency	Hz
Φ	Haacke figure of merit	Ω^{-1}
Φ_B	Schottky-barrier height	eV
δ	partial charge	C
θ	XRD incident angle	°
A	area	cm^2
A*	Richardson constant	A cm^{-2} K^{-1}
d	thickness	nm
E	energy	eV
e	elementary charge	1.6022 x 10^{-19} C
E_{CB}	conduction band energy	eV
E_{vac}	vacuum level energy	eV
E_F	Fermi level energy	eV
E_g	band gap energy	eV
E_{VB}	valence band energy	eV
EN	electronegativity	unitless
EQE	external quantum efficiency	unitless
FF	fill factor	%
GPC	growth per cycle	nm
h	Planck constant	6.6261 x 10^{-34} J Hz^{-1}
HLB	hydrophilic lipophilic balance	unitless
I	current	mA
I_0	saturation current	mA
J	current density	A cm^{-2}
$J_{0,rad}$	radiative thermal recombination current density	A cm^{-2}
J_{gen}	generated current density	A cm^{-2}
J_{inj}	injected current density	A cm^{-2}
J_{Ph}	photocurrent density	A cm^{-2}
J_{rec}	recombination current density	A cm^{-2}

symbol / constant	**meaning**	**unit / value**
J_{SC}	short circuit current density	A cm^{-2}
k_b	Bolzmann constant	1.3806 x 10^{-23} m^2 kg s^{-2} K^{-1}
L_D	Debye length	nm
m	mass	g
m*	effective mass	g
n	refractive index	unitless
n_c	charge carrier density	cm^{-3}
n_i	ideality factor	unitless
PCE	power conversion efficiency	%
q	charge	C
$Q_{x,y,z}$	reciprocal distance	$angstrom^{-1}$
QFLS	quasi-Fermi level splitting	eV
R	resistance	Ω
r_{eq}	equivalent radius	nm
R_{sh}	sheet resistance	Ω sq^{-1}
R_p	parallel resistance	Ω cm^2
R_s	series resistance	Ω cm^2
rH	relative humidity	%
T	Temperature	K or °C
T_{av}	average transmittance	%
v	velocity	m s^{-1}
V	voltage	V
V_{OC}	open circuit voltage	V
WF	work function	eV
WVTR	water vapour transmission rate	g m^{-2} d^{-1}

1 Introduction

Climate change keeps human society in its grasp and confronts us with unprecedented global threads. [1] In order to at least milder its catastrophic impact, society, economy and technology are constrained to perform a drastic transformation in the way how resources and most importantly energy is harvested. Instead of using fossil energy sources like coal, oil or gas, all energy sources used in the future economy need to be climate-neutral, namely renewable. The most abundant energy source available on the earth is the sun. Its energy is converted and used in a plethora of different forms like e.g. wind (temperature driven convection), bio-mass (photosynthesis) or hydropower (water evaporation & convection). Aside from using these secondary energy sources, a direct energy conversion is highly desirable. This can either be done by using solar thermal power conversion, synthesis of solar fuel or by photovoltaics, which directly transforms solar irradiance into electricity.

Currently the market for photovoltaics is vastly dominated by silicon technology accounting for about 95 % of the solar cell production worldwide. [2] While this technology proves reliable and stable, it carries some inevitable downsides originating from mandatory high temperature processes needed to produce solar grade silicon wafers, combined with its indirect bandgap and resulting thickness requirements. As a result, after power conversion efficiency has almost saturated, the main optimization throughout the last few years has been to reduce the material usage by optimizing wafer cutting and module design. Still, after a strong decline in the beginning of the last century, prices for solar modules began to level. [2] Also additional costs originating from the crystalline and rigid nature of silicon wafers, such as mounting, installation etc. need to be considered. Therefore vigorous research is directed towards alternative technologies, that are not subject to the same limitations. Among the most promising candidates are emerging thin film solar cell technologies based on organic or perovskite semiconductors as active materials. [3–7] They carry the potential to overcome the limitation of high temperature processing and provide prospects for lightweight and flexible module design. Facades, windows, cars, fences and many other creative applications can become viable

as a consequence, which might change the way how we think about photovoltaics in the first place. Anyway, until commercialization can be undertaken, technologies have to reach a certain technology readiness level in order to be market relevant. As such, for solar cells a critical combination of cost, stability and efficiency has to be achieved. The presented work aims to contribute new insights and novel strategies to eventually enable the large, global endeavour of bringing perovskite and organic solar cells to a level, where market introduction is viable.

As means of reducing expected cost, which is intimately linked to the reproducibility of perovskite active material deposition, we aimed to increase yield and to simplify perovskite formation for follow-up upscaling efforts. This is achieved by combining the so-called gas quenching procedure with a precursor formulation, that warrants optimal surface coverage of the active perovskite material. Stability of perovskite based solar cells upon various stressing conditions is greatly improved by the introduction of internal permeation barrier layers. This enabled perovskite thermal stability of several thousand hours under demanding stress conditions. At the same time these stabilization measures enabled several low cost strategies for the design of semi-transparent perovskite solar cells, that are needed on the path to the versatile application scenarios. Finally fundamental device efficiency limits are tackled by combining perovskite and organic solar cells in a tandem concept. By doing so, we set a new efficiency world record (24 %) for this type of devices and demonstrate the realistic prospect to overcome the efficiency threshold of 30 % with these cells.

2 Basics

2.1 Introduction of Perovskites

In general the phrase "perovskite" describes a crystal structure with a composition of AMX_3, where an A cation is embedded in a network of MX_6 octahedra, like shown in Figure 2.1. [8]

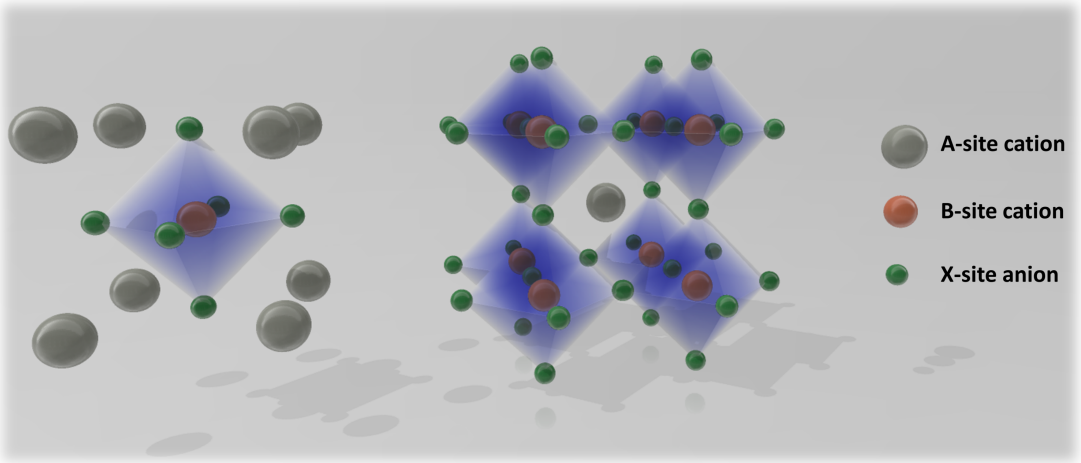

Figure 2.1: Perovskite structure. *(left,) 3D model of the perovskite structure with A, M and X denoting the three ionic components and (right) network of MX_6 octahedra enclosing the A cation.*

Several types of perovskite materials have been investigated over the years and they have been utilized for various purposes like e.g. catalysis or as ferroelectric for capacitors. [9, 10] Anyhow in recent years, a specific type of perovskite aroused serious attention due to its remarkable opto-electronic properties: the hybrid metal-halide perovskite. This type of perovskite material consists of a large organic or inorganic cation embedded in a metal halide octahedra network. [8] Since the discovery of its ability for energy harvesting in 2009, [11] a massive scientific effort has been invested into its investigation, with over 70000 publications listed on Web of Science covering

"perovskite" in general and almost 25000 publications distinctively covering "perovskite solar cells". [12] In the following chapter some basics for solar cells comprising this type of perovskite are covered and for the sake of readability the expression "perovskite" will be used as synonym for hybrid metal-halide perovskites.

2.2 Perovskite Material Properties

Several perovskite materials utilized for electro-optic applications can be deposited from the liquid phase and require a rather moderate energy uptake (often only about 100 °C for some minutes are needed) for crystallization. [13] At the same time the perovskite's optoelectronic properties (band gap tunability, absorption coefficient, carrier diffusion length, defect tolerance, etc. - see chapter 2.2.1) render it almost ideal for an application as absorber in solar cells. [8] Anyhow aside from the understanding of the electronic properties, the controlled formation of a perovskite layer is of the utmost importance. Finally, even if extraordinary power conversion efficiencies of over 25 % can be reached currently, it is even the more important, that those high numbers can actually be maintained over a long period of operation, which qualifies perovskite stability to be one the most pressing topics of perovskite research nowadays. [14]

2.2.1 Electronic, Optical and Structural Properties

In most "classical" semiconductors like GaAs, point defects result in the creation of deep trap states promoting unfavourable Shockley-Read-Hall recombination. In contrast, for hybrid metal-halide perovskites this is not necessarily the case. Several representatives, even classify as very defect tolerant. A strong anti-bonding coupling of the Pb(6s) lone pair and the I(5p) orbital defines the valence band above the bonding molecular orbital of Pb(6p) and I(5p), which is the counterpart to the anti-bonding Pb(6p) - I(5p) molecular orbital forming the conduction band (see Figure 2.2). [16, 17] As indicated by DFT calculations, this electronic line-up causes most positively charged traps induced by point defects to form shallow defects slightly above the valence band edge. [18] On the other hand, the conduction band, that comprises only a rather weak anti-bonding coupling, is mainly governed by the Pb(6p) orbital and is mostly ionic in nature, which leaves it almost unaffected by external defect levels. Some relativistic effects like spin-orbit coupling contribute to a further lowering of the CB, which eventually results in negatively charged defects to be mainly shallow as well. [16, 19]

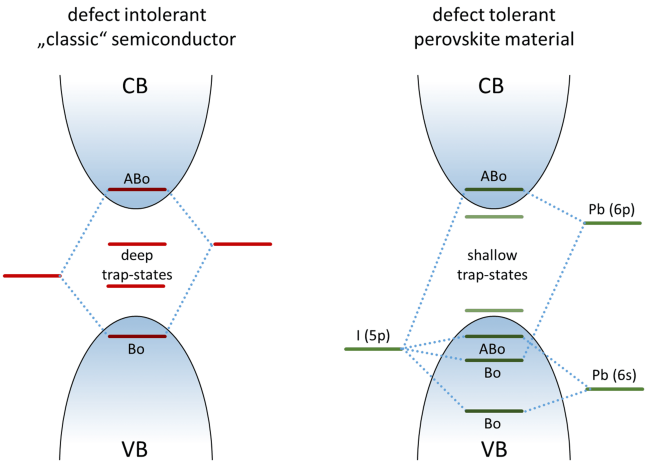

Figure 2.2: Electronic structure / defect tolerance. *(left,) Electronic structure of a "classical" semiconductor material with VB and CB being bonding (Bo) and anti-bonding (ABo) respectively and (right) electronic structure of the perovskite material (methylammonium lead iodide ($MAPbI_3$) as example) with both VB and CB being anti-bonding. Adapted with permission from [15]. Copyright 2017 American Chemical Society.*

It was also evidenced by time of flight measurements, as well as photo hall measurements, that the likeliness of forming a deep trap inside a perovskite crystal is very limited. [20, 21] As a direct consequence, some perovskite materials can express a distinct tolerance against defects, which enables long charge carrier lifetimes and diffusion lengths, that can reach values of several microseconds or micrometers respectively. [21] In contrast to silicon, the band gap of many representatives is direct. As a result hybrid metal-halide perovskite materials can express remarkably high absorption coefficients. [22] This allows the use of very thin active absorber layers ($\leq$ 1 µm), far lower as the determined carrier diffusion lengths. [21]

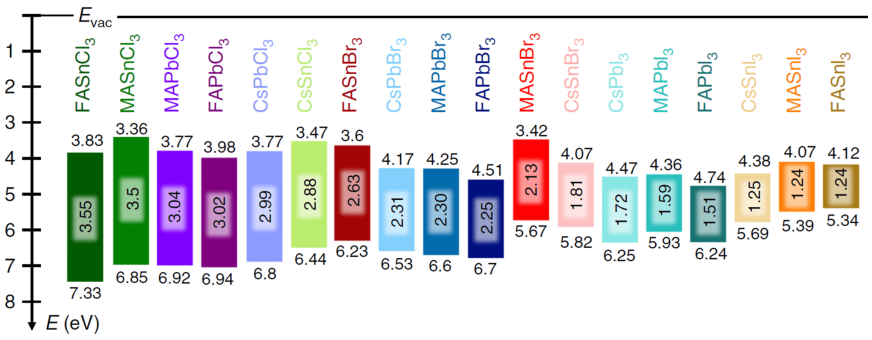

Figure 2.3: Band gap tunability. *Schematic energy level diagram of a selection of 18 metal halide perovskites. Reprinted from [17].*

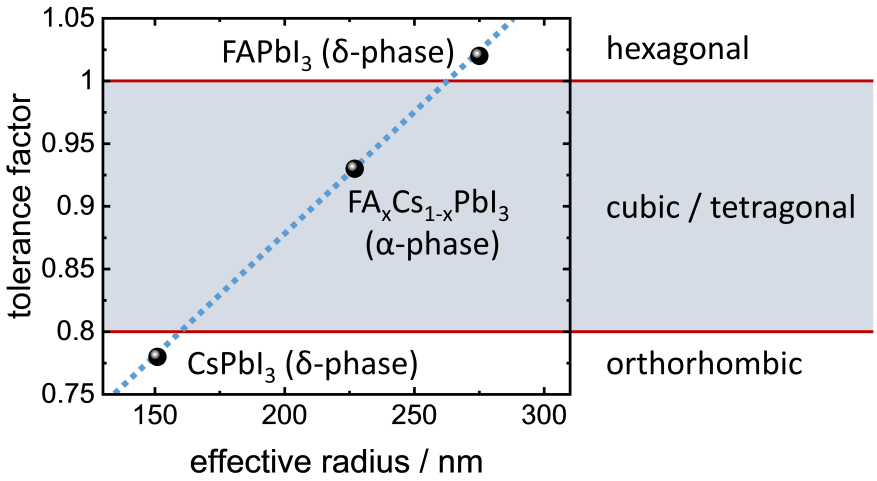

Figure 2.4: Goldschmidt tolerance factor for perovskites. *Correlations between tolerance factor and crystal structure of perovskite materials. Adapted with permission from [25]. Copyright 2015 American Chemical Society.*

At the same time, the perovskite material offers a versatile band gap tunability, since its components are exchangeable to a certain degree, allowing to vary the position of CB and VB by compositional engineering. Since it does not participate in the formation of CB and VB, the impact of the A site cation on the energetic structure is limited. [23, 24] As a consequence the band gap of perovskite materials is most prominently determined by the choice of the B- and X-site (see Figure 2.3). [17] The tunability of perovskite band gap is mainly limited by phase instability of the resulting perovskite material. To this end the Goldschmidt tolerance factor is used as an estimate for the tendency of a certain composition to form a stable perovskite phase at room temperature:

$t = \frac{R_A + R_X}{\sqrt{2}\,(R_B + R_X)}$ [26]

with $R_{A,B,X}$ being the atomic radii of the respective constituents. As visible an Figure 2.4 a tolerance factor ranging between 0.8 and 1.0 indicates a stable perovskite composition, while values beyond and below that tend to transition into other, possibly non-perovskite crystal structures (e.g. hexagonal). [25]

2.2.2 Layer Formation / Crystallization

While the above mentioned properties prove highly promising for solar cell application, another key feature of perovskite solar cells is expected to be low cost. To achieve

this goal, layer deposition techniques viable for upscalable fabrication have to be used. Some of the most prominent approaches (aside from evaporation - for more infos please see [27, 28]) are solution-based deposition techniques. While spin-coating is prominently used on a lab scale, deposition strategies that are finally transferable to roll to roll techniques like doctor blading or slot-die coating are to be established.

The key challenge of the liquid deposition process is to control the growth of the perovskite crystals during deposition. This is especially challenging, if a single step (or one-step) process (like also used in some parts of this work) is used, since several processes take place simultaneously (solvent evaporation, supersaturation, nucleation, crystal growth, ...). As a consequence, already small deviations from an original processing protocol can result in severe changes in the end result (see chapter 3). Therefore strategies were developed aiming to uncouple the singular processes of crystallization and warrant better control to the deposition process.

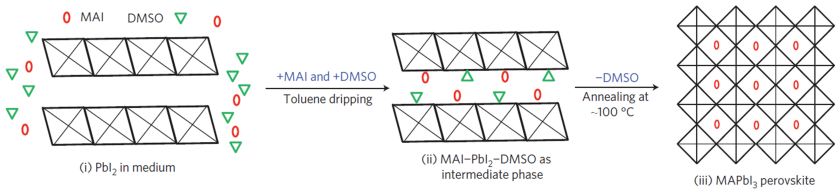

Figure 2.5: Complex assisted perovskite deposition. *Scheme for the formation of the perovskite material via a MAI–PbI_2–DMSO complex based intermediate phase. Adapted with permission from [29]. Copyright 2014 Nature Publishing Group.*

The arguably most popular and currently most frequently used strategy to reach a higher level of control over the crystallization process, is an utilization of a complex mediated, supersaturated, so-called "intermediate state". [29–32] A mixture of two solvents, e.g. dimethylformamide (DMF) and dimethyl sulfoxid DMSO with two largely different vapour pressures are combined in the precursor solution. At the same time the low vapour pressure solvent (i.e. DMSO) is able to form a stable complex intermediate with the precursor molecules. [30, 33] If now the superfluous solvent is removed, see Figure 2.5, a stable AX-MX-solvent complex remains. A follow-up annealing step is then used to remove the solvent molecules from the complex and form the final perovskite structure. This approach allows for a plethora of extraction methods for the superfluous solvent. Aside from simply waiting for the solvent to dry (which often results in inhomogeneous layer morphology), temperature gradient annealing, solvent-solvent extraction with orthogonal (anti-)solvents, vacuum and gas flow assisted fast drying approaches as well as rapid infrared spot annealing can be utilized for this purpose. [29, 30, 34–40]

Regardless which strategy is used, the general aim of these techniques is to de-couple the precursor drying step from the final crystallization and thus to gain better control over the final film morphology. Eventually this leads to a reduction of process variables and enables a significant improvement in terms of process reproducibility. This work also contributes on the path towards highly reproducible perovskite deposition by modification of the gas quenching technique (chapter 3.3).

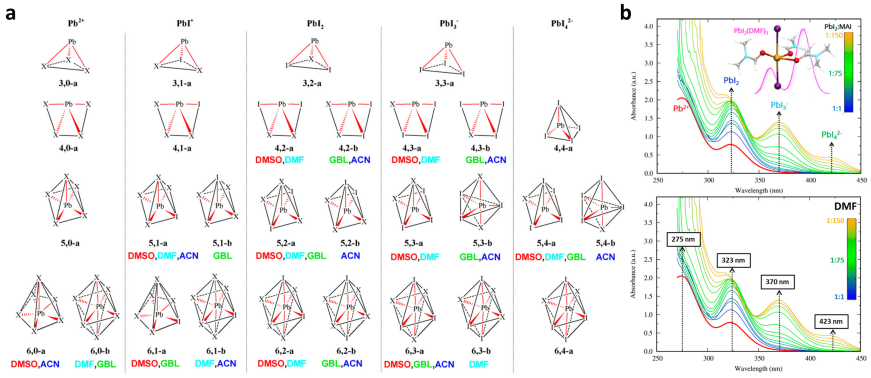

Figure 2.6: Lead complexes in perovskite precursors. ***a,*** *Calculated stable coordination variants for lead iodide with several aprotic solvents (row deducing the coordination number).* ***b,*** *Optical fingerprints detected by UV-vis absorption measurements in highly diluted (< 1 mM) solutions upon variation of the PbI_2 : MAI ratio. Reprinted with permission from [41]. Copyright 2019 American Chemical Society.*

Still, even though deposition of perovskite materials has become comparably robust by the complex assisted approach, the underlying mechanisms dominating the crystallization process are still subject to vigorous debate. [42] The existence of colloidal complex structures consisting of the lead halide as an acceptor and the aprotic solvent as donor molecules, already present in highly diluted perovskite precursors, is widely accepted and well evidenced. [42–46] To underline the plethora of possible lead complexing / coordination an overview of some of the most likely lead complexes, as well as an optical evidence of complexing are shown in Figure 2.6. [41]

While there is substantial evidence for the ability of the solvent to form complexes, its impact on the final perovskite layer remains unclear. [47–49] A frequently cited theory is that the nucleus for perovskite crystallization evolves from Pb^{2+} - MA^{+} - I^{-} clusters that coordinate into the above mentioned edge-sharing $[PbI_6]^{4-}$ octahedra that eventually evolve into corner sharing structures that, as concentration increases, grow in size eventually seeding the final crystallization (see Figure 2.7). [49–52] This implies a strong impact of the precursor nucleation and crystallisation process by complexing and coordination inside the precursor solution. Since the lead site acts as an acceptor

(i.e. lewis acid) inside the precursor solution this theory matches well with several reports stating the beneficial impact of various lewis base additives for the crystallization process. [53–55] As of yet, the above theory still requires experimental confirmation. On the one hand there is striking evidence for the presence of the intermediate phase, but on the other hand so far there is no direct evidence that unequivocally links the precursor complexing to the final layer formation. To this end, this work also covers some additional understanding of the precursor chemistry (see chapter 3.2).

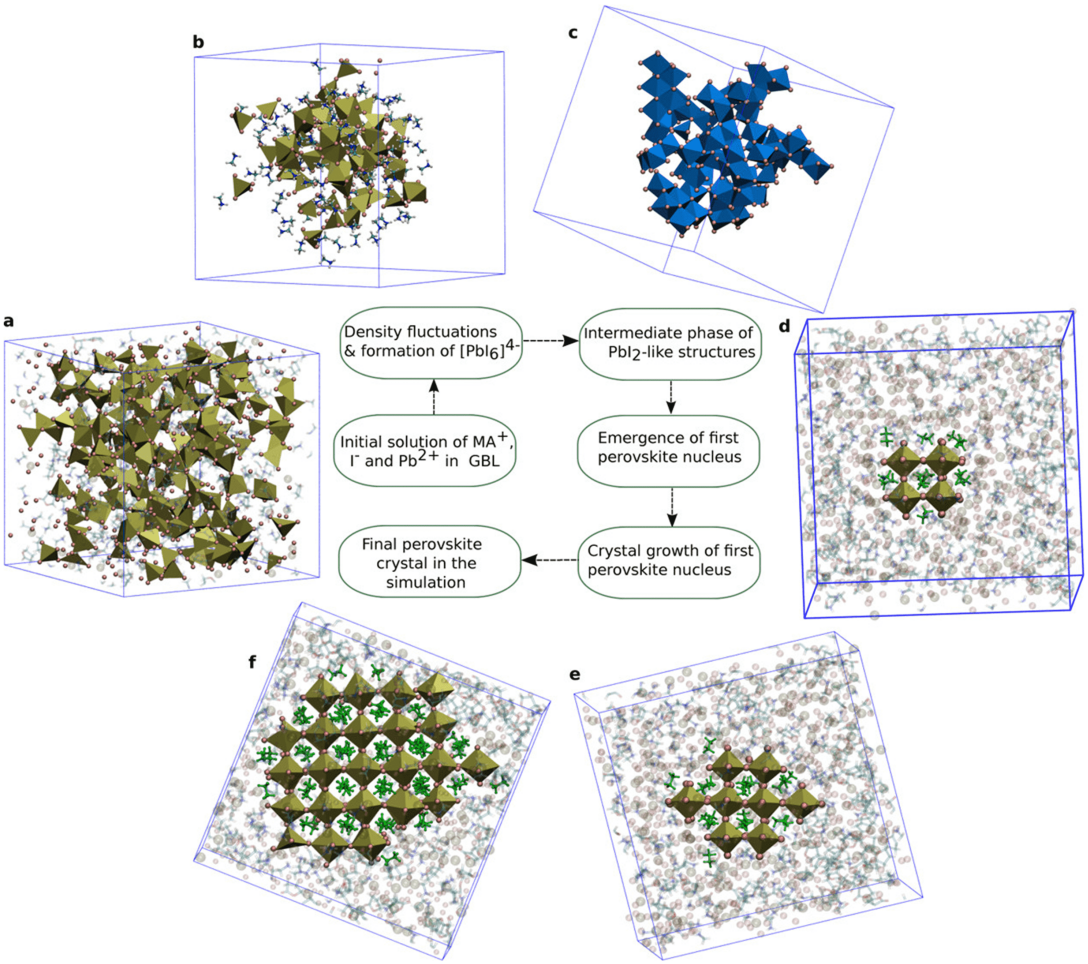

Figure 2.7: Perovskite nucleation process. *Simulated nucleation pathway. Pb-I complexes are displayed with golden and blue polyhedra with Pb^{2+} in the center and I^- at the corners.* ***a,*** *Initial solution showing random distribution of Pb^{2+} and I^-* ***b,*** *Initial cluster formation of Pb^{2+} and I^- surrounded by MA^+ ions.* ***c,*** *Edge-sharing $[PbI_6]^{4-}$ octahedra.* ***d,*** *First perovskite nucleus.* ***e,*** *Growth of the initial nucleus.* ***f,*** *Formation of 3D perovskite structures. Reprinted with permission from [51]. Copyright 2019 American Chemical Society.*

2.2.3 Degradation Mechanisms

While demonstrating highly promising opto-electronic properties, one of the most pressing issues hindering market introduction of perovskite solar cells, is the limited stability of most perovskite compositions, that provide high power conversion efficiencies. Depending on the structure of the perovskite composition, degradation routes and thresholds, at which they are triggered, can differ. For the sake of readability, here we will mainly concentrate on the fruit-fly perovskite structure $MAPbI_3$, (see also chapter 4). In general, there are three main factors inducing degradation in perovskite materials during operation: ambient air (oxygen, moisture, ...), temperature (caused by heating due to the incident sunlight) and photo-degradation due to sunlight irradiation.

Maybe the most obvious cause of degradation is exposure to ambient air. Mainly moisture, but also oxygen can cause the degradation of the perovskite material. The actual decomposition route is not entirely unravelled, yet, and several possible (and maybe in parallel occurring) routes are reported. While it is clearly evidenced, that small amounts of H_2O can cause a reversible hydration of the perovskite material, [56] an extended exposure to a larger amount of humidity evidently results in a decomposition of the material leaving behind PbI_2, which was frequently evidenced by X-ray diffraction methods. [57–59] Apart from these observations it is widely expected that water in general acts as a catalyst for the perovskite decomposition, [59, 60] even though this might conflict with the above mentioned observation, that low amounts of water do not necessarily harm a perovskite layer. Also several reports about the influence of interfaces on the moisture sensitivity of perovskite materials exist. [61]
A possible pathway of perovskite degradation induced by moisture is displayed in Figure 2.8. Here water forms an intermediate complex by taking up a proton from the perovskites, eventually breaking it up to form HI, CH_3NH_2 and PbI_2: [62–64]

$$CH_3NH_3PbI_3(s) \leftrightarrow PbI_2(s) + CH_3NH_3I(aq) \tag{2.1}$$

$$CH_3NH_3I(aq) \leftrightarrow CH_3NH_2(aq) + HI(aq) \tag{2.2}$$

$$4HI(aq) + O_2(g) \leftrightarrow 2I_2(s) + 2H_2O(l) \tag{2.3}$$

$$2HI(aq) \leftrightarrow H_2(g) + I_2(s) \tag{2.4}$$

Especially the formation and eventual follow-up reactions of HI would cause the degradation to be irreversible. The acidic HI is able to take part in a follow-up reaction corroding the top electrode or might decompose into hydrogen and iodine. [65] Similar observations have also been made as part of this work (see chapter 4).

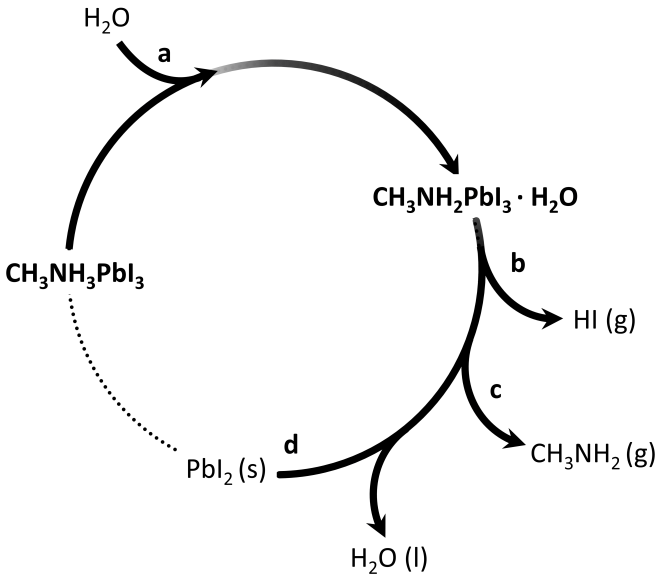

Figure 2.8: Possible pathway of moisture catalysed $MAPbI_3$ degradation. *Poposed by [62–64].* ***a,*** *A water molecule initiates the process, in which $MAPbI_3$ decomposes into both volatile and water soluble components* ***b,*** *hydrogen iodide and* ***c,*** *methylammonia.* ***d,*** *Eventually observable decomposition product PbI_2 and water.*

In any case stability in ambient air is considered a lesser issue for the commercialization of perovskite based applications, as it can be overcome by proper encapsulation strategies that are already existent. [66] Generally more critically is the thermal instability of the perovskite material, since during operation it would require active cooling, which contradicts the paradigm of low cost application. It is well evidenced that most of the above perovskites decompose even under inert conditions, if exposed to elevated temperature. [67, 68] As no additional chemical compound is involved, direct evidence of the volatile species could be found and combining it with evidence of PbI_2 formation, obtained by X-ray diffraction, the following degradation pathways have been derived: [67]

$$CH_3NH_3PbI_3(s) \quad \leftrightarrow \quad PbI_2(s) + CH_3NH_2(g) + HI(g) \tag{2.5}$$

$$CH_3NH_3PbI_3(s) \quad \leftrightarrow \quad PbI_2(s) + CH_3I(g) + NH_3(g) \tag{2.6}$$

Please note, that all mentioned degradation mechanisms have to be understood as equilibrium reactions that become irreversible by the evasion of volatile degradation products (see Figure 2.9 also compare chapter 4.2). Follow-up reactions of e.g. HI causing degradation of layers as covered in chapter 6.1 are also possible causes for irreversibility of thermal decomposition.

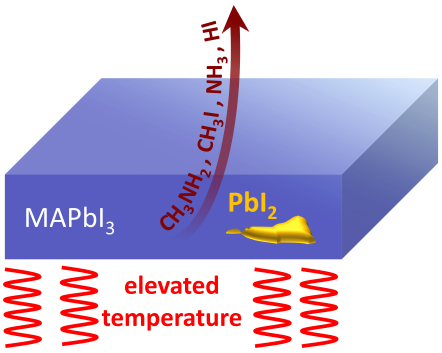

Figure 2.9: Degradation at elevated temperature. *Schematic illustration of the degradation process at elevated temperatures, with solid PbI_2 remaining in the perovskite layer, whilst other, volatile degradation products evade from the layer, making the reaction irreversible.*

Finally the arguably most critical, as naturally inevitable cause for perovskite degradation is the photo-degradation. Here, one has to distinguish between photo-catalytic degradation of the perovskite structure and light induced halide segregation, in case of mixed halide materials. [61] Most importantly it has been evidenced, that photoinduced degradation, just like thermal decomposition, can occur even under vacuum conditions. [69–71] By in-situ compositional analysis a degradation pattern strongly resembling the thermal decomposition was proposed:

$$CH_3NH_3PbI_3(s) + h\nu \quad \leftrightarrow \quad PbI_2(s) + CH_3NH_2(g) + HI(g) \tag{2.7}$$

$$CH_3NH_3PbI_3(s) + h\nu \quad \leftrightarrow \quad PbI_2(s) + CH_3I(g) + NH_3(g) \tag{2.8}$$

$$PbI_2(s) + h\nu \quad \leftrightarrow \quad Pb(s) + I_2(s) \tag{2.9}$$

The main difference here is the possibility of the lead iodide to also decompose to elementary lead and iodine under illumination, whilst iodine vapour is also expected to cause follow-up chemical reactions. [72]

Mixed halide perovskites are frequently used to achieve band gaps in the range between the pure halide compositions; e.g. between 1.6 eV ($MAPbI_3$) and 2.3 eV ($MAPbBr_3$). For these perovskites, irradiation can cause a de-mixing of the halide components resulting in Br-rich wide band gap and I-rich lower band gap regions. [73, 74] Halide segregation typically manifests in a notable red shift of the photoluminescence as visible in Figure 2.10. In general this redshift of the photoluminescence accompanies a significant deterioration of photovoltaic parameters, since the low band gap, iodine rich, regions can act as charge traps and recombination centres reducing solar cell performance, that manifests in a severe loss of current density. [75]

While most detected halide segregation is reported to be reversible, there is also evidence for an irreversible phase reconstruction as a result of prolonged illumination, indicating halide segregation not only as a short term, but also long term stability issue. [76] Investigations targeting halide segregation can be found in chapter 7.

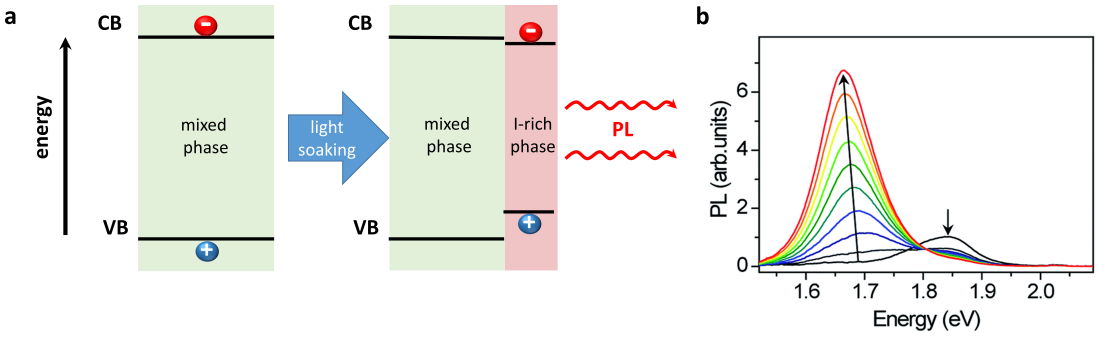

Figure 2.10: Light induced halide segregation. ***a,*** *Schematic illustration of the mechanism of halide segregation and its impact on the photoluminescence (PL) of the material.* ***b,*** *Development of PL upon continuous irradiation. b, reprinted from [73].*

2.3 Perovskite Solar Cell Application

Since most of the perovskite structures used for solar cell applications have a direct band gap, they show rather high absorption coefficients. [22] In combination with the pronounced defect tolerance discussed in 2.2, this allows for efficient absorption of incident light well within the diffusion length of the charge carriers. At the same time the exciton binding energy (10 - 15 meV) is typically significantly below the thermal energy at room temperature ($k_BT \approx 25$ meV), which means that essentially free carriers are created. [77] Anyhow the mere generation of free, long lived charge carriers alone does not readily result in a good solar cell. To extract charges from the active material, it is of crucial importance to provide the charge carriers with a preferred direction to eventually extract electrons and holes at the cathode and anode, respectively. In a silicon solar cell extraction is facilitated by doping of the active silicon material generating a p-i-n (or a n-i-p) junction by respective p and n doping of the silicon material. [78] For perovskite solar cell technology, at the current state of the art, this strategy is not eligible. Therefore charge extraction has to be facilitated by dedicated, so called extraction layers. [79]

2.3.1 Charge Extraction

As visualized in Figure 2.11 a potential gradient in the perovskite active layer is realized by sandwiching it between a high- and a low work function material. Respectively, the two materials thereby act as electron and hole extraction layer. Several reports found the charge carrier density in perovskites structures to be low (e.g. 10^{11} - 10^{13} cm^{-1} in [80]). Hence Debye lengths can be expected to by far exceed the active layer thickness. As a consequence the gradient of the vacuum level, in a first approximation, can be considered to be unaffected by potential shielding from intrinsic charge carriers in the perovskite. The gradient in vacuum level E_{vac}, conduction band (CB) and valence band (VB) of the perovskite are therefore expected to be governed by the potential difference of the adjacent extraction layers (and potential interface effects). This band gradient over the perovskite active material is commonly called a "built-in potential". [81] If now a photon is absorbed, in yet another rough approximation (ignoring effects like quasi-Fermi level splitting, ion induced field screening, etc.), the generated charge carriers are provided with a preferred movement direction. Additionally at the direct interface to the perovskite active material, typically electron and hole selective layers (ESL / HSL) are used to warrant only the respective charge carrier species to be extracted at the interface. Thereby parasitic recombination at the interfaces can be suppressed.

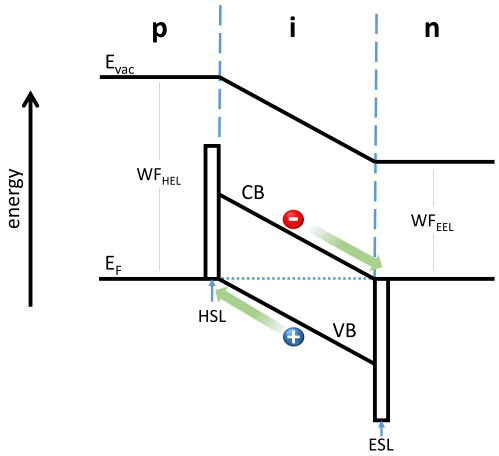

Figure 2.11: Concept of charge extraction. *Schematic illustration of the basics of charge extraction in a perovskite solar cell. It is shown how the different work functions (WF) of hole and electron extraction layer (HEL and EEL) define a potential gradient that, due to alignment of the Fermi level (E_F) in contact, translates on the vacuum level (E_{vac}), conduction and valence band (CB and VB) of the perovskite active layer. The respective areas are labelled p (hole extraction), i (active material) and n (electron extraction). Hole- and electron selective contacts (HSL / ESL) are displayed at the interfaces of the perovskite active material.*

2.3.2 Open Circuit Voltage vs. Recombination

When light is shone onto a semiconductor, it is no longer in thermodynamic equilibrium and a splitting of the Fermi level into so called quasi-Fermi levels occurs. [82] The quasi-Fermi level splitting (QFLS) is a measure for the density of electrons and holes in non-equilibrium, which is immediately affected by the band gap, the rate of carrier excitation and the rate of recombination. For non degenerate semiconductors QFLS can be estimated from parasitic non-radiative recombination current density (J_{rec}) and the total amount of generated charge carriers described by the generation current density (J_{gen}) at open circuit conditions:

$$QFLS = k_B T \times ln(\frac{J_{gen} - J_{rec}}{J_{0,rad}})$$

k_B denotes the Bolzmann constant, T the temperature and $J_{0,rad}$ radiative recombination current in darkness caused by temperature. [83] Fortunately, non-radiative recombination can be calculated from a material's PL quantum yield (PLQY), which is why QFLS can be derived from singular layers and does not necessarily require a full solar cell stack. Therefore QFLS can be used to evaluate the impact of individual interfaces in partial solar cell stacks. In ideal Shockley-Queisser Theory the values of the quasi-fermi-level splitting and the open circuit voltage are corresponding to each other by $V_{OC,max} = QFLS/e$ with e being the elementary charge. [84] Accordingly it could be inserted in the open circuit case of the ideal Shockley equation:

$$V_{OC} \times e = QFLS = n_i \, k_B T \times ln(\frac{J_{Ph}}{J_0} + 1)$$

with J_{Ph} being the photocurrent density and J_0 the the reverse saturation current density. Anyhow, in reality, the quasi-Fermi level splitting alone does not necessarily state the actual open circuit voltage, since band alignment of the adjacent extraction layers can limit the achievable V_{OC}. [85] Also the built in potential can set an upper limit to the maximal V_{OC} of a solar cell. Anyhow the QFLS is still a good indicator, as the equation $V_{OC} \leq QFLS/e$ states the upper limit to the open circuit voltage of a layer (or a layer-stack, compare chapter 7). A high recombination rate, e.g. in the perovskite bulk, at grain boundaries or interfaces, directly impacts on the maximal reachable open circuit voltage by limiting the QFLS. Hence, employing highly selective interface layers, that ideally simultaneously passivate perovskite surface defects, is key to exploit the full potential of a perovskite as photoactive material.

2.3.3 J-V Hysteresis

A well evidenced fact is the ability of ions inside the perovskite material to migrate. [87–90] Taking into account that during operation or characterisation electric fields are present inside the perovskite solar cell, the ions redistribute according to their respective charge and mobility. [90–92] If this phenomenon now pairs with limited charge carrier selectivity at the perovskite interfaces, a scanning rate depending current-voltage hysteresis can occur upon scanning in either - $\rightarrow$ + (forward) or + $\rightarrow$ - (reverse) direction. The exact origin of this phenomenon is not yet entirely unravelled. One plausible explaination might be parasitic recombination at defect-rich interfaces, supported by an ion driven charge accumulation induced by the applied field during measurement. [93] Here two different types of ionic accumulation are distinguished: so-called "negative accumulation" ($V < V_{OC}$), where positive ions accumulate on the HTL site and negative on the ETL and the "positive accumulation" ($V > V_{OC}$) where places are reversed. Negative accumulation might be thought as constituting a depleted n-doped region directly on the HTL and a depleted p-doped region at the ETL interface. A resulting build-up of photo-generated charge carriers caused by this depletion could then promote detrimental interface recombination and lead to an underestimation of the cell performance. [93] Additionally the depletion region might screen the built-in potential and hinder charge extraction. For positive accumulation a detrimental depletion effect is not to be expected, since the accumulated charge carrier species match the polarity of the extraction site.

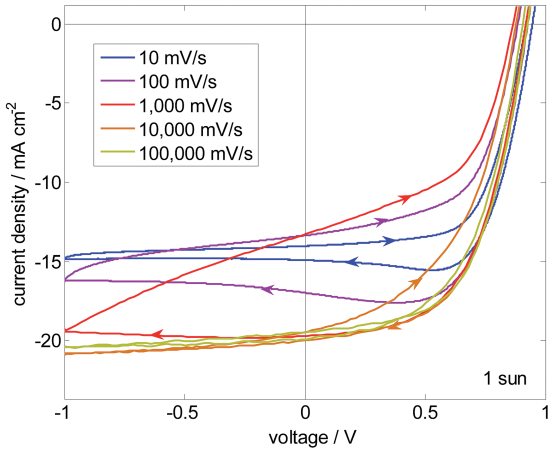

Figure 2.12: Hysteresis in perovskite solar cells. *Rate dependent hysteresis of n-i-p $MAPbI_3$ solar cells based on a planar TiO_2 EEL with scan rates between 10 and 100000 mV s^{-1}. Reprinted with permission from [86]. Copyright 2015 The Royal Society of Chemistry.*

On the contrary an hysteresis effect might even lead to an overestimation of the solar cell's J_{SC} and FF in case of a fast J-V scan. This overestimation is frequently attributed to a capacitive effect that might be caused by one or maybe a combination of different perovskite properties, like e.g. the ferroelectricity, ionic charge redistribution or trapping and de-trapping in shallow defects. [94–96] Operating in the 1st quadrant would charge the presented capacity leading to a discharge after passing into the 4th quadrant on time scales of ms, which, for fast measurements, would add to the measured photo-current. [96, 97] This theory is supported by reports describing notable improvement of J-V scans performed on solar cell, that are subject to hysteresis, when they are operated in the 1st quadrant for longer timespans before measurement. [95] In any case the observed hysteresis in the J-V characteristics can entirely obscure the actual device performance as e.g. shown in Figure 2.12. [86, 87, 91, 96] On the other hand it has also been evidenced, that proper defect passivation and selective contacts can substantially suppress the J-V hysteresis observed. [98] Still, as a consequence, PCE values reported in this work derived from J-V scans are regularly accompanied by steady state measurements, to confirm the correctness of PCE values derived from J-V scans.

2.4 Brief Digression on Organic Solar Cells

In contrast to crystalline semiconductors, amorphous organic semiconductors do not possess continuous band structures and therefore no valence or conduction band. Alternatively overlapping p-orbitals of sp^2-hybridized carbon atoms form a so-called conjugated de-localized π-electron system that can extend over a single organic molecule. [99] On the other hand, there is typically no orbital overlap with the van-der-Waals bonded neighbouring molecules. The delocalized π molecular orbital can form bonding and anti-bonding electronic states, which in turn enables two delocalized energy states, namely the highest occupied molecular orbital (HOMO) and the lowest unoccupied molecular orbital (LUMO). [99, 100] The ability of a molecule to carry one or several excited carriers in the delocalized anti-bonding π^* LUMO enables it to express optoelectronic properties in partial analogy to classical semiconductors and eventually the usage as active material for thin film solar cells.

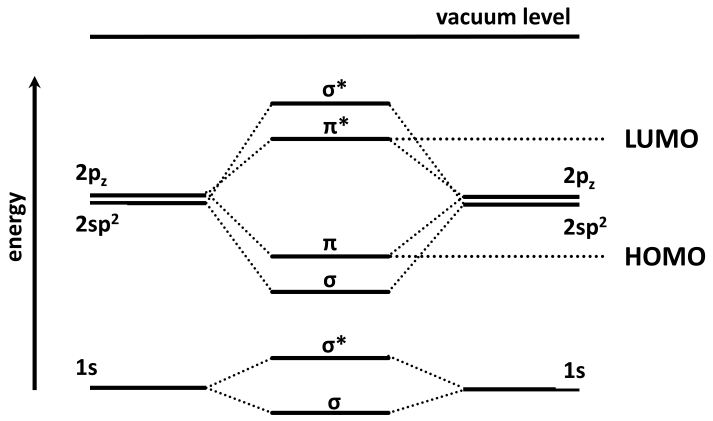

Figure 2.13: HOMO and LUMO in organic semiconductors. *Simplified energy level diagram illustrating the formation of π and π^* bonding and anti-bonding orbitals eventually forming the highes occupied molecular orbital (HOMO) and the lowest unoccupied molecular orbital (LUMO).*

2.4.1 Transport and Exciton Splitting in Organic Semiconductors

Non-continuous, spatially limited, π-electron systems in combination with a typically low dielectric permittivity of organic semiconductors, result in a strong localization of electron hole pairs. As a consequence, optical excitation of charge carriers results in the formation of a so called Frenkel exciton, which is localized on the molecule and typically closely bound (0.5 - 1.0 eV). [101, 102] This is in stark contrast to Wannier-Mott Excitons, like formed in the perovskite material (see chapter 2.3). Charge transport in amorphous organic semiconductors differs substantially from crystalline semiconductors: While intramolecular charge transport can be considered to be band-like through the extended delocalized π electron system, intermolecular transport is governed by a thermally activated hopping transport and presents the bottleneck for charge carrier mobility (e.g. the mobility of the frequently used fullerene PCBM was found to be as low as 10^{-3} cm^2 V^{-1} s^{-1}). [100, 102–104] In turn exciton diffusion lengths inside organic semiconductors are typically limited to a 5 - 10 nm range. [105] In order to use a Frenkel exciton in a solar cell, it needs to be split into charge carriers. Due to the high exciton binding energy, a donor-acceptor system with tailored energy offset in the HOMO or LUMO is utilized as displayed in Figure 2.14. [103, 106] If the energy offset is larger than the exciton binding energy, the exciton is split. After exciton splitting charge extraction, similar to perovskite solar cells, can happen (compare chapter 2.11). [102, 106] The energy offset needed for exciton splitting implies an inevitable voltage loss, which is why extensive ongoing research targets the reduction of exciton binding energy in order to reduce these

losses. [107] Another issue is the limited diffusion length of the exciton, which makes it challenging for each generated exciton to reach the donor-acceptor (D-A) interface before it recombines. [105] This requirement limits the maximum thickness of a donor and an acceptor bi-layer to about 20 nm, which is disadvantageous, because it limits the absorbance of the device. Alternatively, the concept of a bulk heterojunction (BHJ), an intermixed blend of donor and acceptor material is used to enable higher active layer thicknesses, while simultaneously warranting D-A interfaces well within the diffusion length of the exciton. [103, 106] In turn vigorous research is aimed at BHJ morphology, which can be manipulated e.g. by processing conditions or dedicated additives. [108]

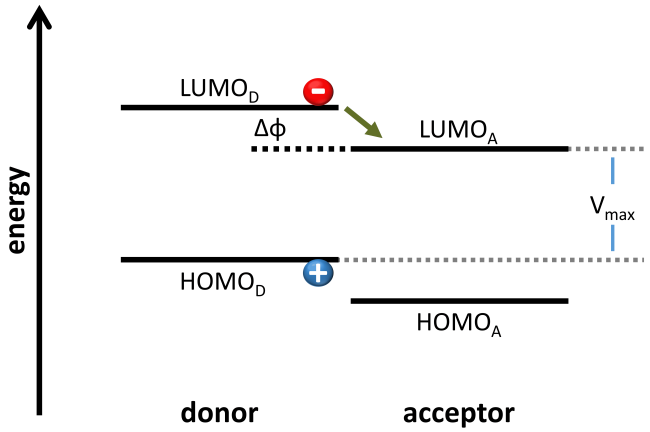

Figure 2.14: Donor-acceptor system. *Illustration of an exciton splitting process taking place at a donor-acceptor interface. $\Delta\Phi$ denotes the energy offset between $LUMO_D$ and $LUMO_A$, V_{max} the maximum reachable open circuit voltage.*

2.4.2 Non-Fullerene Acceptors

After great progress following the introduction of organic solar cells, the development reached a plateau slightly below 13% in 2012. [109] The plateauing was associated with the use of fullerenes as acceptor systems in organic solar cells, that provided the highest efficiencies for over a decade. [110] While providing good properties for exciton splitting and charge transport, the given electronic properties and negligible contribution to the photocurrent hindered further progress. This situation changed entirely with the introduction of non-fullerene acceptors, that caused a skyrocketing development with record PCEs of organic cells exceeding 19 % nowadays. [111] Intense research on molecular design afforded a reduced voltage loss and absorption onsets in the low energy gap region. [110, 112–114] The improved absorbance enables organic solar cells

to show high EQEs over a broad range of the solar spectrum, extending well into the infrared. Thereby organic solar cells with short circuit current densities exceeding 26 mA cm^{-2} were achieved. [115] An example is shown in Figure 2.15 for PBDB-TF (donor) and Y6 (acceptor). Note that in order to improve morphology and stability small amounts of fullerenes are often also blended into the BHJ, to obtain a so-called ternary blend. [116–118]

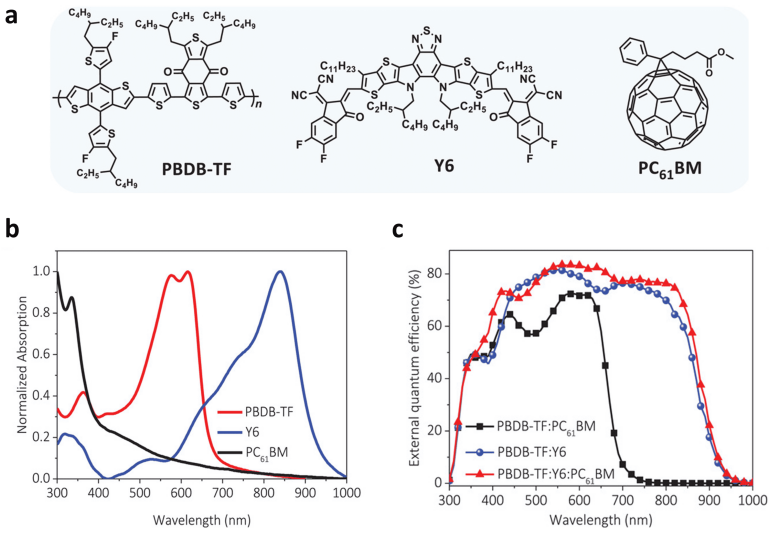

Figure 2.15: Non-fullerene acceptors. ***a,*** *Molecular structure of all ingredients of a ternary blend BHJ comprising the very commonly used non fullerene acceptor Y6.* ***b,*** *Respective absorption spectra and* ***c,*** *external quantum efficiencies displaying the wide coverage of the solar spectrum by the ternary blended BHJ. Reprinted with permission from [116]. Copyright 2019 Wiley-VCH.*

2.5 Multi-Junction Solar Cells

While PSCs further approach the PCE of solar cells based on silicon, eventually a consideration of fundamental efficiency limits is becoming more and more important. [109] Silicon as well as GaAs single cell efficiencies are basically plateauing for years now, a phenomenon that is slowly starting to appear also in PSCs. Therefore fundamental efficiency limits of single junction solar cells and strategies how to overcome them need to be considered.

2.5.1 Shockley Queisser - Limit of Single Junctions

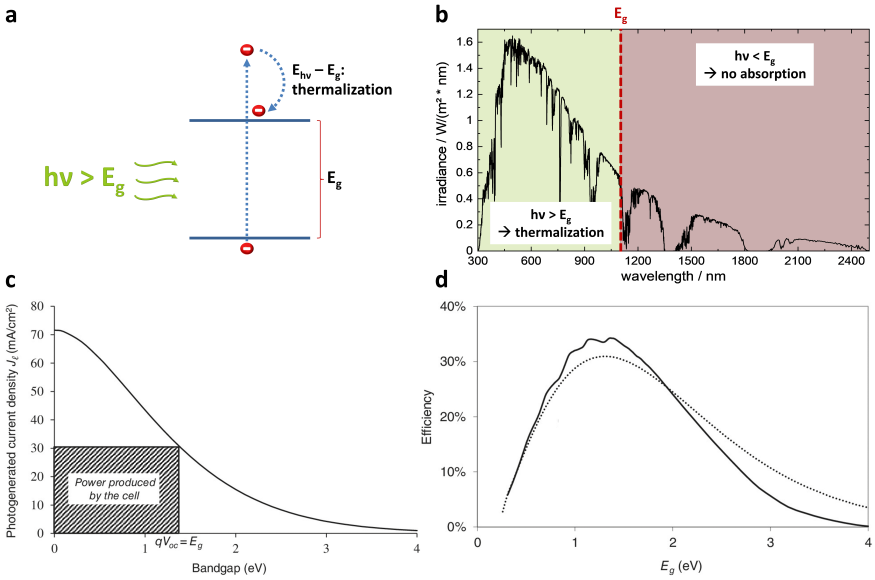

Figure 2.16: The Shockley-Queisser limit for single junctions. ***a,*** *Illustration of thermalization losses occurring, when a photon with energy larger than the band gap is absorbed and* ***b,*** *a solar AM 1.5 spectrum where for an exemplary band gap the regions of transmittance (red) and thermalization losses (green) are indicated.* ***c,*** *Maximum generated Photocurrent density over the band gap showing the trade-off between current and potential voltage. The rectangle indicates the maximal possible generated power.* ***d,*** *The actual Shockley-Queisser limit for AM 1.5 (solid line) and an ideal black body irradiation at 6000 K (dotted line). Images c and d reprinted from [119].*

Maybe the most fundamental limit for solar cell efficiency is the limit William Shockley and Hans J. Queisser introduced as "detailed balance limit" and which is simply called the Shockley-Queisser (SQ) limit nowadays. [120] First and foremost a very fundamental trade-off defines the ultimately achievable power output of a solar cell: The fact that photo-generated charge carriers relax towards the band edges very rapidly, rendering charge extraction of such "hot" carriers close to impossible. [121] As a result, the highest usable energy of an electron-hole pair generated by an absorption process is limited by the band gap (E_g) of the absorbing material. As schematically illustrated in Figure 2.16 a, any energy exceeding the band gap ($h\nu$ - E_g) is transformed in so called thermalization losses by a relaxation process. [122] At the same time, photon energy below the band gap of the absorbing material, (except very rarely occurring processes, e.g. two photon absorption [123]) results in transmission and no charge carrier excitation (Figure 2.16 b, red area). Thus an obvious trade-off between the amount of photons absorbed and the usable energy per absorbed photon results.

One can draw a graph targeting the maximum generated photo current density at AM 1.5 versus the wavelength as shown in Figure 2.16 c. [119] Since the band gap energy simultaneously defines an upper limit for the open circuit voltage ($E_g \geq e\ V_{OC}$), one can get a first impression of the efficiency limits by calculating the maximum generated power as area defined by the curve and the two axis. Now assuming ideal diode characteristics of a cell at room temperature and an internal quantum efficiency of unity, we can then calculate the maximum theoretically reachable efficiency of a solar cell under AM1.5 conditions depending on the band gap (see Figure 2.16). [119, 120] In case of silicon, an ultimate limit for power conversion efficiency of about 32 %, can be stated. Taking further inevitable losses into account, such as radiative recombination or free carrier absorption the efficiency limit for silicon is reduced further to levels of about 29 %. [124–126] Consequently with current efficiency records of 26.7 % for silicon solar cells (and 25.7 % for perovskite solar cells), the possible progress for single junctions is fundamentally limited.

2.5.2 Prospects and Challenges of Tandem Cells

Several strategies have been considered to overcome the fundamental limitations of single junctions. Many of them are geared towards minimized thermalization losses. [122] Besides strategies like graded band gaps [127] or photon down conversion [128, 129] the tandem solar cell concept is very promising. [130] As shown in Figure 2.17 a, the tandem

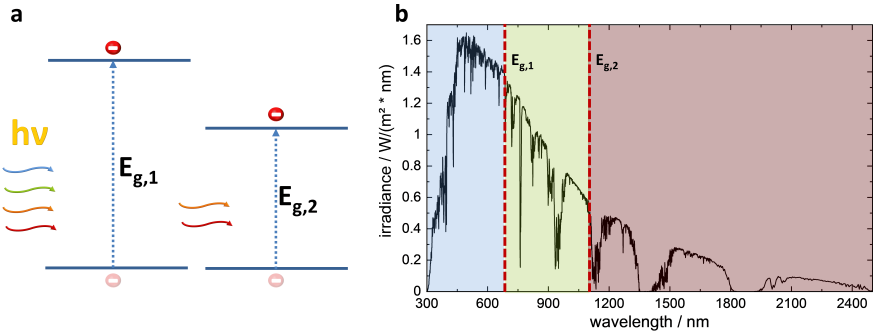

Figure 2.17: The tandem concept. ***a,*** *Energy diagrams and* ***b,*** *an AM 1.5 solar spectrum illustrating the concept of a tandem solar cell comprising two band gaps ($E_{g,1}$ and $E_{g,2}$).*

approach is based on the combination of two solar cells with different band gaps. A wide gap solar cell is utilized to efficiently convert high energy photons and a lower band gap cell is optimized to absorb lower energy photons, that are transmitted by the wide gap solar cell.

In turn light will get converted into electrical energy more efficiently, since thermalization losses now can be estimated as either $h\nu$ - $E_{g,2}$ for photon energies positioned between both band gaps (Figure 2.17 b green area) and $h\nu$ - $E_{g,1}$ for higher energies (Figure 2.17 blue area). In sum those thermalization losses can be substantially lower than inevitable losses of $h\nu$ - E_g in single junctions (Figure 2.16 b, green area). By this strategy it is theoretically possible to increase the efficiency limit to 42 % for tandem cells and finally 68 % for a hypothetical device with an infinite number of junctions. [131] Generally there are two main strategies that are applied to design tandem solar cells: the two terminal (2T) and the four terminal (4T) device architecture. Alternative concepts like three terminal approaches are mostly hybrids, combining partial aspects of both device architectures and will not be covered here in further detail. As shown in Figure 2.18, the fundamental difference between 2T and 4T concepts originates from the type of stacking used to connect the sub-cells. While a 4T tandem solar cell concept relies on the mechanical stacking of two separate solar cells, the 2T concept consists of two monolithically integrated solar cells. [132] This gives rise to very different requirements and challenges for both tandem concepts. Since for 4T solar cells light has to be transmitted through the high gap cell into the low gap sub-cell, two additional semi-transparent electrodes are necessary. [133–136] This requires on the one hand highly optimized semi-transparent electrodes, with a high electrical conductivity and high optical transmittance, most importantly in the near infrared. [133, 134] On the other hand, light out-coupling and subsequent in-coupling has to be optimized with minimum reflection losses. [137, 138]

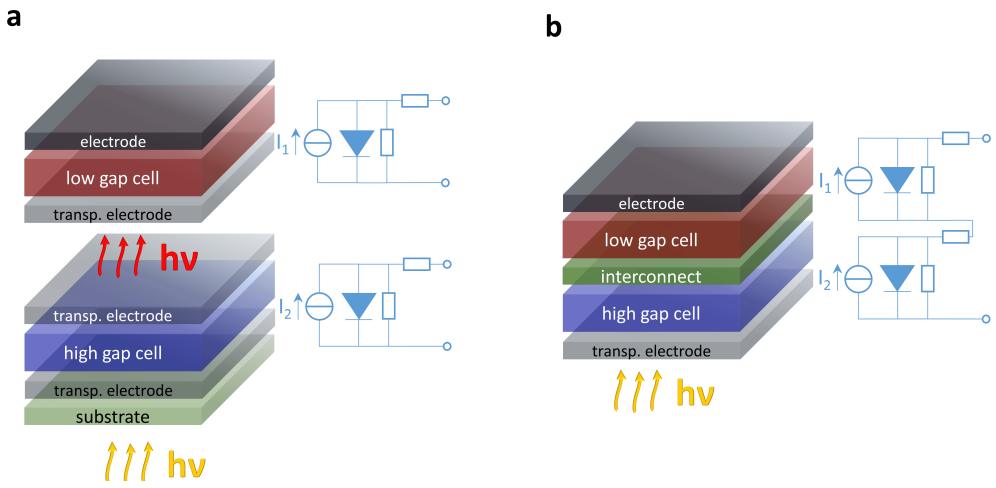

Figure 2.18: Tandem implementation. ***a,*** *Functional layer stack and according equivalent circuit models of 4 terminal (4T) and* ***b,*** *2 terminal (2T) tandem solar cells.*

In any case, electrode design and light management are the major challenges for 4T tandem solar cells. Electronically the 4T approach is rather advantageous due to the opportunity to separately root the sub-cells. For 2T tandem approaches, in stark contrast, the electronic configuration imposes one of the great challenge for monolithic integration of the two sub-cells. [130, 139] Firstly the recombination of charge carriers from the bottom cell needs to be facilitated with their counterparts originating from the top cell. [132, 140]

For this purpose often dedicated interlayers, so called "interconnects", are utilized. This is of special importance since typically a high and a low work function material are to be matched, which might lead to the formation of Schottky barriers. Since a solar cell, in the first approximation, can be described as a current source, a diode and two parasitic resistors (parallel R_p and series R_s) this leads to issues in case the current generated in both sub-cells does not match. [139, 141] In case of ideal subcells with $R_p \to \infty$ this means, according to Kirchhoff's law, that the sub-cell with lowest current will be limiting the overall current of the device. Consequently, great effort is invested to tune the optics of the two subcells in a way to achieve current matching in order to fully exploit the potential of monolithically integrated 2T tandem solar cells.

3 Formation of Perovskite Layers

On the path to perovskite solar cells with competitive power conversion efficiencies, control over the deposition and most importantly the crystallization process of the perovskite material is of utmost importance.

3.1 Perovskite Deposition Techniques

Please note that some of the one-step deposition solar cell data has already been shown in my master-thesis titled "Metalloxidbasierte Ladungsextraktionsschichten für Perowskit-Solarzellen". [142] The overlap with my thesis, which is mainly included in the first passage of this chapter, was introduced, to provide a full picture, since optimization of perovskite deposition was a continuous process extending from the beginning of my master thesis throughout my full PhD work and is still ongoing.

An obvious technique for the deposition of perovskite films from precursor solutions, is apparently a simple one-step spin coating process with a subsequent thermal annealing step. Over several years, most perovskite solar cell efficiency records were achieved using modified one-step deposition methods. Development of perovskite deposition in this work also started out by utilizing the one-step deposition approach. Here, several parts of the crystallization are taking place simultaneously. [29, 143] Supersaturation, nucleation and crystal growth are simultaneously triggered by thermal energy during the annealing step. Consequently, already small deviations in processing parameters like e.g. spin-coating speed or precursor concentration can result in drastic changes of the resulting perovskite layers. This is visible in Figure 3.1 a, where scanning electron microscopy images taken from nominally identical processing conditions in a one-step approach with $MAPbI_3$ deposited from DMF are shown. While it is possible to achieve continuous and vastly pinhole free layers, also irregularly formed, rough layers with a high density of pinholes are frequent results. Anyway we found, that integrating respective perovskite layers into a solar cell architecture as shown in Figure 3.1 b

and c can yield functional solar cells (Figure 3.1 d). Still the large variation of layer morphology causes an significant experimental spread in device properties. Due to the large statistical variation and the resulting need to process a large amount of devices, our first step of development was the implementation of alternative deposition strategies, that offer better control over the perovskite crystallisation process. To this regard we considered the so called complex assisted approach, that utilizes the ability of perovskite precursor materials like methylammonium iodide or lead iodide to form stable complexes with lewis bases like DMSO and enable a supersaturation of the precursor, without triggering the final crystallization (see chapter 2.2.2). To achieve this supersaturated state, in the so-called anti-solvent approach shown in 3.2 a is most frequently used.

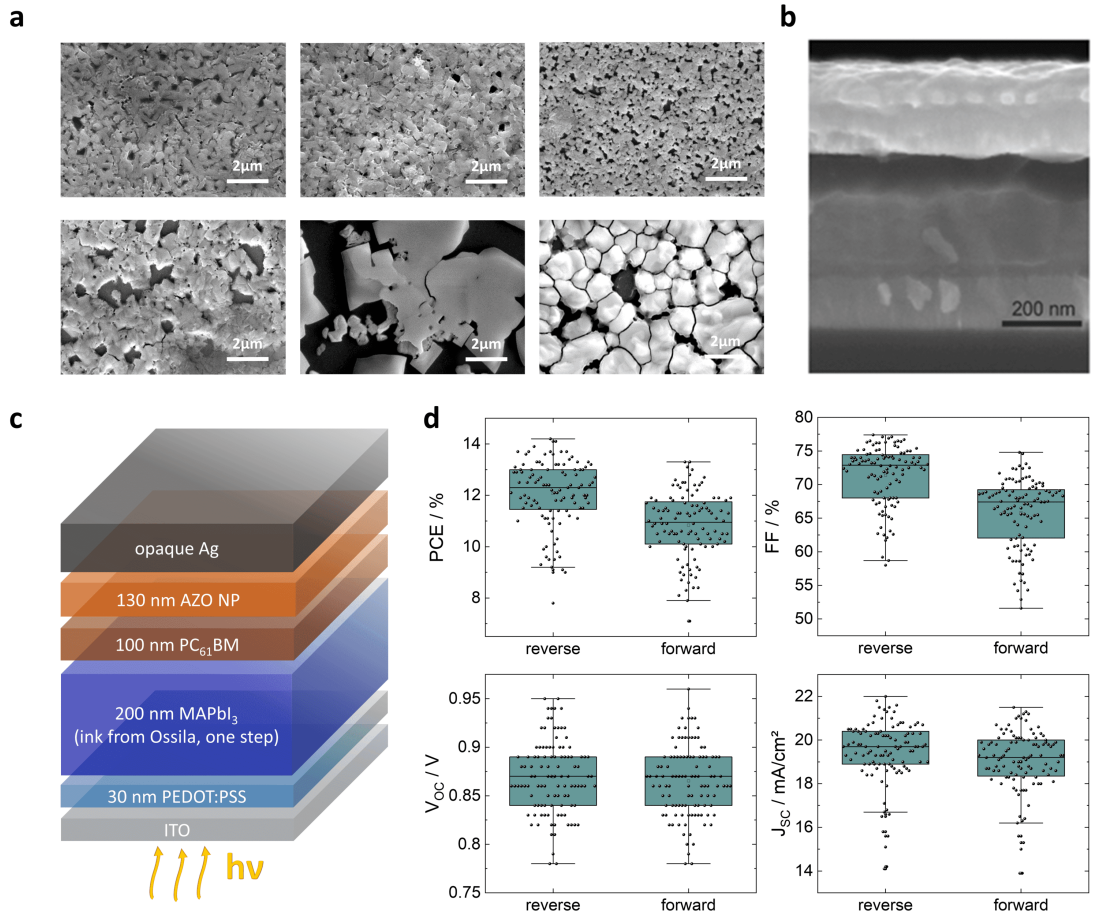

Figure 3.1: One-step processed perovskites. ***a,*** *$MAPbI_3$ layers deposited with nominally similar processing conditions.* ***b,*** *Cross sectional image of a full solar cell stack as also shown in* ***c,*** *as well as* ***d,*** *a statistical overview of solar cell characteristics from respective solar cells (box plots; median line with upper and lower box ranges denoting the 25 % and 75 % margins. The bars denote the outermost data points that are still inside another 1.5 interquatile range)*

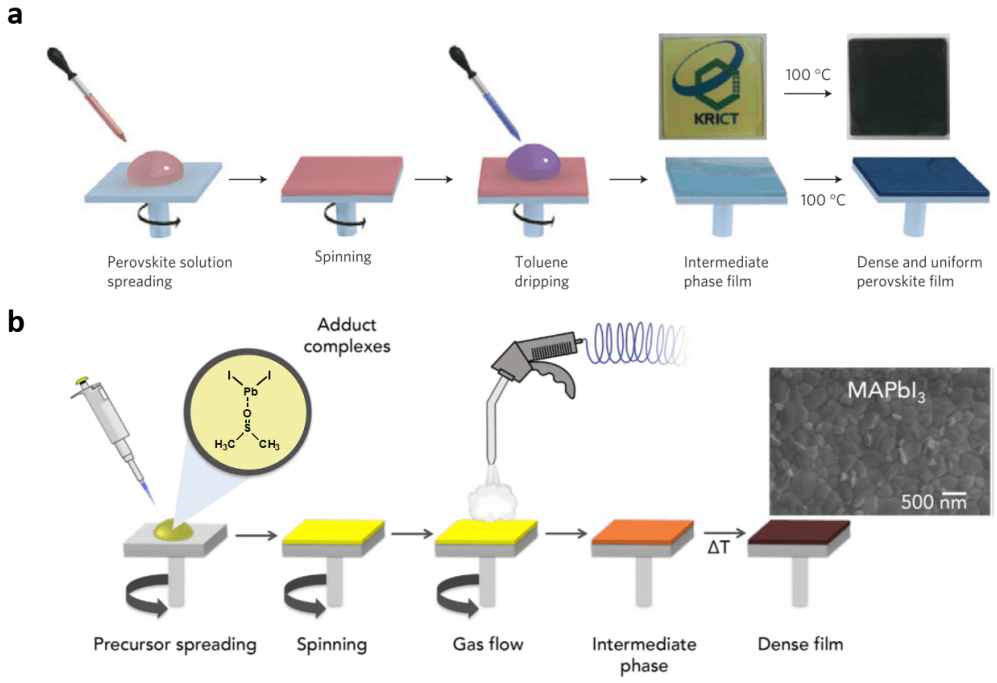

Figure 3.2: Complex assisted deposition techniques. ***a,*** *Schematic illustration of the anti-solvent assisted perovskite deposition process and* ***b,*** *the nitrogen gas flow assisted "gas quenching" approach. a, reprinted with permission from [29]. Copyright 2014 Nature Publishing Group. b, reprinted with permission from [37]. Copyright 2018 Elsevier.*

This deposition strategy relies on a rapid solvent-solvent interaction which again is subject to several uncertainties, as e.g. the properties of the anti-solvent impact greatly on the film formation. [144] Hence, precise timing and a strict deposition protocol has to be established and already small deviations result in significant experimental spread, as evidenced in Figure 3.3. These process deviations are becoming even more severe, if devices are prepared by different persons. Alternatively Conings et. al. established a strategy to achieve supersaturation by using a directed nitrogen gas flow that is used to drastically speed up the drying process without the need for anti-solvents (see Figure 3.2 b). [36, 37] Application of this strategy yields solar cells with a significantly reduced experimental spread as clearly visible in Figure 3.3. We experienced that this low experimental spread persists, if the respective layers and solar cells are processed by different persons, in part with very little experimental practice. As a consequence the gas quenching technique was chosen as standard perovskite deposition technique for this work.

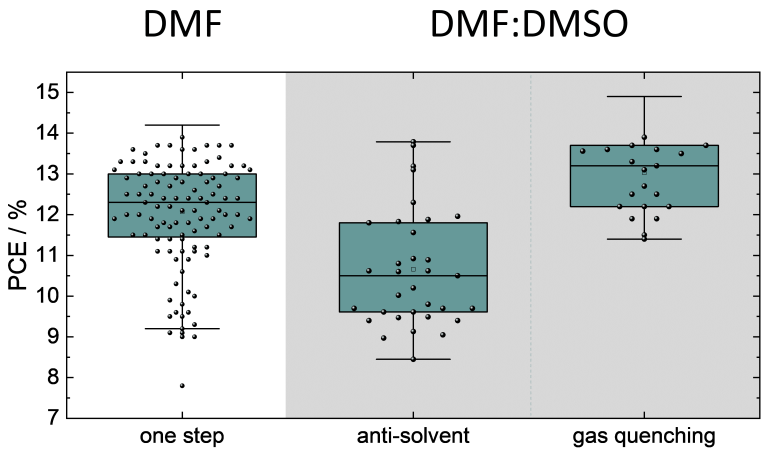

Figure 3.3: Statistical comparison of deposition techniques, *displaying the experimental spread of solar cell efficiencies. Box plots: median line with upper and lower box ranges denoting the 25% and 75% margins. The bars denote the outermost data points that are still inside another 1.5 interquatile range. The full data set for anti-solvent and gas quenching can be found in the Appendix Figure 11.1.*

3.2 Perovskite Layer Formation and Precursor Chemistry

While the gas quenching procedure enabled us to deposit perovskite layers very reproducibly, still the formation of crystals, their size and aspect ratio are highly important. Therefore we strived to understand what driving forces govern the perovskite crystallization process and how to manipulate them in a way to achieve active layers suitable for solar cell application, i.e. pinhole free, smooth coverage, consisting of large vertical continuous crystallites. Rough layers will compromise coverage of follow-up layers, while small, vertically inhomogeneous grains often comprise grain boundaries that hinder of charge transport, which is unfavourable for extraction efficiency. In addition, grain boundaries have been shown to provide trap states, recombination centres and are linked to degradation and ion migration. [88, 145] For highly efficient perovskite solar cells it is therefore necessary to minimize the number of grain boundaries in the active material.

3.2.1 Solvent Removal Speed and Contact Angle

One very frequently quoted potential driving force for perovskite crystallization is the speed with which supersaturation, nucleation and crystal growth are achieved. [146, 147] The already proposed deposition techniques (one-step, gas quenching and anti-solvent) provide a wide range of different timings for solvent removal. Hence, we conducted a direct comparison of perovskite layers deposited under otherwise similar processing conditions (100 °C annealing and 120 s spin coating) in order to systematically investigate the impact of solvent removal speed on the crystal formation of $MAPbI_3$ layers. For comparison, we also introduced a drop casting method as reference case with extremely slow solvent removal. All four deposition techniques were undertaken on the one hand with DMF as relatively high vapour pressure solvent (3.77 hPa at 20 °C) and on the other hand with DMSO, which has a significantly lower vapour pressure (0.56 hPa at 20 °C), to extend the scope of the comparison yet further. [148, 149] In this approach, as a measure for the solvent removal speed, we define the time between the start of the deposition or respective treatment and the observability of the brownish colour change in the deposited material.

Surprisingly, as visible in Figure 3.4, we did not observe significant differences in crystallite size (equivalent radii of grain areas observed in the SEM images). Please note that for the drop casted layers, charging impaired SEM image quality and only a small amount of larger grains could be evaluated. Due to the irregular morphology, also the incident angle of the electron cannot be guaranteed to be 90° and therefore some projection related misinterpretation cannot be entirely excluded. Anyhow we conclude that the observable crystal size is well within the size distributions also evidenced from other deposition techniques. This is even the more surprising, as solvent removal speeds between < 1 s (anti-solvent) and > 600 s (drop-casting) and therefore almost tree orders of magnitude are covered by this experiment. While we found clear morphological differences originating from the choice of deposition technique (see chapter 3), the crystallites, of which those structures consist, remained almost identical in size. Therefore we infer, that for the investigated precursor system, the speed in which supersaturation is reached may not be the dominant driving force for the development of crystallites.

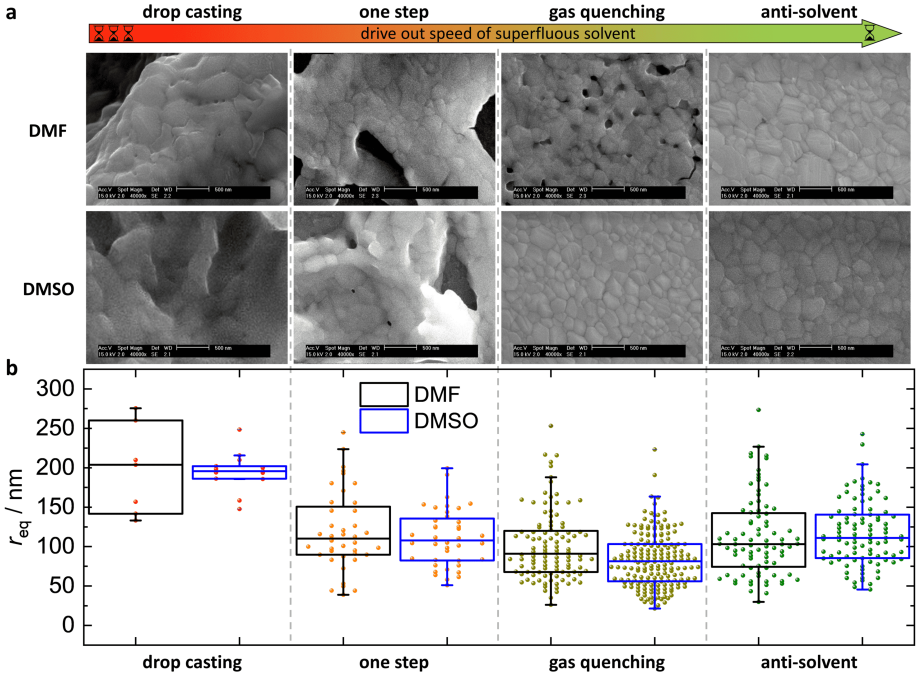

Figure 3.4: Solvent removal speed. ***a,*** *Scanning electron microscope images of perovskite layers made by different deposition strategies to realize various drying speed of the precursor solvent. The arrow on the top depicts the order of the processes with rising solvent removal speeds (For DMF drop casting: $>$ 10 min, one-step: $\approx$ 5 s, gas quenching $\approx$ 1 s; anti-solvent: $<$ 1 s. For DMSO drop casting: $>$ 10 min, one-step: $\approx$ 30 s, gas quenching $\approx$ 5 s; anti-solvent: $<$ 1 s)* ***b,*** *Box plots depicting the respective grain size distribution. For drop casting, due to strong morphological changes, only a small amount of larger grains could be evaluated. Box plots: median line with upper and lower box ranges denoting the 25% and 75% margins. The bars denote the outermost data points that are still inside another 1.5 interquatile range.*

Another readily quoted possible influence on the crystallization, is the substrate hydrophobicity. [52, 150, 151] A common measure for it, is the contact angle between the substrate and the perovskite precursor ink. To this end we chose PTAA as a hydrophobic substrate layer (and frequently used hole transport layer) and compared the resulting perovskite layers deposited on top to that deposited on ITO, which was already used in the previous experiments (Figure 3.5 a). Contact angle measurements of precursor ink droplets positioned on top of the two layers reveal significant differences, i.e. contact angles of approximately 36 ° on PTAA and $<$ 10 ° on ITO, (Figure 3.5 b). Still the gas quenching procedure affords a layer with similar size of the crystallites on both substrates (Figure 3.5 c, d). Accordingly, alike solvent removal speed, precursor contact angle with the underlying substrate appears to not majorly influence the crystallization of the perovskite.

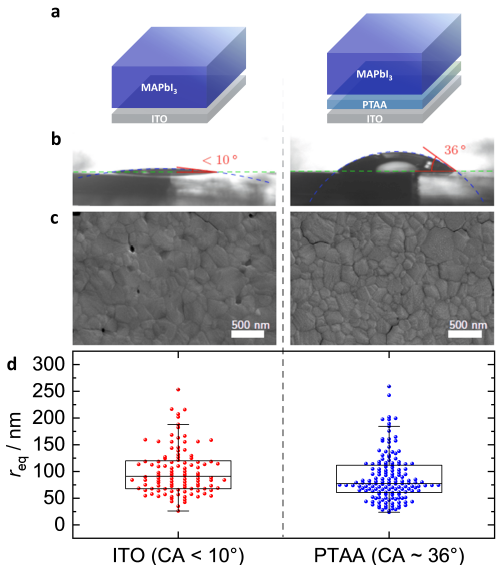

Figure 3.5: Contact angle influence. ***a,*** *Stack of $MAPbI_3$ layers deposited on undergrounds of ITO and PTAA that show significantly different contact angles with the perovskite precursor.* ***b,*** *Respective contact angle measurements and* ***c,*** *top view scanning electron microscope images showing similar grain size distribution. This is plotted in* ***d,*** *the derived equivalent radii as box plots. Box plots: median line with upper and lower box ranges denoting the 25% and 75% margins. The bars denote the outermost data points that are still inside another 1.5 interquatile range.*

3.2.2 Lead Complexes in Perovskite Precursors

Note: some parts of the measurement data used in this chapter were obtained in a collaboration with Dr. Feray Ünlü of the University of Cologne from the group of Prof. Dr. Sanjay Mathur and this data has also been used in her PhD thesis. [152] A respective manuscript is currently in preparation for publication. Other parts were published in:

Brinkmann, K.O. et al. "Extremely Robust Gas-Quenching Deposition of Halide Perovskites on Top of Hydrophobic Hole Transport Materials for Inverted (p–i–n) Solar Cells by Targeting the Precursor Wetting Issue" ACS Appl. Mater. Interfaces 2019, 11, 43, 40172–40179. [153]

Since solvent removal speed and substrate hydrophobicity did not show noticeable impact on the crystallite growth, we reasoned there must be another parameter that governs the crystallization process. Several reports evidence the presence of lead complexes in perovskite precursor solutions [41, 43] and some papers evidence the impact of lewis bases on the crystallization. [154–156] Additionally recent reports confirm the presence

of colloidal structures of perovskite complexes forming inside the precursor solution, that are assumed to act as seeds (see chapter 2.2.2) for perovskite crystallization. [44, 46] Currently most investigations targeting the nature of lead complexes inside perovskite precursor solutions are conducted optically in highly diluted precursor solutions on the order of 10^{-1} mM. Perovskite precursors used for layer deposition on the other hand are typically more concentrated (0.1 - 3 M). Therefore we teamed up with the group for Inorganic and Materials Chemistry of the University of Cologne (M.Sc. Feray Ünlü, Prof. Sanjay Mathur) and the department of Organic Chemistry (Dr. Andreas Kotthaus, Prof. Stefan Kirsch) from the University of Wuppertal to conduct nuclear molecular resonance spectroscopy (NMR) on precursor solutions with relevant concentrations. As reference solvent systems, similar as above, we chose the two most common solvents for perovskite inks: DMF and DMSO. From their chemical structure (see Figure 3.6) one can reason some similarities in their ability to act as lewis bases. Both structures display two lone electron pairs on the oxygen atom and another one either on the nitrogen (DMF) or on the sulphur (DMSO) atom. On the other hand, DMSO is reported to show a slightly higher donor number (a common measure for lewis basicity) of 29.8 kcal mol^{-1} in comparison to DMF with 26.6 kcal mol^{-1}. [157, 158] Taken together we might expect a notable, yet no fundamentally different behaviour of the two solvent systems with respect to their ability to interact with perovskite precursors like PbI_2 or MAI. Since the amount of available material has been shown to impact on the complexes in highly diluted perovskite precursors, [41, 43] we first conducted our investigations as concentration series. Figure 3.7 presents the ^{207}Pb NMR chemical shifts observed in the $MAPbI_3$ perovskite and PbI_2 solutions in deuterated variants of DMF and DMSO (DMF-d_7 and DMSO-d_6) as a function of the concentration. A high chemical shift (down field) indicates diminishing electron density (de-shielding) around the Pb centre and lower chemical shifts (up field) indicates a higher electron density around the lead centre, which shields the Pb nucleus from the external field.

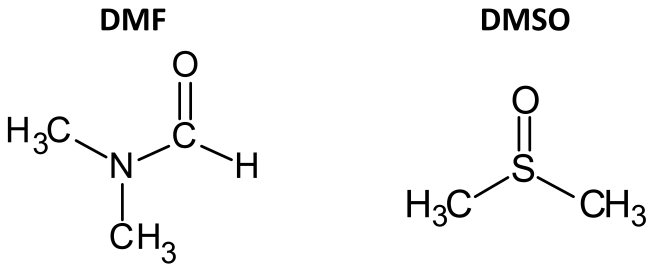

Figure 3.6: *Chemical structure of dimethylformamid (DMF) and dimethylsulfoxide (DMSO).*

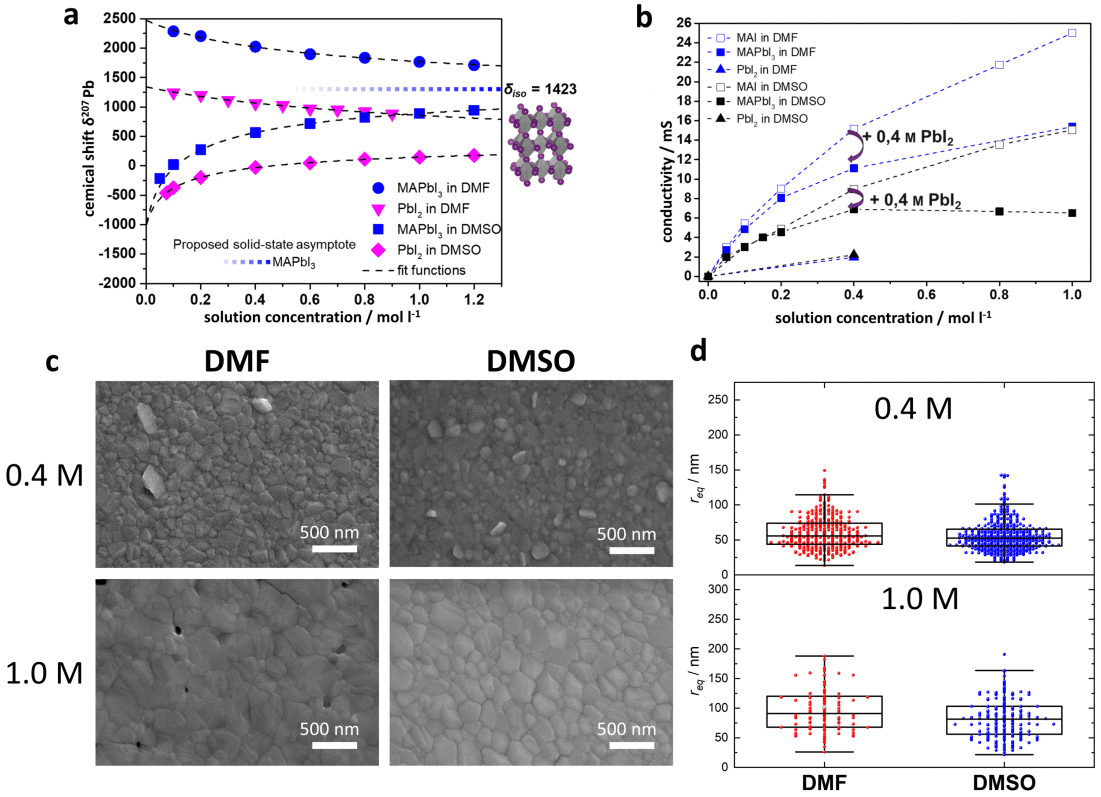

Figure 3.7: Lead complexes in $MAPbI_3$ precursors. ***a,*** *^{207}Pb NMR chemical shifts of concentration series of PbI_2 and $MAPbI_3$ dissolved in either DMF or DMSO. The dotted line depicts the solid state $MAPbI_3$ NMR. [159]* ***b,*** *Electrochemical conductivity measurements of PbI_2, MAI and $MAPbI_3$ in DMF and DMSO.* ***c,*** *Scanning electron microscopy images of $MAPbI_3$ layers deposited 0.4 M and 1.0 M concentrated stoichiometric solutions in DMF, DMSO and* ***d,*** *respective grain size distributions. Box plots: median line with upper and lower box ranges denoting the 25% and 75% margins. The bars denote the outermost data points that are still inside another 1.5 interquatile range.*

Chemical shifts in this work are reported on a ppm scale relative to the standard $Pb(CH_3)_4$. In all NMR measurements, only a single resonance peak was observed for all measured solutions. This is indicative of a chemical exchange among different iodoplumbate species, which is fast on the NMR scale and thus delivers only an averaged resonance signal. [160] Already for PbI_2 solutions, a clear difference between both solvents is evident, with PbI_2 solutions in DMF being located more in the down field than solutions in DMSO. A lower electron density (de-shielding) of the lead core in DMF than in DMSO, can therefore be expected, a trend that is likewise found in the stoichiometric mix (PbI_2 and MAI). This is in line with the higher donor number of DMSO which implies a higher likeliness of DMSO to act as an electron donor and consequently increase electron density around the lead core by complexation.

If now the concentration of both solutions is increased,we evidenced up field shift in DMF, while for DMSO based solutions we found a clear down field shift. Most intriguingly the development of the both signals with rising concentrations continuously approach each other on a seemingly asymptotic path. An estimated asymptote for both series could be located at 1400 - 1450 ppm, which is in striking resemblence with values that have been reported for $MAPbI_3$ solid state NMR measurements (i.e. 1423 ppm). [159] As outlined above the chemical shift for lead cores has to be understood as an average over all species present inside the precursor solution. Therefore, we reason this observation to depict a more frequent appearance of corner-sharing 3D perovskite like colloidal structures, as has been anticipated in very recent literature. [44, 46] Following this theory, in extremely low concentrations, like e.g. used for optical complex characterisation, a huge abundance of solvent molecules is available to separate the singular complexes by solvatisation, which might be the reason for the strongly different behaviour with respect to the chemical shift of DMF and DMSO in these regions compared to that found in our work. [41, 43] With further increasing the concentration, the separation of complexes is less and less pronounced and larger colloidal, corner sharing structures (indicated by the trend towards the solid state 3D $MAPbI_3$ NMR signal) might appear, which is in line with observations by dynamic light scattering reported recently. [41, 43] As an complimentary experiment, we performed conductivity measurements in $MAPbI_3$ precursor solutions and in pure MAI and PbI_2 solutions. As visible in Figure 3.7 b the first obvious observation is a strikingly higher impact of the MAI concentration on the conductivity, than that of the PbI_2 concentration. This can be explained by the stronger ionic nature of MAI than that of PbI_2, where solvation or complexation rather than dissociation is becoming increasingly important. [161] Also we evidenced a generally lower conductivity of precursors based on DMSO than those based on DMF, which is very likely linked to different viscosities ($\eta_{DMSO,25\,^\circ C}$= 1.99 cP; $\eta_{DMF,25\,^\circ C}$ = 0.89 cP) of the two solvents. [162, 163] It is well known that higher viscosity directly impacts ion mobility and therefore conductivity. [164] Viscosity is likely also the origin of the levelling of MAI conductivity, as it typically likewise increases with increasing concentration. Anyhow the direct comparison of MAI and $MAPbI_3$ offers most intriguing insight: While for low concentrations (< 0.2 mol l^{-1}) the conductivity of $MAPbI_3$ almost resembles that of MAI, for higher concentrations (> 0.2 mol l^{-1}) the conductivity of the $MAPbI_3$ solution falls significantly below that of the pure MAI solution. This is yet another strong indication for the theory of solid state like perovskite structures being already present in the precursor solution. Colloidal 3D-perovskite-like structures inside the precursor solution would be expected to bear a far lower charge/volume ratio, which therefore significantly reduces their contribution to electrical conductivity.

While this reasoning might provide a new viewpoint on the mechanisms taking place inside the perovskite precursor solution, it stresses a more faceted view on the role of lead complexing on the final crystallization. Since liquid deposition techniques usually rely on an increase of concentration until crystallisation occurs, it could be expected, that the progressing formation of 3D corner sharing structures might diminish the impact of lead-solvent complexes on the final crystallization process. By a direct comparison of perovskite layers deposited from DMF and DMSO solution at both 0.4 M and 1.0 M concentration (Figure 3.7 c,d) accordingly we did not evidence significant differences in crystal sizes.

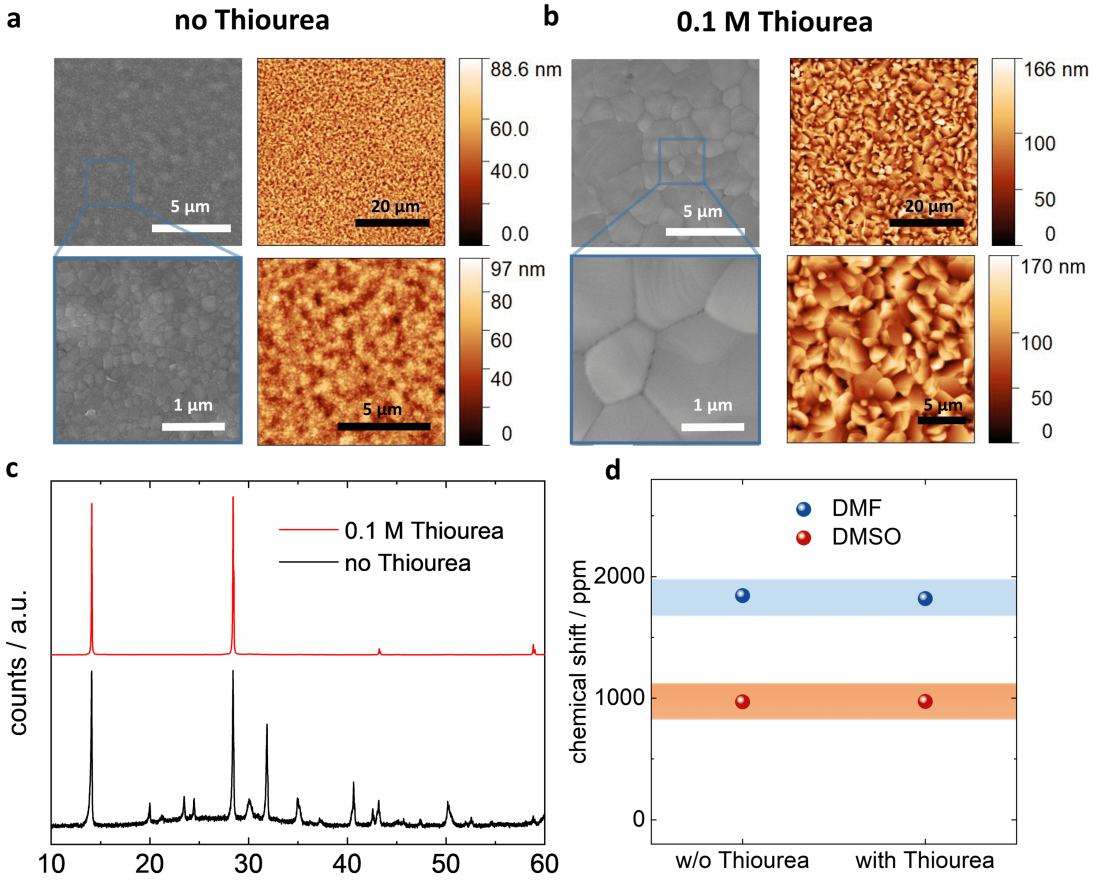

Figure 3.8: Impact of thiourea. ***a,*** *Scanning electron and atomic force microscopy images of $MAPbI_3$ layers deposited from 1 M solution of DMF:DMSO 7:3 without and* ***b,*** *with addition of 0.1 M of thiourea to the precursor solution.* ***c,*** *X-ray diffractograms of respective layers and* ***d,*** *chemical shifts of 1 M $MAPbI_3$ precursors with and without thiouread additive in both DMF and DMSO as solvent. a, b, c, reprinted with permission from [153]. Copyright 2019 American Chemical Society.*

To investigate this topic from a different perspective, we chose the lewis base additive thiourea, that has already been reported to significantly increase the size of crystallites in perovskite layers, which so far typically is attributed to a potential interaction with lead. [154, 155] We decided to not use the commonly used $Pb(SCN)_2$, since it would add additional lead atoms to the solution, that might change the effective lead concentration and might bring along additional effects caused by concentration like discussed above. As shown in Figure 3.8 a, b the effect of adding 0.1 M thiourea to the precursor solution (without changing the original precursor concentration) resulted in a drastic increase in crystallite size. Simultaneously in X-ray diffraction (Figure 3.8 c), distinct ordering occurs. With the thiourea additive, only the 110, 220, 330 and 440 reflexes are detected, which confirms the strong impact of the additive on crystallization. Anyhow comparing the chemical shifts determined by NMR (Figure 3.8 d), for 1 M solutions in either DMF or DMSO, we were not able to detect any significant change upon addition of thiourea. This is indeed surprising, since thiourea is known as a sulphur donor and has been predicted to show very strong coordination tendency with PbI_2, even more than in the case of DMF or DMSO. [47] Nevertheless we clearly see, that at least in the original precursor, the addition of thiourea does not strongly affect the electrostatic environment of the lead core and is hence most likely not a dominant factor for lead complexing in the precursor. Finally, in light of the above set of experiments, we conclude, that while they might have influence on perovskite ink stability and processability (see e.g. [47]), the lead complexing in the original solution might not necessarily be indicative for the shape and size of resulting crystallites. Still we want to highlight that this, by no means excludes the possible impact of lead complexes in the very moment of crystallization. Possibly in the original precursor solution the abundance of solvent molecules dominates the complexation of lead, while throughout the drying process, the balance shifts towards coordination of the additive with lead precursors. To investigate this issue, a series of in situ grazing incidence wide angle X-ray scattering experiments in collaboration with M.Sc. Lena Merten, M.Sc. Ekaterina Kneschaurek, Dr. Alexander Hinderhofer and Prof. Frank Schreiber from the University of Tübingen are scheduled in order to unravel crystallisation dynamics during the gas quenching procedure. Unfortunately, this falls beyond the time frame of this work and will be published separately.

3.3 Gas Quenching on Hydrophobic Surfaces

Note: parts of this chapter have been published in:

Brinkmann, K.O. et al. "Extremely Robust Gas-Quenching Deposition of Halide Perovskites on Top of Hydrophobic Hole Transport Materials for Inverted (p–i–n) Solar Cells by Targeting the Precursor Wetting Issue" ACS Appl. Mater. Interfaces 2019, 11, 43, 40172–40179. [153]

While the introduction of gas quenching in chapter 3.1 significantly reduced process deviation and improved robustness of perovskite deposition on top of PEDOT:PSS, using PEDOT:PSS carries fundamental downsides. Aside from the frequently cited ones, namely being hygroscopic, acidic and optically absorbing, its application in perovskite solar cells often induces unintentional doping and a consequently typically very high charge carrier density of the PEDOT:PSS HTL. [165–167] It has been reported that PEDOT:PSS' conductivity can significantly increase, if exposed to DMF or MAI, common perovskite precursor ingredients, which even renders it viable as semitransparent electrode. [165, 168] While being potentially beneficial for an application as electrode, it proves disadvantageous for its application as hole selective contact in perovskite solar cells, since an abundance of charge carriers located at the interface to the perovskite, tends to compromise the interface's selectivity and also might cause hysteresis (see Chapter 2.3.3). [169, 170] While it is possible to achieve highly efficient solar cells with PEDOT:PSS as HTL, it usually requires rather distinct chemical tailoring. [170, 171] As the need for sophisticated interface modification counteracts on our pursuit for a robust and easy to use perovskite solar cell fabrication protocol, that yields high efficiency, we considered alternative hole transport materials. Several high performing p-i-n devices rely on polymer hole transporting layers (HTLs), such as polytriarylamine (PTAA) and poly(4-butylphenyldiphenylamine) (poly-TPD), that are highly non-polar and hydrophobic. [52, 144, 172–174] Unfortunately, perovskite precursor solvents on the other hand are usually highly polar, which leads to high contact angles and severe wetting issues of the perovskite precursor on these polymers, that typically results in poor surface coverage and pin-holes. [52, 175–177] This was clearly evident when we directly transferred our gas quenching approach from the PEDOT:PSS to the PTAA hole extraction layer. On the upside, using PTAA as HTL afforded device efficiencies of up to 17 % (see Figure 3.9 b). Anyhow, the introduction of PTAA as HTL also caused a dramatically increased process variation, which in turn necessitated huge sets of devices to achieve statistically significant conclusions for follow up experimentation.

In some works, wetting issues are circumvented by introducing an interlayer of a conjugated polyelectrolyte, such as Poly[(9,9-bis(3'-(N,N-dimethylamino)propyl)-2,7-fluorene)-alt-2,7-(9,9–dioctylfluorene)] (PFN) or an ionic surface treatment by e.g. pheylethylammonium iodide (PEAI) or adding dedicated surfactants to the perovskite solution. [144, 174, 177] Our distinct aim was to study the wetting issue on a more fundamental level.

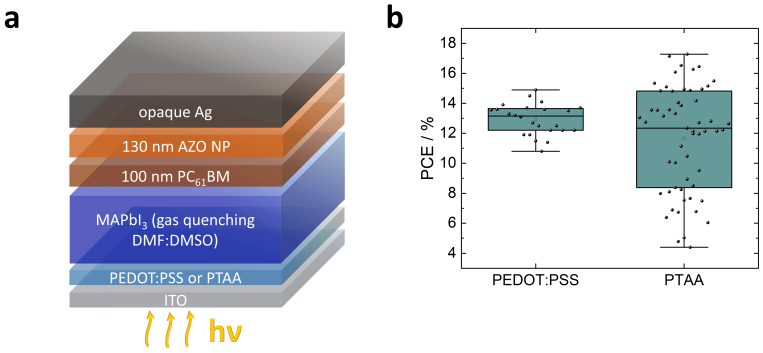

Figure 3.9: ***a,*** *Solar cell stack and* ***b,*** *statistical solar cell PCE distribution on top of PEDOT:PSS and PTAA undergrounds. Box plots: median line with upper and lower box ranges denoting the 25% and 75% margins. The bars denote the outermost data points that are still inside another 1.5 interquatile range. The full data set for both techniques are included in Appendix Figure 11.1 and Figure 3.16 respectively.*

3.3.1 Origin of Precursor De-Wetting and How to Overcome it

To estimate the wetting and solubility behaviour of solvents, different factors have to be taken into account. As is shown in Table 1, for all solvents in this study (DMF, DMSO and n-methyl-pyrrolidone (NMP)) the Snyder polarity index, which is a measure for the ability of a solvent to dissolve polar solutes (calculated from measurements on test solvents by Rohrschneider et al. [178]), ranges between 6.4 (DMF) and 7.2 (DMSO), which would render them roughly similar in their ability to solve lead halide salts, such as PbI_2 or $PbBr_2$. [179, 180] Additionally the surface tension of NMP is located between that of DMF and DMSO. [181, 182] Nevertheless, measurements of contact angles of all three solvents on PTAA surfaces are showing obvious differences (Table 1). In order to explain this phenomenon, one has to take into account the dipole-related solid-liquid interaction. The (static) dielectric constant, which can be used as a measure of solvent polarity, shows a clear decline from DMSO via DMF to NMP, in line with the trend in contact angle. [179, 180, 183] Due to similar polar groups, the dielectric constant of DMF and NMP is differing only slightly.

Table 3.1: *Important parameters of DMF, DMSO and NMP: Polarity index, [179, 180] surface tension, [181, 182] permittivity, [180, 183] hydrophilic-lipophilic balance (HLB), [184, 185] measured contact angle (derived from 7 drops each) and vapor pressure. [186]*

solvent	**polarity index (Snyder)**	**surface tension / mN m^{-1} at 25 °C**	**permittivity ϵ_r**	**HLB (Griffin, calculated)**	**contact angle with PTAA / °**	**vapor pressure / hPa at 20 °C**
ref.	[179, 180]	[181, 182]	[180, 183]	[184, 185]	measured	[186]
DMSO	7.2	42.9	46.8	12.4	45.6±2.0	0.56
DMF	6.4	38.2	36.7	11.6	25.6±1.3	3.77
NMP	6.8	40.8	32.0	8.2	12.0±0.8	0.32

To access the origin of different wetting behaviour, the Hydrophilic-Lipophilic-Balance (HLB), originally introduced by Griffin for emulsifiers, is calculated (HLB = 20 × (1 - M_L/M) with M_L being the molar weight of the lipophilic part and M stating the overall molecular weight). [184, 185] HLB provides a measure for the ratio of polar to non-polar components within a molecule. A decreasing HLB indicates the increasing ability of a polar molecule to interact with a non-polar counterpart. As NMP contains several non-polar -CH_2 groups, it has a lower HLB-index than DMF and DMSO (see Table 3.1). Taken together, the high contact angle of DMSO on PTAA is a result of a relatively high dipole moment combined with a negligible amount of lipophilic component (high HLB). DMF and NMP exhibit considerably lower dipole moments, and NMP additionally has a notable lipophilic part and consequently low HLB, that combined afford the best wetting behaviour on top of PTAA. For the preparation of perovskite thin films with controlled crystallization, the precursors need to be dissolved in a mixture of DMF with DMSO or NMP as co-solvent. The combined HLB_{res} of the solvent mixture can simply be calculated by the weighted arithmetic mean of the singular HLB values: $HLB_{res} = \frac{W_A \times HBL_A + W_B \times HBL_B}{W_A + W_B}$, with $W_{A/B}$ denoting the respective amounts of solvent A and B. [185] A rough estimate of the resulting dielectric constant can be derived in a similar way. [187] In accordance with this assumption, the measured contact angle of DMF:DMSO and DMF:NMP mixtures on a PTAA surface varies linearly with the mixing ratio of the solvents (Figure 3.10). The overall variation of the contact angle for the most commonly used mixing ratios of co-solvent:solvent of 1:9 and 3:7 would not indicate notable differences as their contact angle on PTAA is almost identical, i.e. 3° and 9° between DMF:DMSO and DMF:NMP, respectively.

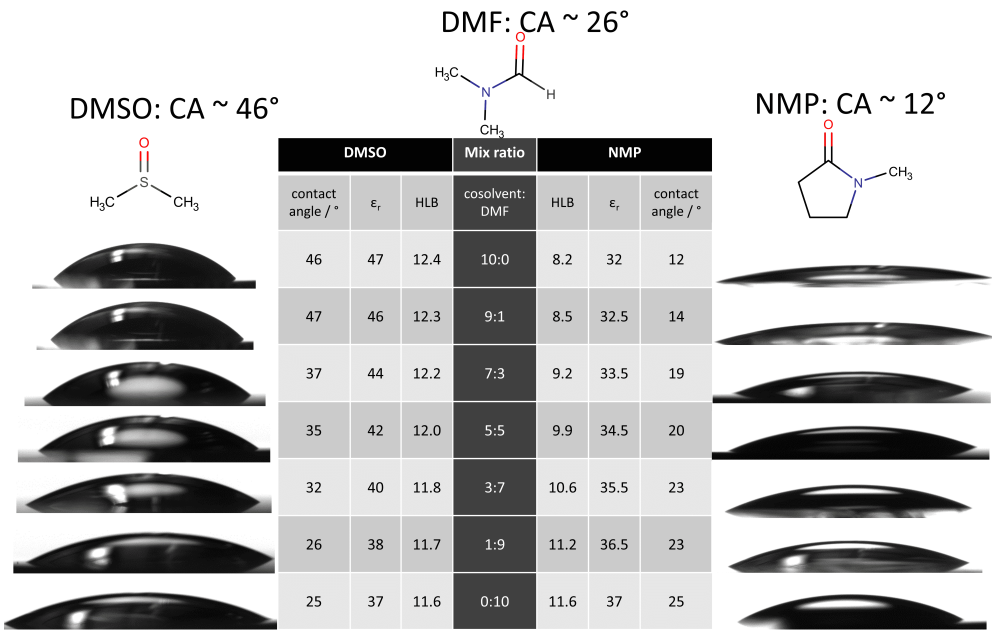

DMSO			Mix ratio	NMP		
contact angle / °	ε_r	HLB	cosolvent: DMF	HLB	ε_r	contact angle / °
46	47	12.4	10:0	8.2	32	12
47	46	12.3	9:1	8.5	32.5	14
37	44	12.2	7:3	9.2	33.5	19
35	42	12.0	5:5	9.9	34.5	20
32	40	11.8	3:7	10.6	35.5	23
26	38	11.7	1:9	11.2	36.5	23
25	37	11.6	0:10	11.6	37	25

Figure 3.10: *Contact angle measurements of DMF:DMSO and DMF:NMP mixtures on PTAA including calculated permittivity and HLB values of the mixtures. The typical relative uncertainty in the determination of the contact angle is 5 %. Reprinted with permission from [153]. Copyright 2019 American Chemical Society.*

Nevertheless, if directly applied in a perovskite deposition process, a striking difference between DMF:DMSO and DMF:NMP is found (Figure 3.11). The crystallinity of all resulting perovskite layers has been studied with XRD (Figure 3.12). According to the Scherrer equation, we do not expect any noticeable broadening of the XRD peaks due to the size of the crystallites (in z-direction), which are larger than 200 nm. [188, 189] Rather, the line width of the XRD peaks is governed by the resolution limits of the XRD equipment. Hence no noticeable difference has been found in the diffractograms indicating well crystallized perovskite materials with negligible crystallized precursor residuals. On the other hand perovskite layers deposited from precursors with increasing the DMSO concentration show an increased general tendency to de-wet. Furthermore, the timing of the gas quenching procedure hugely impacts both surface coverage and perovskite crystal shape (Figure 3.11, Table 3.2). For a 1:9 DMSO content, which shows fairly reasonable surface coverage of 97 % - 99 %, a quenching delay (time span after the ramp is finished until the start of the gas quenching process) exceeding 10 s results in inhomogeneous crystal formation and a concomitant reduction of the mean crystal size. With increased DMSO concentration the surface coverage of the perovskite layers decreases drastically over 81 % - 95 % for 3:7 down to 25 % - 77 % for 5:5 mixing ratio.

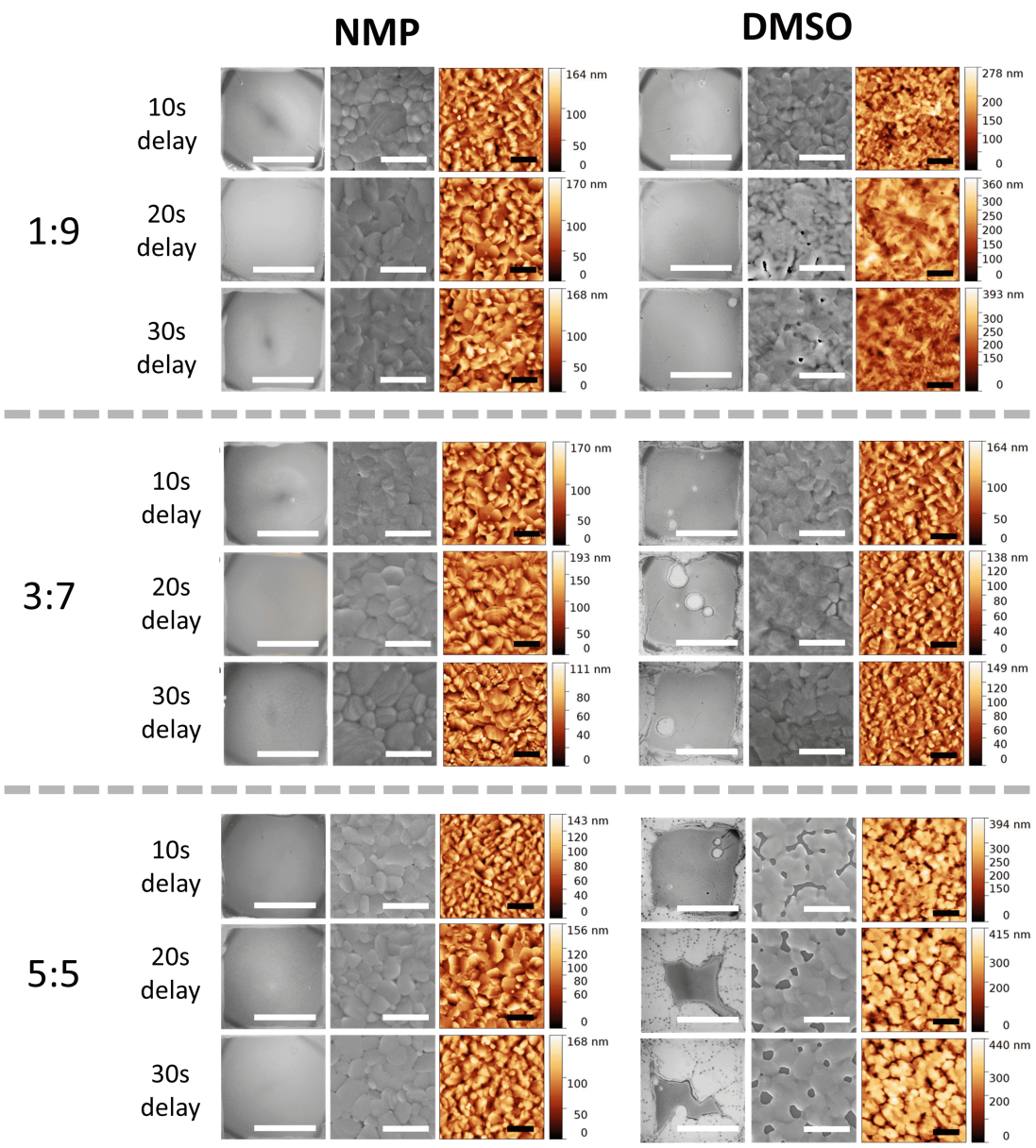

Figure 3.11: *Optical microscope, SEM and AFM images of perovskite layers prepared on PTAA layers with diffrent co-solvent : solvent ratios and varied quenching delay times for DMSO and NMP co-solvent. The bars for microscope images represent 1 cm. In AFM and SEM images the scale for the bars is 5 µm. Reprinted with permission from [153]. Copyright 2019 American Chemical Society.*

In striking contrast, if NMP is used as co-solvent in a NMP:DMF mixture, perfect coverage (>99 %) and favorable perovskite crystal formation is observed, largely independent of the chosen mixing ratio and timing of the gas quenching procedure (Figure 3.11, Table 3.2).

Table 3.2: *Mean grain sizes (equivalent sqare) derived from watershade algorithm (AFM images and microscopy images Figure 3.11) of perovskite layers prepared on PTAA layers with different co-solvent:solvent ratios and varied quenching delay times for DMSO and NMP co-solvent.*

	quenching delay / s	**grain size / µm (equivalent sqare)**		
co-solvent ratio		**1:9**	**3:7**	**5:5**
DMSO	10	0.90	1.01	0.99
	20	0.74	0.97	1.08
	30	0.56	0.84	1.13
NMP	10	0.95	0.95	0.91
	20	1.04	1.19	1.04
	30	0.99	1.08	0.92

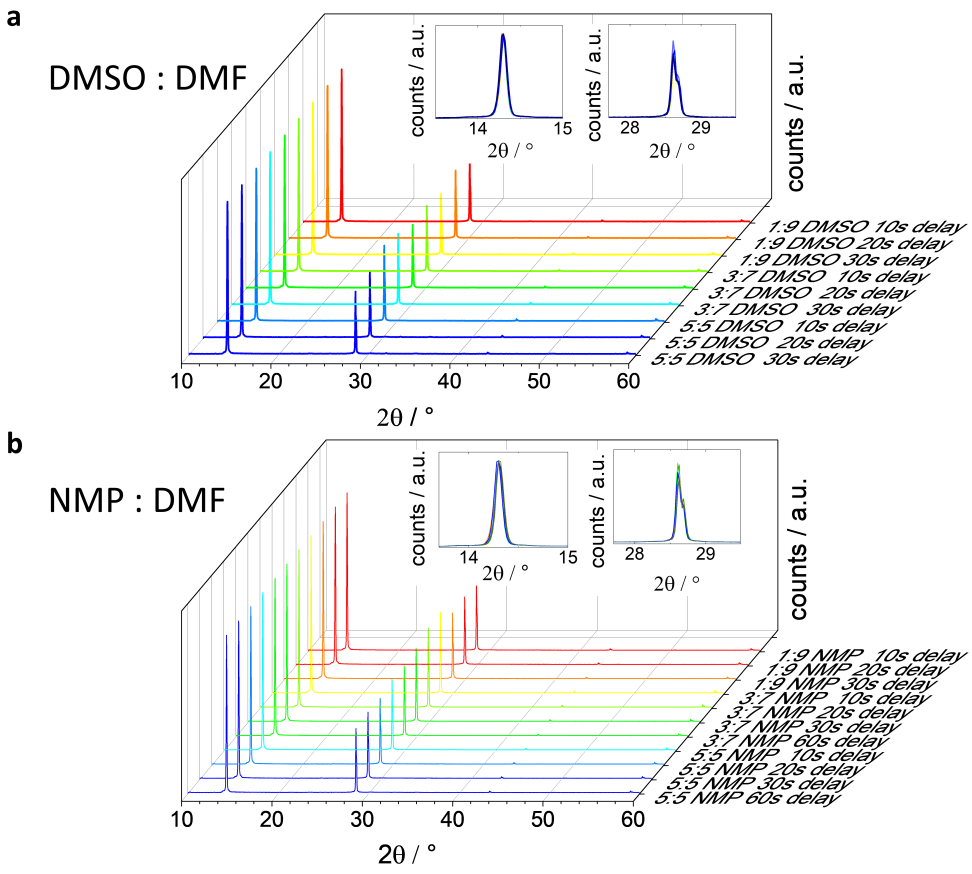

Figure 3.12: *X-ray diffractograms of $MAPbI_3$ layers fabricated with diffrent co-solvent : solvent ratio and processing timing utilizing* ***a,*** *DMSO and* ***b,*** *NMP as co-solvent. Insets are magnified views of the 110 and 220 tetragonal reflex. Reprinted with permission from [153]. Copyright 2019 American Chemical Society.*

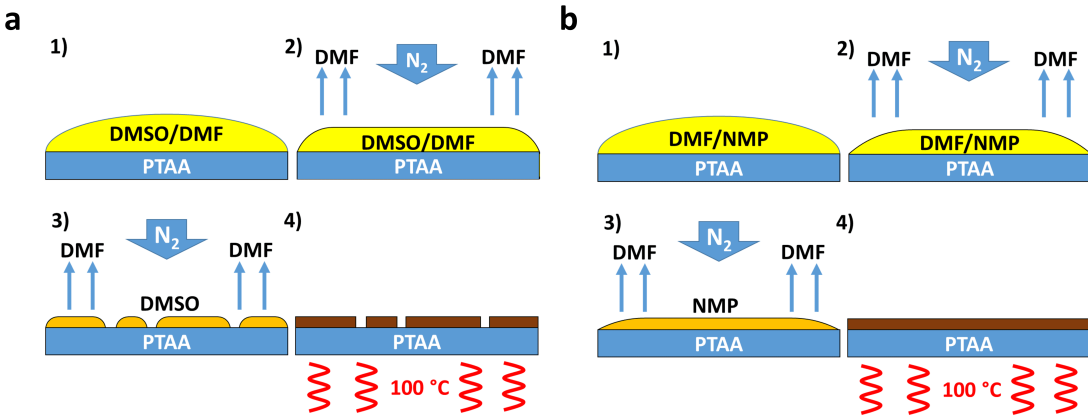

Figure 3.13: *Proposed schematics displaying the drying (and dewetting) process for* ***a,*** *DMSO and* ***b,*** *NMP co-solvent. Reprinted with permission from [153]. Copyright 2019 American Chemical Society.*

For deeper insight into these phenomena, the different boiling points and differing vapour pressures of DMF and its respective co-solvent have to be considered. As shown in Table 3.1 the vapour pressure of DMF at 20 °C exceeds that of the co-solvents by approximately one order of magnitude. The gas quenching technique exhibits a non-negligible delay time for evaporation of the excess solvent before supersaturation occurs. Owing to the lower vapour pressure of the co-solvent this delay-time increases with increasing the co-solvent ratio in the solvent mixture. During the deposition process and even more severely from the moment the gas quenching is started (Figure 3.13 step 2), we can expect that the evaporation rate of DMF is substantially higher than that of DMSO or NMP. Solvents with a high boiling point will cause some retardation of the drying process. In the present case, for a DMSO:DMF or NMP:DMF solvent system the drying process is expected to consist of two superimposed processes: firstly (step 1), the relatively fast evaporation of the DMF main solvent and secondly the by far slower evaporation of DMSO or NMP co-solvent (step 2). Consequently, during the drying process the co-solvent:solvent ratio is continuously increasing, which causes the contact angle with PTAA to ultimately approach that of the pure co-solvent (step 3) before the intermediate forms (step 4). This contact angle transformation can be directly observed, by mimicking the drying process in a dedicated experiment, where a drop of a co-solvent:DMF mixture has been carefully exposed to an air flow to increase the evaporation rate of the solvents (Figure 3.14). While contact angles of NMP:DMF mixtures remain low and fairly unchanged during the drying process, for DMSO:DMF mixtures a notable increase from 33° to 46° can be found. The latter contact angle corresponds to that of pure DMSO on PTAA. The contact angle of pure DMF remains unchanged upon drying as shown in Figure 3.15.

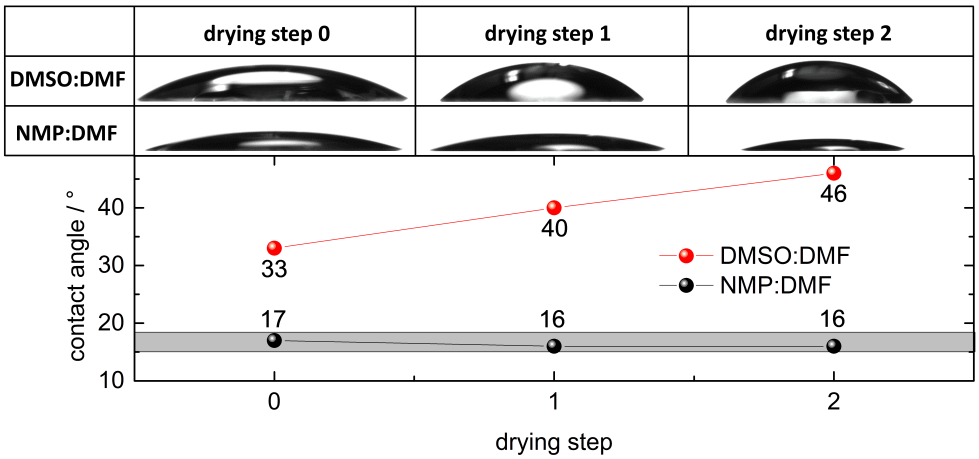

Figure 3.14: *Contact angle development of DMF:co-solvent 5:5 mixtures during drying process (exposure to careful airflow). Reprinted with permission from [153]. Copyright 2019 American Chemical Society.*

Iteration	Contact angle
1	29
2	28
3	29

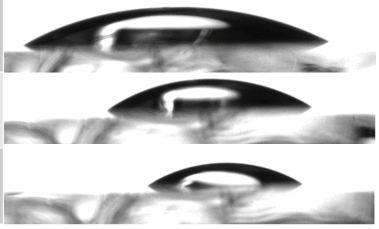

Figure 3.15: *Contact angle development of pure DMF during drying process (exposure to careful airflow). Reprinted with permission from [153]. Copyright 2019 American Chemical Society.*

For a further understanding of surface coverage, the duration of the drying phase 3 (Figure 3.13 step 3) and therefore the residence time of the high contact angle phase on the substrate is considered. Due to the low vapor pressure of DMSO, the transition from precursor film to the intermediate phase is significantly slowed down when going from a solvent ratio of DMSO:DMF = 1:9 to 3:7 to 5:5. After dispensing the precursor solution onto the substrate (step 1), an increased DMSO:DMF ratio allows a longer time for re-distribution of the liquid during the gas-quenching (step 2, 3), before the onset of supersaturation. During this time period the continuous evaporation of DMF and the concomitantly increasing contact angle between solvent and surface gives rise to a more severe de-wetting as found in Figure 3.10. As such, the moment in time the quenching process is started, will impact the window in which to the poorly wetting phase is

given time to de-wet (Figure 3.11). Accordingly we found the perovskite formation with NMP co-solvent to be also insensitive to the distance between nozzle and substrate (modifying the effective flow and therefore solvent removal speed), while DMSO based precursors yield significant variance in homogeneity and surface coverage. For DMSO based precursors, the homogeneity of the perovskite formation could in part be affected by a variation in the formation of the supersaturated phase, as a result of variations of the nitrogen gas flow impinging on the surface. Additionally, the surface coverage might be affected by a gas flow or pressure induced tearing of the precursor film. [190, 191] For DMSO:DMF = 5:5 inhomogeneous crystal formation independent of the onset of the gas-quenching, nozzle distance and quenching delay was observed (Figure 3.11). Taken together, if DMSO is used as co-solvent, our findings evidence a need for the careful optimization of processing conditions (e.g. timing etc.) to obtain satisfactory perovskite layers. In striking contrast to DMSO, NMP turns out to afford a substantially increased processing tolerance. As a result, well-crystallized, homogeneous, and pin-hole free perovskite layers are formed, vastly independent of the NMP:DMF mixing ratio and timing for the gas-quenching procedure.

3.3.2 Highly Reproducible Perovskite Solar Cells

To verify the applicability of the resulting perovskite layers in perovskite solar cells, inverted p-i-n devices were prepared with a layer sequence of glass / ITO / PTAA / perovskite / $PC_{61}BM$ / AZO / (SnO_x) / Ag. A mixing ratio of NMP:DMF = 3:7 and DMSO:DMF = 1:9 has been used to prepare the precursor solutions. The resulting cell characteristics are summarized in Table 3.3. Efficiencies of up to 17.7 % are achieved for $MAPbI_3$ as active material. More importantly for the NMP:DMF solvent system the statistical variation of the device characteristics and therefore the process reproducibility is significantly better than in the case, where DMSO:DMF is used (Figure 3.16). Solar cell J-V scans, stabilized power output and EQE data of champion cell with NMP co-solvent are provided in Figure 3.17.

To further prove the general applicability of our approach, the NMP:DMF solvent system was applied to a double cation ($FA_{0.94}Cs_{0.06}PbI_3$) perovskite system. The corresponding XRD diffractograms are accessible in the supporting information of [153]. As also visible in Figure 3.17 and Table 3.3, without the need for further process optimization, $FA_{0.94}Cs_{0.06}PbI_3$ solar cells with a PCE up to 18.5 % were obtained. It is important to note, that again the statistical variation of various sub-sets of cells is very low (Table 3.3), indicating the robustness of the NMP:DMF solvent system in the gas quenching process.

Table 3.3: *Solar cell characteristics for $MAPbI_3$ and $FA_{0.94}Cs_{0.06}PbI_3$ devices resulting from a deposition process based on DMSO and NMP as co-solvent. $MAPbI_3$ Data was acquired from 57 solar cells (DMSO:DMF) and 32 solar cells (NMP:DMF), $FA_{0.94}Cs_{0.06}PbI_3$ from a total of 18 solar cells. The cells were produced by different persons in several batches.*

	$\mathbf{MAPbI_3}$ **DMSO:DMF**		$\mathbf{MAPbI_3}$ **NMP:DMF**		$\mathbf{FA_{0.94}Cs_{0.06}PbI_3}$ **NMP:DMF**	
	mean	**SD**	**mean**	**SD**	**mean**	**SD**
PCE / %	11.7	3.5	16.6	0.5	17.6	0.7
FF / %	61	10	76	2	72	2
V_{OC} **/ V**	0.94	0.15	1.05	0.02	1.07	0.01
J_{SC} **/ mA/cm²**	20.1	2.5	21.2	0.5	22.9	0.5

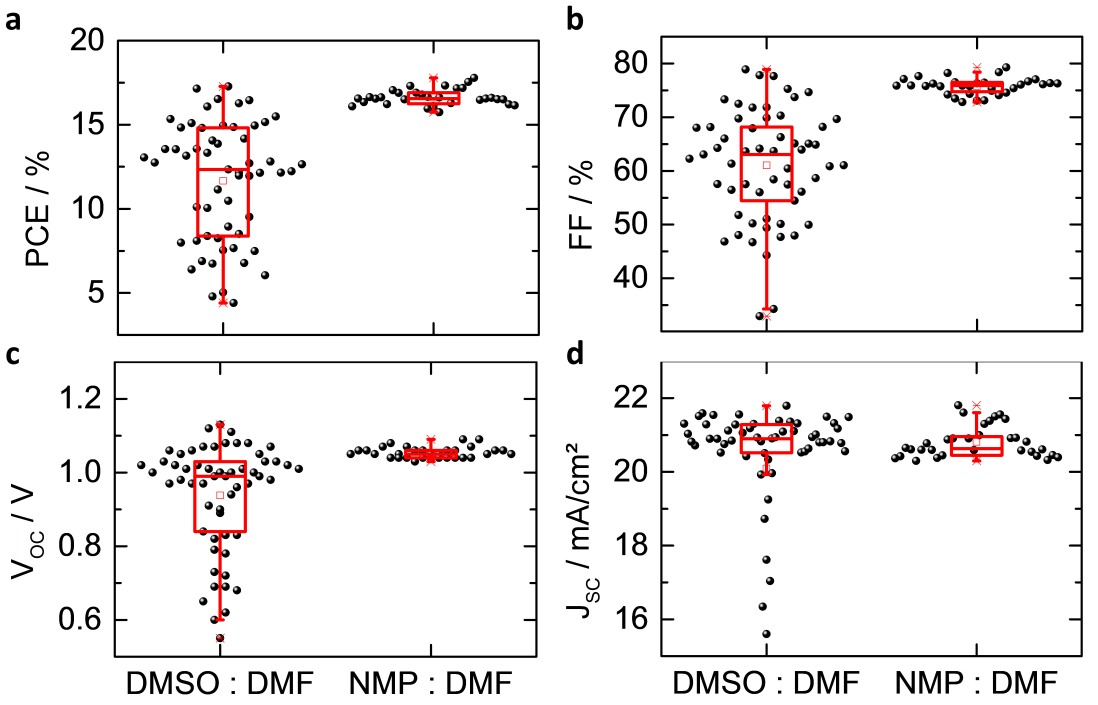

Figure 3.16: DMSO vs. NMP statistics. a, - d, *Box chart diagrams of PCE, FF, V_{OC} and J_{SC}, displaying the process variation of solar cells processed with 1:9 DMSO:DMF (left) and 3:7 NMP:DMF (right) co-solvent:solvent mixture. Box plots: median line with upper and lower box ranges denoting the 25% and 75% margins. The bars denote the outermost data points that are still inside another 1.5 interquatile range. See also Table 3.3. Reprinted with permission from [153]. Copyright 2019 American Chemical Society.*

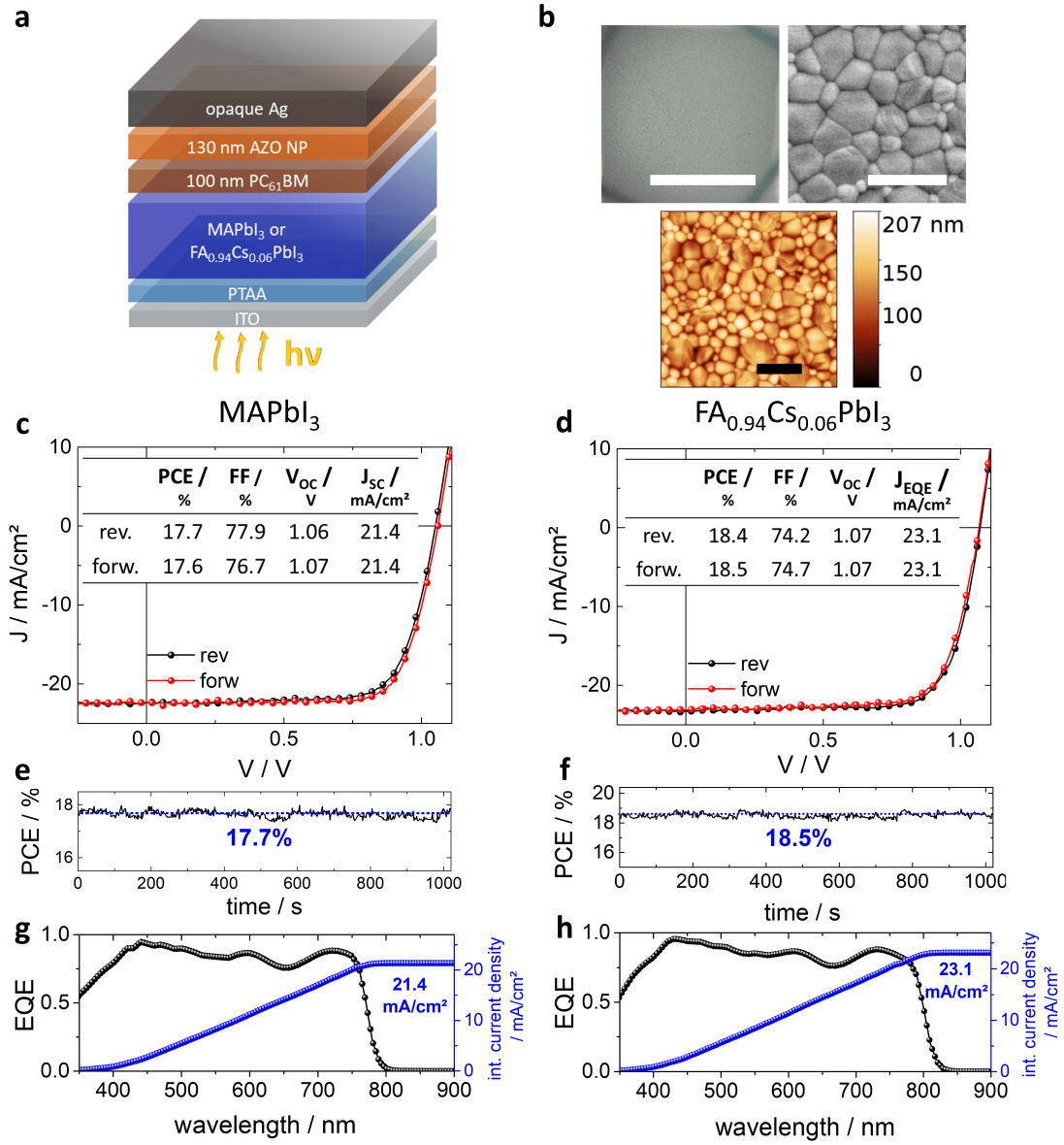

Figure 3.17: General applicability. ***a,*** *Stack of the obtained solar cells* ***b,*** *microscopy, SEM and AFM images showing the layer formation of* $FA_{0.94}Cs_{0.06}PbI_3$ *on top of PTAA,* ***c, d,*** *solar cell characteristics* ***e, f,*** *stabilized power output* ***g, h,*** *EQE data of solar cells with* ***c, e, g,*** $MAPbI_3$ *or* ***d, f, h,*** $FA_{0.94}Cs_{0.06}PbI_3$*. All perovskite layers were processed from 3:7 NMP:DMF co-solvent:solvent system and quenching delay time of 30 s. The scale bars for microscope images are 1 cm. In AFM and SEM image the scale for the bars is 5 µm. Reprinted with permission from [153]. Copyright 2019 American Chemical Society.*

Taken together, we have successfully shown, how to overcome frequently encountered wetting issues in the gas quenching deposition of halide perovskite photo-active layers on hydrophobic hole transport layers. We successfully identified the highly polar and strongly hydrophilic DMSO, which is used as a common complexing agent, as the origin for precursor de-wetting. Further we were able to show that using NMP, which has a low hydrophilic / lipophilic balance, is a co-solvent which can act as stable complexing and wetting agent, simultaneously. As a result, the final perovskite layer quality is extremely tolerant with respect to the mixing ratio (NMP:DMF) and other details of the gas quenching procedure. Finally we achieved highly reproducible solar cells with efficiencies up to 18.5 % that could be readily reproduced by multiple different people. The process was even transferable to other labs (e.g. in the lab of Dr. Selina Olthof, University of Cologne).

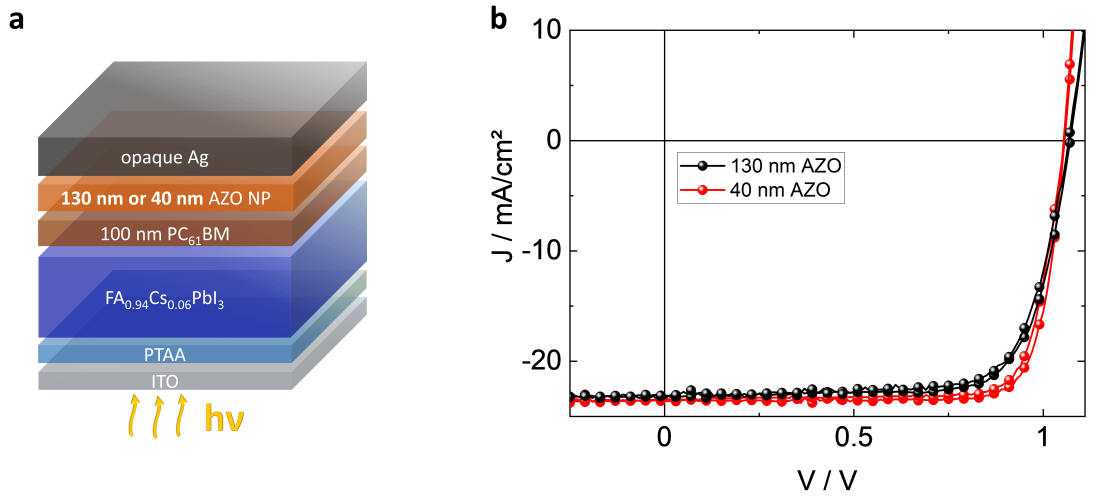

Figure 3.18: AZO-NP optimization to reach 20 % PCE. a, *Solar cell stack and* ***b,*** *solar cell characteristics comparing champion solar cells before and after reduction of the AZO-NP thickness. See also Table 3.4.*

With further optimization of the device layer sequence, we finally intended to achieve solar cells with an efficiency larger than 20%, since for gas quenching this was only shown for n-i-p type cells then. [37] After we found, that the PTAA and $PC_{61}BM$ thickness proved to be already at the lower thickness limit, the thickness of the AZO-NP layer was optimized, narrowing in at an optimum at about 40 nm. As visible in Table 3.4, with this we were able to significantly improve the fill factor (Figure 3.18). We attribute this to improved charge carrier transport since the conductivity of AZO-NP layers appears to be very limited (with Van-der-Pauw 4 point probe measurement no conductivity was

detectable from a 100 nm AZO layer, implying sheet resistances of $R_{SH} > 10^8$ $\Omega/\square$). In turn this AZO optimization significantly improved power conversion efficiency of our solar cells to more than 20 % power conversion efficiency.

Table 3.4: *Champion $FA_{0.94}Cs_{0.06}PbI_3$ solar cells before and after AZO-NP thickness optimization*

AZO-NP thickness	**reverse**				**forward**			
	PCE / %	FF / %	V_{OC} / V	J_{SC} / mA/cm²	PCE / %	FF / %	V_{OC} / V	J_{SC} / mA/cm²
130 nm	18.4	74	1.07	23.1	18.5	75	1.07	23.1
40 nm	20.4	82	1.06	23.5	19.6	80	1.04	23.4

4 Stability of Perovskite Solar Cells

Parts of this chapter have been published in:

Brinkmann, K.O., et al. "Suppressed decomposition of organometal halide perovskites by impermeable electron-extraction layers in inverted solar cells." Nat. Commun. 8, 13938 (2017). [192]

Please also note that some insights presented in this chapter have already been part of my master thesis ("Metalloxidbasierte Ladungsextraktionsschichten für Perowskit-Solarzellen"), since the above paper was published on the transition from master to PhD student. [142] While large portions of device and long term stability data were generated afterwards, XPS and XRD measurement and first portions of the discussion presented were already shown in the master thesis. Since the work done in the master thesis and the follow-up work as PhD candidate are intimately linked and the insights are critical for the understanding of the core messages of the following chapters, the story is presented in full at this point, for the sake of readability.

While the power conversion efficiencies of perovskite solar cells skyrocketed to reach levels beyond 25 %, [193] concerns about their stability were (and are still) intimately linked to this technology. [68, 170, 194–196] In general there is consensus that perovskites, like $MAPbI_3$ show a severe tendency to decompose into their constituents in the presence of water. [197, 198] Moreover, an apparently intrinsic decomposition of $MAPbI_3$ to iodine containing volatile components and PbI_2, which is thermally activated and which occurs even under inert conditions, stated a very fundamental problem. [68, 199] At the same time, secondary effects of perovskite decomposition such as the degradation of functional building blocks in the solar cell due to the corrosive effect of some perovskite decomposition products were reported. [200] Specifically, the corrosion of metal electrodes like Ag or Al has been identified to be a critical issue. [65] Overall, proper concepts to overcome these reliability issues had to be developed, to maintain the prospects of wide-spread application and commercialization of hybrid metal-halide perovskite technology.

To overcome the above mentioned stability issues, several groups had introduced inverted planar perovskite cells based on metal-oxides as electron- and hole-extraction interfacial layers adjacent to the cathode and anode, respectively. [201, 202] E.g. a sol-gel Ti(Nb)O_x electron extraction layer, aimed to protect the perovskite against moisture from ambient atmosphere was introduced. [202] Due to its poor electrical conductivity of 10^{-5} S cm^{-1}, the authors had to limit the thickness of the sol-gel Ti(Nb)O_x to only 10 nm. Moreover, it is known that sol-gel derived layers state only relatively poor permeation barriers. [203] As a result, the device stability tests which afforded a lifetime of 1000 h, were done with additional encapsulation. Also other strategies to stabilize the perovskite by subsequent layers like e.g. Cr_2O_3 / Cr or ZnO on top of the perovskite, were proposed to provide some protection from decomposition as well as concomitant degradation effects like electrode corrosion. [201, 204, 205] Still all these approaches remained non-satisfactory, as degradation had been reduced, yet not really suppressed. Severe degradation was found after some hours or days, which still compromised the prospects of successful perovskite commercialisation in the future. Most critically, none of the presented strategies provided sufficient protection at elevated temperatures. [206] As solar cells in outdoor conditions may reach a temperature significantly above 25 °C, the latter appears to be extremely relevant. Some promising results were achieved with ALD Al_2O_3 layers directly deposited on top of perovskites to improve their resilience against ambient atmosphere and heat. [207] However, these ALD layers were not a functional part of a device and since alumina is an insulator it's applicability inside a solar cell is very limited. Koushik et al. showed, that only atomically thin Al_2O_3 layers (10 - 15 ALD cycles) could be used, without severely compromising device efficiency. [208] Hence we strived to introduce a layer that is conductive and a permeation barrier at the same time.

To this end we considered ALD grown tin oxide, that has been introduced by Behrend and Trost et al. as transparent conductive permeation barrier for organic light emitting diodes and as charge extraction material for organic solar cells. [209, 210] SnO_x layers grown by ALD are optically highly transparent, electrically conductive and provide outstanding gas permeation barrier properties with a water vapour transmission rate (WVTR) as low as 7×10^{-5} g m^{-1} day^{-1}), even when grown at low temperatures ($\leq$ 100 °C). [209] Their WVTR is orders of magnitude better than that of sputtered ITO thin films or that of solution processed metal-oxide layers. The electrical conductivity of the SnO_x layer on the order of 5×10^{-3} S cm^{-1} allowed us to place it between the sensitive electrode and the photoactive layers, without adding any noticeable series resistance.

Please be aware that even though our ALD process used to grow the SnO_x is based on water as oxygen source, which one might intuitively suspect to be detrimental to the active perovskite material, a single dose of H_2O in low pressure ALD typically creates an environment equivalent to a maximum of 0.1 % of relative humidity. [211] This is significantly lower than the large variety of conditions mentioned in the literature to degrade the perovskite. [57, 59] Beneath the ALD grown SnO_x we use a nanoparticle based layer of aluminium doped zinc oxide (AZO). AZO serves a twofold purpose: Firstly it acts as electron extraction layer, providing a work function of 3.9 eV which excellently matches the lowest unoccupied molecular orbital (LUMO) of commonly used C_{60} based fullerenes; [212] Secondly it provides a nano-porous scaffold for the ALD SnO_x layer resulting in an synergistically intermixed hybrid AZO-NP / ALD-SnO_x barrier layer, that outperforms a single ALD layer. These synergistic effects are described in more detail in chapter 5.1.

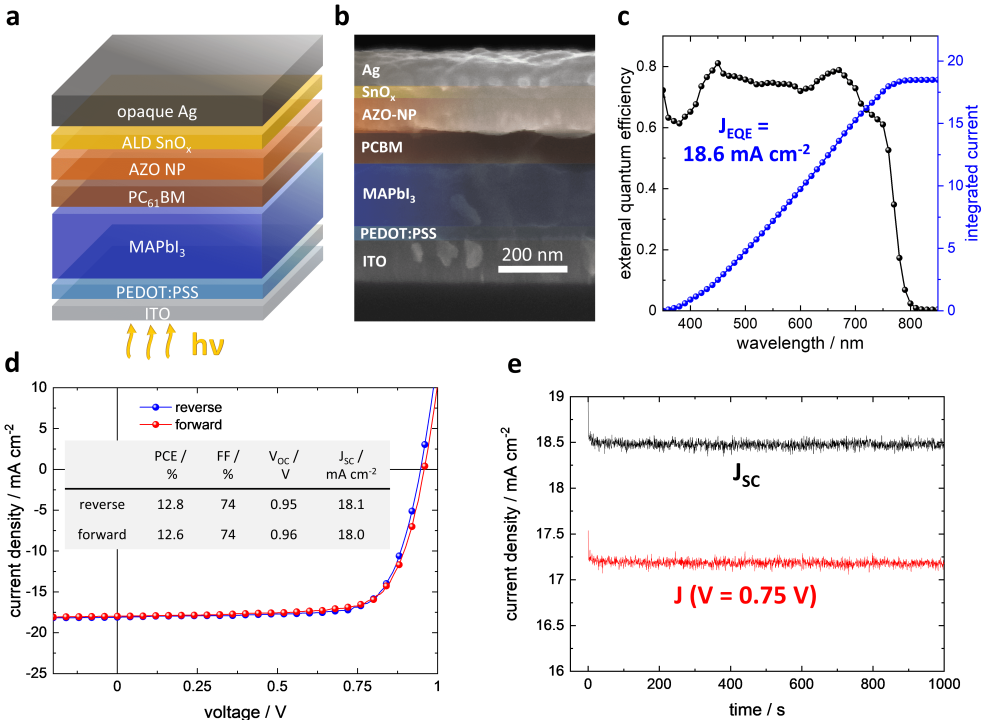

Figure 4.1: Basic solar cell characteristics. ***a,*** *Solar cell stack and* ***b,*** *scanning electron microscopy (SEM) image of the device cross section along with the assignment of the respective layers. In some devices the SnO_x or the AZO layer has been omitted. Note, the contrast between the AZO and the SnO_x layers in SEM is relatively poor.* ***c,*** *External quantum efficiency (EQE) of a representative device based on AZO / SnO_x.* ***d,*** *J-V characteristics measured in forward and reverse direction and* ***e,*** *current density vs. time under 0 V (black) and 0.75 V (red) bias. Adapted from [192].*

Before attending to stability, it has to be noted that we undertook the study presented here before the perovskite solar cell optimization process presented in chapter 3. Hence the single step deposition technique for the perovskite as described earlier was utilized. The layer sequence is shown in Figure 4.1. In some cells a SnO_x layer is deposited on top of the AZO layer by ALD at 80 °C to form the hybrid electron extraction assembly (AZO / SnO_x). A cross sectional SEM image through a full solar cell stack comprising all layers is shown in 4.1 b. External quantum efficiency (EQE) has been measured for the cells used in this chapter to determine a spectral mismatch for this type of solar cells. The respective EQE spectrum is shown in Figure 4.1 c. We derived a spectral mismatch factor of 1.16, which then was applied to all device data shown in this chapter (including J-V characteristics, like shown in Figure 4.1 d). The J-V characteristics of the device measured in forward and reverse direction (scan speed: 500 mV/s) are presented in Figure 4.1 d. No substantial hysteresis is found in the J-V data. The extracted characteristics V_{OC} = 0.95 V, FF = 74 % and a J_{SC} = 18 mA/cm^{-2} result in a power conversion efficiency (PCE) of 12.8 %. As visible in Figure 4.1 e J_{SC} and a operation point close to MPP (V = 0.75 V) are stable over time. In combination with the hysteresis being almost negligible we conclude therefore that transient effects induced by ion migration, like described e.g. in [89, 213–215] and chapter 2.12, do most likely not affect our cell characteristics.

4.1 Manipulating the Air Stability by Internal ALD Barriers

A very straight forward, yet nevertheless striking advantage of the hybrid AZO / SnO_x electron extraction layer in direct comparison to AZO, is displayed in Figure 4.2. Here, the stability of the cell characteristics is shown for devices that were continuously exposed to ambient air at 23 °C and 50 % relative humidity. The devices based on a single layer of AZO as EEL degrade swiftly within about 50 hours. A severe decay of the FF is accompanied by a simultaneous drop of the J_{SC} after only some hours exposure time. We found that an exposure time of < 170 h was able to degrade the solar cell to a level, where no power output could be detected anymore. Opposed to that, the characteristics of the corresponding cells with the hybrid EEL of AZO / SnO_x do not show notable degradation even after more than 600 hours in air. Note, this is valid for thicknesses of the SnO_x layer of only 20 nm.

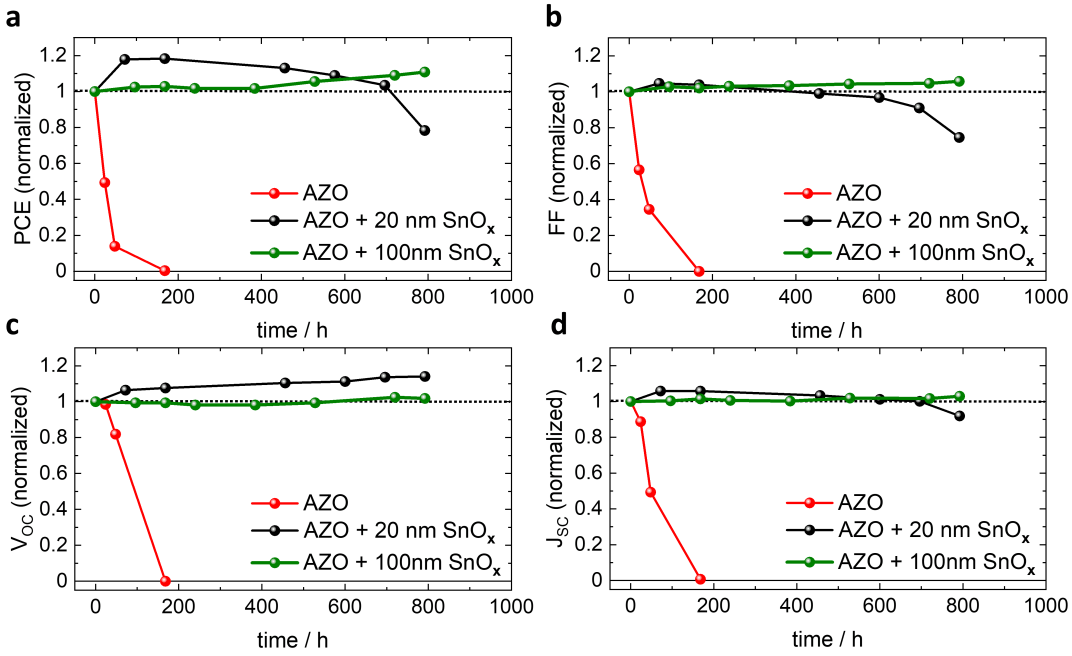

Figure 4.2: Stability upon storage in ambient air. *Normalized characteristics of inverted perovskite solar cells with varied cathode/electron extraction assemblies (AZO / Ag, AZO / 20 nm SnO_x / Ag, AZO / 100 nm SnO_x / Ag) vs. time of storage in ambient air (at 23°C and 50 %rH).* ***a,*** *power conversion efficiency* ***b,*** *fill factor* ***c,*** *open circuit voltage and* ***d,*** *short circuit current. The characteristics have been determined from the J-V measurements in reverse direction. Adapted from [192].*

There is a slight increase of the V_{OC} in the AZO / SnO_x samples that happens on a time scale of several tens of hours. This increase is only observed in the AZO / SnO_x samples, as the AZO cells already undergo strong degradation on the same time scale. A similar increase of V_{OC} on such a long time scale has been seen by other authors and it has been explained by an aging effect that reduces the density of trap states in the perovskite. [216] After 700 h of air storage for devices based on 20 nm SnO_x finally degradation of the solar cell, mainly by reduction of FF is detectable. This can be explained by the limited thickness of the ALD SnO_x layer resulting in an eventual intrusion of moisture and a concomitant degradation that can be evaded by simply increasing the SnO_x layer thickness. Devices comprising nominally 100 nm ALD grown SnO_x (as also presented in Figure 4.2) do not show any sign of degradation after more than 800 hours in air. The influences on barrier properties of AZO / SnO_x layers is sperately discussed in chapter 5.1.

In order to analyse the reasons underlying the strikingly different degradation phenomena shown in Figure 4.2, we have performed XRD and XPS studies on the respective devices. Note, in case of the XPS measurements, a thinner top Ag-electrode was chosen (10 nm) compared to that in the actual solar cells (100 nm), due to the small probing depth of the technique. Looking first at the AZO based device, the XRD spectrum shows the (110) and (220) reflections of tetragonal $MAPbI_3$ at angles of 14.11° and 28.14, respectively. As this XRD measurement has been made on a full device stack, further signals related to the Ag and ITO electrodes are visible. A detailed assignment of these peaks is accessible in the supporting information of [192]. Only a very weak signal due to PbI_2 was found, which did not significantly increase even after seven days in air (Figure 4.3 a, inset). Thus, no severe decomposition of the perovskite to PbI_2 upon storage in air can be inferred from the XRD data. On the other hand, when XPS was used to look for degradation products on the surface, a notable amount of iodine was evidenced on the AZO sample (Figure 4.3 b) after exposure to air for two days, while on identical samples kept in nitrogen no such iodine signal is found. Please note, the peak around 622 eV in the XPS spectrum of the aged AZO cell does not represent another bonding state of the iodine, it is rather a so-called shake-up peak. Such shake-up peaks are commonly observed in strong XPS signals. The survey XPS spectra can be found in the supporting information of [192]. Plan-view SEM images of the AZO samples aged in air show the formation of spot-like degradation motifs (Figure 4.3 c). These spots point to the local ingress of moisture and out-diffusion of decomposition products of the perovskite, supported by the appearance of the iodine signal in XPS. In the degraded spots, needle-like features occur. Similar features have been reported for Ag electrodes corroded by the decomposition products of $MAPbI_3$. [217] Our findings are also in line with the results of Kato et al., who unveiled a moisture promoted corrosion mechanism of Ag which resulted in the formation of products like AgI. [65] The role of water in the electrode corrosion is further clarified below in cells aged under inert conditions.

To explain the spot-like degradation, we can assume that structural defects in the AZO NP layer, such as pinholes, would give rise to locally enhanced water permeation. Opposed to that, the sample with the hybrid EEL of AZO / SnO_x does not show any sign of degradation in SEM (Figure 4.3 c) under identical conditions. In XPS only a negligible amount of iodine at the surface of the AZO / SnO_x samples can be detected. Figure 4.3 d illustrates the specific differences between AZO and AZO / SnO_x as EEL in devices exposed to air. As indicated before, the AZO layer prepared from the NP dispersion does not provide a significant diffusion barrier against the local ingress of moisture from the ambient air. As a result, decomposition of the $MAPbI_3$ perovskite occurs and yields iodine-based products that migrate to the surface.

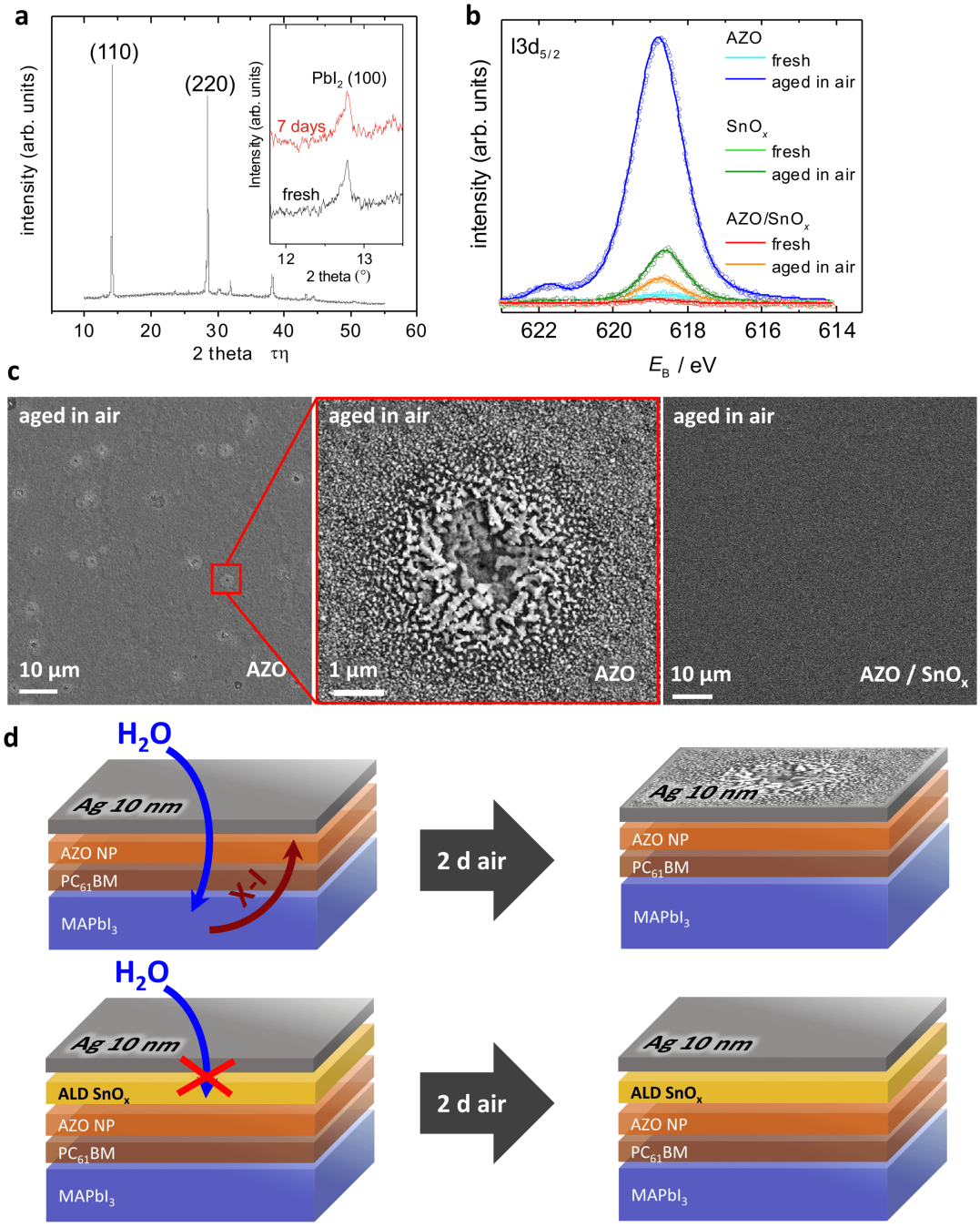

Figure 4.3: Unravelling the aging mechanism in air. ***a,*** *XRD spectrum of a perovskite cell based on AZO as EEL after storage in air for seven days (inset: magnified view of the (100) PbI_2 reflection for a fresh sample and one that has been stored in air for seven days; spectra were vertically offset for clarity).* ***b,*** *Photoemission spectra of the iodine $I3d_{5/2}$ peak for fresh and aged cells based on AZO, SnO_x and hybrid AZO / SnO_x EELs, respectively. Aged samples comprising only 10 nm Ag after storage in air for two days.* ***c,*** *Corresponding plan view SEM images of the Ag layer in case of the AZO and the AZO / SnO_x sample.* ***d,*** *Schemes of aging for the AZO and the AZO / SnO_x samples. Adapted from [192].*

In the case of AZO / SnO_x, substantially better moisture barrier properties prevent the penetration of water. The claim of superior moisture barrier properties of the hybrid AZO / SnO_x EEL compared to that of AZO NP (and singular ALD grown SnO_x) layers is discussed in detail in chapter 5.1. It has to be noted that the detrimental effects of ambient air could in principle be avoided by using a proper encapsulation of the entire solar cell. However, the out-diffusion of decomposition products from the perovskite and the degradation of the metal electrode may impose a more fundamental issue, that would not be prevented by an external encapsulation. This is even the more important, as earlier reports evidenced the thermally activated decomposition of the $MAPbI_3$ perovskite even under inert atmosphere. [67, 68]

For comparison, we have also studied layer stacks where only SnO_x, i.e. without AZO between the $PC_{61}BM$ and the SnO_x, has been used as EEL. Our group showed previously that SnO_x with a work-function of 4.1 eV forms an excellent EEL layer in inverted organic solar cells. [210] Here, the resulting perovskite solar cells based on SnO_x were more stable than the devices based on AZO. However, they showed a statistical failure on a time scale of 200 hours (Figure 4.4; also see Appendix Figure 11.2). This finding could be explained by a non-ideal ALD growth of the SnO_x directly on top of the organic $PC_{61}BM$ layer. ALD as a chemical deposition technique relies on self-limiting chemical reactions on the sample surface. [218] For the ALD deposition of oxide layers, –OH surface-groups form the nucleation sites for layer growth. In this sense, on organic surfaces like $PC_{61}BM$ the nucleation of an ALD layer may deviate significantly from the growth on a surface rich of –OH groups. [219]

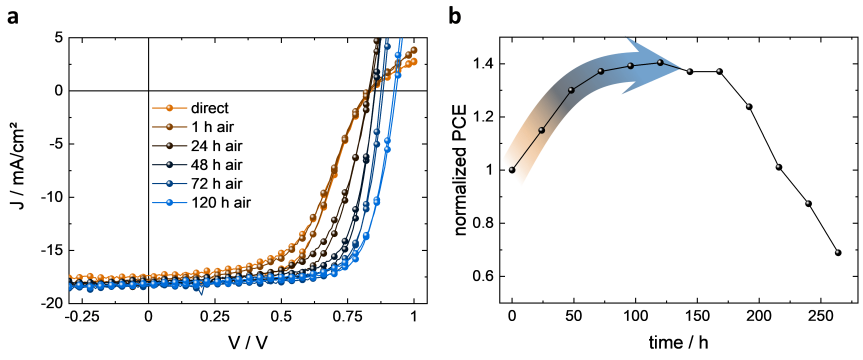

Figure 4.4: Solar cells with SnO_x deposited directly on PCBM. ***a,*** *J-V characteristics of respective solar cells at diffrent aging states, if stored in ambient air (23 °C and 50% rH) and* ***b,*** *evolution of the normalized power conversion efficiency, referenced to the initial value. Adapted from [192].*

Therefore, we can assume that the SnO_x layer grown on $PC_{61}BM$ is not free of some pin-hole defects, which compromise its functionality as diffusion barrier. Consequently, substantially more iodine is detected on the surface after exposure to air, if compared to the AZO / SnO_x device (Figure 4.3 a). Respective solar cell efficiency, as well as stability, of the resulting SnO_x devices was inferior to that of the AZO / SnO_x cells, as shown in Figure 4.4 b. Devices with SnO_x deposited directly on top of PCBM (omitting the AZO-NP layer) initially show strongly s-shaped J-V characteristics, that require several days of storage in ambient air to disappear and to reach the performance of devices with AZO-NP as extraction layer. This might be attributed to the need for water molecules that can form an accumulation layer at SnO_x interfaces and therefore significantly lower its work function (as is necessary for electron extraction from the PCBM). [220–222] Since water is simultaneously responsible for the degradation of perovskite solar cells in ambient air, the requirement of water intrusion to achieve well-behaved J-V characteristics, is highly undesirable. The dilemma is readily displayed in Figure 4.4 b, where the efficiency strongly decays after hitting a rather narrow plateau of approx. 50 hours. On top of this we observed that for devices without AZO-NP degradation sets in far earlier than for devices employing AZO-NP. Both observations nicely display the two-fold purpose of the AZO-NP layer:
1. It's low work function ($\approx$ 3.9 eV) is beneficial to form a favourable interface to the electron transport layer $PC_{61}BM$ ($LUMO_{PCBM} \approx$ 3.9 eV) and
2. It provides a nano-porous scaffold for the subsequent ALD process warranting improved barrier properties, as further discussed in chapter 5.

4.2 Suppressed Thermal Decomposition by ALD Barriers

To study the long term stability of our solar cells under inert conditions, we have stored a set of devices in a glove box under nitrogen atmosphere. All the devices were placed on a hot-plate at 60 °C and their characteristics were measured repeatedly. Most remarkably, the characteristics of devices based on AZO EELs, degraded on a time scale of 100 h (Figure 4.5). While the J_{SC} and V_{OC} of these devices remain fairly stable, the decay of the FF results in the severe drop of PCE to about 20 % of its initial value after 360 h. The degradation motif in the AZO based cells is essentially different from that found in ambient air, where all cell characteristics decayed within a day (Figure 4.2). Again in striking contrast, the characteristics of devices based on the hybrid AZO / SnO_x EEL remain almost unchanged even after more than 1000 h. Note, the hysteresis did not increase in the course of aging.

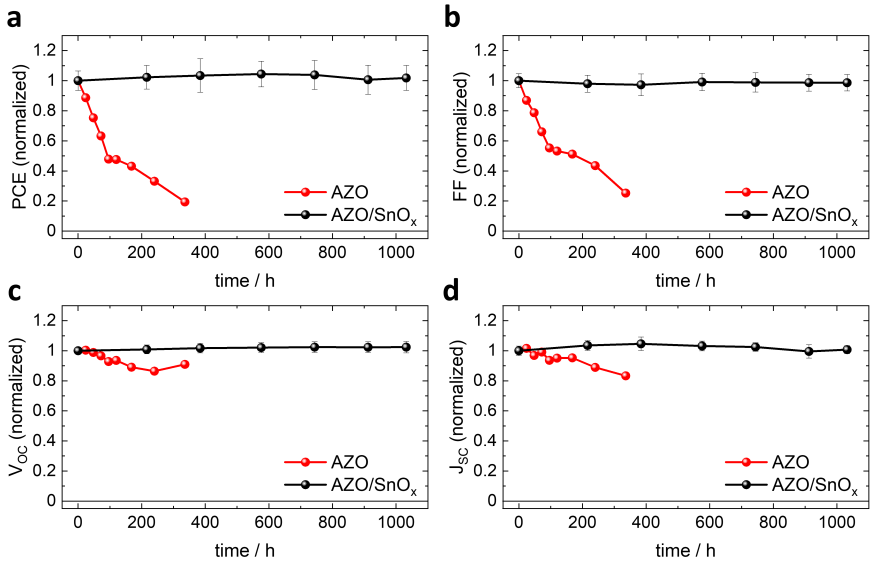

Figure 4.5: Stability upon storage at 60°C in nitrogen atmosphere. *Normalized characteristics of inverted perovskite cells with varied cathode electron extraction assemblies (AZO / SnO_x / Ag, AZO / Ag) vs. time.* ***a,*** *Power conversion efficiency* ***b,*** *fill factor* ***c,*** *open circuit voltage and* ***d,*** *short circuit current density. The characteristics have been determined from J-V measurements in reverse direction. Error bars were derived from a total of 14 stressed solar cells. Adapted from [192].*

To unravel the mechanisms behind these results, we have again performed XRD and XPS studies of the respective device structures. After heating the device stacks for six days under inert atmosphere, the XRD spectrum of the AZO samples reveals a significant signal due to PbI_2, which is absent in pristine stacks (Figure 4.6 a). The formation of PbI_2 indicates the thermally activated decomposition of the perovskite upon heating, in agreement with earlier reports. [67, 68] Opposed to that, the devices based on the hybrid AZO / SnO_x EEL do not show any signature of a PbI_2 phase after identical aging conditions (Figure 4.5 b). The formation of PbI_2 in the AZO samples is in contrast to the degradation in air, where no PbI_2 phase was found in XRD (Figure 4.3 a). At the same time, a magnified view of the $I3d_{5/2}$ XPS signal (Figure 4.6 c) does not reveal any significant increase of the amount of iodine at the surface of any of the samples aged in nitrogen. Please note, the noise in the XPS spectra indicates that the concentration of $I3d_{5/2}$ at the surface of all the samples is close to the detection limit and variations between the samples are within the measurement error. A plan-view SEM image of the aged AZO samples does not reveal any degradation of the Ag electrode, in contrast to degradation in air (Figure 4.3 c). Thus, we conclude that in the case of AZO, volatile decomposition products of the $MAPbI_3$ perovskite evaporate from the cell stack without degradation of the Ag electrode.

In air, other than in nitrogen, the presence of water would promote the corrosion of Ag due to MAI and other halide compounds. [65] However, here the loss of MAI etc. apparently drives the further decomposition of the perovskite. Taken together, the device characteristics (Figure 4.5) and the XRD and XPS spectroscopy point to a scheme of degradation as shown in Figure 4.6 e, f: Under inert atmosphere, the thermally activated degradation of the perovskite leads to decomposition products that can easily diffuse through the PCBM / AZO / Ag layers on top of the perovskite. The less volatile PbI_2 phase remains in the active layer leading to a substantial decay of the FF of the corresponding devices (Figure 4.6 c). Moreover, it has been shown earlier that a change in film stoichiometry (Pb-poor to Pb-rich) may substantially alter the electronic

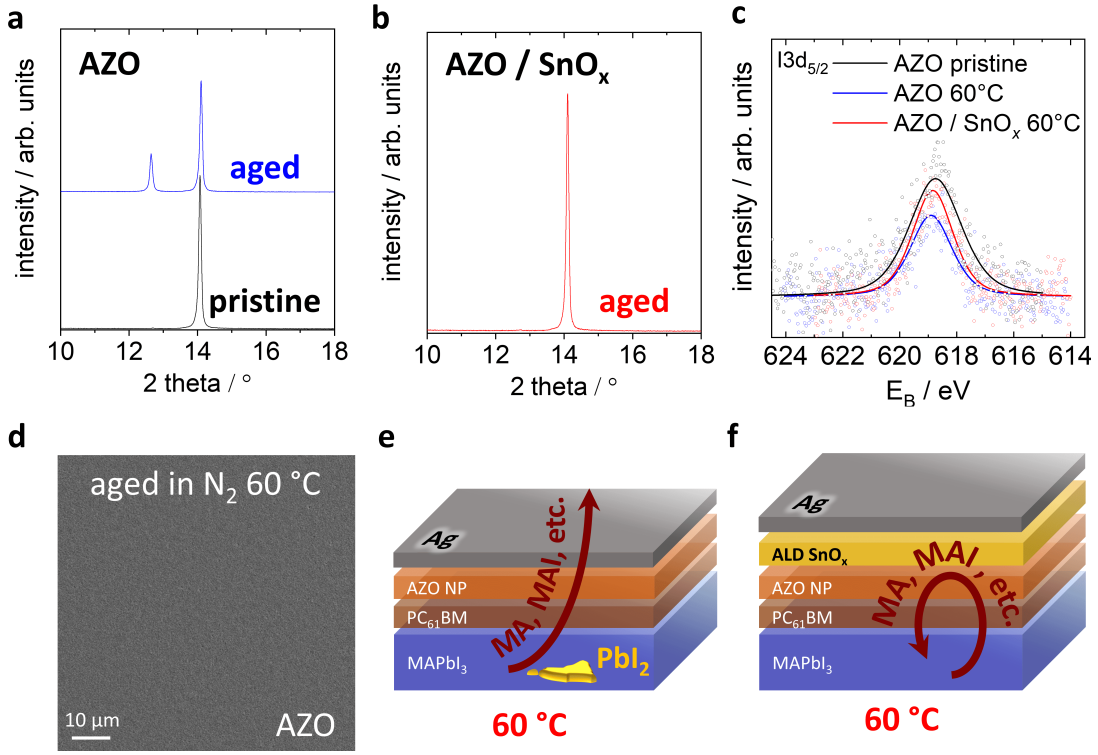

Figure 4.6: Why impermeable AZO / SnO_x EELs afford stable devices. ***a, b,*** *XRD spectra of a perovskite cell based on AZO and AZO / SnO_x as EEL before and after heating in nitrogen for six days.* ***c,*** *Photoemission spectra of the iodine $I3d_{5/2}$ peak for cells based on AZO and hybrid AZO / SnO_x EELs, respectively. As a reference, an AZO sample stored in N_2 ambient has been used. The other measurements are for samples aged at 60°C in nitrogen for six days. The open symbols represent the raw measurement data while the solid lines are a result of a peak fit. The colours are defined in the figure legend. Note, the top Ag electrode was chosen to be 10 nm.* ***d,*** *Corresponding plan view SEM image of the 10 nm Ag layer in case of the aged AZO sample.* ***e,*** *Schemes of aging and decomposition of the perovskite in case of the AZO and* ***f,*** *the AZO / SnO_x samples. The yellow spot in the scheme of the AZO sample symbolizes the formation of PbI_2. Adapted from [192].*

properties of the perovskite and especially the position of the conduction and valence band with respect to the vacuum level. [223] Towards increasingly Pb-rich conditions, the ionization energy of the perovskite has been shown to increase significantly to values in excess of 6 eV, which would render the extraction of holes more and more challenging. Alternatively an accumulation of PbI_2, which is an insulator, at the interfaces between perovskite and adjacent layers might induce an extraction barrier concomitantly lowering the fill factor of the device. Opposed to the case of the AZO cells, the AZO / SnO_x based cells do not show any formation of PbI_2 under otherwise identical conditions. We therefore conclude, that the decomposition products are contained inside the cell stack due to the dense SnO_x layer that forms a permeation barrier. Thus, the decomposition of the perovskite obviously is slowed down significantly and the cells do not show any degradation even after heating for more than 1000 h (Figure 4.5). It has to be noted, that it is favourable to position the permeation barrier between the perovskite and the Ag electrode, as thereby the known long term corrosive effect of residual halide components on the Ag electrode [65] and on the interface EEL / Ag can be efficiently suppressed (also compare chapter 6.1).

4.3 Combined Thermal and Illumination Stress

Aside from so-called mono-stress conditions, like elevated temperature, multi-stressing can be considered. To this end, we conducted a set of long-term light soaking tests at 60 °C under nitrogen, in which the devices were simultaneously illuminated with a white LED to achieve the same J_{SC} as upon AM1.5G solar irradiation. The results of this multi-stress experiment are shown in Figure 4.7 a-d (white LED spectrum is shown in Figure 4.7 e). It is clearly visible that again the AZO / SnO_x cells are substantially more stable than the AZO cells under combined heat and illumination stress. This difference is in part due to the suppressed decomposition of the perovskite due to heat in case of the AZO / SnO_x (in agreement with the discussion of Figure 4.5, 4.6). However, there is a clear degradation even of the AZO / SnO_x samples where the PCE decays to roughly 60 % of its initial value after 300 hours. This is in contrast to the case where only thermal stress has been used. Earlier work has unravelled the photo-induced degradation of solar cells based on $MAPbI_3$. While Misra et al. identified a photo-activated decomposition mechanism, [224] Nie et al. reported that continuous illumination of $MAPbI_3$ caused the formation of trap states which spoiled the solar cells performance, especially J_{SC}. [225] While our sealing approach based on the impermeable AZO / SnO_x electron extraction layer has been shown to efficiently suppress the decomposition of the perovskite, it

cannot suppress the formation of trap states in the perovskite. In the report of Nie et al., the cell characteristics recover after stressing, if the cells are kept in darkness. As the degradation motif we observed under illumination likewise proved to be reversible(Figure 4.7 f), we conclude that it most likely originates from illumination induced trap state formation like Nie et al. described. [225] On the other hand we expect photo-activated decomposition to be suppressed along with the thermal effect discussed above, especially since degradation of AZO based devices proofed to be non reversible.

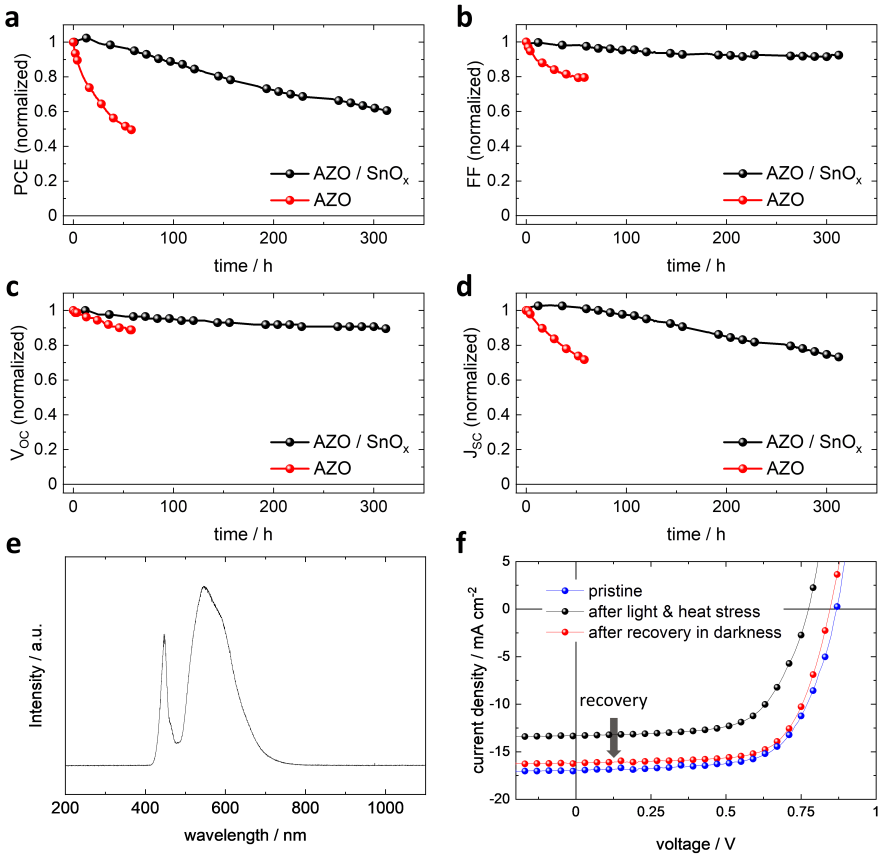

Figure 4.7: Additional illumination stress. *Characteristics of inverted perovskite solar cells with varied cathode electron extraction assemblies (AZO / SnO_x / Ag, AZO / Ag) vs. time of storage at 60 °C in nitrogen atmosphere and simultaneous illumination with a white LED to achieve the same current as under the solar simulator.* ***a,*** *Power conversion efficiency* ***b,*** *fill factor* ***c,*** *open circuit voltage and* ***d,*** *short circuit current density. The characteristics have been determined from J-V measurements in reverse direction.* ***e,*** *Spectrum of the white LED used for the light-soaking stress test under concomitant heating.* ***f,*** *J-V characteristics of an AZO / SnO_x / Ag cell, non-stressed (fresh), stressed for 300 hours (light / heat), and subsequently recovered in in darkness at room temperature for nine days (in the glove box). Adapted from [192].*

5 Hybrid Metal Oxide Barrier Layers

For the part of this chapter covering spatial atomic layer deposition (S-ALD), I collaborated with Dr. Lukas Hoffmann, an expert on the technique of (S-ALD). While Lukas Hoffmann provided the technology of S-ALD and characterisation of singular tin oxide layers, my main focus was perovskite stability as well as the formation of the hybrid AZO-NP / SnO_x layer. Drawing from our joint efforts, parts of this chapter have been published in:

Hoffmann, L; Brinkmann, K.O. (contributed equally) et al. "Spatial Atmospheric Pressure Atomic Layer Deposition of Tin Oxide as an Impermeable Electron Extraction Layer for Perovskite Solar Cells with Enhanced Thermal Stability" ACS Appl. Mater. Interfaces 2018, 10, 6, 6006–6013. [226]

and with regard to batch ALD:

Brinkmann, K.O., et al. "Suppressed decomposition of organometal halide perovskites by impermeable electron-extraction layers in inverted solar cells." Nat. Commun. 8, 13938 (2017). [192]

5.1 Hybrid Metal Oxide Layers Grown by Batch or Spatial ALD

In the previous chapter we could show that SnO_x layers can be introduced into the stack of a PSC, where they efficiently prevented the ingress of moisture, while at the same time, they suppressed the decomposition of the perovskite active layer and concomitantly protected sensitive metal electrodes against the corrosive halide constituents of the perovskite. A severe drawback of our SnO_x layers is their preparation by classical batch based ALD (B-ALD) under vacuum conditions. The limitations of classical ALD contradict the paradigm of low-cost, high-throughput preparation at atmospheric pressure, which is a particular selling point frequently associated with PSCs. There are efforts to overcome the limits of classical B-ALD by the introduction of spatial

ALD (S-ALD), which can operate in a continuous fashion at atmospheric pressure. [227] Our group had demonstrated earlier that high-performance gas diffusion barriers based on Al_2O_3 and SnO_x can be prepared by S-ALD at atmospheric pressure. [228, 229] In this chapter we introduce for the first time SnO_x grown by S-ALD at atmospheric pressure, as impermeable electron extraction layers in perovskite solar cells. Thereby, these key stabilizing constituents become compatible with the demands of roll-to-roll manufacturing. This is especially of interest, since the route of ALD deposition is expected to impact on the formation of the hybrid AZO-NP / ALD-SnO_x. Therefore, in this chapter we cover the formation of the hybrid barrier layers both grown from batch and spatial ALD.

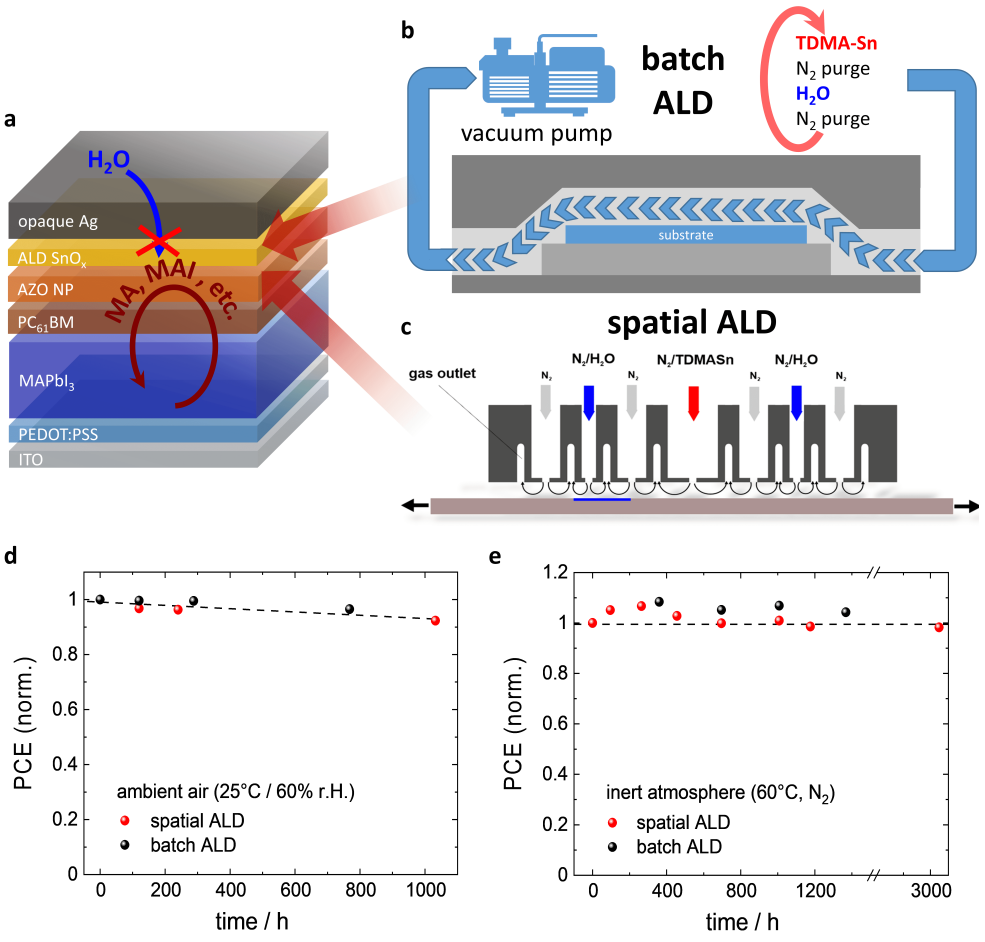

Figure 5.1: Spatial versus batch ALD. ***a,*** *solar cell stack (p-i-n) used in this chapter.* ***b,*** *Schematic of the employed batch ALD and* ***c,*** *the spatial ALD assembly.* ***d,*** *PCE vs. time of storage in ambient air (25 °C, 60 % rH) and* ***e,*** *at elevated temperature (60 °C, inert atmosphere). Adapted with permission from [226]. Copyright 2018 American Chemical Society.*

Before deeper growth studies were undertaken, we compared our B-ALD grown layers to those grown by S-ALD (substrate velocity of 20 mm s^{-1} and a substrate temperature of 80 °C). The refractive indices of the S-ALD (1.88 @ 633 nm) and B-ALD (1.89 @ 633 nm) layers are quite similar. Moreover, within the accuracy of the experiment the S-ALD process yields SnO_x layers that show the same permeation barrier properties (water vapor transmission rate of 100 nm SnO_x: WVTR = 2×10^{-4} gm^{-2} d^{-1}) and electrical conductivity ($\sigma = 10^{-4}$ S cm^{-1}) as their analogues grown by vacuum based B-ALD. Following up on this observation we prepared perovskite solar cells comparing both types of SnO_x deposition. The characteristics of representative PSCs incorporating an impermeable SnO_x electron extraction layer prepared by S-ALD and B-ALD are shown in Table 5.1 (for statistical data please see Appendix Figure 11.3). Note, all current density data was calibrated with dedicated EQE measurements. The corresponding EQE spectra are shown in the Appendix Figure 11.4. Both sets of samples show a remarkable similarity in their cell characteristics.

In order to compare the stability of the PSCs, mono-stress tests under ambient conditions (25 °C / 60 % rH) (Figure 5.1 d) and at elevated temperature (60 °C, inert atmosphere) (Figure 5.1 e) were conducted. Strikingly, under both conditions, excellent long-term stability of PSCs based on SnO_x grown by S-ALD is found. Note, for PSCs without the SnO_x layer, as known from the previous chapter 4, the devices degrade within tens of hours under ambient conditions (25 °C / 60 % rH) and within 200 h at elevated temperature (60 °C, inert atmosphere). Please see Appendix Figure 11.5 for a full set of cell characteristics during temperature mono stress testing. Taken together, SnO_x prepared by S-ALD, affords PSCs with outstanding thermal stability even on a time scale of $>$ 3000 h without noticeable decay in cell characteristics.

Table 5.1: *Comparison of perovskite solar cells (one-step deposition) comprising spatial (S-ALD) and batch ALD (B-ALD) deposited SnO_x layers.*

deposition technique	**reverse**				**forward**			
	PCE / %	FF / %	V_{OC} / V	J_{SC} / mA/cm^{-2}	PCE / %	FF / %	V_{OC} / V	J_{SC} / mA/cm^{-2}
S-ALD	12.7	78	0.88	18.6	11.2	72	0.86	18.2
B-ALD	12.6	77	0.89	18.8	11.2	70	0.87	18.5

As already mentioned in chapter 5, the AZO layer is deposited from a nanoparticle dispersion. As such, the AZO layer contains pores that can be partially coated with SnO_x due to the conformal nature of the ALD process. As a consequence we expected that the result of the ALD coating is not a separated bi-layer of AZO / SnO_x, but rather an intermixed hybrid layer. To verify this hypothesis we conducted Rutherford backscattering (RBS) studies on the layer stacks shown in Figure 5.2 a and b, comparing ALD SnO_x layers grown on top of ALD grown AZO or AZO-NP layers. The RBS signal is attenuated by the material as the ion beam passes through it (the measurement is conducted from the SnO_x side) and therefore the energy axis can provide a qualitative depth profile through the probed layer stack (lower energy = positioned deeper inside the sample).

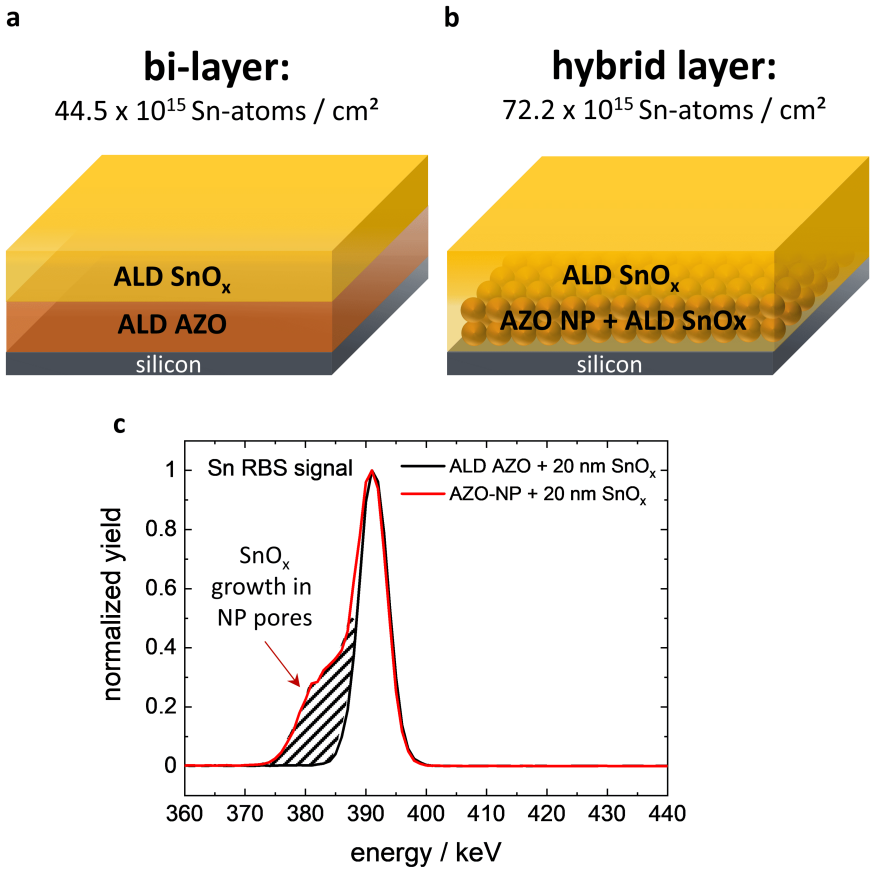

Figure 5.2: RBS study of the AZO / SnO_x EEL. a, *Layer sequence of samples used to study the ALD growth of the SnO_x on top of an AZO layer grown by ALD, which is expected to have no pores and* ***b,*** *on top of an AZO layer processed from a nanoparticle dispersion.* ***c,*** *The resulting RBS spectra attributed to Sn, which allow to determine the area density of Sn atoms (written above the layer stacks). Growth inside the NP-layer is visible as shoulder of the Sn-signal towards lower energy (= beneath the pure Sn layer). Adapted from [192].*

Zooming in on the characteristic energy of the tin atom (the full RBS spectrum is available in the supporting information of [226]), we could clearly evidence the intermixing of ALD-SnO_x and the AZO-NP layer: While for an ALD-AZO / ALD-SnO_x stack the obtained signal is symmetric, which indicates a homogeneous, clearly separated SnO_x layer, for AZO-NP / ALD-SnO_x we observed a shoulder manifesting towards lower energies. We therefore conclude that a substantial amount of SnO_x grows within the pores of the AZO-NP layer, which is also supported by the number of Sn-atoms per cm^2, which shows that a factor of approximately 1.6 more tin-atoms are present in the AZO-NP / ALD-SnO_x compared to the ALD-AZO / ALD-SnO_x layer stack (Figure 5.2 a, b), even though a similar amount of ALD cycles (i.e. 166 cycles) was used. This effect eventually results in a thicker effective barrier comprising 1. 20 nm of SnO_x and 2. an underlayer of synergistically intermixed AZO / SnO_x contributing to the eventual barrier properties.

To shine some more light on the ALD growth on top of nano-porous AZO-NP layers, we then investigated the net layer thickness of the hybrid layer and compared it to layers grown on silicon oxide. As visible in Figure 5.3 we observed a linear growth of SnO_x in both cases. This observation proofed valid for a reactor temperature of only 80 °C, like used for perovskite solar cells, as well as for a temperature of 150 °C. A growth rate of 0.11 nm / cycle at a reactor temperature of 80 °C and 0.07 nm / cycle at 150 °C was determined (Figure 5.3 a, c). Most notably the growth rates were the same on top of the native oxide of a silicon wafer and our AZO-NP layers.

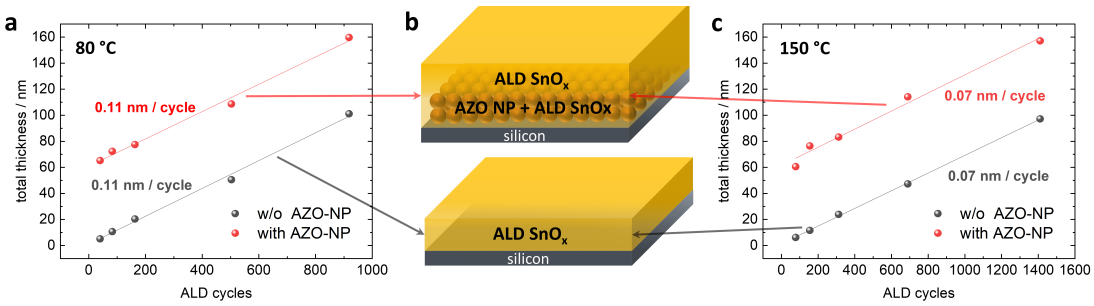

Figure 5.3: ALD growth on top of AZO-NP layers. ***a,*** *Total thickness of the hybrid layer shown over the number of ALD cycles on 80 °C reactor temperature on top of a silicon substrate with and without 60 nm of AZO-NP scaffold layer. Respective SnO_x growth rates on top attributed to Si and AZO-NP underlayers are displayed.* ***b,*** *Respective layer stacks and* ***c,*** *thickness over ALD cycles with a reactor temperature of 150 °C also showing respective growth rates.*

This observation combined with the striking resemblance of the RBS signal towards higher energies (see Figure 5.2 c), lead us to the conclusion that aside from the intermixing, a dense, high quality ALD SnO_x layer is grown in both cases. Since optical parameters of the single constituents of the intermixed AZO / SnO_x proofed utterly impossible to disentangle, follow-up experiments are either conducted on bare SnO_x layers, or the AZO / SnO_x layer is considered as one hybrid layer of a certain combined thickness. Next, we studied the advantages of the hybrid barrier. Therefore, we slightly modified the setup for the optical calcium tests, to enable implementation of spin-coated layers from isopropanol, that would otherwise degrade unprotected calcium pads. Specifically, we grew a 10 nm Al_2O_3 protection layer on top of the calcium sensors. As shown in Figure 5.4 a and b the test setup for optical calcium tests is then finished either with a hybrid AZO / SnO_x or with a solitary ALD grown SnO_x layer.

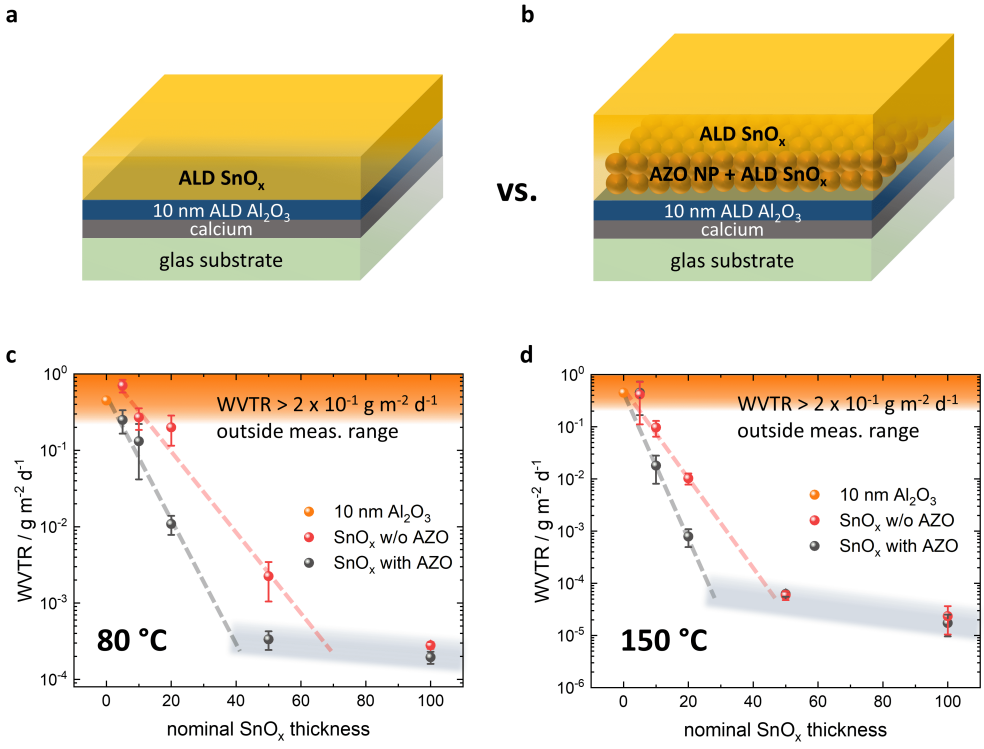

Figure 5.4: Superior barrier properties of AZO-NP / ALD-SnO_x hybrid layers. ***a,*** *Layers sequence utilized for calcium test to compare water vapour transmission rate of bare ALD SnO_x layers with* ***b,*** *hybrid layers comprising a spin coated AZO-NP layer.* ***c, d*** *Derived water vapour transmission rates at 40 % relative humidity drawn over the nominal thickness of ALD SnO_x. This is displayed for ALD reactor temperatures of* ***c,*** *80 °C and* ***d,*** *150 °C. WVTR derived for only 10 nm of ALD grown Al_2O_3 (80 °C reactor temperature) is also displayed indicating the upper confidence range of the measurement approach. The dashed lines are a guide to the eye.*

Water vapour transmission rates (WVTR) in dependency of the nominally deposited thickness of ALD SnO_x are displayed in Figure 5.4 c for ALD reactor temperatures of 80 °C and Figure 5.4 d for 150 °C. Please note the different scales of the y-axis. Importantly, already 10 nm of Al_2O_3 provided a WVTR of 2 x 10^{-1} g m^{-2} d^{-1}. Accordingly, this is the upper limit for our measurement (marked by orange in Figure 5.4 c and d), which results in some uncertainties when probing very thin (nominally 5 nm) SnO_x layers. Anyhow, looking at SnO_x layers with nominal thicknesses exceeding 10 nm the advantages of the hybrid AZO-NP / ALD-SnO_x over the solitary ALD layers is clearly evident. Both for reactor temperatures of 80 °C and 150 °C for layer thicknesses between 10 nm and 50 nm the hybrid barrier shows approximately an order of magnitude lower WVTR. Towards nominally thicker SnO_x layers the WVTR of hybrid and single SnO_x layers become similar. A levelling of the WVTR after a certain critical thickness is a frequently reported phenomenon for thin film barrier layers and has been attributed to defect-dominated gas diffusion, which is less affected by additionally deposited material. [230–234] We therefore conclude that by the usage of the hybrid barrier concept the critical number of ALD cycles needed to reach this WVTR threshold is roughly cut in half, which underlines the superiority of the hybrid barrier over solitary ALD layers. Since the above discussed dependencies were exclusively evaluated for low pressure batch ALD processes (see Figure 5.1 b), the impact of deposition parameters for spatial atomic layer deposition (S-ALD) was investigated additionally and related with solar cell results. While we already showed that with optimized process parameters similar results as with batch ALD are achievable (Figure 5.1 d & e), especially the possible web speed (substrate velocity v) is of interest. Consequently we evaluated the role of substrate speed in the S-ALD process on the functionality and stability of the resulting PSCs. First, the GPC vs. substrate speed is studied at otherwise fixed process parameters, e.g. gas flows (Figure 5.5 a). Obviously, the GPC is constant for a substrate speed below 60 mm s^{-1}. Further increasing the speed results in a reduction of the GPC, as the precursor dose is no longer sufficient to fully saturate the reactive surface sites. The decay of GPC with increasing the substrate speed was approximated with $GPC = GPC_{sat} \times (1 - exp(a\, t^{\,q}))$, similar to an equation proposed by Poodt et al. [235] Here, GPC_{sat} represents the GPC at low substrate speeds, t is the precursor exposure time and a and q are fit parameters. For a more detailed discussion on the topic, see references [229, 235]. In addition to the drop in GPC, the refractive index at 633 nm decreases with increasing the substrate speed, i.e. from 1.88 at 20 mm s^{-1} to 1.80 at 160 mm s^{-1}, indicating a lower film density. In principle, the regime of constant GPC can be extended to even higher substrate speeds by further increasing the amount of precursor delivered to the precursor exposure zone (e.g. by increasing the flow of carrier gas through the bubbler).

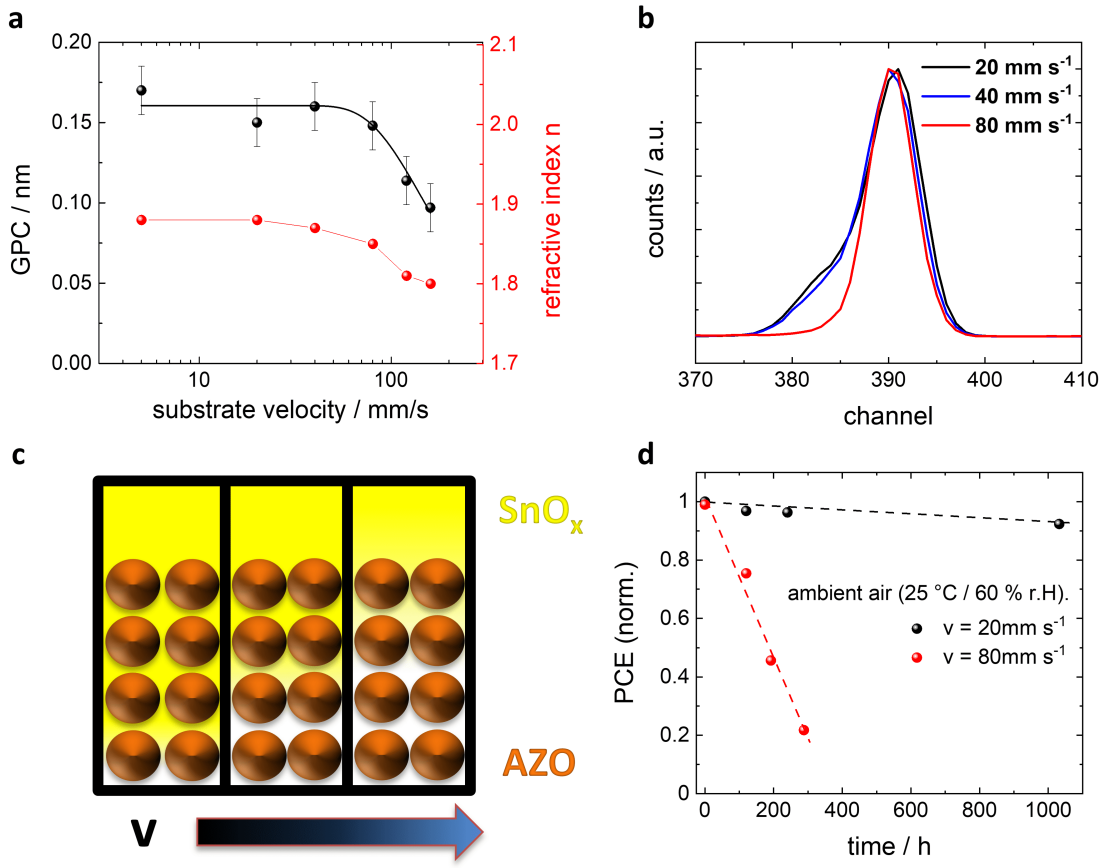

Figure 5.5: Influence of substrate velocity on the hybrid layer. ***a,*** *GPC and refractive index at 633 nm vs. substrate velocity at 80 °C deposition temperature* ***b,*** *RBS signal related to tin of the hybrid AZO / SnO_x layer for SnO_x deposited at varied substrate speed. Note, the Sn-spectra were normalized.* ***c,*** *Schematic of the growth of SnO_x (yellow) inside the AZO-NP layer* ***d,*** *Normalized PCE vs. time of storage in ambient air (25 °C, 60 % rH) for solar cells with SnO_x layer grown at 20 mm s^{-1} and 80 mm s^{-1}, respectively. Adapted with permission from [226]. Copyright 2018 American Chemical Society.*

At the same time, higher amounts of precursor would require higher purge gas flows or a spatial extension of the respective purge gas zones. Unfortunately, both these possibilities cannot be tested due to limitations of our home-built S-ALD system. Aside from the changes of layer properties, increasing the substrate velocity reduces the exposure time of the porous layer to the respective precursor species in the S-ALD process. Thereby the time for diffusion of precursors into the pores of the AZO layer is shortened. As suggested above (Figure 5.4 and Figure 5.2), the functionality of the hybrid AZO / SnO_x layer as a permeation barrier relies critically on the penetration of ALD precursors into the pores of the AZO layer and the concomitant growth of SnO_x inside these pores. To further study the consequences of increased substrate speed, we

analysed the resulting AZO / SnO_x hybrid layers by Rutherford Backscattering (RBS). The degree of penetration of tin atoms into the pores of the AZO layer becomes obvious form the Sn related RBS spectra (Figure 5.5 b). For relatively small substrate speeds of 20 mm s^{-1} and 40 mm s^{-1} the Sn-peak in the RBS spectrum shows a notable shoulder, indicating the penetration of tin atoms into the AZO layer underneath (see above). On the contrary, for SnO_x grown at elevated substrate speed of 80 mm s^{-1}, a rather symmetric Sn-peak is found, indicating a substantially reduced penetration of tin into the pores of the AZO-NP layer. Note, for SnO_x grown on a flat, non-porous substrates the tin RBS spectrum is fully symmetric (compare 5.2), regardless of substrate speed. A schematic of the penetration of SnO_x in the AZO-NP layer is shown in Figure 5.5 c.

The WVTR of SnO_x single layers (100 nm) grown at 80 mm s^{-1} show inferior permeation barrier properties (WVTR 4×10^{-3} g m^{-2} d^{-}1 @ 60 % rH) compared to their analogue grown at lower speed (WVTR 2×10^{-4} g m^{-2} d^{-}1 @ 60 % rH). This indicates an overall deterioration of layer density at elevated substrate speed, in agreement with the observed drop of the refractive index, as discussed above. As a result, the lifetime of PSCs based on the respective AZO / SnO_x is critically affected by the choice of substrate speed, when the devices are exposed to ambient air (25 °C / 60 % rH) (Figure 5.5 d). The PCE of the PSCs based on the SnO_x grown at a substrate speed of 80 mm s^{-1}, which does not afford filling of the AZO pores, decreases dramatically within the first 300 hours in air, while those cells, in which the SnO_x has been grown at 20 mm s^{-1} show only minimum degradation even after more than 1000 hours.

While we have found that increasing the substrate speed compromises the barrier properties of the AZO / SnO_x hybrid layer, deposition temperature is a likewise critical parameter. For other material systems, an elevated growth temperature has been shown to have a beneficial impact on the layer density, electrical conductivity and reduced concentration of precursor residues of the resulting ALD layers. [209, 229, 236] Hence increasing the temperature might be a viable option to enable S-ALD growth of high quality intermixed AZO-NP / SnO_x layers for perovskite solar cells.

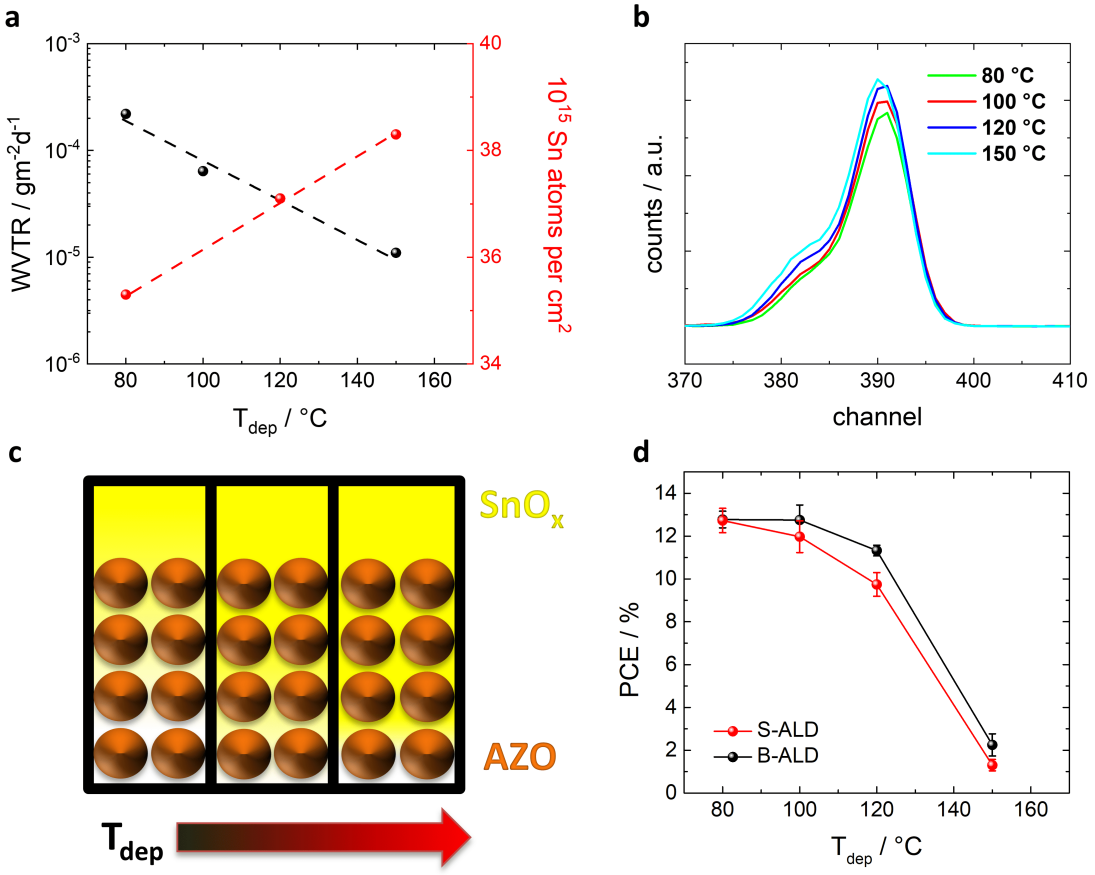

Figure 5.6: Spatial ALD: Influence of substrate temperature on the hybrid layer. a, *Water vapor transmission rate of SnO_x thin films (layer thickness: 100 nm)) and tin atom density (by Rutherford Backscattering) for neat S-ALD SnO_x layers of each 20 nm thickness* ***b,*** *RBS spectra of Sn measured on AZO (60 nm) / SnO_x hybrid layers with increasing deposition temperature.* ***c,*** *Corresponding partial growth of SnO_x inside the pores of the AZO-NP layer (schematically).* ***d,*** *PCE of the corresponding perovskite solar cells based on SnO_x grown at various temperatures. The substrate speed was 20 mm s^{-1} in this set of experiments. Adapted with permission from [226]. Copyright 2018 American Chemical Society.*

To analyze the influence of deposition temperature in case of our SnO_x layers grown by S-ALD, we performed a series of RBS studies. We were able to show that the areal density of tin atoms (for a 20 nm thick layer) increases slightly from 3.5×10^{16} atoms cm^{-2} to 3.8×10^{16} atoms cm^{-2} with increasing the deposition temperature. Concomitantly, the WVTR of 100 nm thick solitary SnO_x layers at 60 % rH. decreases by about an order of magnitude from $\approx 10^{-4}$ g m^{-2} d^{-1} to about 10^{-5} g m^{-2} d^{-1} (Figure 5.6 a). These observations are in line with results shown for low pressure ALD in 5.4 and have been, together with other layer properties, reported for solitary SnO_x layers in [228]. Moreover, for the hybrid AZO-NP / ALD-SnO_x layers the characteristic shoulder in the RBS spectra

towards lower channel numbers indicating the partial growth of SnO_x in the pores of the AZO layer shows a notable dependence on the deposition temperature (Figure 5.6 b). As expected, higher deposition temperatures infer an increased penetration of the SnO_x into the porous AZO (Figure 5.6 c). This is very likely due to thermally activated precursor diffusion. [218] Owing to an improved mass density, lowered WVTR and better pore filling of the SnO_x, increasing the deposition temperature appears to be attractive for the application in PSCs. Unfortunately, temperatures in excess of 100 °C result in PSCs with substantially deteriorated characteristics (Figure 5.6 d and for a full set of device characteristics see Appendix Figure 11.6). Here, it is important to note that the post-deposition annealing of the perovskite layers was done at 100 °C. It has been shown, that $MAPbI_3$ degrades very rapidly at temperatures higher than 100 °C. [202, 237] For both S-ALD and B-ALD some exposure-time to the growth temperature prior to the actual deposition is inevitable. Thus, the observed deterioration of our PSC at an ALD deposition temperature > 100 °C is very likely related to the thermal instability of the perovskite. To further exploit the superior properties of SnO_x grown at $T > 100$ °C, the use of more temperature stable perovskite materials will certainly be very rewarding, but is beyond the scope at this point.

6 Semi-Transparent Cells with Hybrid Metal Oxide Layers

For this chapter I teamed up with both Dr. Jie Zhao and Dr. Tobias Gahlmann, who provided thorough expertise in the fabrication of semi-transparent solar cells and electrodes, while my focus was mainly on the perovskite stability and interface part of the work.

Parts of this chapter have been published in:

Zhao, J.; Brinkmann K.O. et al. "Self-Encapsulating Thermostable and Air-Resilent Semitransparent Perovskite Solar Cells" Adv. Energy Mater. 7, 1602599 (2017). [238]

and

Gahlmann, T; Brinkmann, K.O. et al. "Impermeable charge transport layers enable aqueous processing on top of perovskite solar cells." Adv. Energy Mater. 10, 1903897 (2020). [239]

6.1 Sandwiched Ultra-Thin Silver Layers

For a number of applications, PSCs require semi transparent top electrodes, e.g. for building integration (windows), multi-junction architectures, or cases where an opaque substrate is considered (i.e. top-illuminated devices). The most widely established semi-transparent electrodes based on indium-tin-oxide (ITO) are typically prepared by sputtering followed by a high-temperature annealing step (around 450 °C) to achieve a combination of a low sheet resistance (R_{sh}) and a high optical transmittance. [240–242] As semi-transparent top-electrode for a PSC, annealing at temperatures in this range would thermally decompose the perovskite. An alternative concept for the realization of semitransparent electrodes is based on ultra-thin metal films with a thickness of

less than 10 nm (see e.g. Figure 6.1 a). This is achieved by carefully tailoring optical admittance of the sandwich metal oxide / metal layer stack to bring it as close as possible to (n_{AIR}, 0) and significantly reduce transmittance losses (see Figure 6.1 b). [243–245] Unfortunately, these ultra-thin metal layers are particularly prone to be attacked by potential perovskite decomposition products like MAI, HI, etc. (chapter 4).

As an alternative, gold may provide enhanced resilience, but on the other hand the best figures of merit for gold-based semi-transparent electrodes are substantially inferior compared to those based on silver. [243] Moreover, the cost of gold may be a further concern. Nevertheless, first semi-transparent perovskite solar cells with a MoO_3 / Au / MoO_3, MoO_3 / Au / Ag / MoO_3 and MoO_3 / Ag / ZnS top-electrode were already demonstrated before 2016. [246–248] Unfortunately, neither of these reports commented on the stability of their devices upon exposure to air / elevated temperature. In view of the susceptibility of ultra-thin metal layers to corrosion by halide compounds, stability must not be taken for granted and remains a serious concern. In this regard, it is essential to suppress the decomposition of the perovskite active layer and to protect the ultra-thin metal film against the chemical attack by the halide compounds eventually leaking out from the perovskite. Thereby, the applicability of ultra-thin silver layers along with their superior optical properties as semitransparent electrodes would be afforded, without compromising the long term stability of the cells.

To achieve this goal we further developed the approach of a hybrid AZO / SnO_x internal barrier, that already proved to significantly suppress device degradation, into a semi-transparent electrode. For integration into a solar cell stack, as introduced in previous chapters, the most straight-forward approach is to deposit the ultra-thin metal layer directly on top of the AZO electron extraction layer. However, it turned out that the nucleation and growth of the ultra-thin Ag layer on top of AZO is substantially different from the growth on SnO_x. For a deeper study, we discussed the conductivity and transmittance of ultra-thin silver layers deposited by either RF magnetron sputtering or thermal evaporation on top of AZO or AZO / SnO_x (Figure 6.2). Indeed, the SnO_x layer on top of the AZO layer is essential to facilitate the wetting of the Ag layer and thereby to achieve a percolated Ag layer at an overall smaller amount of deposited silver. For example, a 7 nm thin layer of Ag sputter deposited on top of AZO / SnO_x provides a sheet resistance of 10 Ω sq^{-1}., while the same Ag layer sputtered directly on top of AZO only affords 180 Ω sq^{-1}. The reason for this striking difference is the preferred island-like growth of Ag on top of AZO compared to SnO_x as evidenced by SEM studies (Figure 6.2 c). A further conclusion of these orienting experiments is the clear advantage of sputter deposition vs. thermal evaporation of the Ag layer to

achieve a percolated thin film. For the same nominal Ag thickness, thermal evaporation affords a sheet resistance about 60-100 higher than sputtering. Therefore we chose a top electrode of SnO_x (20 nm) / Ag (7 nm) / SnO_x (20 nm), where the Ag layer has been deposited by sputtering (see Figure 6.1 a). Figure 6.1 c shows the transmittance spectrum and average transmittance (T_{av}) from 390 to 780 nm of SnO_x, Ag, SnO_x / Ag, and SnO_x / Ag / SnO_x, respectively. Optical photographs of the as-prepared stacks on glass substrates can be seen in Figure 6.1 d along with their electrical sheet resistance (R_{sh}). Expectedly, when the 7 nm thin silver layer is directly deposited onto the glass substrate, only relatively poor numbers for T_{av} = 59 % and R_{sh} = 22 Ω sq^{-1} are achieved, which are not further improved by adding a SnO_x capping layer (T_{av} = 60 %, R_{sh} = 32 Ω sq^{-1}). The situation changes drastically if the Ag layer is deposited on top of a SnO_x layer, in which case notably improved T_{av} = 77 % and R_{sh} = 10 Ω sq^{-1} are achieved.

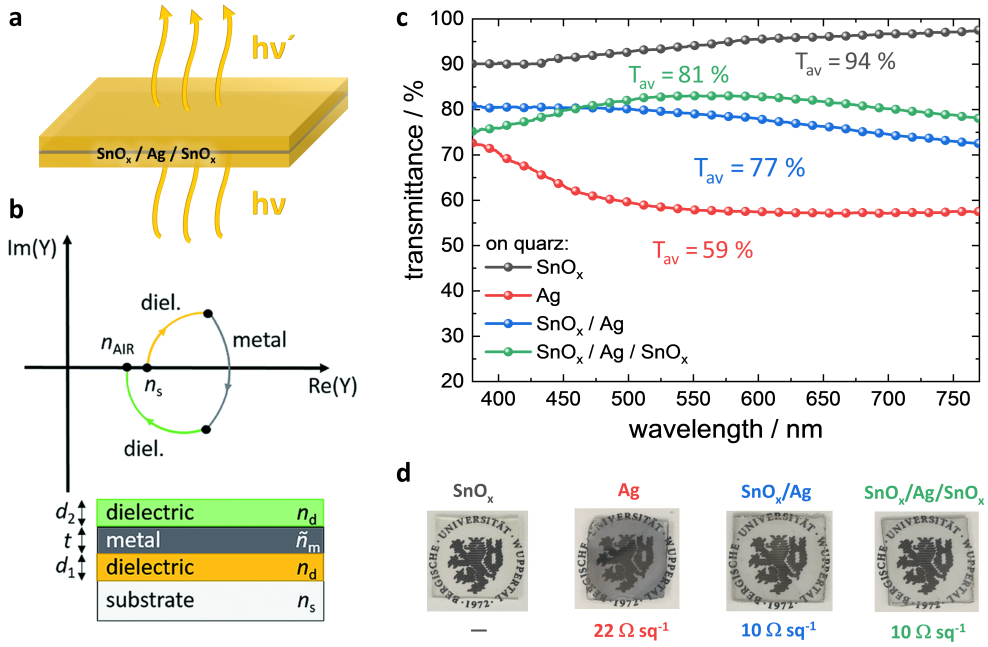

Figure 6.1: Ultra-thin metal layers as semitransparent electrodes. ***a,*** *Layer stack indicating the setup of the semi-transparent SnO_x / Ag / SnO_x electrode* ***b,*** *Exemplary admittance plots taken from [243]* ***c,*** *Optical transmittance spectrum of the Ag and SnO_x based films in the visible spectral range from 390 to 780 nm.* ***d,*** *Photographs of the corresponding layers on glass substrates along with their electrical sheet resistance R_{sh}. The Ag layers were deposited by RF magnetron sputtering (thickness: 7 nm). Note, for the 20 nm thin SnO_x layer we were not able to determine a sheet resistance. b, adapted from [243]. c, d, adapted with permission from [238]. Copyright 2017 WILEY-VCH.*

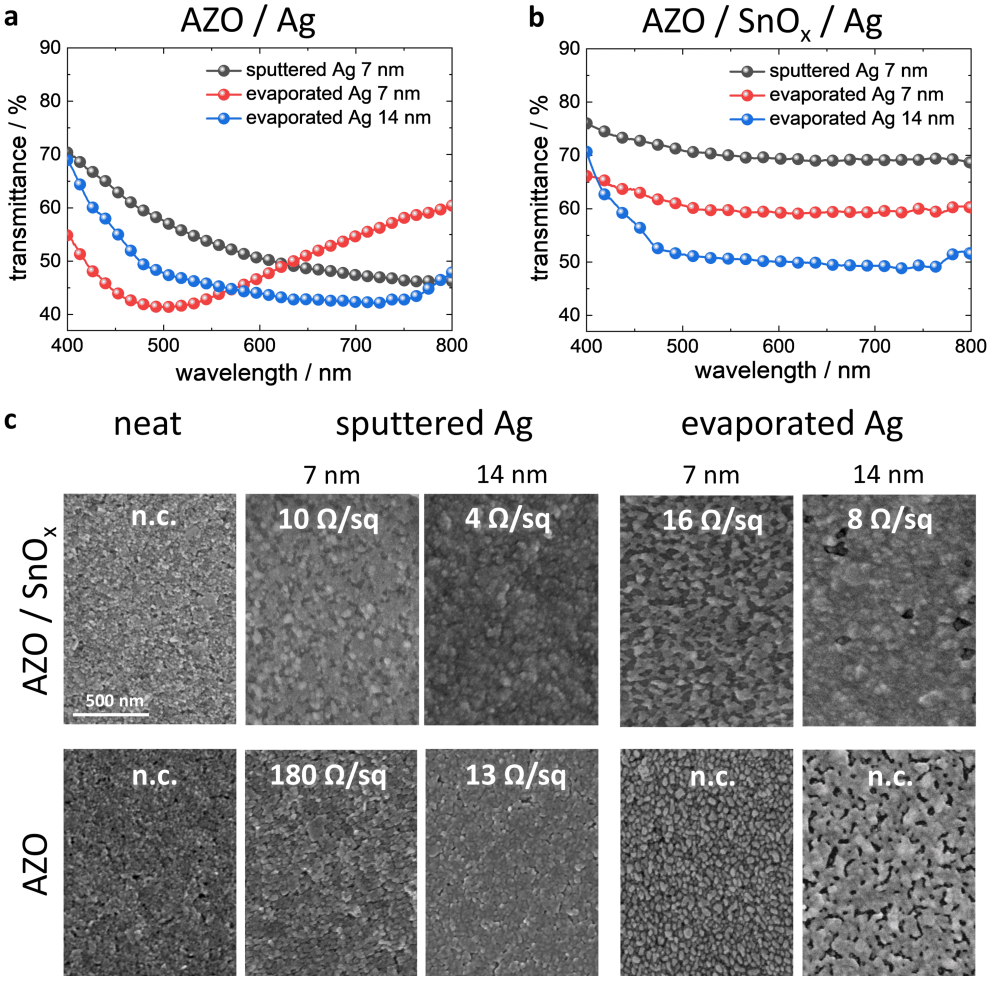

Figure 6.2: Formtion of ultra-thin silver. ***a,*** *Transmittance spectra of Glass / AZO / SnO_x / Ag structures and* ***b,*** *Glass / AZO / Ag structures as a function of the Ag layer.* ***c,*** *SEM images of the surface morphology of glass / AZO / SnO_x / Ag and glass / AZO / Ag structures where nominally 7 and 14 nm of Ag were either sputtered or evaporated. Adapted with permission from [238]. Copyright 2017 WILEY-VCH.*

In the case where the Ag layer is sandwiched between two SnO_x cladding layers the transmittance can be further optimized (T_{av} = 81 %, R_{sh} = 10 Ω sq^{-1}.). The corresponding Haacke Figure of merit [249] $\Phi = (T_{av}{}^{10}/R_{sh})$ = 1.2 x 10^{-2} Ω^{-1} is significantly better than that of ITO, that has been deposited by sputtering without thermal post treatment (Φ = 2.4 x 10^{-3} Ω^{-1}). [250] Note, the thickness of the upper SnO_x layer has been optimized using a transfer matrix algorithm (SETFOS^{TM}). [244, 245] For further details, please see supplementary information of [238].

We furthermore note, that our transmittance values T_{av} are determined in reference to air and not in reference to the glass substrate (which would significantly increase T_{av}). As the maximum processing temperature of the SnO_x / Ag / SnO_x electrode assembly is only 80 °C, it is a suitable candidate to be applied as a semitransparent top-electrode in semitransparent PSCs.

Finally we prepare perovskite solar cells employing the semi-transparent SnO_x / Ag / SnO_x top electrode. The respective solar cell stack is shown in Figure 6.3 a. Please note that these experiments were undertaken before our perovskite was optimized and therefore one-step deposition was utilized (compare chapter 3). Respective J-V scans are shown in Figure 6.3 and derived solar cell characteristics are summarised in Table 6.1. The semitransparent solar cells were illuminated from the top and the bottom (glass) side, respectively, and are presented in comparison with an opaque device. Illumination from the glass side shows a higher performance than illumination from the top-side, mainly because of a higher J_{SC} of 17.6 mA cm^{-2} vs. 15.1 mA cm^{-2}.

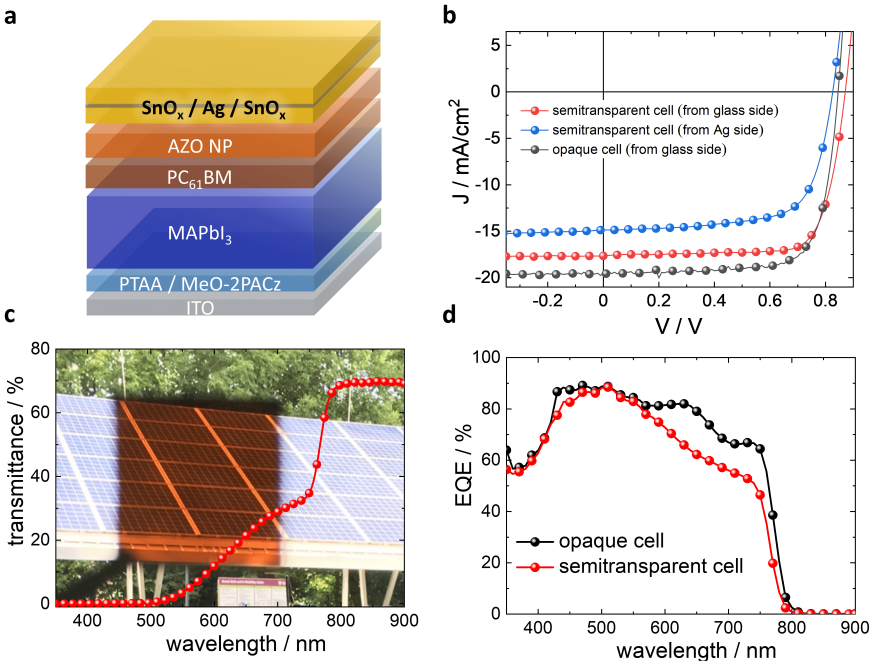

Figure 6.3: Semitransparent solar cells with ultra-thin metal top electrode a, *Layer stack of the semitransparent solar cell* ***b,*** *J-V characteristics of semitransparent solar cells with 7 nm Ag electrode upon illumination via the top or bottom electrode. The characteristics of an opaque cell are shown as a reference.* ***c,*** *Transmittance spectrum and photograph of the entire semitransparent solar cell stack.* ***d,*** *External quantum efficiency (EQE) spectra of the semitransparent cell with SnO_x / Ag / SnOx electrode compared to an opaque cell. Adapted with permission from [238]. Copyright 2017 WILEY-VCH.*

Table 6.1: *Solar cell characteristics of opaque and semi-transparent perovskite solar cells (one-step deposition) comprising either 7 nm sputtered or 100 nm evaporated (opaque) electrodes. For semi-transparent devices both illumination directions are displayed. Forward direction measurements are omited, since no hysteresis invariant of scan speed was observed.*

	PCE / %	FF / %	V_{OC} / V	J_{SC} mA cm^{-2}
semi-transp.; glass illum.	11.8	78	0.87	17.6
semi-transp.; Ag illum.	8.6	66	0.83	15.1
opaque	12.6	77	0.89	19.4

We attribute the higher efficiency in the former case to some reflection by the top electrode and absorption caused by the electron transport layer, which in turn results in a lower J_{SC} upon top illumination. The transmittance spectrum and a photograph of the semitransparent solar cell stack are shown in Figure 6.3 c. Our semitransparent cells show an elevated transmittance in the range of 500 to 750 nm, which causes the brownish appearance of the device. In the assessment of the transmittance, one has to note that the polycrystalline perovskite layer leads to some substantial light scattering. Thus, we had to take both the normal specular transmittance as well as the diffuse scattered transmittance into account by applying a routine as discussed in our previous work. [251] The transmittance spectrum, exhibits an average transmittance of 17 % in the visible region (= 500 - 750 nm) and a relatively high transmittance of about 70 % in the near-infrared region (> 800 nm). The external quantum efficiency (EQE) spectra of a semitransparent cell compared with that of the opaque reference cell with a 56 nm thick opaque Ag top electrode are shown in Figure 6.3 d. The lowered EQE of the semitransparent cell in the region of 500 - 750 nm is in good agreement with the elevated transmittance in this region (Figure 6.3 c).

The most striking property of our SnO_x / Ag / SnO_x top-electrodes is, that the resulting semitransparent cells show an outstanding long-term stability as shown in Figure 6.4. Our devices have been continuously exposed to ambient atmosphere (23 °C and 50 % rH), room temperature in nitrogen, or 60 °C in nitrogen for a long time measurement. As the SnO_x / Ag / SnO_x inherits the barrier properties of the ALD SnO_x cladding layers, it is suitable to protect the perovskite cells against the ingress of moisture. After 4500 h of continuous exposure to ambient air, the cells still show 81 % of their initial PCE. V_{OC} even shows a slight increase over time. An increase of V_{OC} on similar time scales has been reported by other authors and it has been explained by an aging effect that reduces the density of trap states in the perovskite. [252] The dominating effect for the reduction of the PCE is a concomitant decay of the FF and J_{SC} to about 86 %

of their initial values, which may be due to the onset of some degradation of the Ag electrode after more than 4500 h, in-spite of it being sandwiched between the 20 nm SnO_x permeation barriers. This effect may be mitigated by using thicker SnO_x layers or by an additional external moisture barrier. At an elevated temperature of 60 °C under N_2, the PCE does not change after 4500 h. Thus, we conclude that the SnO_x not only functions as permeation barrier that prevents the ingress of moisture from ambient air, but it also states a sufficient barrier to protect the ultra-thin Ag layer against attack due to the corrosive halide moieties that may leak out from the perovskite upon heating.

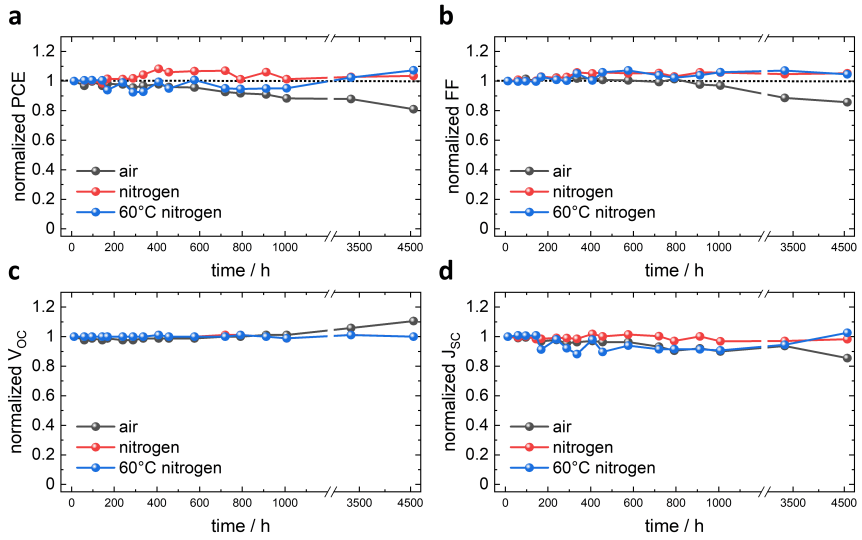

Figure 6.4: Stability of semi-transparent solar cells *employing a 7 nm sputtered Ag electrode sandwiched between two 20 nm ALD SnO_x layers.* ***a,*** *Normalized power conversion efficiency (PCE)* ***b,*** *fill factor (FF)* ***c,*** *open circuit voltage (V_{OC}) and* ***d,*** *short circuit current density (J_{SC}) over a time period of 4500 hours either in ambient air, nitrogen or in nitrogen at elevated temperatures (60 °C). Adapted with permission from [238]. Copyright 2017 WILEY-VCH.*

To further address this topic, we elucidate the importance of the SnO_x as a permeation barrier underneath the ultra-thin Ag layer. In a dedicated set of experiments we prepared devices with AZO / Ag and AZO / SnO_x / Ag that were then similarly sealed with the ALD SnO_x cap on top. As the nucleation of the Ag layer on top of AZO is inferior to that on SnO_x, we decided to use 14 nm of Ag in this set of samples to be sure to achieve a low R_{sh} on the order of 10 Ω sq^{-1} also in the AZO / Ag case. Further, to avoid the requirement of an inert gas break we deposited the Ag layer by thermal evaporation in a high-vacuum chamber directly connected to the glovebox. As visible in Figure 6.5, the initial device performance of the fresh cells (glass side illumination) is similar to that of devices based on a sputtered Ag electrode.

Table 6.2: *Initial characteristics of semitransparent PSCs with or without SnO_x between the AZO layer and the ultra-thin Ag layer. The Ag layer in this set of samples was 14 nm and it has been prepared by thermal evaporation. Note, current density values have been corrected for spectral mismatch of our AM1.5G light source by using EQE data.*

	PCE / %	FF / %	V_{OC} / V	J_{SC} mA cm^{-2}
AZO / Ag	10.0	70	0.84	16.9
AZO / Ag / SnO_x	8.4	62	0.84	16.0
AZO / SnO_x / Ag /	11.4	72	0.86	18.3
AZO / SnO_x / Ag / SnO_x	11.2	73	0.86	17.9

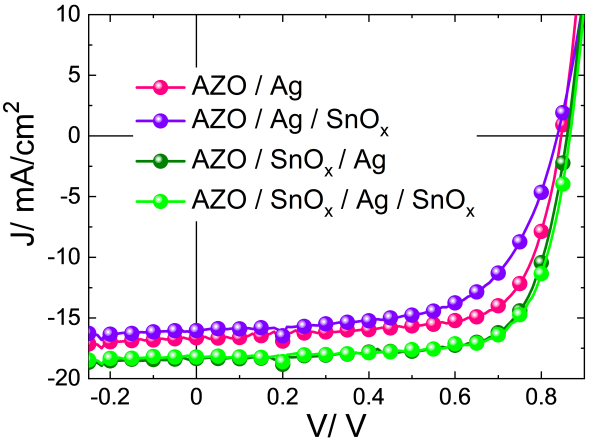

Figure 6.5: *J-V characteristics of devices based on AZO / Ag and AZO / SnO_x / Ag with or without an additional SnO_x cap deposited by ALD on top. The Ag layer thickness was 14 nm in this set of samples. The cells were illuminated via the substrate side. Note, current density values have been corrected for spectral mismatch of our AM1.5G light source by using EQE data. Adapted with permission from [238]. Copyright 2017 WILEY-VCH.*

The device characteristics of the freshly prepared cells are summarized in Table 6.2. The J-V characteristics of PSCs based on AZO / Ag and AZO / SnO_x / Ag without and with an additional SnO_x capping layer are shown in Figure 6.5. While the cells based on AZO / SnO_x / Ag are quite comparable to those with SnO_x capping layer (i.e. AZO / SnO_x / Ag / SnO_x), the cells where the SnO_x cap has been deposited on top of the AZO / Ag show some significant deterioration, mainly in the FF. To understand this behaviour, we need to keep in mind that the SnO_x layers are deposited by ALD at a temperature of 80 °C. As the devices are not degraded by the deposition of the SnO_x layer on top of the AZO in the AZO / SnO_x / Ag samples, we can assume that the ALD process itself does not damage the perovskite active layer. Moreover, we can rule out direct damage of the Ag layer by heat or the precursors of the ALD process, as this

would have been apparent in the devices based on AZO / SnO_x / Ag / SnO_x, which did not show any sign of degradation. However, it is known that the elevated temperatures in the ALD process may infer some (vestigial) decomposition of the perovskite whose decomposition products would then leak out through the permeable (porous) AZO layer that might partially degrade the ultra-thin Ag layer. We have measured R_{sh} of the top electrode in the AZO / Ag and AZO / Ag/ SnO_x solar cells and found that it was almost identical, 9.7 Ω sq^{-1}. and 10.4 Ω sq^{-1}, respectively. Therefore, we conclude that the degradation of the Ag layer most likely happens at the interface between Ag and AZO, which results in the observed low FF of the AZO / Ag / SnO_x cells. The proposed decomposition mechanism is displayed in Figure 6.6 a & b. This is also in line with observations made in chapter 4, where in Figure 4.6 XPS is used to investigate the surface of thermally stressed perovskite solar cell stack with thin evaporated metal layers.

In strong contrast, Ag layers on top of the impermeable SnO_x in the AZO / SnO_x / Ag assembly would remain unaffected (Figure 6.5). Note, for Au electrodes thermally induced migration of the metal has been identified to be an important source of degradation. [253] While we cannot rule out Ag migration in our AZO / Ag based devices, there are reports using (in-situ) TEM that identified out-diffusion of perovskite decomposition products to be the dominating effect. [199, 254] Also our own XPS provided strong support of out-diffusing iodine compounds that destroyed the Ag electrode as the most relevant degradation mechanism (chapter 4). This finding is in-line with an earlier report by Kato et al., who clearly identified corrosion of the Ag electrode due to migrating iodine compounds in perovskite solar cells. [65] Finally, we tested the long term stability of devices with AZO / Ag / SnO_x and AZO / SnO_x / Ag / SnO_x at 60 °C in N_2 atmosphere (Figure 6.6 a-d). In striking contrast, the device efficiency of the AZO / Ag / SnO_x based devices decreases dramatically, while the devices based on AZO / SnO_x / Ag / SnO_x once again remained essentially stable for more than 3000 h (95 % of it's initial PCE). In our devices, in stark contrast to previous reports of thermally instability of perovskites, [68, 199, 255] the outstanding barrier property of our AZO / SnO_x layer separating the perovskite and the ultra-thin Ag layer efficiently protects the metal against chemical attack by perovskite decomposition products. This enables outstanding stability not only in ambient air, but also unprecedented robustness at elevated temperatures (60 °C in N_2) over more than 4500 h.

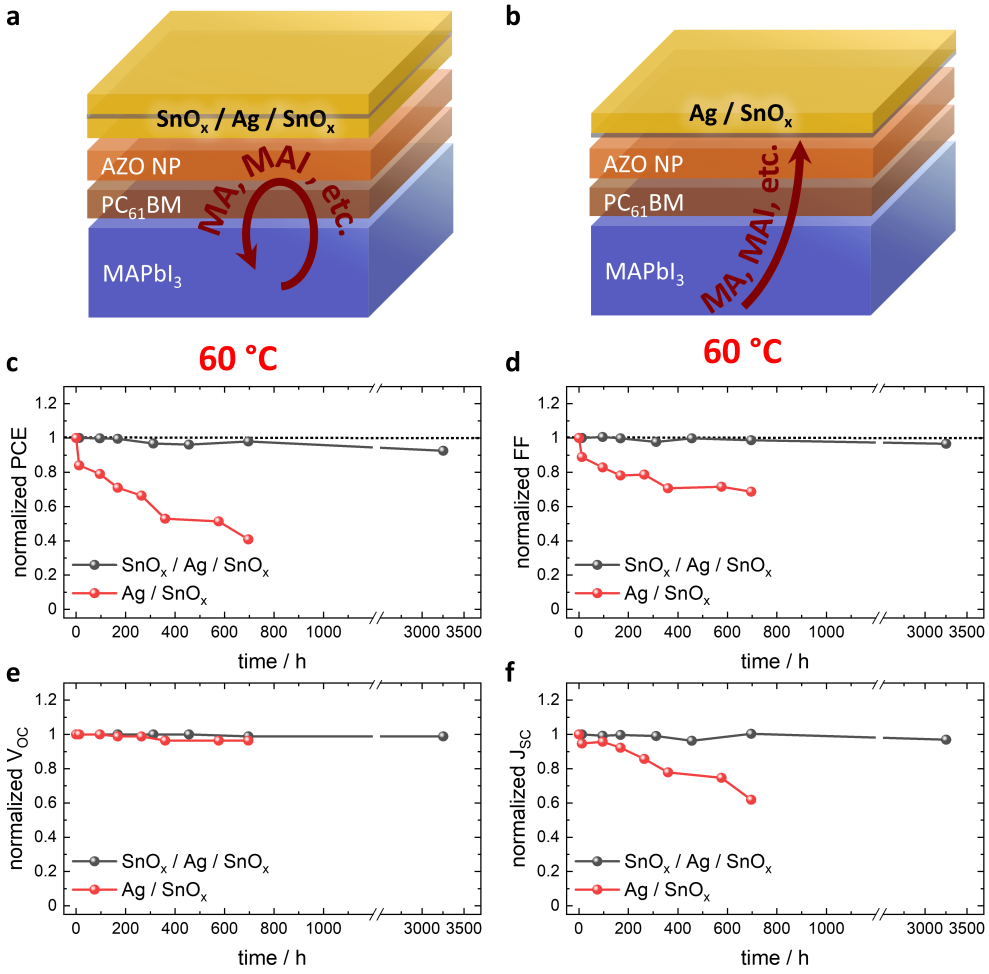

Figure 6.6: Essential function of internal barrier. *Schemes of the proposed mechanisms for* ***a,*** *AZO / Ag and* ***b,*** *AZO / SnO_x / Ag samples covered with ALD SnO_x.* ***c-f,*** *Stability of solar cells employing a 14 nm Ag electrode either sandwiched between two 20 nm ALD SnO_x layers or just covered by ALD SnO_x.* ***c,*** *Normalized power conversion efficiency (PCE)* ***d,*** *fill factor (FF)* ***e,*** *open circuit voltage (V_{OC}) and* ***f,*** *short circuit current density (J_{SC}) over a time period of over 3000 hours at elevated temperatures (60 °C). Adapted with permission from [238]. Copyright 2017 WILEY-VCH.*

6.2 Water Processed Silver Nanowire Top Electrodes

While the above discussed metal nanostructures rely on vacuum based processes like evaporation or sputtering, metal-nanowires are a promising alternative semi-transparent electrode, that can be processed at low temperature from liquid dispersions. [243] Silver nanowires (AgNW) in dispersions of alcohol or water are the most prominent representatives. Water is an especially favourable dispersing medium as it is environmentally friendly and does not impose safety concerns typically associated with alcohols, such as flammability. On the other hand, water is widely recognized as a serious threat to lead-halide perovskites. [58, 195, 198, 256] Therefore, a protection layer would be required, that simultaneously forms an electronic interface between the device and the AgNWs. A number of well-established protection layers are insulators that cannot be used for this purpose. [257–259] On the other hand, in the preceding chapters, we introduced electron transport layers grown by atomic layer deposition, that protected the perovskite against the detrimental impact of ambient gases. Similar approaches have been undertaken as protection from high-energy particles of sputtering processes. [237] However, water-based processing of functional layers, such as electrodes, on top of a perovskite device stack had not been reported. Hence we decided to investigate the feasibility of our hybrid AZO / SnO_x barrier layer to protect a perovskite solar cell from an aqueous follow-up process like spray-coating.

To assess the resilience of the devices to water exposure, a drop of water has been dispensed on top of the cell and was dried subsequently at 60 °C on a hotplate (Figure 6.7 a, c). In the case where there is only a PCBM / AZO layer on top of the perovskite, water readily penetrates the entire device stack and causes some notable decomposition of the perovskite to PbI_2 (see yellow region in Figure 6.7 b). In X-ray diffraction a clear peak associated with PbI_2 occurs, whilst reflections due to the perovskite have almost disappeared (Figure 6.7 c). On the contrary, for devices employing our hybrid AZO / SnO_x barrier layer, no decomposition of the perovskite due to water exposure is observed. Please note the drop of water shows some better wetting on top of the hydrophilic ALD layer, but neither the optical image nor XRD indicate the presence of PbI_2 after the drop has dried. Previously, we have quantified the water vapor transmittance rate (WVTR) of similar ALD-grown SnO_x layers (100 nm) to be on the order of 10^{-5} g m^{-2} d^{-1}, which is comparable to that of excellent permeation barriers used for the encapsulation of organic electronics (see chapter 5 and [209, 260]).

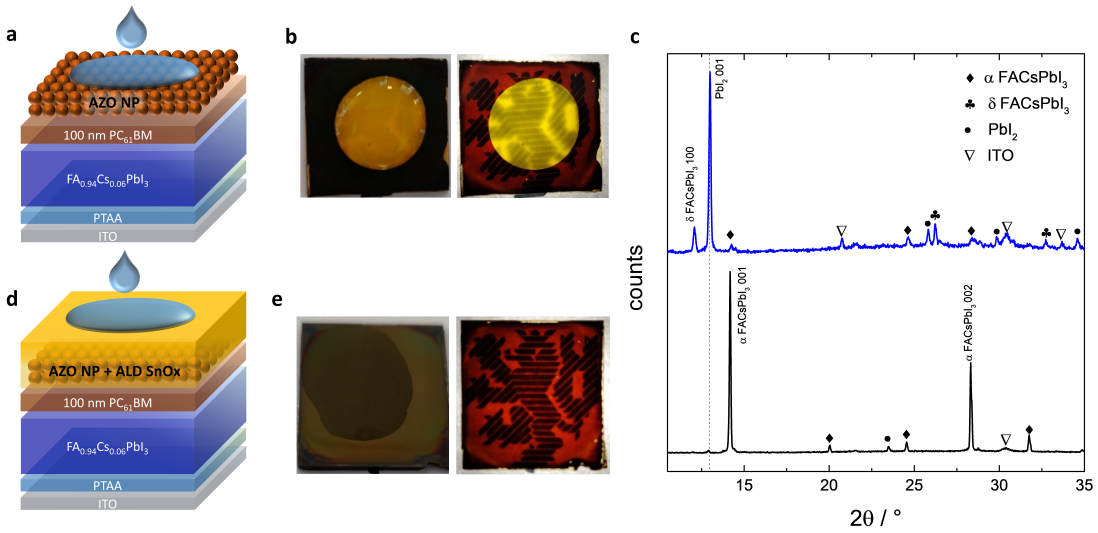

Figure 6.7: Water droplet test on cell stacks. ***a,b*** *Solar cell device stacks without ALD SnO_x and photographs of the respective samples with a drop of water dispensed on top (illuminated from top, left) and after drying (illuminated from the backside, right)).* ***d,e*** *Similar cell stacks and photographs for a water droplet dispensed on a stack employing 20 nm of ALD SnO_x on top of the AZO-NP layer and* ***c,*** *X-ray diffractograms of the respective samples after water exposure. The graphs were vertically offset for clarity. Adapted from [239].*

Encouraged by these promising orienting experiments, we spray coated a semi-transparent AgNW-based electrode from an aqueous dispersion on top of devices with a PCBM / AZO / SnO_x ETL (Figure 6.3 a, b). Details of the AgNW dispersion and the spray coating process can be found in [239]. Following an initial optimization of spray-coating parameters, our AgNW electrodes deposited on glass substrates show an average transmittance (T) of 87 % in the spectral range of 350 - 1200 nm, with R_{sh} as low as 12 Ω sq^{-1}. Surprisingly, the J-V characteristics of the resulting AgNW based PSCs show a striking dependence on the direction of illumination (top or bottom) (Figure 6.3 c). Bottom illumination results in s-shaped J-V characteristics with a low fill factor < 40 % and low power conversion efficiency of only about 6 %. On the contrary, top illumination affords well-behaved solar cell characteristics with a high FF of ≈ 79 % and a PCE above 13 %. Note, the short-circuit current density (J_{SC}) upon top illumination is on average 4.4 mA cm^{-2} lower than upon bottom illumination (Figure 6.3 c). By an optical simulation, the contribution of the ETL to this loss is determined to be 2.5 mA cm^{-2}, while 1.9 mA cm^{-2} are lost in the AgNW top-electrode (see [239]). Note, opaque reference devices with a 100 nm thick evaporated Ag electrode show a J_{SC} of 23 mA cm^{-2} and a PCE exceeding 18 %, like shown in chapter 3. The solar cell characteristics are summarized in Table 6.3.

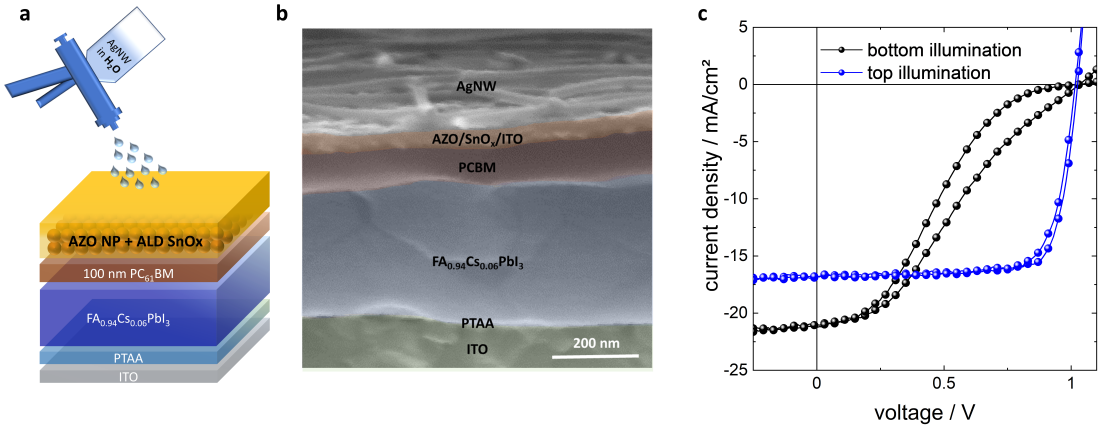

Figure 6.8: Solar cells employing water processed silver nanowires (AgNW). a, *Layer sequence and* ***b,*** *respective cross sectional SEM images of the solar cell.* ***c,*** *J-V characteristics of solar cells with Ag-NW top electrode upon illumination from the bottom (ITO) or top (Ag-NW) side. Adapted from [239].*

Table 6.3: *Cell characteristics of representative solar cells with AgNW top electrodes processed from water on solar cell stacks with an ALD SnO_x electron extraction layer. J_{EQE} is the short circuit current density determined from the EQE data.*

illumination	**reverse**			EQE	**forward**		
	PCE / %	FF / %	V_{OC} / V	J_{EQE} / mA cm^{-2}	PCE / %	FF / %	V_{OC} / V
bottom-side	6.4	30	1.03	21.1	5.6	25	1.03
top-side	13.4	79	1.02	16.7	12.7	75	1.02

To better understand the origin of the notably different cell characteristics upon top/bottom illumination, we constructed a set of test devices as shown in Figure 6.9 a, where a layer sequence of ITO / SnO_x / AgNW is used, without any perovskite involved. Remarkably, the J-V characteristics of these devices also show a rectifying behavior (Figure 6.9 b). On the contrary, if the AgNW electrode is replaced by an evaporated Ag electrode, the J-V characteristics are ohmic. In an aim to find a possible root cause of the diode-like behavior in case of the AgNWs, it is essential to consider, that the AgNWs are capped with polyvinylpyrrolidone (PVP), which is a typical capping agent for AgNWs in liquid dispersion. On the other hand, PVP has earlier been used to lower the work function (WF) of oxide-based electrodes. For example, Shim et al. have shown that PVP capping of an ITO electrode afforded a lowering of the WF by about 0.8 eV. [261] In a similar manner, we have tested a thin intentional PVP coating of our SnO_x layers and found a lowering of the WF by 0.3 eV.

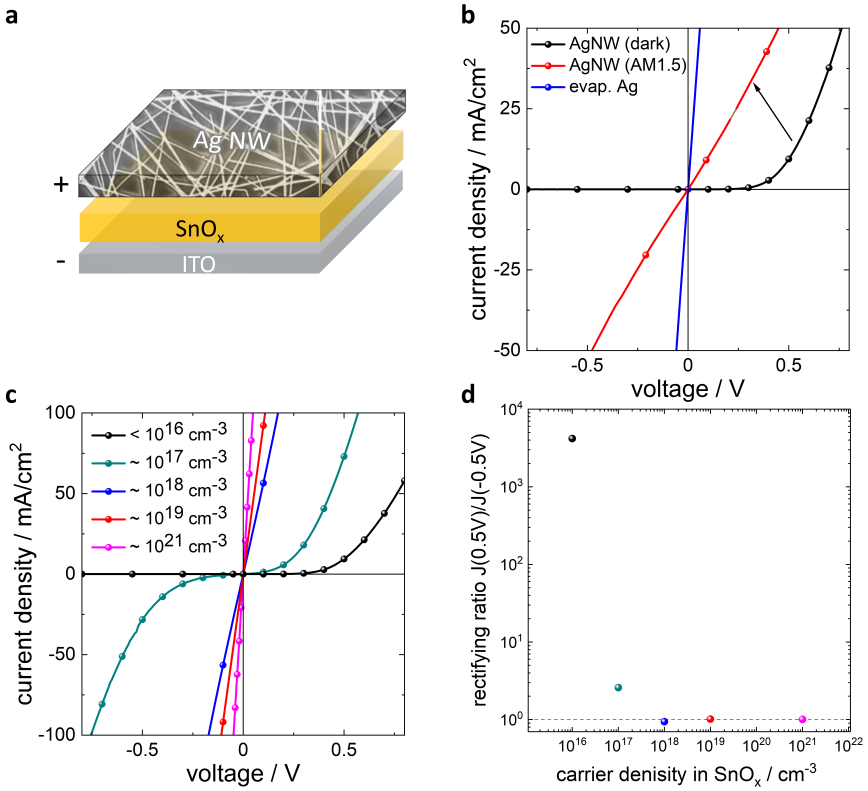

Figure 6.9: Spotlight on the SnO_x / silver nanowire (AgNW) interface. ***a,*** *Schematic illustration of the test stack used to investigate the SnO_x / AgNW interface* ***b,*** *J-V characteristics of test devices in darkness and under AM 1.5 illumination* ***c,*** *J-V characteristics of AgNW test devices based on SnO_x with varied charge carrier density and* ***d,*** *the resulting rectification ratios J(0.5 V) / J(-0.5 V). Adapted from [239].*

Corresponding test devices (ITO / SnO_x / PVP / thermally evaporated Ag electrode) also showed s-shaped J-V characteristics (see [239]). Therefore, these results may present a possible explanation for the rectifying behaviour. The absence of an s-kink in the J-V characteristics of PSCs upon illumination form the AgNW side can be understood if the J-V characteristics of test devices are considered, which likewise turned ohmic upon illumination with AM1.5G simulated sunlight (Figure 6.9 b). Illumination of the SnO_x / AgNW structure may either lead to charge generation in the SnO_x by direct band-band absorption or by the transfer of hot carriers from the AgNWs. [262, 263] Furthermore, it has to be noted that the effect of illumination is reversible and the J-V characteristics of the test devices return to their diode-like behavior after about 10 minutes in darkness. To assess the effect of an increased carrier density in the SnO_x on the device characteristics, the carrier density was deliberately varied in the range from $< 10^{16}$ cm^{-3} to 8×10^{20} cm^{-3} by tuning the growth conditions (temperature,

choice of oxidant). [209] Details of the respective growth conditions can be found in [239]. Note, for the SnO_x typically used in our PSCs, that is grown at 80 °C using TDMA-Sn and water, we estimated a carrier density below 10^{16} cm^{-3} using the Hall effect. Most notably, the J-V characteristics of our test devices become ohmic (rectifying ratio equal to 1) for a carrier density in the SnO_x of 10^{18} cm^{-3} or higher (Figure 6.9 c, d). According to textbook semiconductor physics, the width of the depletion region in a rectifying metal-semiconductor junction correlates with the Debye length (L_D), which is a characteristic length scale for the screening of an electrical field. L_D depends on the carrier density n in the semiconductor ($L_D \approx n^{-0.5}$), which can explain the strong dependence of the J-V characteristics of the test devices on the carrier density of the SnO_x. Unfortunately, the growth conditions of SnO_x to achieve a carrier density larger than 10^{18} cm^{-3} are not compatible with the deposition on top of the PSC, because they require precursors such as ozone or O-plasma and a growth temperature of 150 °C. Most perovskite solar cell architectures are unable to withstand these harsh conditions. [68] Please also compare the results presented in Figure 5.6 above. As a workaround, a 5 nm thin interlayer of ITO between the SnO_x and the AgNW electrode was implemented (Figure 6.10 a). The ITO layer is deposited by sputtering at room temperature and provides a carrier density of about 10^{21} cm^{-3}. The SnO_x has been shown to provide efficient protection of the underlying layers against the detrimental impact of the sputter process.

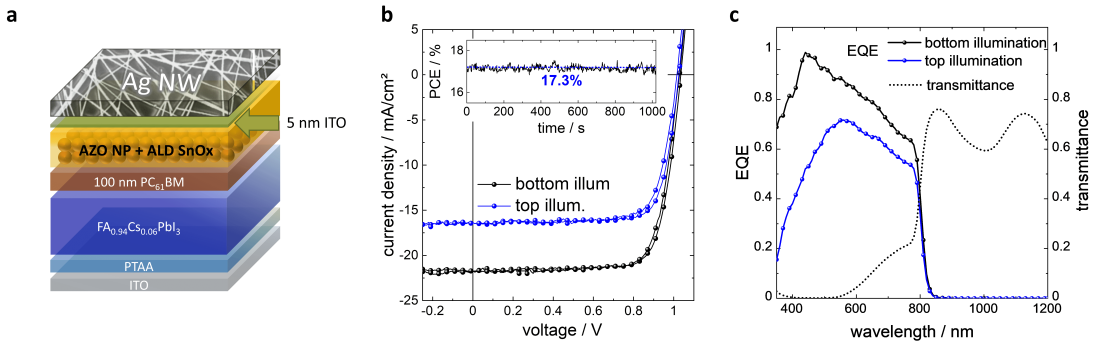

Figure 6.10: Ultra-thin ITO work around. ***a,*** *Cell stack with AgNW top electrode employing a 5 nm thin ITO buffer layer,* ***b,*** *champion J-V characteristics upon AM1.5G illumination with stabilized power output as intet and* ***c,*** *EQE (straight lines) and transmittance spectra (dotted lines) for the respective cell. Adapted from [239].*

In PSCs based on our standard SnO_x ($n < 10^{16}$ cm^{-3}) with a 5 nm thin ITO interlayer, we evidenced well-behaved ohmic J-V characteristics with a FF in excess of 77 % as well as PCEs up to 17.3 % upon illumination from the bottom (substrate) side and 13.4 % for top-side illumination (Figure 6.10 b). EQE and transmittance data is shown in 6.10 c. Derived solar cell characteristics are summarized in Table 6.4. Statistical data can be found in Appendix 11.7. Therefore we were able to show that our hybrid AZO / SnO_x hybrid layer can enable aqueous processing and we presented the first perovskite with water deposited top electrode. Additionally, the resulting solar cell stated the highest PCE value reported for AnNW based perovskite solar cells, at the time.

Table 6.4: *Cell characteristics of representative solar cells with AgNW top electrodes processed from water on solar cell stacks also employing an ultra-thin ITO layer. J_{EQE} is the short circuit current density determined from the EQE data.*

illumination	**reverse**			EQE	**forward**		
	PCE / %	FF / %	V_{OC} / V	J_{EQE} / mA cm^{-2}	PCE / %	FF / %	V_{OC} / V
bottom-side	17.4	77	1.04	21.4	17.2	76	1.03
top-side	13.4	78	1.03	16.6	13.1	79	1.03

7 Interfaces of Wide Gap Perovskite Solar Cells

Please note that the results from the introduction (until 7.1) of this chapter originate from a work done mainly by F. Peña-Camargo and M. Stolterfoht, in which only limited experimental contribution was done by me:

F. Peña-Camargo, ... , K. Brinkmann, ..., M. Stolterfoht, "Halide segregation versus interfacial recombination in bromide-rich wide-gap perovskite solar cells" ACS Energy Lett. 5, 2728 (2020). [264]

Nevertheless a short summary is presented, since the mutually developed scientific theories during the collaborative work (which also warranted my co-authorship), set the foundation for the subsequent progress on wide gap perovskite solar cells described in the follow-up work published in:

K. O. Brinkmann, et al. "Perovskite - organic tandem solar cells with indium oxide interconnect" Nature 604, 280 (2022). [265]

Additionally some parts of this chapter have been published in

K. O. Brinkmann, et al. "The Optical Origin of Near-Unity External Quantum Efficiencies in Perovskite Solar Cells" Solar RRL 5, 2100371 (2021). [266]

The versatile band gap tunability of perovskite materials renders them attractive building blocks for integration in tandem solar cell concepts (compare 2.5.2). [17, 267–269] There is a wide range of options for the low band gap sub-cell, where aside from low gap perovskites, silicon, cadmium-indium-gallium selenide and also organic solar cells (see chapter 8) are viable candidates. [265, 270–272] While tandem concepts with each of this list carry their specific up- and downsides, for all of them a highly efficient wide band gap perovskite solar cell with minimal voltage loss is required, in order to optimally exploit the advantages of the tandem concept. [73, 273, 274]

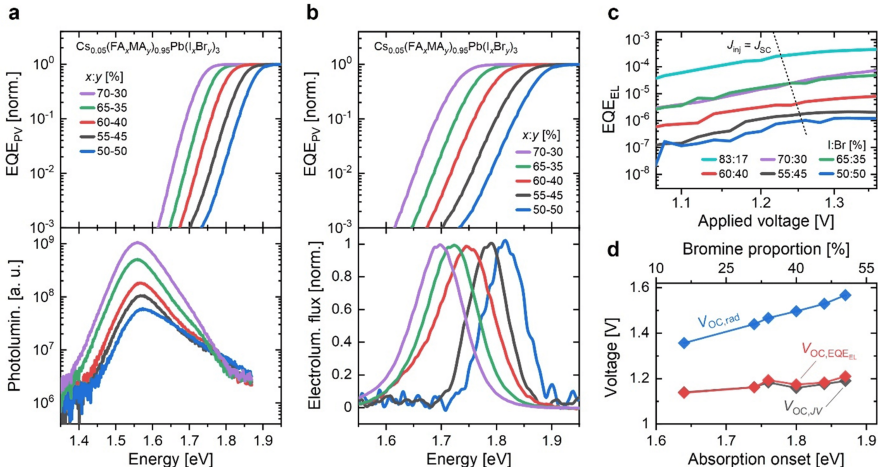

Figure 7.1: Photoluminescence versus electroluminescence in wide gap perovskites. ***a,*** *Normalized external quantum efficiency (EQE_{PV}) of the wide-bandgap perovskite solar cells for several iodine:bromine (x:y) ratios and steady-state photoluminescence (PL) emission spectra showing the position of the peak is centered at ≈ 1.55 eV.* ***b,*** *Normalized electroluminescence spectra at an applied voltage of ≈ 1.2 V showing that the peak emission follows the bandgap of the different perovskite compositions.* ***c,*** *Electroluminescence quantum efficiency (EQE_{EL}) as a function of applied voltage for the selected compositions. The dashed line intersects with the EL curves when the injected current equals short-circuit current density (1 sun).* ***d,*** *Open-circuit voltage (V_{OC}, calculated from EQE_{EL} in comparison to the value obtained from the J–V scan. Adapted with permission from [264]. Copyright 2020 American Chemical Society.*

This is typically done by tuning the halide ratio of the employed perovskite material (c.f. chapter 2.2). Early studies have shown, that for PSCs with high Br content (band gaps exceeding 1.7 eV), the V_{OC} did not concomitantly increase with E_g, which has frequently been attributed to photo-induced halide-segregation inside the perovskite towards bromine- and iodine-rich domains. [73, 273, 274] On the other hand, the collaborative work with the University of Potsdam evidenced a phenomenon, that contradicted this almost paradigmatic statement to some extent: In a systematic study the iodide to bromide ratio was tuned and photoluminescence (PL) and the electroluminescence (EL) spectra were compared. As shown in Figure 7.1 a rather unexpected result was found, as the peak position of the electroluminescence spectrum followed the band gap edges determined by photovoltaic EQE measurements of the respective solar cells. For PL on the other hand, the emission was dominated by a lower band gap, iodine rich (segregated) phase. The work further states, that for high induced carrier densities, halide segregation was also observed via the EL measurements. The EL measurements allowed to optically probe perovskite samples that have not undergone halide segregation and to calculate the external quantum efficiency for EL (EQE_{EL}) of the mixed I-Br phase. In turn, via the $V_{OC} = V_{OC,rad} + \frac{k_B T}{e} \times ln(EQE_{EL})$, [275] the ($EQE_{EL}$) could be

used to calculate a potential open circuit voltage of the mixed I-Br phase under injection conditions resembling AM1.5 illumination ($J_{inj} = J_{SC}$) (Figure 7.1 c). Eventually it was possible to pinpoint, that severe deterioration of radiative efficiency is already present in the mixed phase, since calculated $V_{OC,EQE,EL}$ are in good agreement with V_{OC} values derived from J-V characterisation. Thereby, this study successfully separated the losses in V_{OC} from losses due to halide segregation and demonstrated that the formation of iodine rich domains is not necessarily responsible for V_{OC} losses observed in wide gap perovskite solar cells. On the contrary, interface recombination was assumed to be the critical factor. Therefore, partial stack PL quantum yield (PLQY) analysis allowed to pinpoint the origin of the observed recombination losses. As shown in Figure 7.2 an increasing impact of the hole transport contact with increasing the Br-content of the probed perovskite material became apparent. While for low Br ratio (17 %) the PLQY loss caused by the ETL strongly dominates the PLQY signal, for higher Br contents (40 % or 50 %) non-radiative recombination, caused by the presence of the hole contact, are similarly critical. As a consequence the presented work concludes, that especially for wide band gap perovskite materials, an optimization approach had to tackle both interfaces and not exclusively focus on the perovskite surface, which is frequently done to optimize lower gap perovskite solar cells. For further optimization we then selected $FA_{0.8}Cs_{0.2}Pb(I_{0.5}Br_{0.5})_3$ as suitable perovskite composition with a bandgap of 1.85 eV.

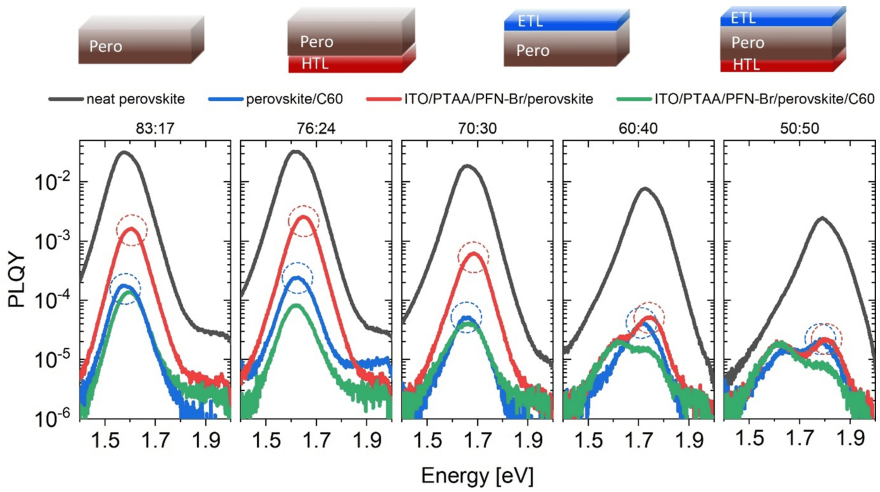

Figure 7.2: Photoluminescence quantum yield of partial solar cell stacks *after short exposure to light (≈ 1 s) highlighting the strong reduction in the PL emission from the perovskite, in particular in the presence of the transport layers, upon increasing the bromine content. The emission flux on the y-axis has been scaled to represent the photoluminescence quantum yield at the peak position. The upper label stands for the proportion (in molar %) of $FAPbI_3$ (x) and $MAPbBr_3$ (y) in the triple-cation perovskite $Cs_{0.05}(FA_xMA_y)_{0.95}Pb(I_xBr_y)_3$. Adapted with permission from [264]. Copyright 2020 American Chemical Society.*

7.1 Top- and Bottom-Side Interface Optimization

In a first step, we analyzed the quasi-Fermi level splitting (QFLS) in the perovskite upon illumination (see chapter 2.3.2). The QFLS provides an excellent indication (and upper limit) of the V_{OC} that can be expected in an actual solar cell and it allows to determine the potential loss in V_{OC} associated with the respective charge extraction layers adjacent to the perovskite. PTAA is currently the most prominent hole extraction layer (HEL) in p-i-n PSCs (c.f. chapter 3). However, PTAA comes with serious limitations due to the tradeoff between efficient hole transport, which requires the PTAA to be as thin as possible, and selectivity, that has been found to impose a lower limit to the PTAA thickness. [173] To overcome the issues associated with PTAA, we use [2-(3,6-Dimethoxy-9H-carbazol-9-yl)ethyl]phosphonic Acid (MeO-2PACz) as HEL, that forms a dense, pinhole-free self-assembled monolayer on the indium tin oxide (ITO) bottom electrode, which has previously only been used to improve the FF of lower gap solar cells. [272] In a direct comparison, perovskite layers on MeO-2PACz as HEL afford a 90 meV larger QFLS compared to their analogues on PTAA (Figure 7.3).

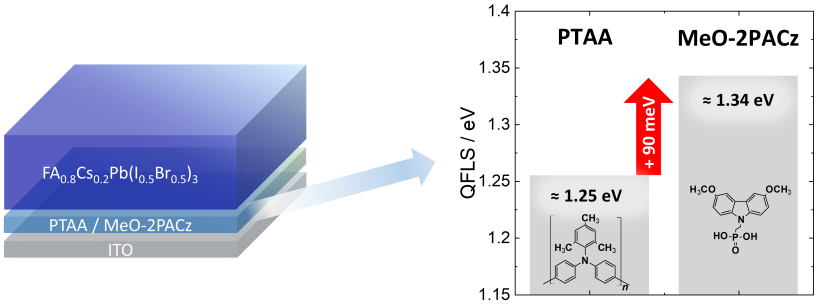

Figure 7.3: Substrate dependent quasi Fermi level splitting. *(left) Investigated solar cell stack and (right) quasi-Fermi level splitting derived von photoluminescence quantum yield measurements. Adapted with permission from [265]. Copyright 2022 Springer Nature.*

Interestingly, in stark contrast to PTAA, with MeO-2PACz as HEL, we also did not observe notable halide segregation under a one sun equivalent illumination on a timescale of several minutes, despite using a Br:I ratio of 0.5:0.5 (Figure 7.4). This is rather unexpected, as literature suggests halide segregation for Br concentrations in this range. [74] Our findings therefore demonstrate that the proper choice of HEL allows to mitigate halide segregation in perovskites, even with elevated Br-concentrations. To identify the possible origin of this effect, it is important to note that in recent work it was possible to map parasitic recombination by means of PL-intensity mapping and link nonradiative recombination to the tendency of a perovskite to segregate. [276]

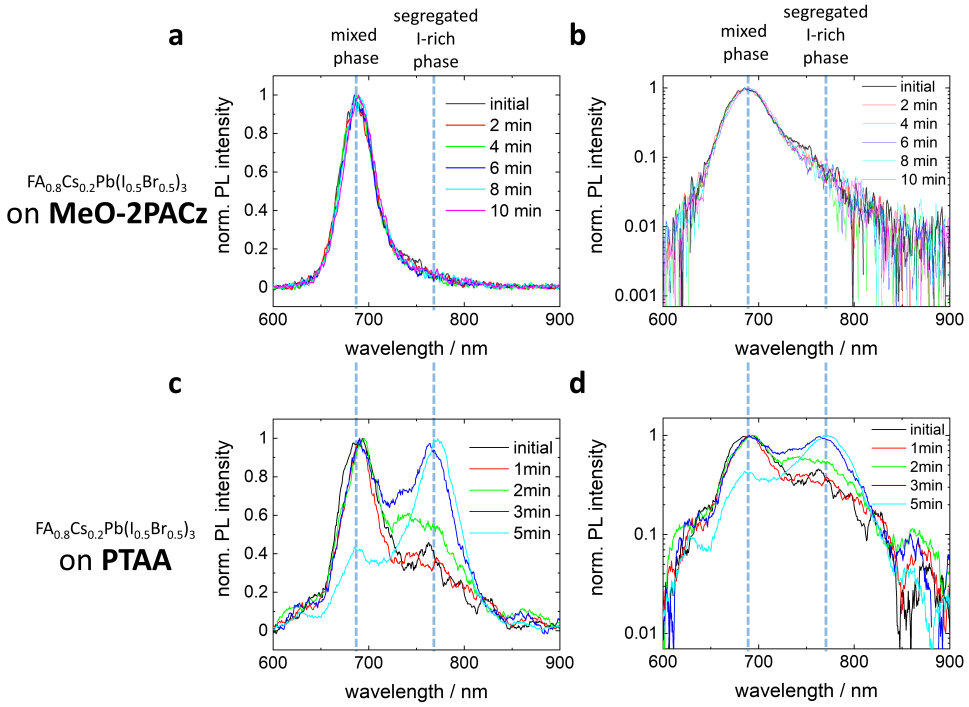

Figure 7.4: Development of photoluminescence under continuous illumination. *$FA_{0.8}Cs_{0.2}Pb(I_{0.5}Br_{0.5})_3$ on top of* ***a, b,*** *MeO-2PACz and* ***c, d,*** *PTAA in* ***a, c,*** *linear and* ***b, d,*** *logarithmic scale. The dashed lines indicate the photoluminescence maxima of the mixed and the segregated, iodine rich (segregated) phase. Excitation was done with one sun equivalent (520 nm). Adapted with permission from [265]. Copyright 2022 Springer Nature.*

It could be shown that segregated, low bandgap, domains predominantly form at sites that initially show a low photoluminescence intensity. This correlation strongly indicates, that halide segregation is linked to charge trapping and concomitant parasitic recombination. Considering that we significantly decreased parasitic recombination by the introduction of MeO-2PACz as HEL, we believe that this might likewise be the origin of the reduced tendency of halide segregation. A somewhat similar observation was presented by Belisle et al., who reported reduced halide segregation upon topside defect passivation with trioctylphosphine oxide (TOPO) in their $MAPb(I_{0.66}Br_{0.33})_3$ layers. [277] Other passivation agents have also been reported to reduce halide segregation. [74] To further analyze halide segregation in our MeO-2PACz / perovskite assembly we increased the duration of illumination up to 30 min. We found that halide segregation was indeed not entirely eliminated on this time scale, as some PL signal indicative for (reversible) segregated perovskite occurs (Figure 7.5). As such, the proper use of suitable charge extraction layers, that afford reduced interfacial recombination, may be a key to at least slow down detrimental halide segregation.

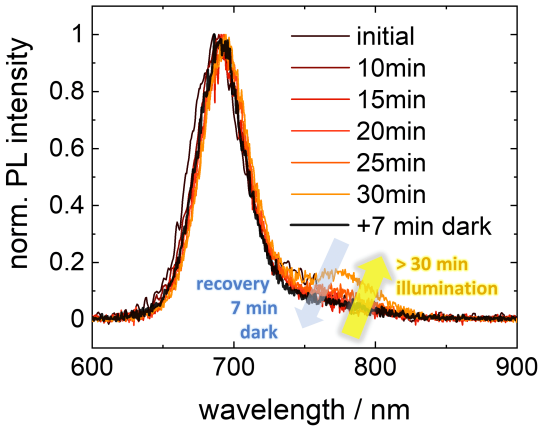

Figure 7.5: Evolution of photoluminescence under continuous illumination *of $FA_{0.8}Cs_{0.2}Pb(I_{0.5}Br_{0.5})_3$ perovskite on top of MeO 2PACz over time, showing first signs of halide segregation after 30 minutes, followed by a 7 minutes period of darkness and a follow-up measurement evidencing the reversible nature of the effect. Adapted with permission from [265]. Copyright 2022 Springer Nature.*

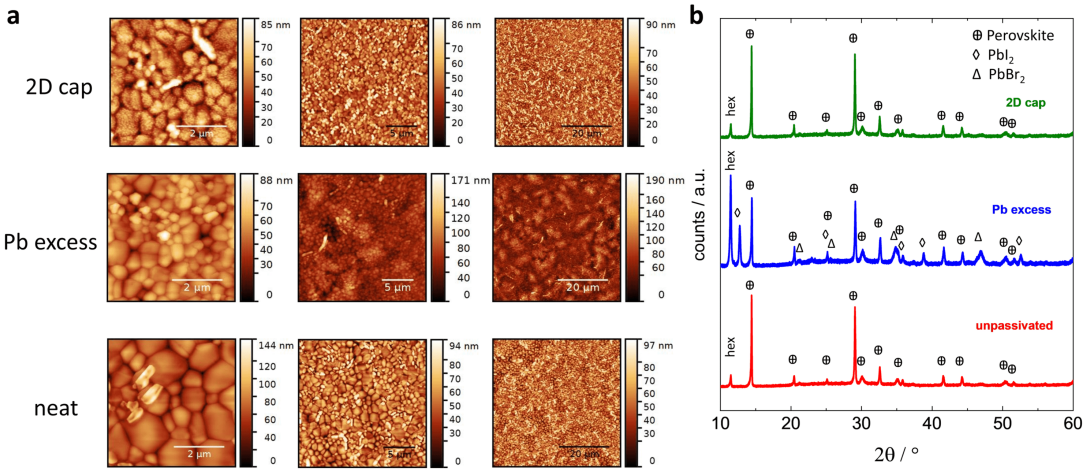

Figure 7.6: Formation of perovskite layers with different passivation strategies. a, *Topography measured by atomic force microscopy of perovskite layers w/o and with Pb excess and 2D cap passivation strategy.* ***b,*** *XRD diffractograms of perovskite layers w/o and with Pb excess and 2D cap passivation strategy. Adapted with permission from [265]. Copyright 2022 Springer Nature.*

Before studying the impact of the electron extraction layer (EEL), we implemented passivation strategies, such as the addition of excess lead [278] or the modification of the perovskite surface by the organic halide salt phenethylammonium iodide (PEAI), which promotes the formation of a 2-dimensional perovskite capping layer. [279, 280] In order to obtain some insight about the the perovskite formed by these strategies we

first conducted atomic force microscopy (Figure 7.6 a) and X-ray diffraction (XRD) studies (Figure 7.6 b). As visible in Figure 7.6 a, all perovskite layers were smooth and pinhole-free. For samples employing PbI_2 excess some additional structures were found on top of the perovskite. This additional material might be crystalline residues of the initially introduced excess lead iodide that is also evidenced in XRD in Figure 7.6 b. Another possible explanation, since there is apparently also some additional material on top of the neat perovskite layer, could be the hexagonal phase perovskite that is also evidenced in XRD. Note that there is no clear difference in XRD between unpassivated and 2D passivated samples. We also confirmed by an encapsulated experiment (see Appendix Figure 11.8), that the observed hexagonal phase is not a result of degradation due to air exposure, but the hexagonal phase is most likely formed during the perovskite deposition process. Further, in collaboration with Lena Merten (University of Tübingen), we conducted angle dependent GIWAXS measurements as shown in Figure 7.7.

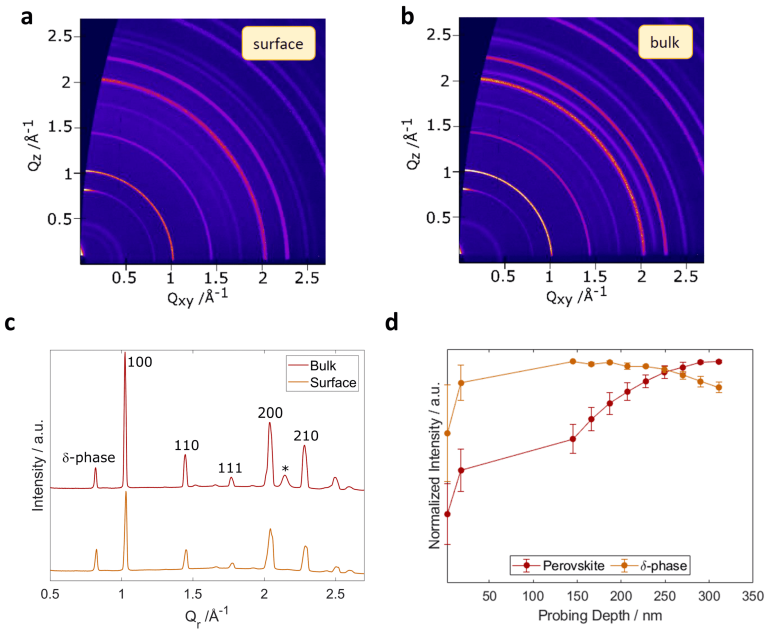

Figure 7.7: Probing hexagonal phase by angle dependent GIWAXS. *Reciprocal space maps at incidence angles of* ***a,*** *0.12 °, representing the film surface and* ***b,*** *0.3 °, representing the bulk of the film.* ***c,*** *Radial profiles of the reciprocal space maps.* ******* *marks the substrate signal.* ***d,*** *Normalized intensities of the first scattering signals of perovskite and hexagonal phase. Adapted with permission from [265]. Copyright 2022 Springer Nature.*

If one takes a closer look at the development of the intensity of the hexagonal phase in comparison to the α-phase signal with dependence of the angle of incidence, it is possible to plot a depth profile of the relative distribution of tetragonal α and hexagonal δ-phase. As shown in Figure 7.7 d the δ-phase reaches its maximum much closer to the surface

than the α phase, indicating an accumulation of hexagonal delta phase at the surface of the otherwise mainly α phase material. Please note, that GIWAXS always probes the full layer thickness and therefore the hexagonal phase signal originating from the surface of the sample is also visible in the bulk measurement. Since we also evidenced a significantly higher amount of hexagonal phase in case of lead excess we speculate the larger structures on the perovskite might be attributed to δ-phase perovskite material accumulating at the surface.

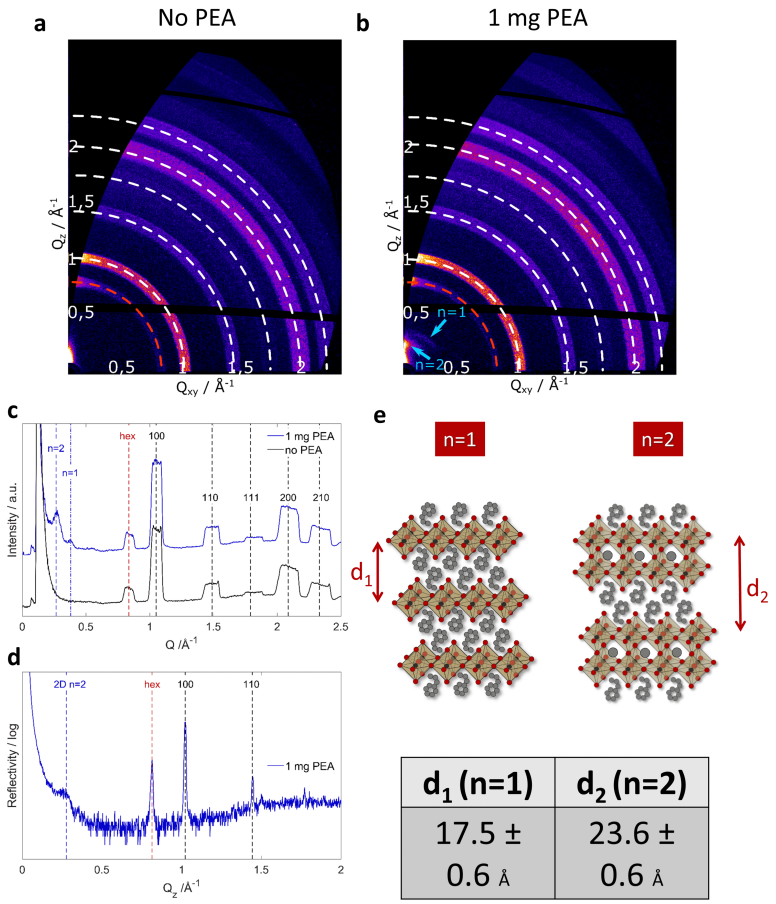

Figure 7.8: Grazing incidence X-Ray scattering on 2D cap. ***a, b,*** *Reciprocal space maps from grazing incidence wide angle X-ray scattering of perovskite films with and w/o PEAI surface treatment.* ***c,*** *Radial profile obtained by azimuthal integration of reciprocal space maps evidencing the presence of (predominant n=2) 2D phase in the case of PEAI treated perovskite films.* ***c,*** *X-ray reflectivity measurement probing the z-axis not covered by GIWAXS measurements, also evidencing the n = 2 2D phase.* ***d,*** *Schematic illustrations (top) and layer spacing calculated from the peak positions (bottom). The difference d_2 - d_1 of ≈ 6 angstrom corresponds with the height of one PbX_6 octahedron, indicating the presence of n = 1 and n = 2 layered structures. Adapted with permission from [265]. Copyright 2022 Springer Nature.*

In the higher resolution AFM images (Figure 7.6 a) of perovskite material, employing the 2D-capping strategy, we observed also a very fine surface structure of the single grains. These structures might be attributed to the desired 2D capping layer. To confirm the formation and to identify the type of the formed 2D material, we conducted yet another GIWAXS as well as X-ray reflection study comparing neat and PEAI treated perovskite materials. As clearly evidenced in Figure 7.8 we were able to confirm the formation of a 2D perovskite structure on top of the 3D perovskite material. We want to note that we mainly observed n=2 type of Ruddlesden Popper 2D material, [281] as we identified by matching the derived lattice spacings in real space to the respective calculated repetition unit's lengths. Targeting yet again the QFLS of the layer stacks employing different passivation strategies, we found that in the absence of an EEL, the surface passivation does not affect the QFLS (Figure 7.9 a, b), which indicates that defects at the surface or grain boundaries do not impose a limit in this scenario.

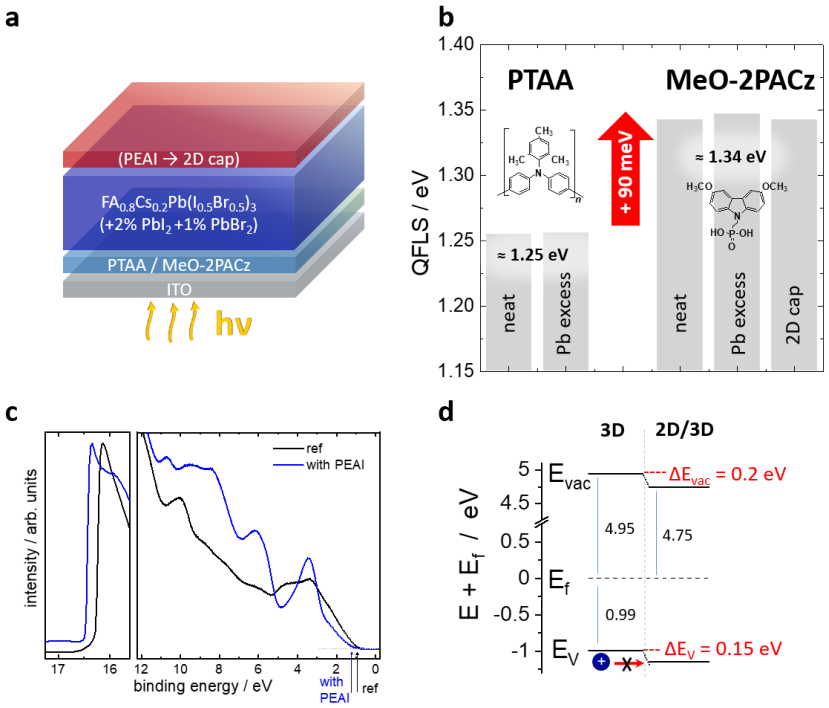

Figure 7.9: Double-side passivated perovskites. ***a,*** *Layer stack displaying passivation strategies and* ***b,*** *respective QFLS measurements on PTAA and on MeO-2PACz.* ***c,*** *UPS measurement of a reference 3D sample and a sample treated with PEAI. The shape of the density of states significantly changes due to the modification by PEAI.* ***d,*** *Resulting energy level diagram of E_{vac} and E_V aligned at E_f of pristine 3D and PEAI treated 2D / 3D perovskite. Adapted with permission from [265]. Copyright 2022 Springer Nature.*

As evidenced by photoelectron spectroscopy, the insertion of PEA^+ leads to some notable lowering of the perovskite valence band maximum (Figure 7.9 c, d), which in turn will prevent photo-generated holes from reaching the EEL and may thereby improve the selective extraction of electrons.

This effect is particularly visible, if we complete our p-i-n PSCs by adding $PC_{61}BM$ and AZO NP as EEL (Figure 7.10 a, b). [192] Note, for the integration of the PSCs in the tandem cells, an additional SnO_x layer, grown by low temperature atomic layer deposition (ALD), is used that serves as permeation barrier, which not only improves the long term stability but also protects the layers underneath against chemical attack by the solvents of subsequent wet chemical processes (compare chapter 4 and 6). In striking contrast to PTAA, with MeO-2PACz as HEL, the addition of the EEL infers a substantial reduction of the QFLS. The resulting V_{OC} can be notably improved by passivation with excess lead and even more by the formation of a 2D perovskite cap (Figure 7.10 c). As for devices with MeO-2PACz and the 2D perovskite cap the observed mean V_{OC} values agree with the measured QFLS, we conclude that interface recombination rather than energetic misalignment is the main limiting factor.

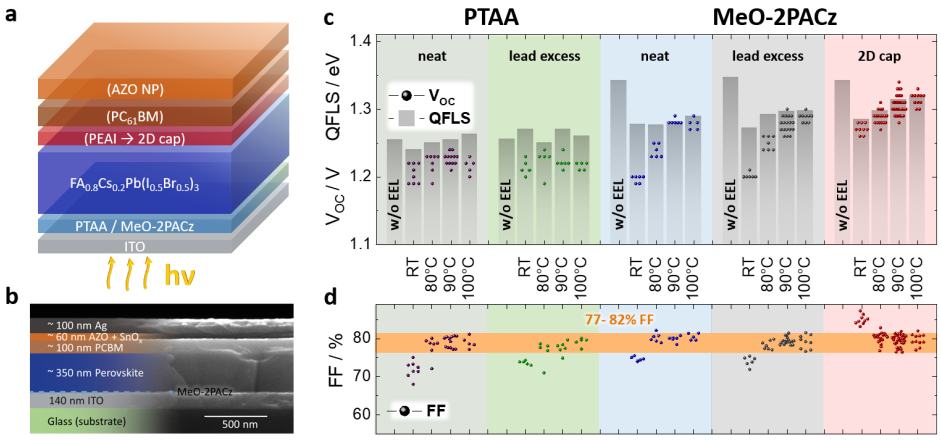

Figure 7.10: Double-side passivated perovskites. ***a,*** *Solar cell layer stack and* ***b,*** *respective cross sectional image.* ***c,*** *Comparison of the open circuit voltage (V_{OC}) of actual perovskite solar cells (PSCs) with the corresponding splitting of the quasi Fermi level (QFLS) of representative layer stacks with and w/o electron extraction layer (EEL) and varied device annealing temperature.* ***d,*** *The FF of each cell type is shown in the lower panel. The different temperatures refer to the annealing conditions after deposition of the AZO NP layer. The dots represent the results of individual devices and indicate the experimental spread. Adapted with permission from [265]. Copyright 2022 Springer Nature.*

For champion devices V_{OC} even reaches the QFLS of the bare perovskite (on MeO-2PACz) indicating superior suppression of recombination losses at the EEL side. Ultimately, PSCs with hysteresis-free current-voltage characteristics are achieved, that provide a very high stabilized V_{OC} = 1.34 V (Figure 7.10 c) with a FF that falls within a narrow range of 77-82 % (Figure 7.10 d). In previous reports, an increase of V_{OC} typically came at the cost of a lowered FF and a loss in EQE. A comparison with the literature on PSCs with a high Br content and an E_g in the range of 1.8-1.9 eV shows that our careful mitigation of losses at the interfaces unlocked access to previously unreached territory of combined high V_{OC} and FF (Figure 7.11 a). J-V characteristics as well as the final solar cell stack are shown in Figure 7.11 b and c. When operated continuously for more than 100 h, the PCE of the wide-gap PSCs remains above 80 % of its initial value (Figure 7.11 d). Finally from the 1st derivative of the EQE a band gap of 1.85 eV is confirmed from the perovskite (Figure 7.11 e, f). [282]

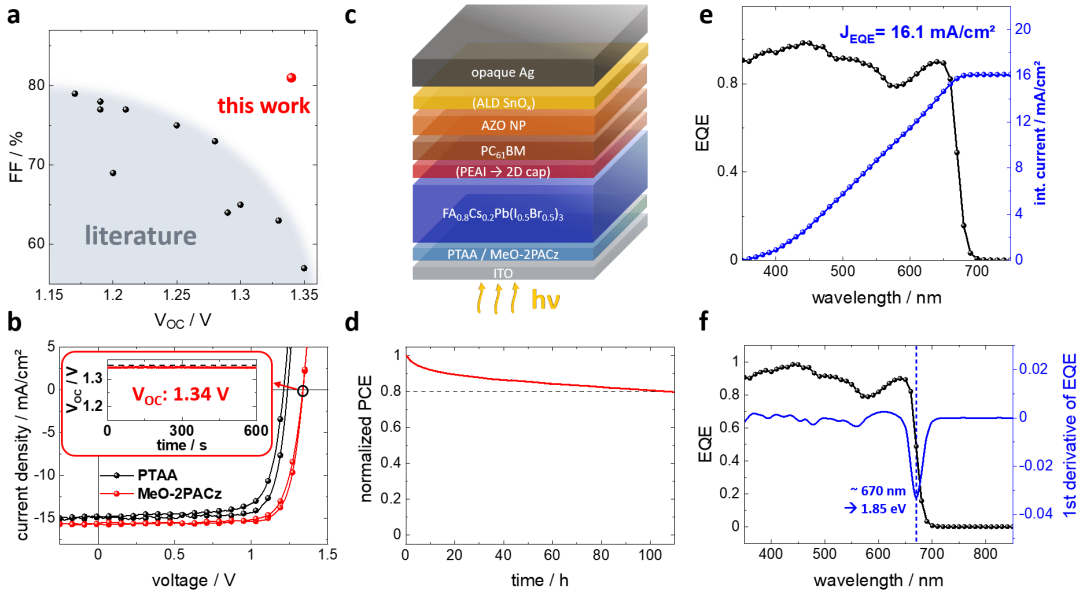

Figure 7.11: High V_{OC} wide gap solar cells. ***a,*** *Comparison of the V_{OC} and FF of our PSCs with E_g = 1.85 eV to PSCs (with E_g in the range of 1.8 - 1.9 eV) reported in the literature. The respective references can be found in Table 7.1.* ***b,*** *Current density vs. voltage characteristics for champion PSCs with a 2D capping layer (MeO-2PACz SAM as HEL) or PbI_2 excess (PTAA as HEL) on the perovskite active layer. The inset shows the stabilized V_{OC} of 1.34 V for the cell with the SAM as HEL.* ***c,*** *Layer sequence of the p-i-n perovskite single junction.* ***d,*** *Normalized PCE vs. time of the PSCs illuminated with a white LED and operated in the maximum power point.* ***e,*** *EQE of a representative PSC (90 °C annealing) and* ***f,*** *estimated bandgap by 1st derivative of the EQE spectrum. [282] Adapted with permission from [265]. Copyright 2022 Springer Nature.*

Table 7.1: *Literature underlying Figure 7.11 a.*

E_g / eV	V_{OC} / V	FF / %	PCE / %	J_{SC} / mA cm^{-2}	E_g / e - V_{OC} / V	reference
1.8	1.05	74	11.1	14.3	0.75	[283]
1.8	1.12	58	9.8	15.1	0.68	[284]
1.87	1.21	77	10.6	11.4	0.65	[285]
1.82	1.30	65	11.6	12.9	0.52	[286]
1.83	1.33	63	7.5	10.2	0.50	[286]
1.84	1.35	57	3.3	5.1	0.49	[286]
1.82	1.29	64	11.5	13.8	0.53	[287]
1.82	1.20	69	12.5	15.1	0.62	[288]
1.8	1.25	75	15.8	17.1	0.55	[289]
1.8	1.17	79	17.0	18.0	0.63	[264]
1.84	1.19	78	16.2	17.0	0.65	[264]
1.88	1.19	77	15.2	16.5	0.69	[264]
1.86	1.25	73	15.2	15.3	0.58	[268]
1.85	1.35	81	16.8	15.6	0.51	this work

7.2 Optical Origin of External Quantum Efficiencies Near Unity

Upon measuring the external quantum efficiency of the wide band gap perovskite solar cell, also a very curious phenomenon was observed: for wavelengths in the region ≈ 450 - 500 nm the EQE exceeded the value of 95 %. Some literature research revealed an even more curious phenomenon, which is very surprising at a first glance: In a large number of papers an extremely high EQE up to 98 % is encountered (Figure 7.12 a, b) including our own data, that we shown in Figure 7.12 c. Considering the abundance of papers that likewise report an EQE_{max} exceeding 95 % it is also interesting, that their EQE peak positions are almost exclusively located inside a very narrow spectral region between 400 nm and 500 nm (Figure 7.12 b). Even though very high internal quantum efficiencies up to unity have been reported for perovskite solar cells quite early, [290, 291] the high EQE is even the more puzzling as the transmittance of commonly used glass / ITO substrates is below 90 % (even with anti-reflection layer) in the wavelength range where these high EQE values are typically reported. Therefore, reports of perovskite solar cells with EQE values of 95 % or higher appear somewhat unrealistic and are sometimes subject to doubts or concerns of erroneous EQE measurements. Hence we decided to unravel the root cause of the high EQE by a combination of experimental data and optical simulations.

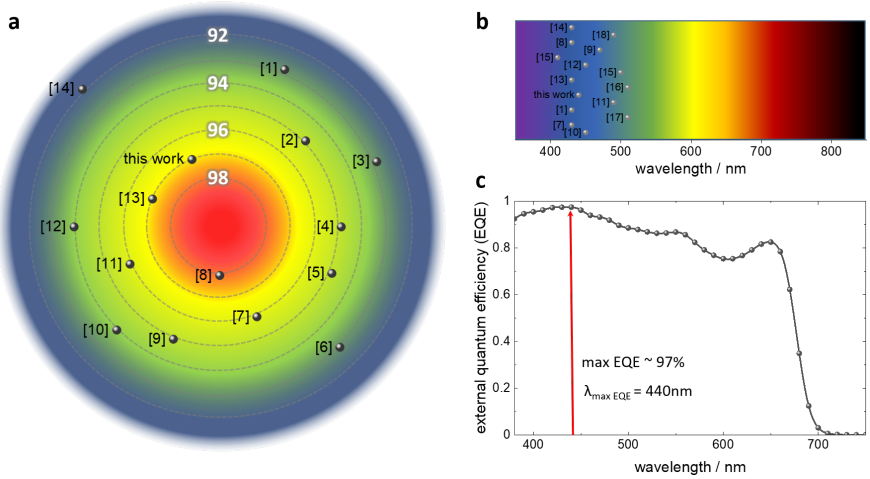

Figure 7.12: High external quantum efficiencies (EQEs) in literature. ***a,*** *Radial diagram of maximum EQE values of high efficiency cells taken from the literature. Please note the numbers are consecutively for the sake of readability and do not represent entries in the bibliography. For actual references please see source Table 7.2.* ***b,*** *Diagram displaying the wavelength at which high EQEs have been recorded.* ***c,*** *EQE spectrum of the respective cell with the maximum EQE marked with a red arrow. Adapted from [266].*

Table 7.2: *Literature underlying Figure 7.12 a and b.*

Nr	Reference	DOI	λ_{max} / nm	EQE_{max} / %
1	[292]	10.1038/s41560-019-0466-3	430	93
2	[293]	10.1002/adfm.201909919	430	95
3	[294]	10.1126/science.abc4417	470	93
4	[295]	10.1002/aenm.201700228	450	95
5	[296]	10.1038/s41467-020-15077-3	490	95
6	[297]	10.1126/science.aay9698	450	93
7	[298]	10.1039/D0TA07005J	430	96
8	[299]	10.1038/s41586-021-03406-5	430	98
9	[300]	10.1002/aenm.201602120	430	95
10	[301]	10.1002/adma.201904494	410	94
11	[301]	10.1002/adma.201904494	500	96
12	[302]	10.1039/c9ta05422g	510	94
13	[303]	10.1126/science.abb7167	510	97
14	[304]	10.1021/acsaem.8b02042	490	92
15	[266]	this work	440	97

We started by conducting an optical simulation using the layer sequence shown in Figure 7.14 a. We further considered an assembly of an ITO coated glass substrate with a thickness of the ITO layer of about 140 nm (compare Figure 7.10 b), that provides a sheet resistance of 12 Ω sq^{-1}. As an anti-reflection layer we added a 100 nm thick MgF_2 layer on the backside of the glass / ITO substrates. Owing to the thickness of the glass substrate (0.7 mm) the MgF_2 only serves as an anti-reflection layer to lower the reflectance at the air/glass transition without affecting the optical properties on the opposite side ("ITO-side") of the substrate. In view of the very high absorption coefficient in the spectral region between 400 nm and 500 nm of many halide perovskites used for solar cells, [22, 305, 306] we assumed that all the light, that is finally coupled (transmitted) into the perovskite, will be absorbed. Therefore, we considered the stack shown in Figure 7.14 a to be sufficiently thick and additional layers (charge transport layers and electrode) on top of the perovskite are not expected to substantially alter the result. We calculated the transmittance into the adjacent layer, as well as the reflectance of the incident light in case of a (photo-active) material with a varied refractive index at 440 nm in the range between 1 (air) and 4 (Figure 7.14 b, with Figure 7.13 a also showing the influence of anti-reflective coating) on top of the ITO. While we find a simulated reflectance of about 25 % and a transmittance of 75 % at 440 nm

in case of n = 1 (i.e. air), we see that the transmittance into the adjacent medium increases (reflectance decreases) substantially for materials with larger n. Specifically, our perovskite $FA_{0.8}Cs_{0.2}Pb(I_{0.5}Br_{0.5})_3$ has a refractive index of n ≈ 2.65 at 440 nm. [307] Exemplary transmittance spectra for n = 1 (air) and n = 2.65 (perovskite) are shown in Figure 7.14 c.

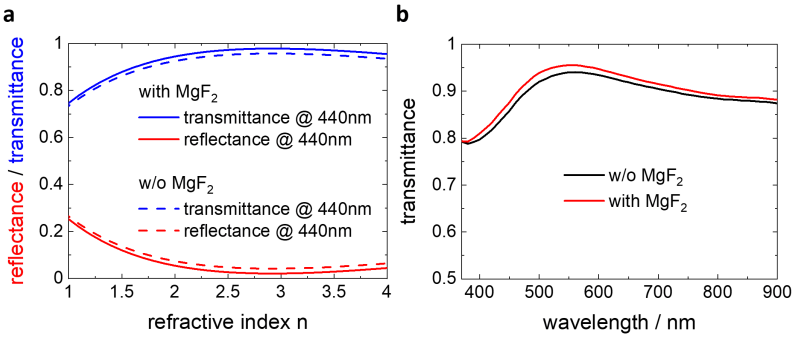

Figure 7.13: Impact of anti-reflection layer. ***a,*** *Transmittance and reflection at 440 nm with respective stack in dependency of its refractive index both with and without 100 nm MgF_2 antireflective coating.* ***b,*** *Transmittance of an exemplary Glass / ITO substrates used for solar cell fabrication. Adapted from [266].*

Remarkably, in case of the perovskite, we observed a maximum of the transmittance into the perovskite of more than 97 % at around 410 nm with overall less variations in the spectral region between 400 - 900 nm. On the other hand, for n = 1 (air) the transmittance shows a minimum between 400 - 500nm and overall a strong spectral variation. Notably, the simulated spectrum of the transmittance in case of air is in good agreement with the measured transmittance spectrum of the ITO / glass substrate (see Figure 7.13 b). Consequently, even though a pristine ITO / glass substrate provides a significantly lower spectral transmittance, the high refractive index of the perovskite absorber on top of the ITO gives rise to a very high fraction of the incident light to be coupled into the active medium. This is supported by a measurement of reflectance comparing glass / ITO to glass / ITO / $FA_{0.8}Cs_{0.2}Pb(I_{0.5}Br_{0.5})_3$ for the targeted wavelength region as shown in Figure 7.14 d. In case of our solar cells, we built as demonstrators in this work, we can now directly compare the measured EQE spectrum with the spectral transmittance resulting from our simulation data. In the spectral region of the maximum EQE, there is a favorable agreement of measurement and simulation as shown in Figure 7.15 a, b. For simplicity we assumed an internal quantum efficiency of 100 %, as has been reported earlier for perovskite photovoltaics. [290, 291] Note, a similar agreement between measurement and simulation is found for samples without the MgF_2 antireflective coating (Figure 7.15 c).

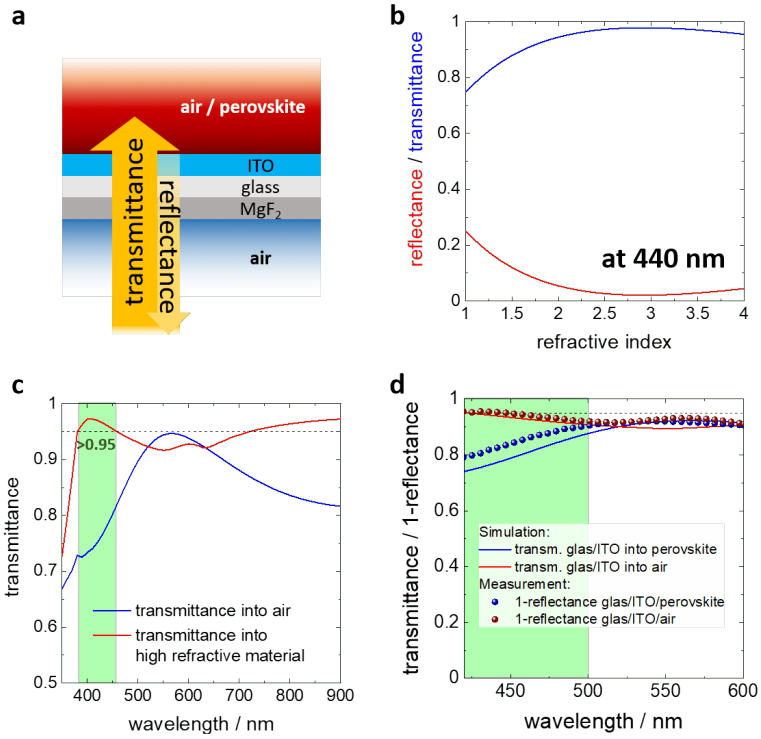

Figure 7.14: Optical simulation of the transmission process. ***a,*** *Layer sequence of the simulated cell stacks.* ***b,*** *Transmittance and reflectance at 440 nm in dependency of the refractive index of the material on top of the ITO electrode* ***c,*** *Simulated transmittance spectra in case of perovskite or air adjacent to the ITO electrode. The green area marks the spectral region where the transmittance exceeds 95 %.* ***d,*** *Comparison of simulated transmittance with measured (1 - reflectance). Adapted from [266].*

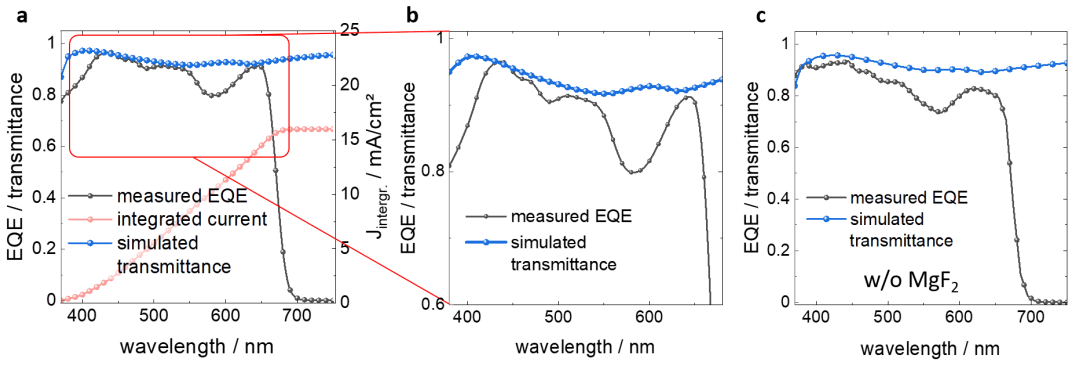

Figure 7.15: Agreeance measurement vs. simulation. ***a, b,*** *Measured EQE spectrum of our exemplary solar cells in direct comparison with simulated data for transmittance into the perovskite and calculated integrated current density.* ***c,*** *Similar comparison omitting the MgF_2 anti-reflection coating. Adapted from [266].*

The spectral variations of the measured EQE spectrum for wavelengths above 500 nm can be explained by the limited thickness and absorption coefficient of the perovskite layer for higher wavelength regions, while in the simulation the absorber medium was assumed to be infinitely thick. In our cells with a perovskite layer thickness in the range of 300-450 nm, light with a wavelength above 500 nm is partially transmitted by the perovskite. As such, the subsequent layers of the device stack, such as the PCBM, AZO / SnO_x and the metal electrode are important for the optics and affect the spectral shape of the EQE. To exemplify this phenomenon, we conducted an optical simulation of the absorbance in the perovskite for varied perovskite layer thickness and varied PCBM thickness (Figure 7.16). While the absorbance in the spectral region below 500 nm remains almost unaffected, there are strong spectral variations for values higher than 500 nm with notable hills and valleys due to optical effects.

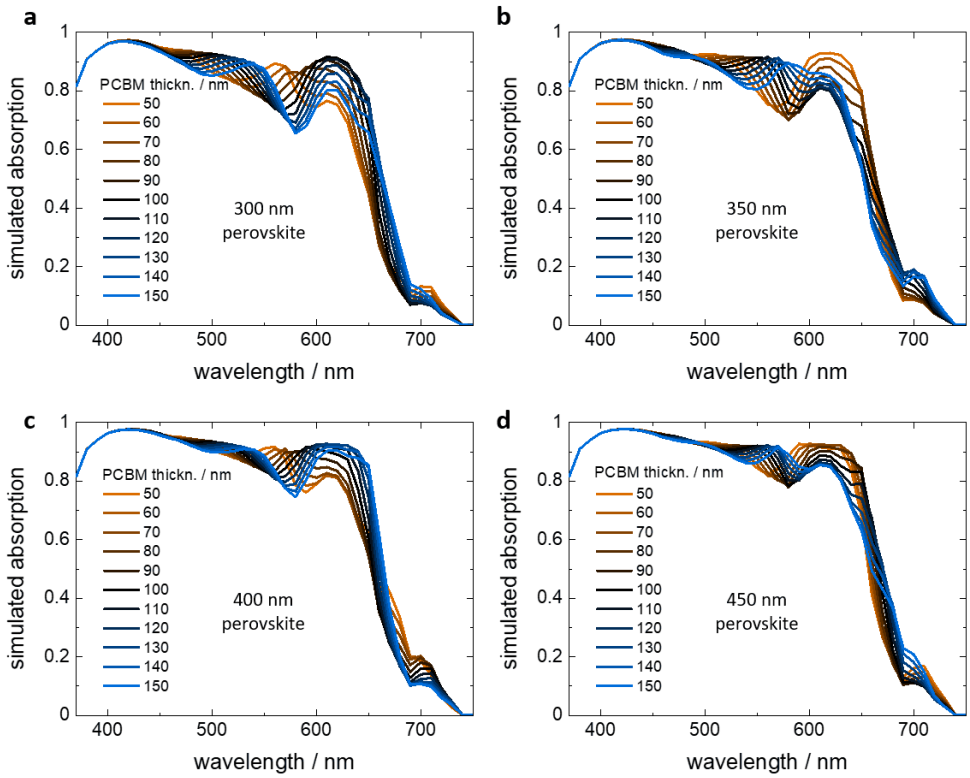

Figure 7.16: Optical influence of PCBM transport layer thickness. *Simulated absorption in the active material of a full device stack with varied PCBM thickness for* ***a,*** *300 nm,* ***b,*** *350 nm,* ***c,*** *400 nm and* ***d,*** *450 nm assumed thickness of the active material. Adapted from [266].*

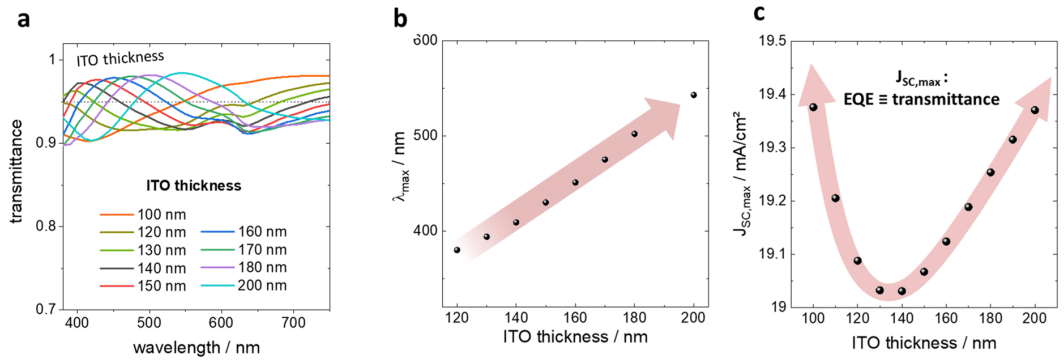

Figure 7.17: Impact of the ITO thickness. ***a,*** *Simulated transmittance into the perovskite for a varied thickness of the ITO electrode* ***b,*** *Position of the transmittance maximum in dependency of the ITO thickness* ***c,*** *Maximum integrated current ($J_{SC,max}$), assuming EQE equal to the respective transmittance displayed in (a) and an internal quantum efficiency of unity for various ITO thicknesses. Adapted from [266].*

In the next step we clarify the origin of variations in the spectral position λ_{max} of the maximum in the EQE (EQE_{max}) as displayed in Figure 7.12 c. To this end, we varied the thickness of the ITO electrode between 100 and 200 nm in our simulations and determined the spectral transmittance into the perovskite. Very strikingly λ_{max} shows a notable red-shift with increasing the ITO layer thickness (Figure 7.17 a, b). As a result, the thickness of the transparent bottom electrode may be an important means to tune the spectral absorption characteristics and it is therefore another important aspect for further optimization of the optics of the device stack. To identify a possible optimum in transmittance that would afford a maximum in J_{SC}, we assumed for simplicity an internal quantum efficiency of unity and EQE equal to the respective transmittance (displayed in Figure 7.17 a) for the perovskite over the spectral range from 400 nm to 700 nm and calculated a hypothetical integrated $J_{SC,max}$ in dependency of the ITO layer thickness. As visible in Figure 7.17 c, this estimate gives surprising insight, highlighting that not only thinner, but also thicker ITO layers may prove beneficial for overall cell performance.

8 Perovskite-Organic Tandem Solar Cells

Parts of this chapter have been published in

K. O. Brinkmann, et al. "Perovskite - organic tandem solar cells with indium oxide interconnect" Nature 604, 280 (2022). [265]

In general, multi-junction solar cells are designed as a series connection of wide-bandgap and narrow-bandgap sub-cells with complementary absorption spectra. An improved overlap with the solar spectrum and reduced thermalization losses are the keys to overcome the Shockley-Queisser efficiency limit of single-junctions. [84] The bandgap tunability of metal-halide perovskite solar cells renders them attractive for multi-junction architectures. [308] Combinations with silicon and copper indium gallium selenide (CIGS), as well as all-perovskite tandem cells have been reported. [271, 292, 309–312] All-perovskite tandem cells require narrow-gap materials (E_g below 1.3 eV), where the lead is partially replaced by tin. [313, 314] However, severe stability issues are linked to the unwanted transformation of Sn^{2+} to Sn^{4+}, which leads to non-intentional p-type doping and an overall degradation of device performance. This effect can be slowed down to some extent by additives, such as a surplus of sacrificial Sn(0) inside the active layer. [292] Alternatively, c-Si or CIGS back-cells have been employed [271, 315] in combination with a wide gap perovskite front-cell. Some of these tandems already outperform the best c-Si single junctions. [316] On the downside, perovskite / c-Si tandems are not compatible with low-temperature, low-cost, large-area manufacturing - a paradigm that is frequently quoted for perovskite solar technology. In this regard, organic solar cells (OSCs) represent an attractive option as narrow-gap back-cell. OSCs were typically based on so-called bulk heterojunction architectures, that were formed by a blend of a donor polymer and a fullerene derivative as acceptor. [317] Owing to the limited tunability of the energy levels of the fullerene, progress in OSCs came to a halt at efficiency levels of about 13 %. [318] However, with the recent introduction of non-fullerene acceptors (NFAs), OSCs started to see a second wave of outstanding advancement, which has propelled their efficiencies beyond 19 %. [111, 319–321]

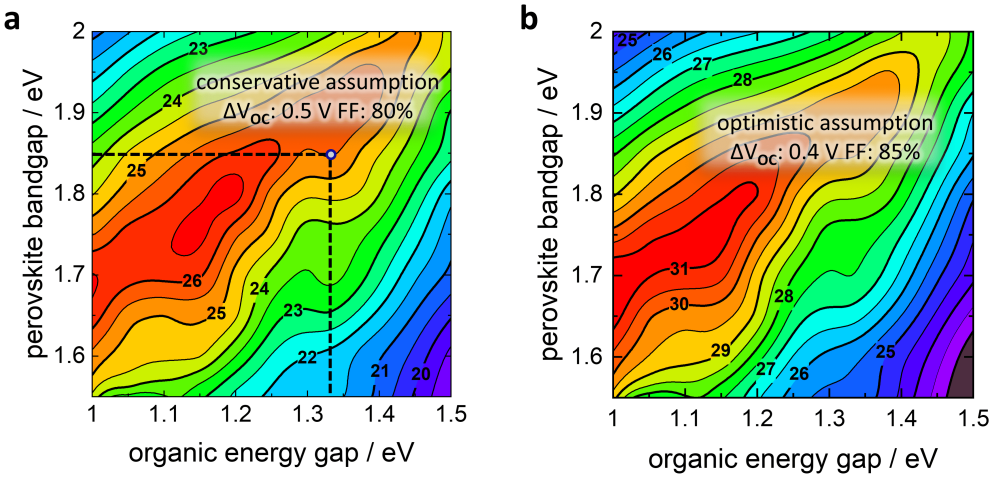

Figure 8.1: Potential efficiency of perovskite-organic tandems. *Semi-empirical model of the tandem cell efficiency vs. the energy-gap of organic and perovskite sub-cells. The intersection of the dashed lines marks corresponds to the energy gap of the PM6:Y6:$PC_{61}BM$ back-cell and the matching energy-gap of the perovskite front-cell.* ***a,*** *states a conservative scenario assuming open circuit voltage loss (ΔV_{OC}) of 0.5V and a fill factor (FF) of 80 %.* ***b,*** *displays a more optimistic (yet still realistic) model (ΔV_{OC} = 0.4 V, FF = 85 %), that yields a maximum efficiency higher than 31 %. Adapted with permission from [265]. Copyright 2022 Springer Nature.*

This progress mainly draws from the narrow energy gap of the acceptor moiety and an efficient exciton dissociation requiring only small energy offsets between donor and acceptor, which is the key to unlock low losses in V_{OC} compared to E_g/e while still providing a high external quantum efficiency (EQE) and thus high short circuit current densities (J_{SC}). [322–324] Anyway, when this project started, perovskite-organic tandems showed only subpar efficiencies of ≈ 20 %, limited by the low open circuit voltage (V_{OC}) of wide-gap perovskite cells and losses introduced by the interconnect between the sub-cells. [325, 326] To show the realistic potential of perovskite-organic tandem solar cells, we conducted a semi-empirical electro-optical simulation assuming an organic system with an energy-gap of 1.33 eV. [327] Details of the simulation can be found in [265]. According to Figure 8.1 a, in a conservative scenario an efficiency of 25.5 % is predicted with a perovskite bandgap in the range of 1.85 eV (c.f. chapter 7), assuming a tandem FF of 80 % and a loss in V_{OC} compared to E_g e^{-1} of 0.5 V, in each sub-cell. In a more optimistic scenario (FF = 85 % and loss in V_{OC} compared to E_g/e of 0.4 V), a tandem of a narrow-gap OSC (E_g = 1.15 eV) with a wide gap PSC (E_g = 1.75 eV) provides the prospect to reach an efficiency of 31.3 % (Figure 8.1 b). As of yet, efficient OSCs with E_g = 1.15 eV have not been developed.

8.1 Organic Sub-Cell Stability under Tandem Conditions

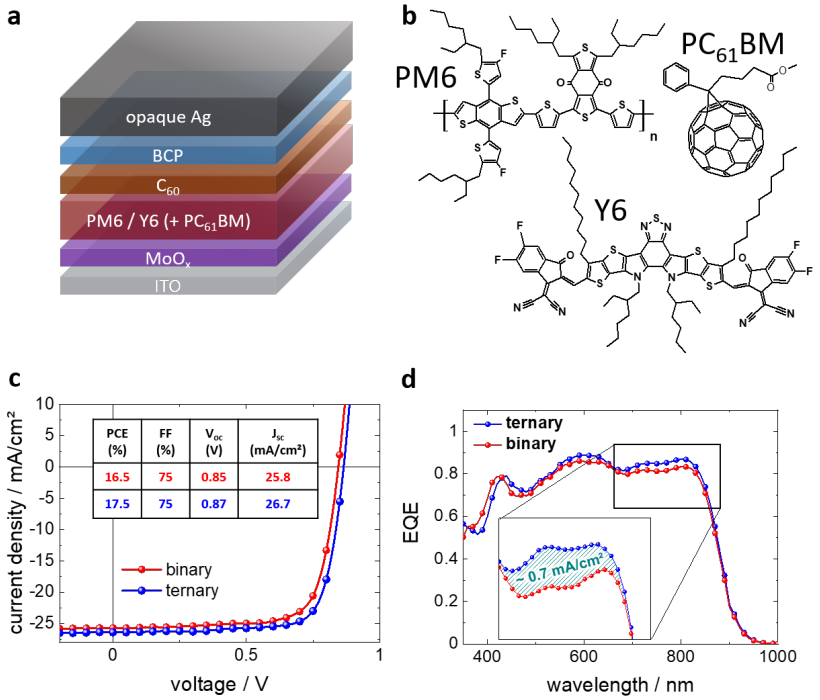

Figure 8.2: Organic solar cell characteristics. ***a,*** *Layer sequence of the single junction OSC and* ***b,*** *chemical structure of the molecules used in the photo-active layer.* ***c,*** *J-V scans and respective cell parameters of of binary (PM6:Y6) and ternary (PM6:Y6:$PC_{61}BM$) cells and* ***d,*** *respective external quantum efficiencies (EQE) with a magnified view of the spectral region beyond 650 nm, which is the relevant range of operation for the OSC in a perovskite-organic tandem cell. Adapted with permission from [265]. Copyright 2022 Springer Nature.*

For the narrow-gap sub-cell in our tandem architecture, we consider an organic photo-active system based on the polymer PM6, that contains a fluorinated-thienyl benzodithiophene, and the NFA Y6, which consists of a ladder-type dithienothiophen[3.2-b]-pyrrolobenzothiadiazole central moiety and two (5,6 difluoro-3-oxo-2,3-dihydro-1H-inden-1-ylidene)malononitrile units (Figure 8.2 a & b).[327] We employ a p-i-n type device architecture with molybdenum-trioxide as hole extraction layer (HEL) and a bi-layer of C_{60} / 2,9-Dimethyl-4,7-diphenyl-1,10-phenanthroline (BCP) for efficient electron extraction. Our cells with binary PM6 : Y6 blends (1 : 1.2) provide a power conversion efficiency (PCE) of up to 16.5 % (see Figure 8.2 c). EQE spectra of these devices extend beyond 900 nm (Figure 8.2 d). Adding a certain concentration of the fullerene derivative [6,6]-phenyl-C_{61}-butyric acid methyl ester ($PC_{61}BM$) into the PM6 : Y6 photo-active

layer to form a so-called ternary system, i.e. PM6 : Y6 : $PC_{61}BM$ (1:1.2:0.2), improves the blend morphology, which results in enhanced charge transport and reduced non-radiative recombination. [118, 328] Thus, a notable boost in cell characteristics is achieved with a PCE up to 17.5 % (for device statistics see Appendix Figure 11.9). We want to highlight a notably enhanced EQE of over 85 % for the ternary cells in the range $\geq$ 650 nm, which is the spectral region of operation when combined with a wide-gap front-cell in a tandem.

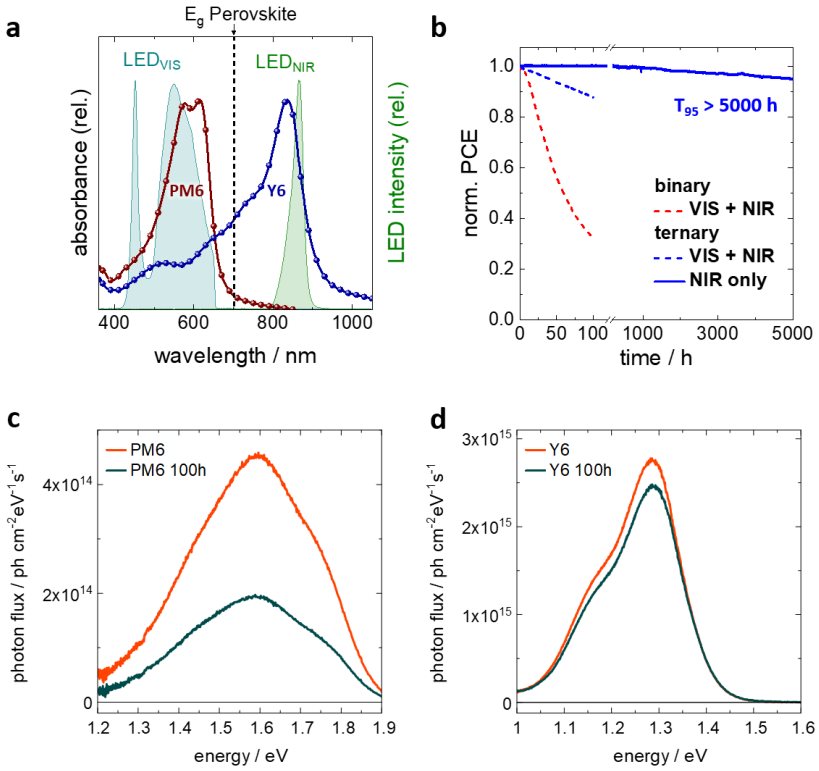

Figure 8.3: Stability of non-fullerene based organic solar cells. ***a,*** *Absorption spectra of the donor and acceptor molecules used in the photo-active layer. The vertical line marks the E_g of a possible wide-gap front cell material. Spectra of (filtered) light emitting diodes used in the stability assessment to selectively excite the donor / acceptor are also shown (labelled "LED_{VIS}" and "LED_{NIR}").* ***b,*** *Normalized power conversion efficiency (PCE) showing the long term stability of binary and ternary organic cells continuously operated using LED light sources with emission spectra shown in a, (one sun equivalent, nitrogen atmosphere, 25 °C) in the maximum power point (MPP) with exciton generation on both acceptor and donor ("VIS + NIR") or only on the acceptor ("NIR"). Please note the break in the x-axis. T_{95} denotes the time, after which the initial PCE has dropped to 95 % of its initial value.* ***c,*** *Photon flux of photoluminescence for PM6 and* ***d,*** *of Y6 layers pristine and after 100 h illumination with both the white (LED_{VIS}) and near infrared (LED_{NIR}) LED. The corresponding photoluminescence quantum yields are summarized in Table 8.1. Adapted with permission from [265]. Copyright 2022 Springer Nature.*

Table 8.1: *Photoluminescence quantum yield of PM6 and Y6 before and after 100 h illumination with LED_{VIS} & LED_{NIR}*

	PLQY (pristine)	PLQY (100 h illumination)
PM6	3.0 x 10^{-3}	1.3 x 10^{-3}
Y6	1.7 x 10^{-2}	1.4 x 10^{-2}

The absorption spectra of PM6 and Y6 (Figure 8.3 a) show that for $\geq$ 650 nm, excitons are predominantly generated on the Y6, which will be shown to be the key, that unlocks outstanding device stability. Stability of NFA cells under continuous operation is still a serious concern and a subject of vigorous scientific research. [117] To assess the stability of our binary and ternary cells under the illumination conditions applicable in a prospective perovskite-organic tandem cell, we used a filtered white LED (labelled: "LED_{VIS}") and a near infrared (NIR) LED (peak at 850 nm; labelled: "LED_{NIR}") as light sources, which predominantly create excitons on the PM6 or Y6, respectively (Figure 8.3 a). Under combined VIS / NIR illumination (experimental details can be found in [265]), binary and ternary cells show a notable decay of the PCE under continuous operation in the maximum power point (MPP) (Figure 8.2 b), mainly due to a loss in fill factor (FF) (see Appendix Figure 11.10). This degradation motif has previously been explained by a photoinduced reorganization in the donor / acceptor blend and the formation of microscopic aggregates of NFA molecules, which was claimed to lead to a reduced electron mobility and enhanced recombination. [329] Owing to their improved blend morphology, the decay of the ternary cells is notably slower than that of the binary cells. [117] However, most strikingly, under NIR illumination, where excitons are solely generated on the Y6, the devices did not show any burn-in, and we found only minimal signs of degradation even under long-term continuous operation in the MPP for more than 5,000 h (retaining 95 % of its original efficiency). These findings indicate that the detrimental morphological changes, discussed above, would require excitation of the donor polymer PM6 and that they can be substantially mitigated if predominantly the Y6 NFA is excited. Beyond this, in dedicated measurements on separate organic absorber layers, we found that upon continuous illumination with the white LED under inert conditions the photoluminescence quantum yield of PM6 shows a notable degradation, while the Y6 is less affected (Figure 8.3 c & d). At the same time atomic force microscopy (AFM) and grazing incidence wide angle X-ray scattering (GIWAXS) did not reveal morphological changes upon continuous illumination with LED_{VIS} + LED_{NIR} under inert conditions (Figure 8.4 and 8.5). while the results of grazing incidence small angle X-ray scattering (GISAXS) indicate only some minor morphological changes at the surface of samples after aging (Figure 8.6).

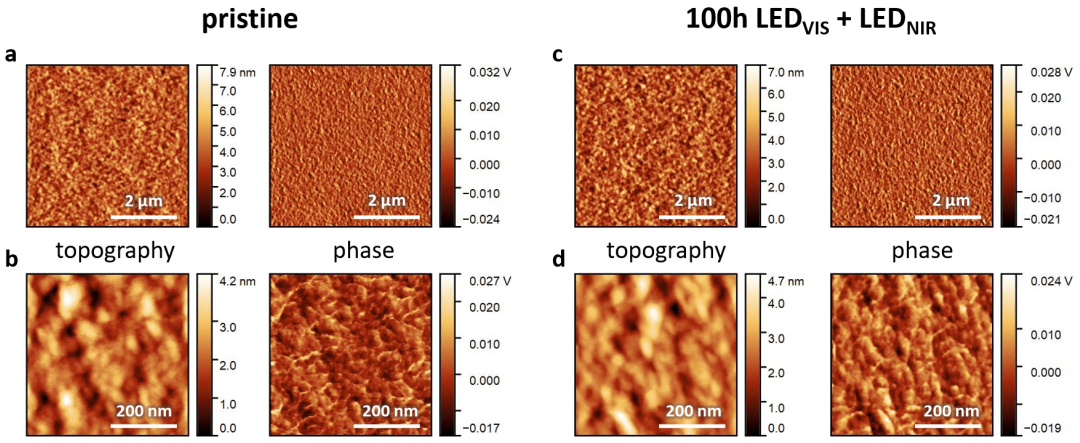

Figure 8.4: BHJ surface upon light stress. *Results of atomic force microscopy (topography and phase images) of ternary (PM6:Y6:$PC_{61}BM$) bulk heterojunctions deposited on top of a silicon substrate* ***a, b,*** *pristine and* ***c, d,*** *after stressing by illumination for 100 h (LED_{VIS} + LED_{NIR}). No obvious changes in the surface morphology can be identified after illumination stress. Adapted with permission from [265]. Copyright 2022 Springer Nature.*

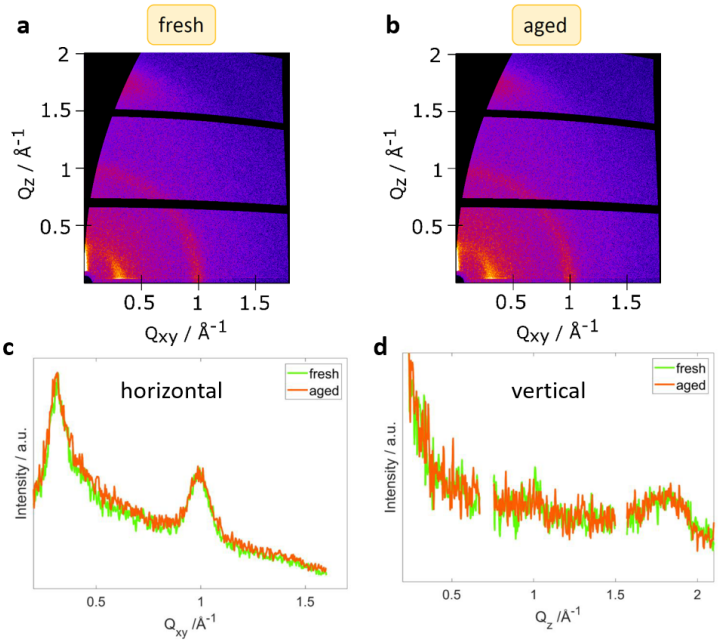

Figure 8.5: Grazing incidence wide angle X-ray scattering (GIWAXS). a, b *Reciprocal space maps of fresh and aged (100 h LED_{VIS} + LED_{NIR}) ternary (PM6:Y6:$PC_{61}BM$) bulk heterojunctions obtained by grazing incidence wide angle scattering (GIWAXS)* ***c,*** *horizontal and* ***d,*** *vertical profiles of the reciprocal space maps showing no detectable sign for changes in the molecular order. Adapted with permission from [265]. Copyright 2022 Springer Nature.*

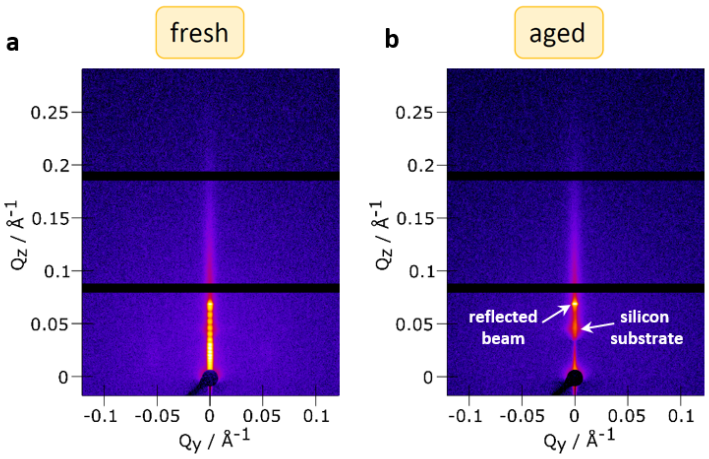

Figure 8.6: Grazing incidence small angle X-ray scattering (GISAXS). a, *Fresh and* ***b,*** *aged ternary bulk heterojunctions on top of a silicon substrate. Adapted with permission from [265]. Copyright 2022 Springer Nature.*

Please note, that in Figure 8.6 the strong peak at around 0.07 $Å^{-1}$ in Q_z corresponds to the reflection from the surface of the primary beam. A further signal, positioned at 0.045 $Å^{-1}$ in Q_z for both samples corresponds to the total reflection edge of the silicon substrate (Yoneda wing). The disappearance of the out-of-plane oscillations as well as of very weak in-plane signals (at 0.05 $Å^{-1}$) in GISAXS might hint to slight changes in the correlations of surface domains. Overall, no clear indication of illumination induced ordering / packing (segregation) of the bulk heterojunction could be detected.

Therefore, we propose that possibly photo-induced degradation of PM6 could likewise play a significant role in addition to possible morphological changes that were not detectable by the above techniques. In any event, our findings contradict the paradigmatic association of non-fullerene solar cells with operational instability, and they present the especially encouraging prospect that the long-term operational stability of perovskite-organic tandem cells will not be limited by the narrow-gap OSC. This is in notable contrast to all-perovskite tandems, where the stability of Sn-based narrow-gap PSCs is still a very serious issue.

8.2 Metal-like Indium Oxide as Universal Interconnect

The interconnect is a key component of monolithic (2-terminal) tandem solar cells (Figure 8.7 a). In a p-i-n tandem, the interconnect facilitates the recombination of electrons from the bottom cell with the holes from the top cell, ideally without any loss of V_{OC} and FF. In the simplest approach, one could omit the top electrode of the perovskite cell and stack the organic cell directly on top. In this case we found, that the interface between the low-work-function SnO_x and the high-work-function MoO_x affords only extremely poor, s-shaped J-V characteristics of the resulting tandem cell (Figure 8.7 b). This is most likely caused by a Schottky barrier, that forms at the SnO_x / MoO_x interface (see Figure 8.8).

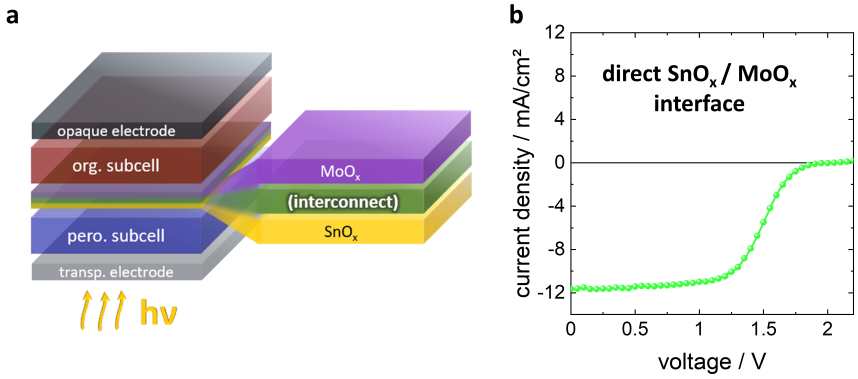

Figure 8.7: Tandem cell without interconnect. ***a,*** *Schematic of a perovskite-organic tandem cell and* ***b,*** *respective J-V characteristics. Adapted with permission from [265]. Copyright 2022 Springer Nature.*

In order to assess the rectifying behaviour inferred by the SnO_x / MoO_x interface, we prepared devices with a layer sequence ITO / SnO_x (20 nm) / MoO_x (5 nm) / gold. Forward bias refers to a positive bias of the MoO_x electrode with respect to the SnO_x electrode. Typically, rectifying current-voltage characteristics are found (Figure 8.8 a). We have used a standard diode model

$$I = I_0 \left(exp \left(\frac{e\,(V - IR_s)}{n_i\, k_B T} \right) - 1 \right) + \frac{V - IR_s}{R_{sh}}$$

to fit the current-voltage characteristics. There, e is the elementary charge, n_i is the ideality factor, R_s and R_{sh} are the series and shunt resistance, respectively. I_0 denotes the saturation current, which can be expressed by $I_0 = A \times A^* \times T^2\ exp(-\frac{e\,\Phi_b}{k_B T})$ with A^* being the Richardson constant, ϕ_b denoting the Schottky-barrier height and A stating the area of the device ($A = 3.14 \times 10^{-2}\ cm^2$) (see Figure 8.8 a).

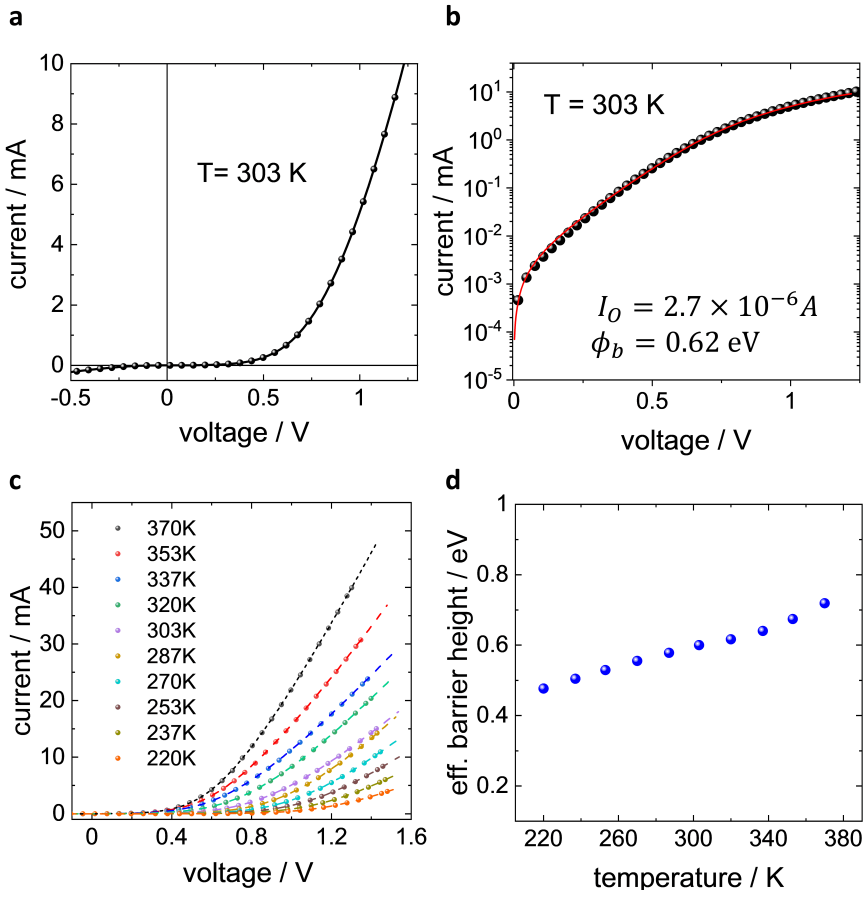

Figure 8.8: Determination of Schottky-barrier height from the J-V characteristics. ***a,*** *Forward J-V scans in linear and* ***b,*** *semi logarithmic scale. The drawn lines depict the respective fits by a standard diode model.* ***c,*** *Temperature dependent J-V scans and* ***d,*** *calculated barrier heights. Adapted with permission from [265]. Copyright 2022 Springer Nature.*

According to Crowell A^* can be expressed as: $\frac{4\pi e m k_B^2}{h^3}$. [330] With the effective mass of tin-oxide $m^* = 0.4\, m_0 \rightarrow A^* = 48\, \frac{A}{cm^2 K}$. [331] I_0 is obtained from a fit of the current-voltage characteristics as shown in Figure 8.8 b and ϕ_b can be derived. Eventually the temperature of the diodes has been varied on a temperature-controlled stage in the range of 220 - 370 K (Figure 8.8 c). At room temperature we find $\phi_b = 0.62$ eV. ϕ_b increases from 0.48 eV at 220 K to 0.72 eV at 370 K (Figure 8.8 d). Note, some variation of ϕ_b with temperature has been frequently observed in earlier studies of Schottky-barriers in other material systems, and they have been attributed to inhomogeneities. [332, 333] Hence we conclude, that indeed striking evidence for a Schottky barrier is found and a barrier height of $\phi_b = 0.6$ eV can be determined at the SnO_x / MoO_x interface, as also separately confirmed in the energy line-up derived from photoelectron spectroscopy.

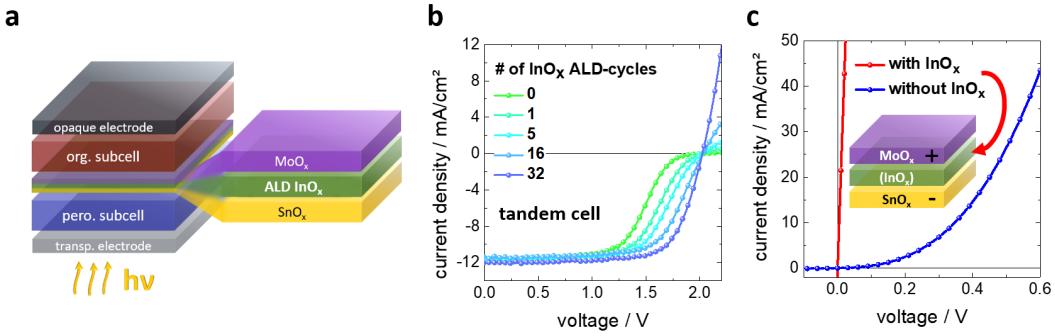

Figure 8.9: Tandem cell employing indium oxide interconnect. ***a,*** *Tandem layer stack highlighting the interconnect.* ***b,*** *J-V characteristics of tandem cells with varied thickness (number of atomic layer deposition (ALD) cycles) of the InO_x interconnect.* ***c,*** *J-V characteristics of SnO_x / InO_x / MoO_x diodes. Adapted with permission from [265]. Copyright 2022 Springer Nature.*

To render the interconnect ohmic, thin layers ($\approx$ 1 nm) of a metal (Ag or Au) are frequently inserted between top- and bottom-cell. [325, 334] However, even an Ag-layer as thin as 1 nm already introduces significant optical losses that lower the EQE of the back-cell and the overall J_{SC} of the tandem cell as shown further below. Thus, we developed an interconnect based on an ultra-thin ALD-grown InO_x layer with a thickness of only $\approx$ 1.5 nm (details of the ALD growth process can be found in [265]).

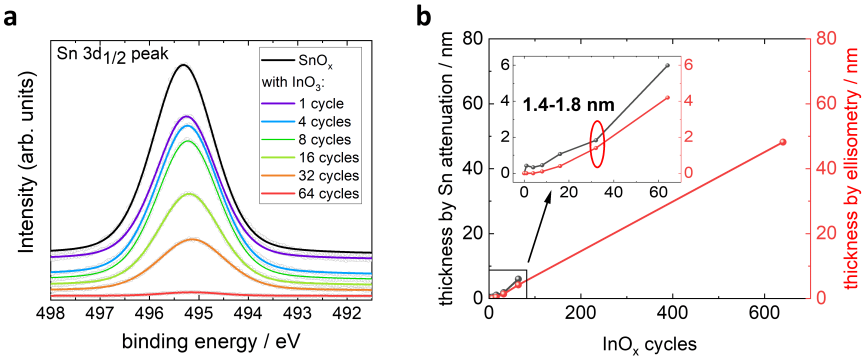

Figure 8.10: InO_x layer thickness. ***a,*** *Sn $3d_{1/2}$ XPS core level signal for pure SnO_x as well as for SnO_x covered by an increasing number of ALD cycles of InO_x.* ***b,*** *Calculated layer thickness of the InO_x overlayer, extracted from the attenuation of the Sn core level peaks (left axis) or derived by ellipsometry (right axis). The inset shows the region of interest confirming a layer thickness of 1.4 - 1.8 nm for 32 growth cycles. Adapted with permission from [265]. Copyright 2022 Springer Nature.*

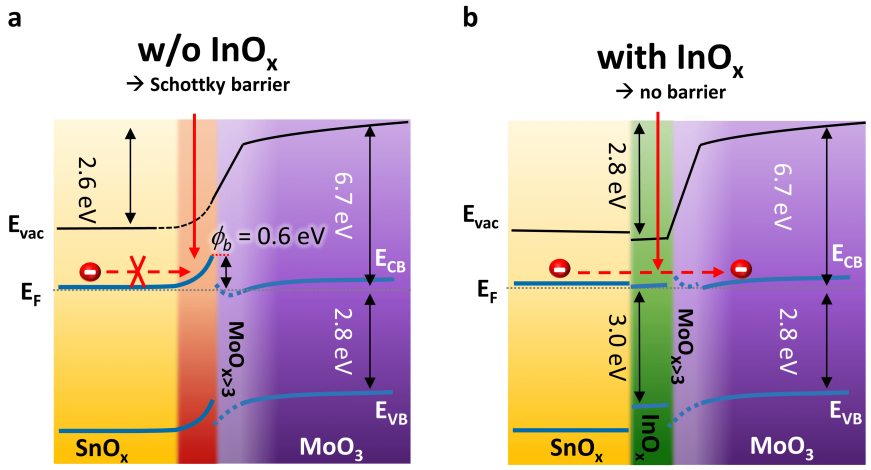

Figure 8.11: Charge transport with interconnect. *Energetic line-up determined* ***a,*** *without and* ***b,*** *with InO_x. Note, in the first 2 nm of the molybdenum oxide layer we found a mix of oxidation states of the molybdenum ranging from Mo^{2+} to Mo^{6+}. The first 2 nm of the molybdenum oxide are characterized by the presence of MoO_4^{2-} clusters (details in [266]). Adapted with permission from [265]. Copyright 2022 Springer Nature.*

We leverage the unique property of ALD to provide utmost control of layer thickness even on the level of angstroms, which is impossible with conventional deposition techniques. The insertion of InO_x between SnO_x and MoO_x outstandingly improves the J-V characteristics of the tandem cells (Figure 8.9 b). Only 32 ALD cycles (thickness $\approx$ 1.5 nm, Figure 8.10) are sufficient to render the SnO_x / InO_x / MoO_x stack ohmic as shown also in ITO / SnO_x / InO_x / MoO_x test devices in Figure 8.9 c. The energetic line-up in the interconnect is unraveled by an extensive study using photoelectron spectroscopy (Figure 8.11 for the full data set of XPS, UPS and IPES measurements and fits please see [265]). The upward band bending (matching the barrier of $\phi_b = 0.6$ eV calculated above), found in case of SnO_x / MoO_x is completely alleviated by the insertion of the ultra-thin InO_x, enabling barrier-free transport of electrons from the bottom PSC across the SnO_x / InO_x / MoO_x layer sequence. Ultimately, these electrons recombine with the holes from the OSC at the MoO_x / organic interface. [140, 260] In a spotlight on the indium oxide layer, we were able to confirm that, after completion of a nucleation phase (32 ALD cycles), the InO_x layer shows a metallic nature with an electron density of about 10^{20} cm^{-3} (Figure 8.12 a, b). This high charge carrier density is maintained (and even increases slightly) for thicker layers, which renders interface effects, like a possible doping of the indium oxide by tin atoms, rather unlikely candidates as origin for the high charge carrier density. A further indication contradicting a possible Sn-doping, is the fact, that a likewise high carrier density is found for InO_x deposited on Al_2O_3 (Figure 8.12 c).

On the other hand a high carrier density is frequently found in nominally undoped InO_x thin films because of oxygen vacancies and surface defects. [335, 336] In our case, we have determined a stoichiometry of $In_2O_{2.8}$ by photoelectron spectroscopy, which indicates oxygen deficiency. As the metallic InO_x layer is ultra-thin, it still provides a very high sheet resistance $> 10^{-6}$ Ω sq^{-1} (Figure 8.12 a), which outperforms carefully optimized sputtered metal oxide interconnects by at least an order of magnitude. [311] Note that a high sheet resistance is of critical importance to avoid shorting of the sub-cells in case of local shunt paths.

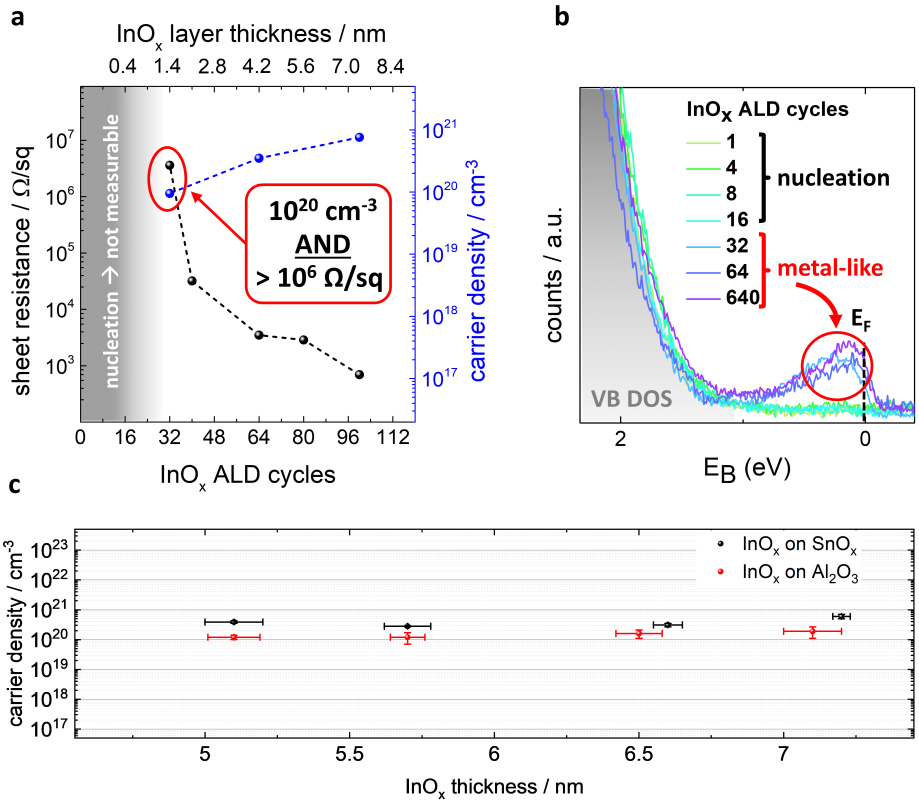

Figure 8.12: Electrical properties of InO_x. ***a,*** *Sheet resistance and carrier density vs. thickness of the InO_x.* ***b,*** *Ultra-violet photoelectron spectroscopy of the valence band (VB) density of states (DOS) of InO_x, showing the onset of a metallic behaviour at 32 cycles of atomic layer deposition (ALD).* ***c,*** *Charge carrier densities (and respective standard error) of InO_x layers of various thickness grown either on a SnO_x or an Al_2O_3 seed layer. Adapted with permission from [265]. Copyright 2022 Springer Nature.*

To better understand the structure of our interconnect, we conducted high-angle annular dark-field scanning transmission electron microscopy (HAADF-STEM), energy dispersive X-ray spectroscopy (EDS) and grazing incidence wide angle X-ray scattering (GIWAXS). These measurements were conducted on separately deposited interconnect sequences (SnO_x / InO_x / MoO_x) on silicon wafers. First and foremost the TEM measurements shown in Figure 8.13 confirm a homogeneous coverage of all ALD layers as well as a continuous InO_x thickness of $\approx$ 1.5 nm.

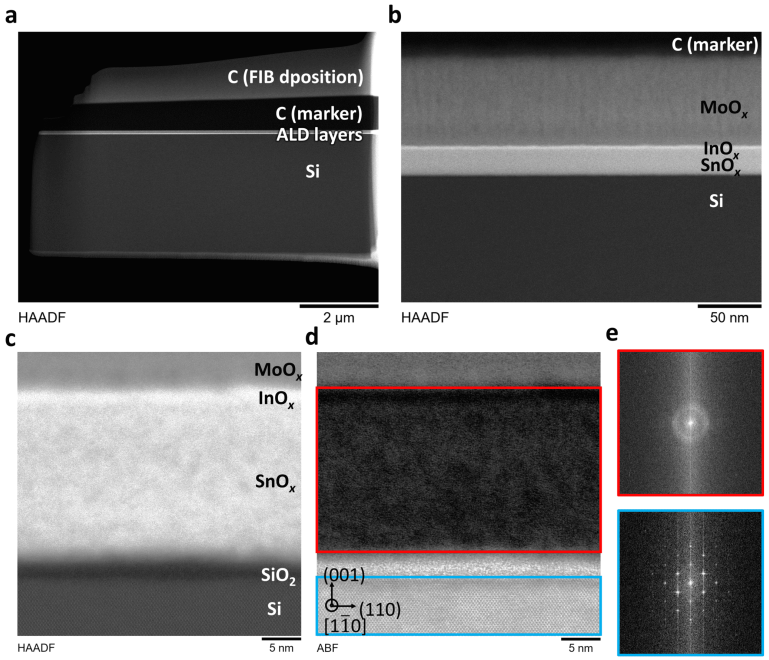

Figure 8.13: TEM analysis of the interconnect. *High angle annular dark field (HAADF)-STEM images of deposited SnO_x / InO_x / MoO_x layers on a silicon substrate at* ***a,*** *2 µm* ***b,*** *50 nm and* ***c,*** *5 nm scale showing continuous ALD growth of both SnO_x and InO_x layers.* ***d,*** *Respective annular bright field and* ***e,*** *fast Fourier transformed images of SnO_x / InO_x (red frame) and Si (blue frame) showing the contrast between the crystalline silicon wafer and the ALD layers covering it. Adapted with permission from [265]. Copyright 2022 Springer Nature.*

Fast fourier transformation of the obtained image also gives strong indication of an amorphous nature of the InO_x layer. The amorphous state of all deposited layers was further confirmed by bulk and surface GIWAXS measurements showing broad and continuous reflection features both for SnO_x and SnO_x / InO_x deposited on top of silicon (Figure 8.15). Further on, regarding possible inter-diffusion of the deposited layers, EDS mapping was conducted on the cross-section shown in Figure 8.13. According to these line profiles displayed in Figure 8.14 c, no sign of indium diffusion into the underlying SnO_x layer could be found.

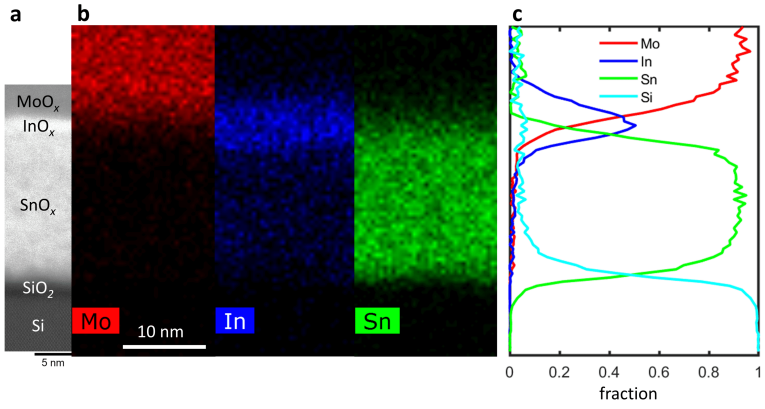

Figure 8.14: EDS analysis of the interconnect. ***a,*** *High angle annular dark field (HAADF) measurement of silicon / native oxide / SnO_x / InO_x / MoO_x and* ***b,*** *respective EDS elemental maps. The EDS count maps of In-L_α and Sn-L_α are plotted together with Mo-L_α. However, as In-L_α (3.29 eV) are very close to Sn-L_α (3.44) and overlap with Sn-L_n (3.27 eV), there are spurious counts inside the SnO_x layer that contribute to the In L_α integration window. To separate the overlapping signals, we applied multivariate statistical analysis to separate EDS signals from the InO_x and SnO_x layers. [337, 338] The resulting line profiles of Mo, In, and Sn are plotted in* ***c****. Adapted with permission from [265]. Copyright 2022 Springer Nature.*

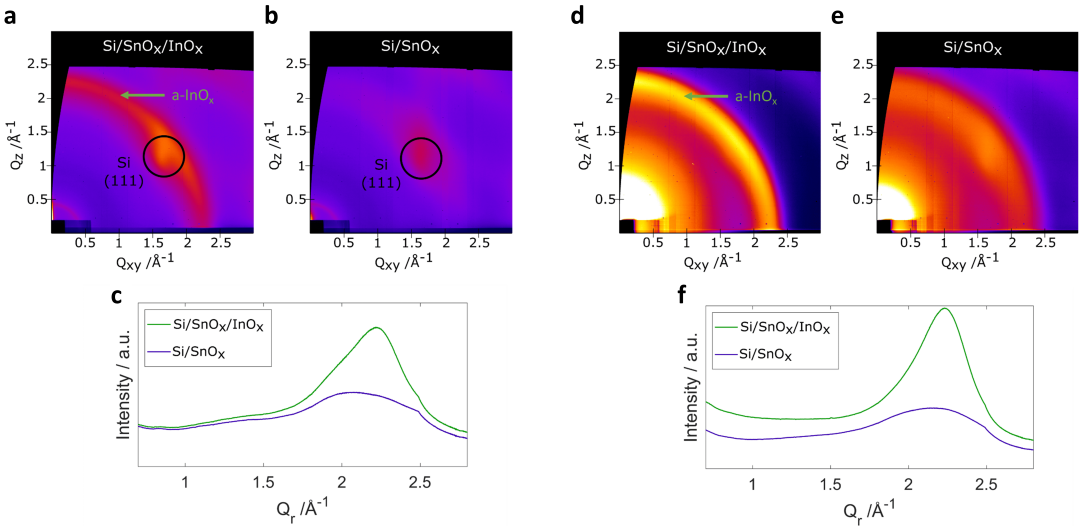

Figure 8.15: GIWAXS analysis of the interconnect. ***a,*** *Bulk GIWAXS measurements of 20 nm InO_x on top of 20 nm SnO_x and* ***b,*** *only 20 nm SnO_x on top of a silicon substrate (incidence angle 0.3°, probing depth > 500 nm). With the probing depth exceeding the deposited layer thickness, some reflection due to the [111] planes of the Si substrate can also be seen (marked by a circle).* ***c,*** *Radial profiles of the data shown in a and b.* ***d,*** *-* ***f,*** *Respective surface GIWAXS measurements showing again* ***d,*** *20 nm InO_x on top of 20 nm SnO_x and* ***e,*** *only 20 nm SnO_x on top of a silicon substrate (incidence angle 0.12° probing depth of about 2 nm) as well as* ***f,*** *respective radial profiles. Adapted with permission from [265]. Copyright 2022 Springer Nature.*

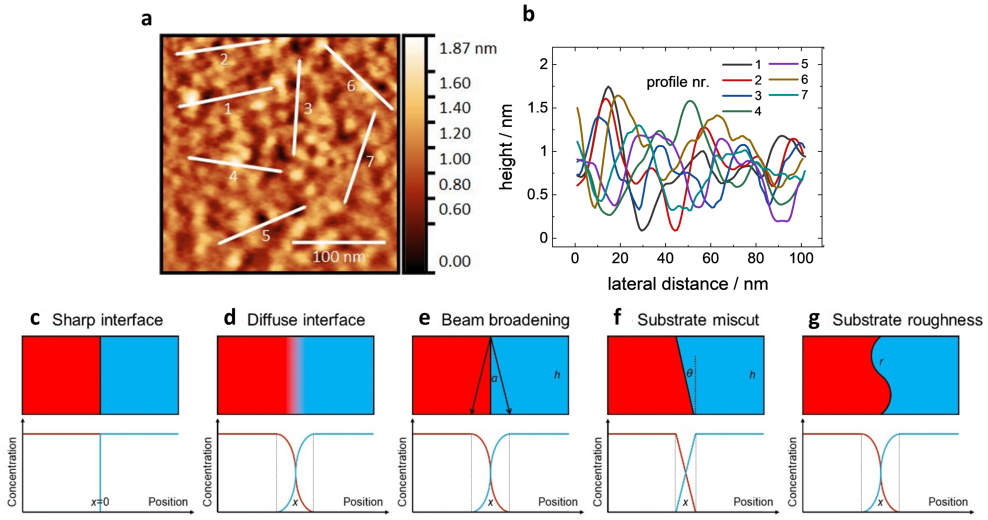

Figure 8.16: Origin of EDS uncertainties. ***a,*** *Topography of a 20 nm thick tin oxide layer grown by ALD on a silicon substrate. Seven 100 nm traces are marked, indicating the extracted height profiles, shown in* ***b.*** ***c*** *-* ***g*** *Exemplary elemental concentration profiles of* ***c,*** *an abrupt interface,* ***d,*** *a diffuse interface, and the effects from* ***e,*** *beam broadening of the STEM probe* α*,* ***f,*** *substrate mis-cut by an angle* θ*, and* ***g,*** *substrate roughness r on the projected concentration profiles, resulting in a broadening, denoted by x, similar to profiles expected in the case of a diffuse interface. Adapted with permission from [265]. Copyright 2022 Springer Nature.*

Soft edges of the elemental profiles of about 2 nm exceed the total thickness of the indium oxide layers and therefore at this state a slight intermixing of the InO_x by Sn atoms can not be entirely excluded. To pinpoint the origin of these soft edges, we conducted atomic force microscopy measurements, evidencing a surface profile with a peak to peak distance of approx 1.5 nm. Hence, in combination with other effects like beam broadening or slight substrate miscut, we conclude, that this effect most likely results from roughness of the layers and the collection of the EDS signals from the entire 100 nm thick TEM lamella, rather than from a real inter-diffusion at the interface.

Still in the aim to enable a statement on possible inter-diffusion and tin doping of the indium oxide, we eventually performed highly surface sensitive UV photoelectron spectroscopy on ITO, SnO_x and SnO_x / InO_x surfaces as shown in Figure 8.17. In contrast to the ITO and the SnO_x layers, for the InO_x (32 cycles; thickness of 1.5 nm) on top of SnO_x no signal of the Sn4d semi-core levels could be detected. With an estimated sampling depth of about 1 nm, this result indicates that, if mixing between the InO_x and the SnO_x layers were to occur, it would be limited to the first 5 angstroms of the InO_x layer adjacent to the SnO_x. We can therefore conclude that our indium oxide interconnect is continuous, amorphous with abrupt interfaces, while providing simultaneously high

charge carrier density and high shunt resilience. Finally optical transmittance is probed. Since high carrier densities typically infer optical absorption, optics is another important reason to keep the thickness of the interconnect to a minimum. [339] Most strikingly, our ultra-thin InO_x interconnect shows a transmittance near unity, meaning it is not expected to introduce any notable optical losses (Figure 8.18 a). In a direct comparison, it boosts the EQE of the organic back-cell and the overall J_{SC} of a tandem by about 1.5 mA^{-2} compared to the case of an interconnect based on 1 nm of Ag, which affords a PCE of only about 20 % in tandem (Figure 8.18).

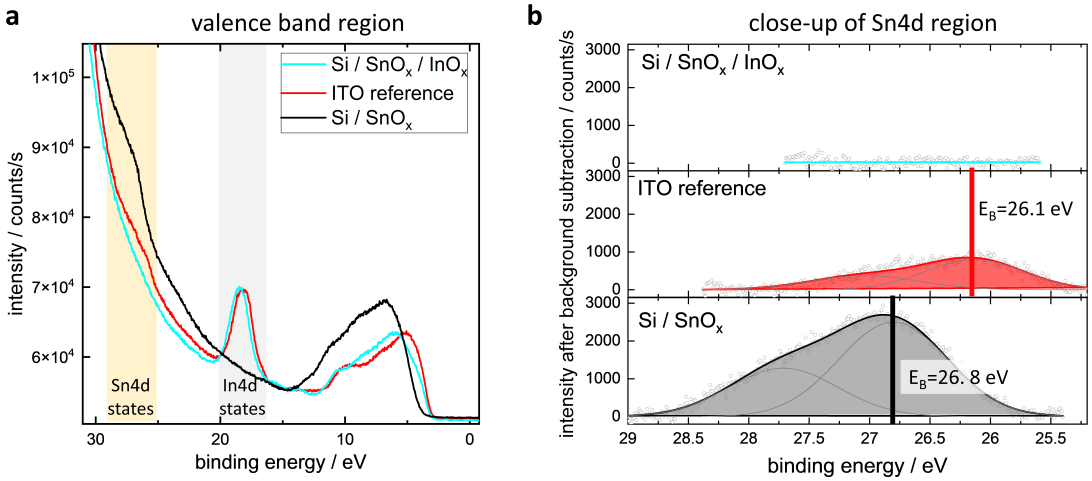

Figure 8.17: Probing inter-diffusion by UPS. *UV photoelectron spectroscopy measurements on SnO_x, SnO_x / InO_x, as well as an ITO reference layer using HeII excitation at 40.81 eV.* ***a,*** *Valence band region of the three samples, showing semi-core signals of Sn4d and In4d.* ***b,*** *Close up of the Sn4d region, after a linear background subtraction has been performed. The data is fitted by two peaks corresponding to the $Sn4d_{5/2}$ and $Sn4d_{3/3}$ doublet. Adapted with permission from [265]. Copyright 2022 Springer Nature.*

Table 8.2: *Solar cell characteristics of the cells shown in Figure 8.18.*

interconnect	**reverse**				**forward**			
	PCE / %	FF / %	V_{OC} / V	J_{SC} / mA cm^{-2}	PCE / %	FF / %	V_{OC} / V	J_{SC} / mA cm^{-2}
InO_x	22.8	76	2.12	14.1	22.1	75	2.08	14.1
1 nm Ag	20.5	78	2.09	12.6	20.2	77	2.08	12.6

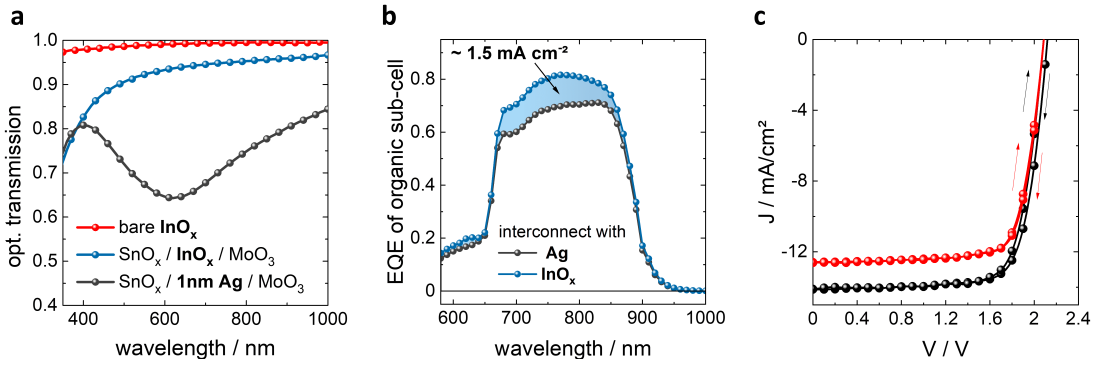

Figure 8.18: Optically almost lossless indium oxide interconnect. a, *Optical transmittance of an interconnect based on 32 ALD cycles (≈ 1.5 nm) of InO_x, bare and sandwiched between SnO_x and MoO_x. For comparison, the InO_x has been replaced by a nominally 1 nm thick layer of Ag.* ***b,*** *Resulting external quantum efficiency (EQE) spectra of the organic back-cell with InO_x or Ag as interconnect demonstrating the significant current losses induced by only 1 nm Ag as well as* ***c,*** *respective J-V characteristics. The cell characteristics are summarized in Table 8.2. Adapted with permission from [265]. Copyright 2022 Springer Nature.*

Finally we want to highlight, that ALD allows for large-area, high-throughput processing (even at atmospheric pressure, see e.g. chapter 5.1), [226] and enables conformal coating of textured surfaces that frequently occur in light trapping concepts. [310] Hence, we foresee that the applicability of our interconnect is not limited to perovskite-organic tandem cells, but it may also be favourably used in other tandem cells.

8.3 Highly Efficient Tandem Cells

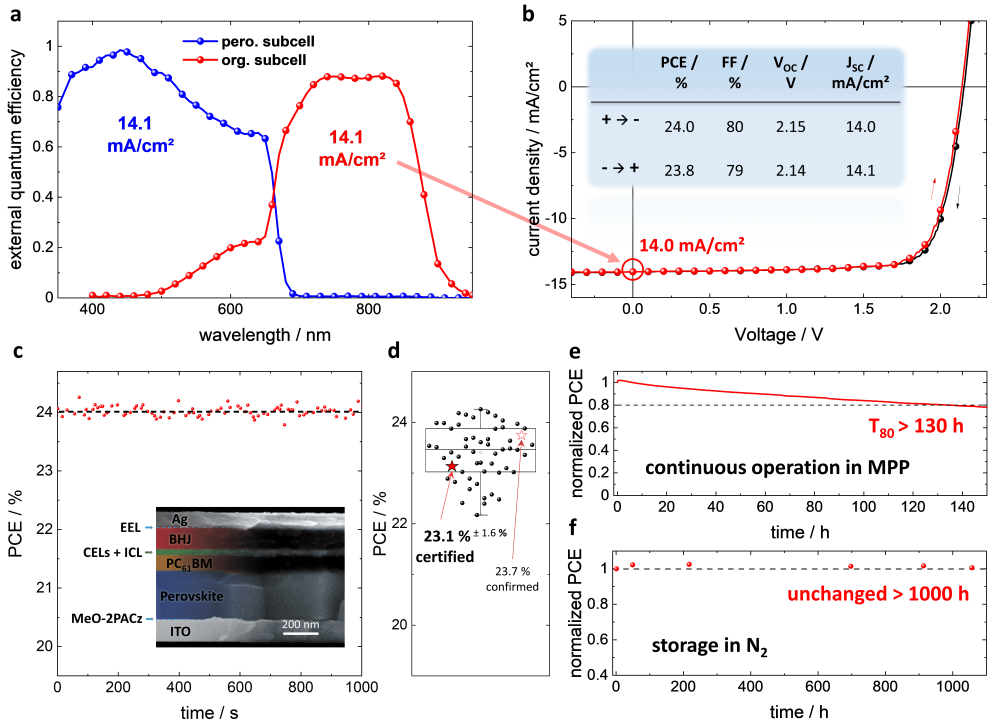

Figure 8.19: Perovskite-organic s. ***a,*** *External quantum efficiency spectra of both sub-cells in the tandem cell. For reduced reflection, the backside of the substrate was coated with a 100 nm thick MgF_2 layer.* ***b,*** *J-V characteristics of tandem cells, with derived power conversion efficiency (PCE), fill factor (FF), open circuit voltage (V_{OC}), and short circuit current density (J_{SC}) as inset.* ***c,*** *Stabilized PCE of the tandem cell. (inset) Scanning electron microscopy image of the cell cross section.* ***d,*** *Statistical data of tandem solar cells as derived from reverse J-V scans also containing the certified and confirmed value measured by the Fraunhofer ISE CalLab (Figure 8.22). Upper and lower box ranges depict interquartile range (25 % - 75 %) with a median line in between. The whiskers show the ultimate data point inside yet another 1.5 interquartile range to identify outliers.* ***e,*** *Stability of the tandem cells under continuous operation in the maximum power point (MPP), and* ***f,*** *when stored in N_2. Adapted with permission from [265]. Copyright 2022 Springer Nature.*

Drawing from the significant progress outlined above, we prepared monolithic perovskite-organic tandem solar cells with outstanding characteristics. The EQE spectra of the PSC and OSC sub-cells of an optimized perovskite-organic tandem are shown in Figure 8.19 a. Excellent current matching, as required in a series connection, is evidenced by the identical integrated current density of 14.1 mA cm^{-2} for both sub-cells. The high EQE values (> 95 %) in the wavelength region between 400 - 500 nm can be explained by optical effects as discussed in section 7.2. The current values obtained from the EQE measurement are in excellent agreement with short circuit current values derived from J-V scans, shown in Figure 8.19 b. A direct comparison of the champion

cell characteristics of each sub-cell, as well as the final tandem cell, is shown in Table 8.3, while statistical data displaying the experimental spread are shown in form of a box plot for tandem devices in Figure 8.19 d, 8.20 and in tabular form in Table 8.4, that also includes the respective single junctions.

Table 8.3: *Solar cell characteristics derived from J-V scans of champion perovskite-organic tandem solar cells as well as the perovskite and organic single junctions*

	scan direction	PCE / %	FF / %	V_{OC} / V	J_{SC} mA cm^{-2}
pero. cell	reverse	16.8	81	1.34	15.6
	forward	16.4	80	1.33	15.5
org. cell	invariant	17.5	75	0.87	26.7
tandem cell	reverse	24.0	80	2.15	14.0
	forward	23.8	79	2.14	14.1

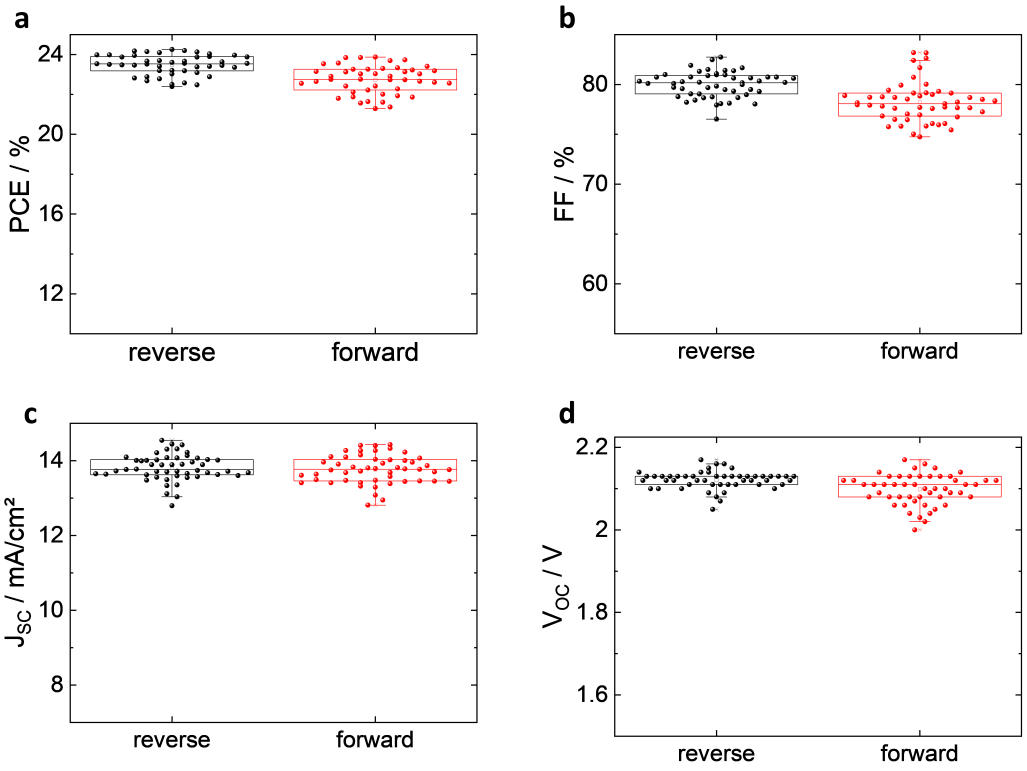

Figure 8.20: Tandem solar cell statistics *(binned) of 48 perovskite - organic tandem solar cells with InO_x interconnect. Box plots: median line with upper and lower box ranges denoting the 25% and 75% margins. The bars denote the outermost data points that are still inside another 1.5 interquatile range. Adapted with permission from [265]. Copyright 2022 Springer Nature.*

Table 8.4: *Overview of statistic cell characteristics with standard deviation of the single junctions and tandem cells derived from J-V scans. This data was calculated from a total of 34 perovskite, 60 organic and 48 tandem solar cells, fabricated in various batches by different persons.*

	scan direction	PCE / %	FF / %	V_{OC} / V	J_{SC} mA cm^{-2}
pero. cell	reverse	16.0 ± 0.5	80 ± 1	1.30 ± 0.02	15.5 ± 0.2
	forward	15.7 ± 0.7	78 ± 2	1.29 ± 0.02	15.5 ± 0.3
org. cell	invariant	16.5 ± 0.4	74 ± 1	0.86 ± 0.01	26.0 ± 0.5
tandem cell	reverse	23.4 ± 0.5	80 ± 1	2.12 ± 0.02	13.9 ± 0.2
	forward	22.7 ± 0.7	78 ± 2	2.13 ± 0.03	13.8 ± 0.4

To evaluate potential losses caused by the indium oxide interconnect exemplarily a measured tandem solar cell is compared with individual sub-cell characteristics of control sub-cell devices made in the same batch. For this, the respective J-V characteristics of the single junctions were scaled in a way that they generate short circuit current values similar as that found in the EQE measurement in Figure 8.19 a. Eventually, as visible in Figure 8.21, both J-V characteristics were added up along the voltage axis, mimicking a series connection to obtain a theoretical tandem ("constructed tandem") derived from the two sub-cells assuming ideal interconnecting conditions.

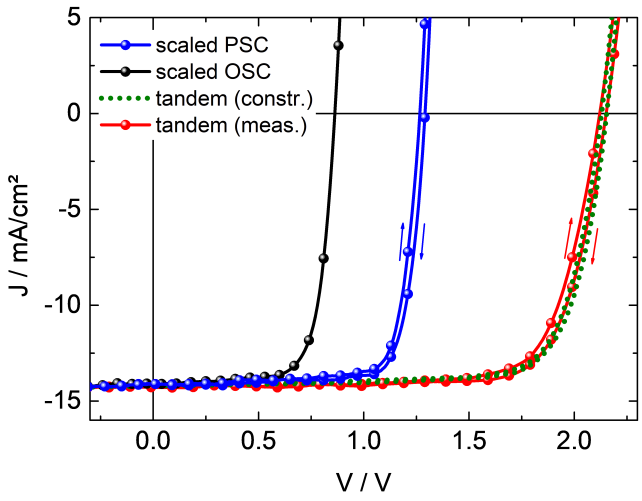

Figure 8.21: Measurement vs. constructed tandem J-V characteristics. *Construction of the theoretical J-V curves of the tandem device from the serial connection of both sub-cells. To emulate the J-V characteristics of the sub-cells, the measured J-V characteristics of representative single junction devices have been scaled to generate the respective short circuit current density that was derived from EQE results of the sub-cells in the tandem device. Adapted with permission from [265]. Copyright 2022 Springer Nature.*

When we compared the calculated to the actually measured tandem solar cell (see Table 8.5), we found a striking resemblance and no noticeable loss in V_{OC}. Therefore we are confident to claim an electronically (and optically, see above) almost lossless tandem interconnect in case of our 1.5 nm thin indium oxide.

Table 8.5: *Solar cell characteristics of the devices shown in Figure 8.21*

	scan direction	PCE / %	FF / %	V_{OC} / V	J_{SC} mA cm^{-2}
PSC in tandem	reverse	14.5	80	1.29	14.1
	forward	14.1	79	1.27	14.1
org. cell in tandem	invariant	8.9	73	0.86	14.1
constructed tandem	reverse	23.5	77	2.15	14.2
	forward	23.2	77	2.13	14.2
measured tandem	reverse	23.7	78	2.15	14.2
	forward	23.0	76	2.12	14.2

Finally we sent some of our champion cells to the Fraunhofer ISE CalLab for certification according to the IEC 60904-3 procedure (Figure 8.22). The certification procedure involves the measurement of the external quantum efficiency prior to J-V certification. This EQE measurement procedure, which is done in ambient air, takes about 1 hour and inflicts some severe asymmetric stressing of each sub-cell due to the necessary monochromatic light biasing. [340] These EQE measurement conditions infer some degradation of the cell, that would not occur under "normal" operation of the cell under AM 1.5 solar illumination. This degradation is clearly visible if one compares the integrated current values derived from the certified EQE measurement ($\geq$ 14 mA/cm^2 for both sub-cells, Figure 8.23 - full data set see [265]) with the value of 13.2 mA cm^{-2} resulting from a J-V measurement thereafter (Figure 8.22). Nevertheless, the Fraunhofer ISE CalLab certified an efficiency of 23.1 per cent for this stressed cell. Due to this asymmetric stressing, additionally a confirmation measurement was undertaken on a sister cell, that had not undergone the stressing in a prior EQE measurement. In this case the spectral illumination characteristics calibrated for the certified sister cell were used. The obtained efficiency of 23.7 % is identical to what we have measured for the same cell prior to shipping the cell to the Fraunhofer ISE CalLab (Figure 8.24).

Fläche / *Area* (da)[1]: = (0.0174 ± 0.0011) cm²

[1] : (t) = total area, (ap) = aperture area, (da) = designated illumination area /7/

Kennlinienparameter des Messobjektes unter Standardtestbedingungen (STC) / *IV-curve parameter under Standard Testing Conditions (STC)* :

		Vorwärtsrichtung / *forwards scan direction*	Rückwärtsrichtung / *reverse scan direction*	steady state MPP
V_{oc}	=	(2160 ± 22) mV	(2163 ± 22) mV	
I_{SC} (Ed.2 - 2008)	=	(0.2301 ± 0.0048) mA	(0.2304 ± 0.0048) mA	
I_{MPP}	=	0.21 mA	0.22 mA	(0.2157 ± 0.0063) mA
V_{MPP}	=	1867.2 mV	1877.8 mV	(1871 ± 37) mV
P_{MPP}	=	0.401 mW	0.405 mW	(0.403 ± 0.012) mW
FF	=	80.64 %	81.25 %	
η	=			(23.1 ± 1.6) %

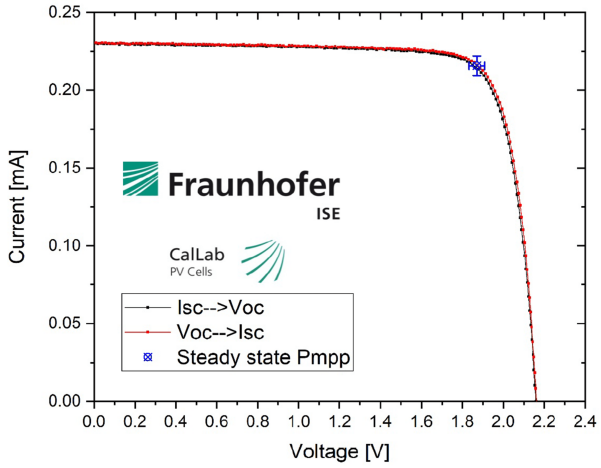

Figure 8.22: Tandem certification J-V. *Abbreviated certificate obtained from J-V measurements performed by the Fraunhofer ISE (Freiburg). The full certificate can be found in [265].*

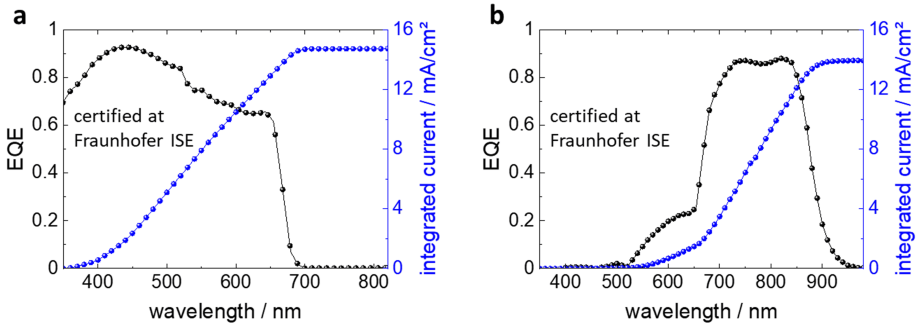

Figure 8.23: Tandem certification EQE. *Spectra measured at the ISE Fraunhofer CalLab as well as derived integrated current values of* ***a,*** *the perovskite and* ***b,*** *the organic sub-cell. The certificate can be found in [265]. Adapted with permission. Copyright 2022 Springer Nature.*

Table 8.6: *Solar cell characteristics of the devices shown in Figure 8.24*

	scan direction	PCE / %	FF / %	V_{OC} / V	J_{SC} / mA cm^{-2}
in house	reverse	23.8	81	2.13	13.7
	forward	23.7	81	2.13	13.8
Fraunhofer ISE CalLab	reverse	23.8	81	2.15	13.6
	forward	23.6	81	2.15	13.6

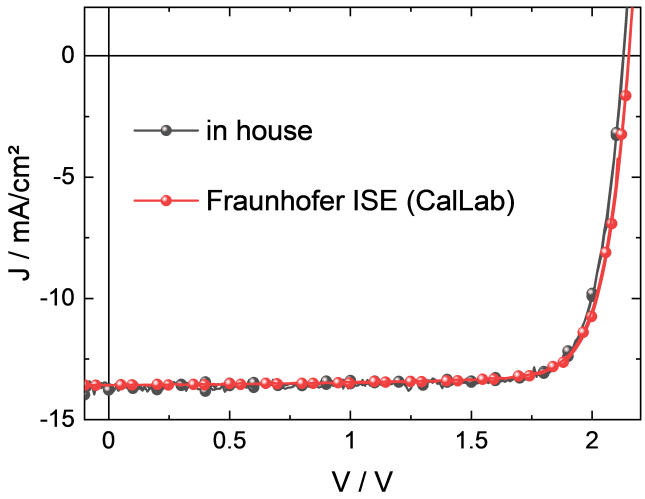

Figure 8.24: Confirming measurement of a tandem cell. *Direct comparison of the same tandem cell measured first in our own lab (in house) and then at Fraunhofer ISE CalLab without stress due to a prior EQE measurement using the light source calibration obtained from the certified cell shown in Figure 8.22. Adapted with permission from [265]. Copyright 2022 Springer Nature.*

As such, we can confirm the validity of our measurement. The respective value is labelled as "confirmed". Our devices state the most efficient monolithic perovskite-organic tandem cells, as of yet. We also evidence an excellent stability of more than 1,000 h with no sign of degradation when the devices are kept under inert atmosphere (Figure 8.19 f). This confirms intrinsic stability of the perovskite-organic tandem solar cell. We want to underline here, that for tin containing low bandgap perovskites, intrinsic stability is still a very serious concern. Therefore perovskite-organic tandem solar cell might be the path to circumvent the use of tin based perovskites, in case no real stabilization strategy might be found. Under continuous operation in the MPP a T_{80} of 130 h was observed (Figure 8.19 e).

With this regard we want to note, the temporal behavior of the tandem under continuous operation is essentially governed by that of the wide gap perovskite sub-cell (Figure 8.25). Therefore, for perovskite-organic tandems, unlike all-perovskite tandems, one of the main future challenges will be the stabilization of the perovskite wide gap sub-cell, whilst for the low gap sub-cell mainly a reduction in the energy gap would be desirable in order to reach the areas of PCEs exceeding 30 %, as predicted in Figure 8.1.

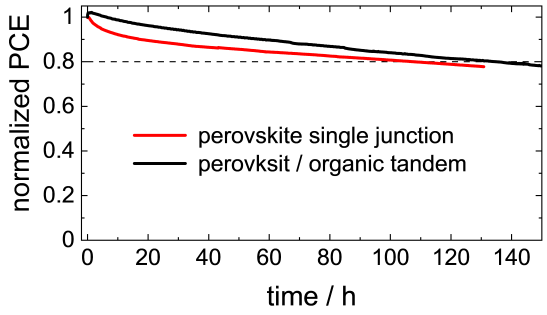

Figure 8.25: Tandem vs perovskite SJ stability. *Comparison of the illumination stability of the tandem solar cell and the perovskite solar cell. The dashed line (T_{80}) displays degradation of the tandem cell in a similar time periods as the perovskite wide gap cell. Adapted with permission from [265]. Copyright 2022 Springer Nature.*

9 Conclusion and Outlook

Emerging thin film solar technologies in general and perovskites in particular carry the very real potential to revolutionize the solar cell market. The prospect of low-price, lightweight, but anyway highly efficient solar cells enables applications far beyond what is commonly available nowadays. Building facades, cars, windows, fences, mobile devices and many more unused areas will become available, which can extend the solar potential many times over. To make this vision possible, the scientific community together with the already invested industry has to overcome some key roadblocks on the way for final commercialization of the technology. In this work we contributed our share to three of the main areas of progress of perovskite solar cell technology:

Improve perovskite cell stability:

- Implement an internal tin oxide barrier grown by atomic layer deposition that not only protects the perovskite from harmful external influences, but also seals perovskite decomposition material, which in turn drastically improved air, temperature and illumination stability.

- Unravel superior stability of non fullerene acceptor Y6 based solar cells under tandem illumination conditions (excitons solely generated in the acceptor). By this, an viable and most importantly readily stable alternative to intrinsically instable, low band gap, Pb-Sn perovskite is found.

- Mitigate detrimental halide segregation in high Br content wide bandgap material, by application of a self assembled monolayer as bottom side hole extraction layer.

Reduce cost

- Significant improvement with regard to the yield of solar cell fabrication, by combining a robust gas quenching technique with a complexing co-solvent that not only loosens the processing window, but also drastically improves precursor wetting.

- Implementation of atmospheric pressure processing of atomic layer deposition on top of perovskite materials to evolve the above mentioned tin oxide sealing into a roll to roll compatible process.

Improve Efficiency

- Introduction of an electronically and optically almost lossless, ultra thin interconnect layer that can be applied on top of a perovskite cell and is readily applicable to a variety of tandem concepts.

- Overcoming of the photovoltaic plateau for wide band gap solar cells with high bromine content, without compromising charge extraction, leading to an unprecedented combination of high open circuit voltage and high fill factor.

- Deployment of a new world record by combining non fullerene acceptor organic and high V_{OC} wide gap perovskite solar cells with the indium oxide interconnect into a perovskite - organic tandem solar cell.

In any event, the road for perovskite solar cells has certainly not reached its end by far. Our simulation has shown that realistic efficiency prospects for perovskite - organic tandems beyond 30 % could be achievable, if proper subcells can be developed and implemented into a tandem structure. This could enable a transition towards a wide gap perovskite material with somewhat lowered band gap in order to better exploit the stability advantage provided by the organic subcell. Also the origin and systematics of non fullerene acceptor based organic solar cells' stability still remains to be clarified. Knowledge of the underlying physical / chemical processes could enable the community to distinctively tailor low gap organic acceptor molecules optimized for tandem applications. Further the mechanism that enabled mitigation of detrimental halide segregation needs to be unravelled, in order to achieve a perovskite wide gap partner cell that can keep up with organic solar cell stability. Still this just rolls out a tiny fraction of promising routes for perovskite solar technology on the path to revolutionize the solar cell market and contribute to certainly one of the greatest challenges in the coming century - to cover our energy demand by renewable energy sources and eventually stop climate change.

10 Publications and Conference Contributions

Publications in Peer Reviewed Scientific Journals

1. **K. O. Brinkmann**, J. Zhao, N. Pourdavoud, T. Becker, T. Hu, S. Olthof, K. Meerholz, L. Hoffmann, T. Gahlmann, R. Heiderhoff, M. Oszajca, N. Luechinger, D. Rogalla, Y. Chen, B. Cheng and T. Riedl: "Suppressed decomposition of organo-metal halide perovskites by impermeable electron extraction layers in inverted solar cells" Nature Communications 7, 13938 (2017)

2. T. Hu, T. Becker, N. Pourdavoud, J. Zhao, **K. O. Brinkmann**, R. Heiderhoff, T. Gahlmann, Z. Huang, S. Olthof, K. Meerholz, D. Többens, B. Cheng, Y. Chen, and T. Riedl: "Indium-Free Perovskite Solar Cells Enabled by Impermeable Tin-Oxide Electron Extraction Layers" Adv. Mater. 29, 1606656 (2017).

3. J. Zhao, **K. O. Brinkmann**, T. Hu, N. Pourdavoud, T. Becker, T. Gahlmann, R. Heiderhoff, A. Polywka, P. Görrn, Y. Chen, B. Cheng and T. Riedl: "Self-Encapsulating Thermostable and Air-Resilent Semitransparent Perovskite Solar Cells" Adv. Energy Mater. 7, 1602599 (2017)

4. L. Hoffmann, D. Theirich, D. Schlamm, T. Hasselmann, S. Pack, **K. O. Brinkmann**, D. Rogalla, S. Peters, A. Räupke, H. Gargouri, and T. Riedl: "Atmospheric pressure plasma enhanced spatial ALD of SnO_x as conductive gas diffusion barrier" J. Vac. Sci. & Technol. A 36, 1, 01A112 (2018)

5. N. Pourdavoud, A. Mayer, M. Buchmüller, **K. O. Brinkmann**, T. Häger, T. Hu, R. Heiderhoff, I. Shutsko, P. Görrn, Y. Chen, H.-C. Scheer, and T. Riedl: "Distributed Feedback Lasers Based on $MAPbBr_3$" Adv. Mater. Technol. 3, 1700253 (2018)

6. L. Hoffmann & **K. O. Brinkmann** (contributed equally), J. Malerczyk, D. Rogalla, T. Becker, D. Theirich, I. Shutsko, P. Görrn, and T. Riedl: "Spatial Atmospheric Pressure Atomic Layer Deposition of Tin Oxide as Impermeable Electron Extraction Layer for Perovskite Solar Cells with Enhanced Thermal Stability" ACS Applied Mater. & Interfaces 10, 6, 6006-6013 (2018)

7. V. S. Mothika, A. Räupke, **K. O. Brinkmann**,T. Riedl, G. Brunklaus and U. Scherf: "Nanometer-Thick Conjugated Microporous Polymer Films for Selective and Sensitive Vapor-Phase TNT Detection" ACS Applied Nano Materials 1, 11, 6483-6492 (2018)

8. **K. O. Brinkmann**, J. He, F. Schubert, J. Malerczyk, C. Kreusel, F. van gen Hassend, S. Weber, J. Song, J. Qu, and T. Riedl: "Extremely robust gas quenching deposition of halide perovskites on top of hydrophobic hole transport materials for inverted (p-i-n) solar cells by targeting the precursor wetting issue" ACS Applied Mater. & Interfaces 11, 40172 (2019).

9. **K. O. Brinkmann**, T. Gahlmann, and T. Riedl: "Atomic Layer Deposition of Functional Layers in Planar Perovskite Solar Cells" Solar RRL 4, 1900332 (2020).

10. T. Gahlmann & **K. O. Brinkmann** (contributed equally), T. Becker, C. Tückmantel, C. Kreusel, F. van gen Hassend, S. Weber, and T. Riedl: "Impermeable charge transport layers enable aqueous processing on top of perovskite solar cells" Adv. Energy Mater. 1903897 (2020).

11. F. Peña-Camargo, P. Caprioglio, F. Zu, E. Gutierrez-Partida, C. M. Wolff, **K. O. Brinkmann**, S. Albrecht, T. Riedl, N. Koch, D. Neher, and M. Stolterfoht: "Halide segregation versus interfacial recombination in bromide-rich wide-gap perovskite solar cells" ACS Energy Lett. 5, 2728 (2020).

12. H. A. Schwartz„ H. Laurenzen, A. Marzouk, M. Runkel, **K. O. Brinkmann**, D. Rogalla, T. Riedl, S. Ashhab, and S. Olthof "Band gap tuning in all-inorganic $CsPb_xSn_{1-x}Br_3$ perovskites" ACS Applied Mater. & Interfaces 13, 4203 (2021).

13. E. Gutierrez-Partida, H. Hempel, S. Caicedo-Davila, M. Raoufi, F. Pena-Camargo, M. Grischek, R. Gunder, J. Diekmann, P. Caprioglio, **K. O. Brinkmann**, H. Kobler, S. Albrecht, T. Riedl, A. Abate, D. Abou-Ras, T. Unold, D. Neher, and M. Stolterfoht: "Large-Grain Double Cation Perovskites with 18 µs Lifetime and High Luminescence Yield for Efficient Inverted Perovskite Solar Cells" ACS Energy Lett. 6, 1045 (2021).

14. A. Mayer, N. Pourdavoud, Z. Doukkali, **K. O. Brinkmann**, J. Rond, J. Staabs, A.-C. Swertz, F. van gen Hassend, P. Görrn, T. Riedl, and H.-C. Scheer: "Upgrading of methylammonium lead halide perovskite layers by thermal imprint" Appl. Phys. A 127, 237 (2021).

15. **K. O. Brinkmann**, T. Becker, F. Zimmermann, C. Kreusel, T. Gahlmann, T. Haeger and T. Riedl: "The Optical Origin of Near-Unity External Quantum Efficiencies in Perovskite Solar Cells" Solar RRL 5, 2100371 (2021).

16. **K. O. Brinkmann**, T. Becker, F. Zimmermann, T. Gahlmann, M. Theisen, T. Haeger, S. Olthof, C. Kreusel, M. Günster, T. Maschwitz, F. Göbelsmann, C. Koch, D. Hertel, P. Caprioglio, L. Perdigon, A. Al-Ashouri, L. Merten, A. Hinderhofer, L. Gomell, S. Zhang, F. Schreiber, S. Albrecht, K. Meerholz, D. Neher, M. Stolterfoht, and T. Riedl: "Perovskite - organic tandem solar cells with indium oxide interconnect" Nature 604, 280 (2022).

Conference Contributions

1. **K. O. Brinkmann**, J. Zhao, N. Pourdavoud, T. Becker, T. Hu, S. Olthof, K. Meerholz, L. Hoffmann, T. Gahlmann, R. Heiderhoff, M. Oszajca, N. Luechinger, D. Rogalla, Y. Chen, B. Cheng and T. Riedl: “Suppressed decomposition of organo-metal halide perovskites by impermeable electron extraction layers in inverted solar cells” Best Poster awarded at MRS Fall Meeting, Boston (USA) ES3.9.09 (2016).

2. **K. O. Brinkmann**, J. Zhao, T. Hu, N. Pourdavoud, T. Gahlmann, R. Heiderhoff, S. Olthof, K. Meerholz, A. Polywka, B. Cheng, Y Chen, P. Görrn and T. Riedl: "Self-Encapsulating Air-Resilent Semitransparent Perovskite Solar Cells with Superior Thermal Stability Beyond 2000h" MRS Spring Meeting, Phoenix (USA) ES1.2.10 (2017).

3. **K. O. Brinkmann**, J. Zhao, T. Hu, T. Becker, N. Pourdavoud, S. Olthof, K. Meerholz, L. Hoffmann, T. Gahlmann, R. Heiderhoff, M. Oszajca, D. Rogalla, N. A. Lüchinger, Y. Chen, B. Cheng, T. Riedl: "Pushing the lifetime of perovskite solar cell beyond 4500 h by the use of impermeable tin oxide electron extraction layers" SPIE Optics and Photonics, San Diego (USA) 10363-32 (2017).

4. N. Pourdavoud, A. Mayer, S. Wang, T. Hu, J. Zhou, **K. O. Brinkmann**, R. Heiderhoff, A. Marianowich, H.-C. Scheer, T. Riedl: "Photonic nanopatterns in organo-metal halide perovskites by thermal nanoimprint lithography" (invited) SPIE Optics and Photonics, San Diego (USA) 10363-32 (2017).

5. N. Pourdavoud, A. Mayer, S. Wang ,M. Buchmüller, **K. O. Brinkmann**, T. Haeger, T. Hu, R. Heiderhoff, A. Marianovich, I. Shutsko, P. Görrn,Y. Chen, W. Kowalsky, H.-C. Scheer, T. Riedl:"Low-threshold Distributed Feedback Lasers Prepared By Direct Thermal Nanoimprint Of Resonator Gratings Into Organo-metal Halide Perovskites" (Best Student Paper Award) Photonics at SG, Singapour (Singapour) 3-1D-5 (2017).

6. L. Hoffmann, **K. O. Brinkmann**, J. Zhao, T. Hu, D. Schlamm, J. Malerczyk, T. Becker, D. Theirich, S. Olthof, K. Meerholz, H. Gargouri, Y. Chen, B. Cheng, T. Riedl: "ALD-Tin Oxide as Impermeable Electron Extraction Layers for Temperature Stable Roll-Ro-Roll-Compatible Perovskite Solar Cells" 17th Conference on Atomic Layer Deposition, Denver (USA) AA1-TuA-11 (2017).

7. **K. O. Brinkmann**, T. Hu, T. Becker, N. Pourdavoud, J. Zhao, R. Heiderhoff, T. Gahlmann, Z. Huang, S. Olthof, K. Meerholz, D. Többens, B. Cheng, Y. Chen, T. Riedl: "Interface Electronic Structure of ALD-Grown SnOx and $MAPbI_3$ in In-Free Perovskite Solar Cells" ISOS-10 (Malta) ID13 (2017).

8. **K. O. Brinkmann**, L. Hoffmann, J. Malerczyk, T. Becker, D. Theirich, T. Riedl: "Spatial Atomic Layer Deposition of Impermeable Tin Oxide Electron Extraction Layers - Towards Roll-To-Roll manufacturing of Temperature Stable Perovskite Solar Cells" MRS Fall Meeting, Boston (USA) ES001.03.20 (2017).

9. S. Olthof, **K. O. Brinkmann**, T. Hu, K. Meerholz, T. Riedl: "Metal Oxide Layers in Perovskite Solar Cells: a Double-Edged Sword" (invited) nanoGe Fall Meeting, Torremolinos (Spain), S5.6-O3 (2018).

10. L. Hoffmann, **K. O. Brinkmann**, T. Hasselmann, J. Malerczyk, T. Becker, D. Theirich, I. Shutsko, P. Görrn, T. Riedl: "Atmospheric pressure spatial ALD of SnO_x for perovskite solar cells" (invited) E-MRS Fall Meeting, Warsaw (Poland), N.6b.4 (2018).

11. T. Becker, T. Gahlmann, N. Köhler, F. Zimmermann, F. Göbelsmann, **K. O. Brinkmann**, and T. Riedl: "Suppressing the photo-induced degradation of inverted non-fullerene organic solar cells" MRS Fall Meeting, Boston (USA), EP05.03.50 (2018).

12. T. Gahlmann, **K. O. Brinkmann**, C. Tückmantel, T. Becker, J. He, J. Bahr, C. Kreusel, and T. Riedl: "Aqueous processing of Ag-nanowire electrodes on top of semi-transparent perovskite solar cells SPIE Optics and Photonics", San Diego (USA), 110940D (2019).

13. **K. O. Brinkmann**, J. He, F. Schubert, J. Malerczyk, C. Kreusel, F. v.g. Hassend, S. Weber, J. Song, J. Qu, T. Riedl: "Robust gas-quenching deposition of halide perovskites by using NMP as complexing agent to overcome the de-wetting issue" best poster awarded at Nanoge Fall Meeting (Berlin) #PerInt 360 (2019)

14. **K. O. Brinkmann**, T. Gahlmann, J. He, C. Tückmantel, M. Theisen, T. Becker, J. Bahr, C. Kreusel, J. Song, J. Qu, T. Riedl: "Intrinsic ALD Barriers Enable Processing on Top of Perovskite Solar Cells from Environmentally Friendly Solvents Nanoge Fall Meeting" (Berlin) #PerFuDe 2.2.263 (2019)

15. F. Zimmermann, T. Gahlmann, M. Theisen, **K. O. Brinkmann**, C. Kreusel, and T. Riedl: "Indium Oxide Grown by Atomic Layer Deposition as Impermeable Top Electrode in Semi-Transparent Perovskite Solar Cells" MRS Fall Meeting, Boston (USA), on-site, EQ17.02.02 (2021).

16. **K. O. Brinkmann**, T. Becker, F. Zimmermann, C. Kreusel, T. Gahlmann, T. Haeger, and T. Riedl: "Optical Origin of External Quantum Efficiencies near Unity in Perovskite Solar Cells" best poster awarded at the MRS Fall Meeting, Boston (USA), on-site, EN05.09.16 (2021).

17. C. Kreusel, **K. O. Brinkmann**, M. Runkel, M. Theisen, D. Rogalla, S. Olthof, F. van gen Hassend, L. Merten, A. Hinderhofer, F. Schreiber, A. Röttger, and T. Riedl: "Non Corrosive Halide Exchange to Form $CsPb(Br_{1-x}Cl_x)_3$ from $CsPbBr_3$ for Light Emission and Lasing" MRS Fall Meeting, Boston (USA), on-site, EN05.03.06 (2021).

18. **K. O. Brinkmann**, T. Becker, F. Zimmermann, C. Kreusel, T. Gahlmann, M. Theisen, T. Haeger, S. Olthof, M. Günster, T. Maschwitz, F. Göbelsmann, C. Koch, D. Hertel, P. Caprioglio, L. Perdigon, L. Merten, A. Hinderhofer, A. Al-Ashouri, L. Gomell, S. Albrecht, F. Schreiber, K. Meerholz, D. Neher, M. Stolterfoht, and T. Riedl: "No Need for Tin—Perovskite/Organic Tandem Solar Cells Approaching 24%" MRS Fall Meeting, Boston (USA), on-site, EN05.03.01 (2021).

19. **K. O. Brinkmann**, R. Heiderhoff, T. Riedl: "Perowskit-Multi-Junction-Solarzellen – Photovoltaik der nächsten Generation" Ret.Con (germany), online (2022)

20. **K. O. Brinkmann**, T. Riedl: "Perovskite solar cells as power source for microelectronic devices" (invited), IC-MPPE Leoben (austria), on-site (2022).

21. **K. O. Brinkmann**, T. Becker, F. Zimmermann, C. Kreusel, T. Gahlmann, M. Theisen, T. Haeger, S. Olthof, C. Tückmantel, M. Günster, T. Maschwitz, F. Göbelsmann, C. Koch, D. Hertel, P. Caprioglio, F. Peña Camargo, L. Perdigón-Toro, A. Al-Ashouri, L. Merten, A. Hinderhofer, L. Gomell, S. Zhang, F. Schreiber, S. Albrecht, K. Meerholz, D. Neher, M. Stolterfoht and T. Riedl: "Perovskite/Organic Tandem Solar Cells reaching 24% - Circumventing Tin Perovskites" , Tandem PV (Freiburg), oral, on-site (2022).

11 Appendix

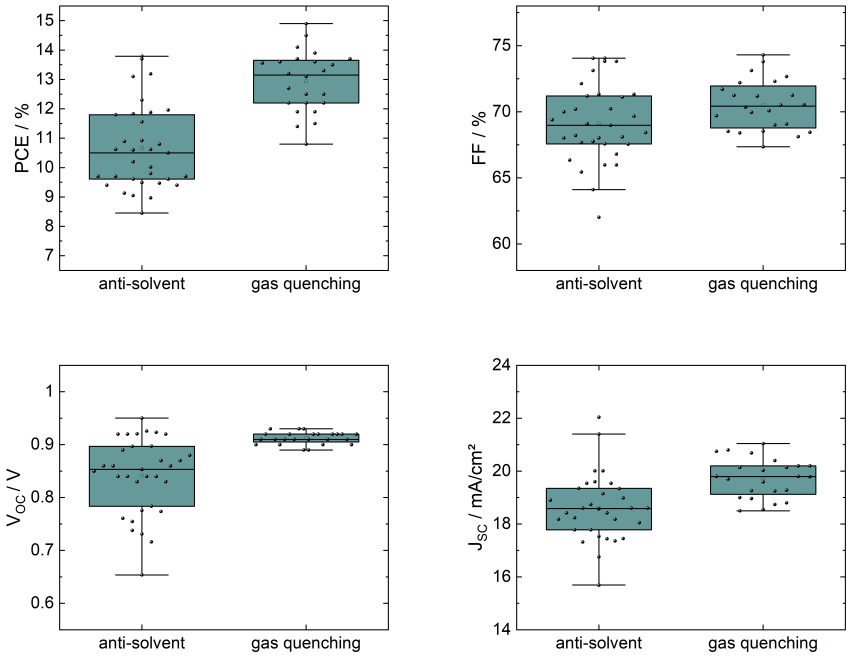

Figure 11.1: *Full set of device parameters for anti-solvent and gas quenching shown in Figure 3.3 on top of PEDOT:PSS hole extraction layer. Box plots: median line with upper and lower box ranges denoting the 25% and 75% margins. The bars denote the outermost data points that are still inside another 1.5 interquatile range.*

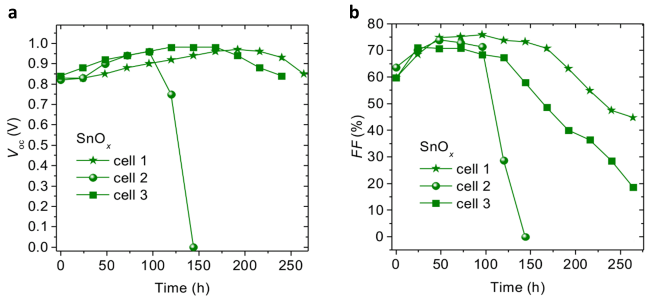

Figure 11.2: Stability of devices based on only SnO_x as EEL. *Characteristics of perovskite cells with 20 nm of ALD SnO_x as EEL upon storage in ambient air (at 22°C, 60 % rH).* ***a,*** *V_{OC} vs. time and* ***b,*** *FF vs. time. Adapted from [192].*

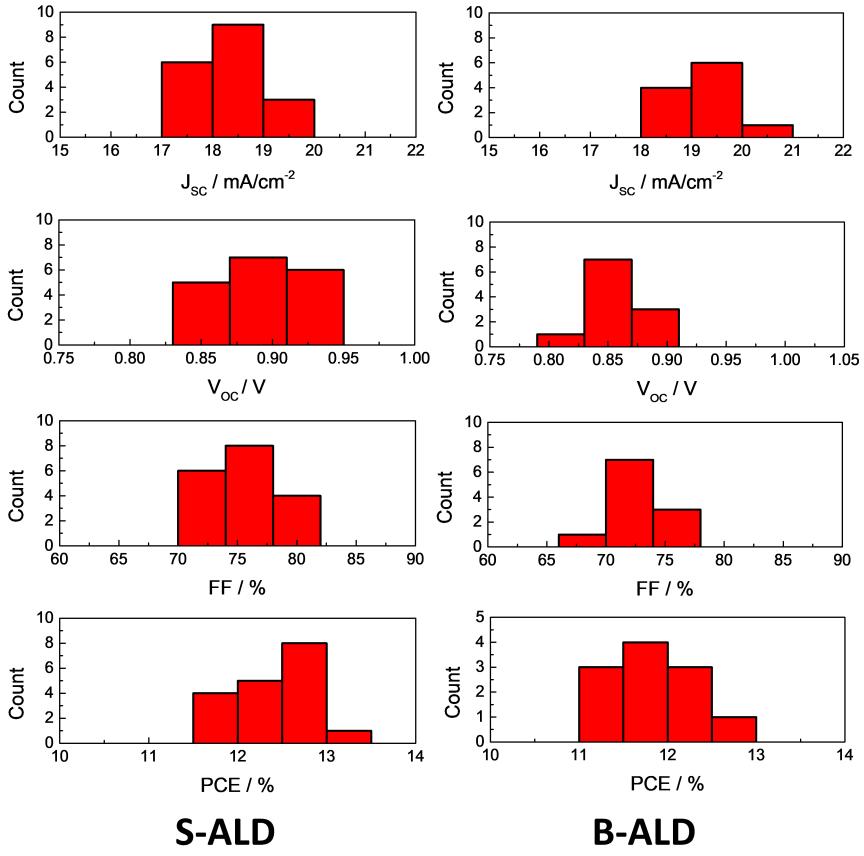

Figure 11.3: *Statistical solar cell characteristics comparing PSCs built with S-ALD (15 devices) and B-ALD (11 devices). Current density values have been derived from EQE measurements. Adapted with permission from [226]. Copyright 2018 American Chemical Society.*

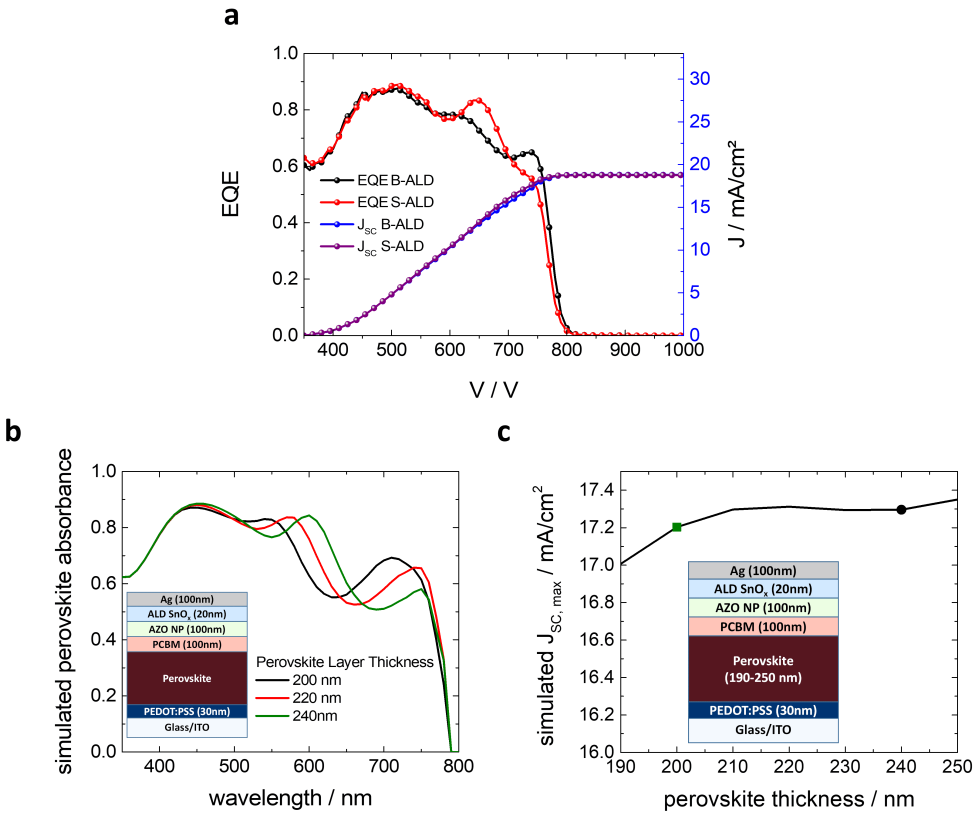

Figure 11.4: EQE of solar cells employing SnO_x grown by batch and spatial ALD. a, *EQE spectra and integrated photocurrent of perovskite solar cells based on S- or B-ALD.* ***b,*** *Simulated absorbance of the perovskite layer in the shown PSC stack for different layer thicknesses and* ***c,*** *resulting simulated photocurrent of the PSC as a function of perovskite layer thickness.* ***b,*** *and* ***c,*** *offer a plausible explaination for the variation in the shape of the perovskite EQE, that can be attributed to small variations of the perovskite layer thickness. Moreover the simulation displays, how thickness variations, that fall within the process fluctuation, only result in minor changes in the J_{SC}. Adapted from [239].*

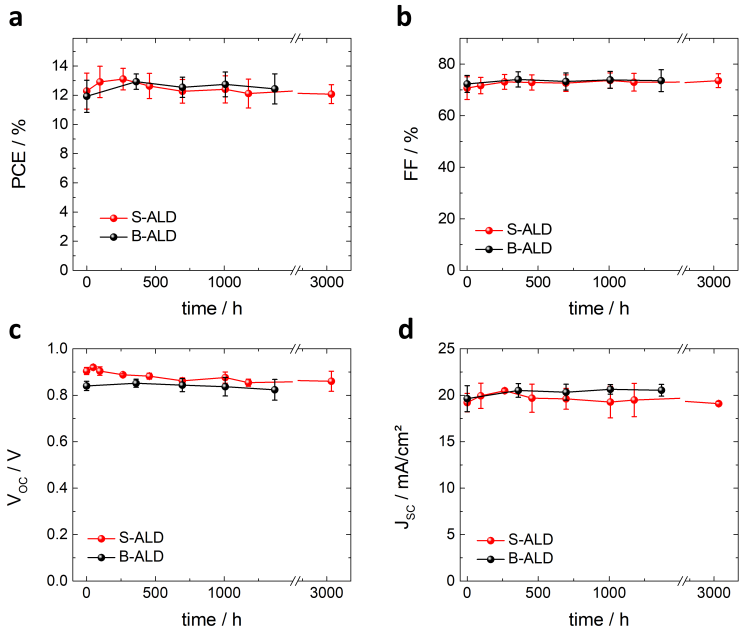

Figure 11.5: *Solar cell characteristics* ***a,*** *PCE,* ***b,*** *FF,* ***c,*** *open circuit voltage and* ***d,*** *short circuit current) vs. time of storage at elevated temperature (60 °C / N_2 atmosphere, 5 devices). Adapted with permission from [226]. Copyright 2018 American Chemical Society.*

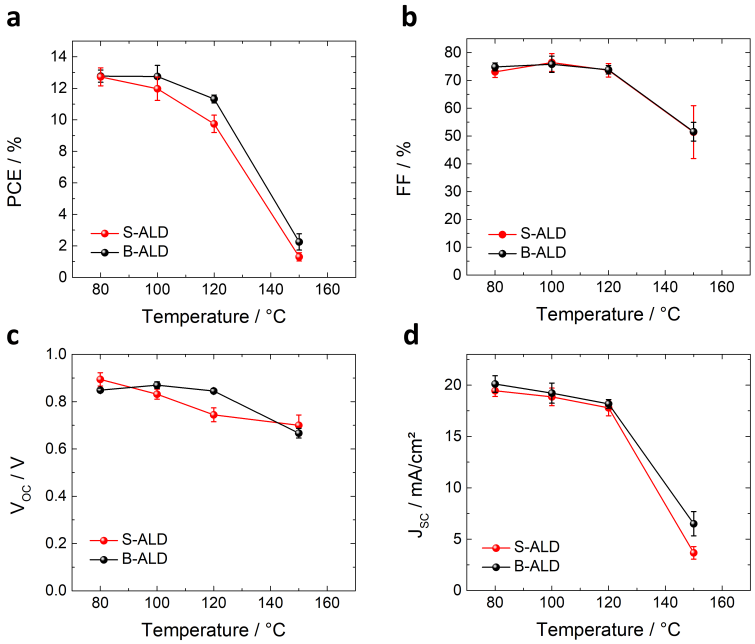

Figure 11.6: *Solar cell characteristics for PSCs with SnO_x from spatial and batch-ALD at different deposition temperatures. Adapted with permission from [226]. Copyright 2018 American Chemical Society.*

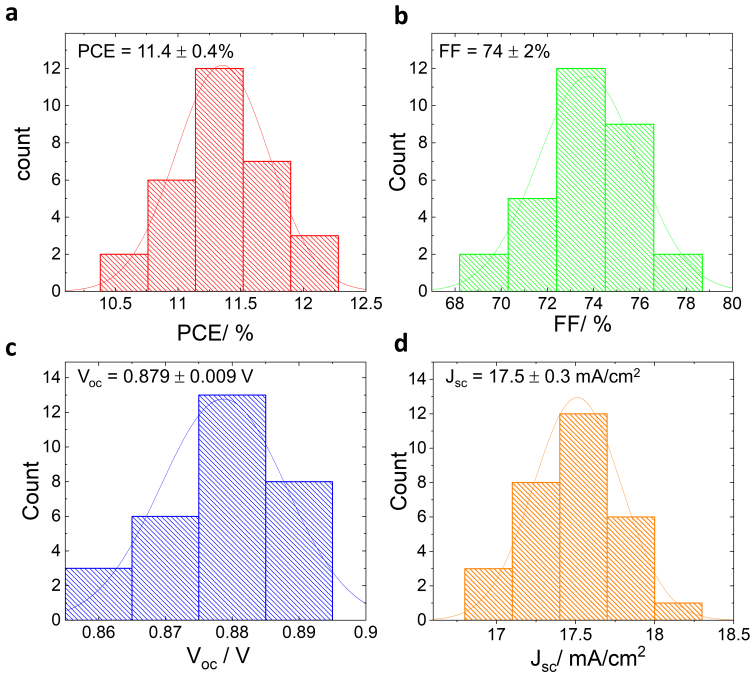

Figure 11.7: *Statistical data of 30 semi-transarent devices with ultra-thin Ag electrode.* ***a,*** *PCE,* ***b,*** *FF,* ***c,*** V_{OC}*, and* ***d,*** J_{SC}*. Adapted with permission from [238]. Copyright 2017 WILEY-VCH.*

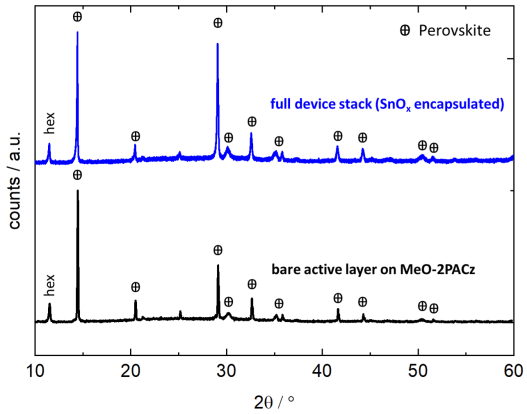

Figure 11.8: *Direct comparison of X-ray diffractograms of a bare perovskite layer with that of a full device stack, which contains an ALD grown tin oxide permeation barrier that prevents the ingress of ambient air. The reflection corresponding to the hexagonal (delta) phase is found in both samples, which confirms that the presence of hexagonal phase is not a result of degradation due to air exposure. Adapted with permission from [265]. Copyright 2022 Springer Nature.*

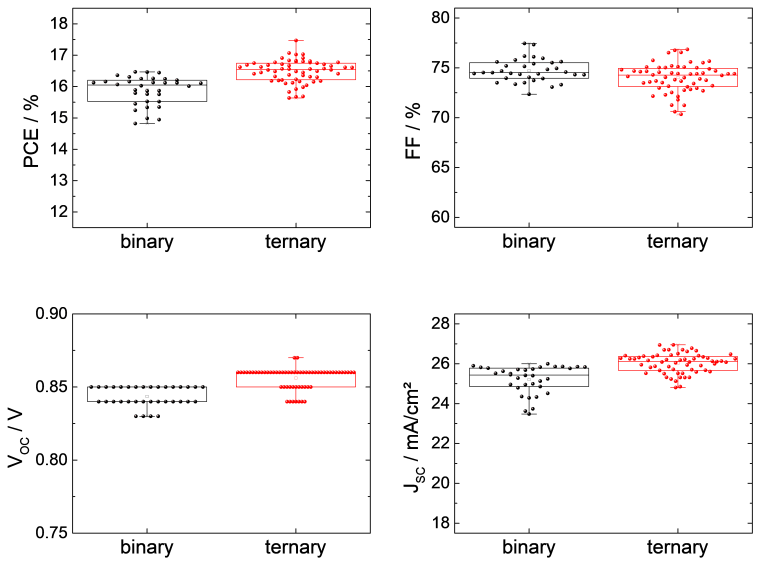

Figure 11.9: *Statistics of 34 binary (PM6 : Y6) and 60 ternary (PM6 : Y6 : $PC_{61}BM$) organic solar cells. Median line with upper and lower box ranges denoting the 25 % and 75 % margins. The bars denote the outermost data points that are still inside another 1.5 interquartile range. Adapted with permission from [265]. Copyright 2022 Springer Nature.*

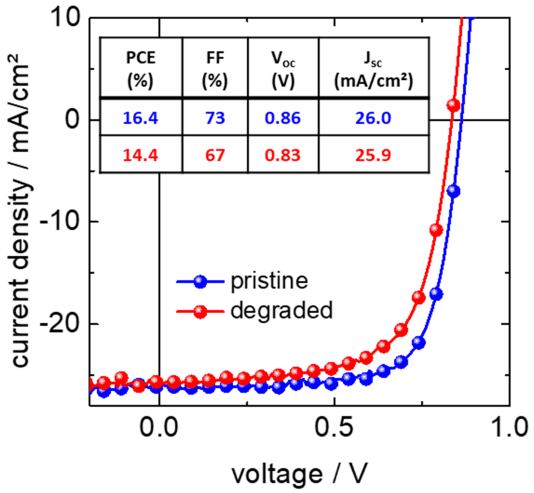

Figure 11.10: *J-V of ternary OSCs before (pristine) and after 90 h continuous illumination (degraded) with $LED_V IS$ + $LED_N IR$. Adapted with permission from [265]. Copyright 2022 Springer Nature.*

Bibliography

1. Pörtner, H.-O. *et al. Climate Change 2022: Impacts, Adaptation, and Vulnerability.* Report (2022).
2. Fraunhofer-ISE. *Photovoltaics Report* Report (updated February 24th 2022).
3. Roy, P., Kumar Sinha, N., Tiwari, S. & Khare, A. A review on perovskite solar cells: Evolution of architecture, fabrication techniques, commercialization issues and status. *Solar Energy* **198,** 665–688 (2020).
4. Rong, Y. *et al.* Challenges for commercializing perovskite solar cells. *Science* **361,** eaat8235 (2018).
5. Cheng, Y. & Ding, L. Pushing commercialization of perovskite solar cells by improving their intrinsic stability. *Energy and Environmental Science* **14,** 3233–3255 (2021).
6. Fukuda, K., Yu, K. & Someya, T. The Future of Flexible Organic Solar Cells. *Advanced Energy Materials* **10,** 2000765 (2020).
7. Riede, M., Spoltore, D. & Leo, K. Organic Solar Cells - The Path to Commercial Success. *Advanced Energy Materials* **11,** 2002653 (2021).
8. Cheng, Z. & Lin, J. Layered organic–inorganic hybrid perovskites: structure, optical properties, film preparation, patterning and templating engineering. *CrystEngComm* **12** (2010).
9. Dimos, D. & Mueller, C. H. Perovskite Thin Films for High-Frequency Capacitor Applications. *Annual Review of Materials Science* **28,** 397–419 (1998).
10. Seiyama, T., Yamazoe, N. & Eguchi, K. Characterization and activity of some mixed metal oxide catalysts. *Industrial & Engineering Chemistry Product Research and Development* **24,** 19–27 (1985).
11. Kojima, A., Teshima, K., Shirai, Y. & Miyasaka, T. Organometal Halide Perovskites as Visible-Light Sensitizers for Photovoltaic Cells. *Journal of the American Chemical Society* **131,** 6050–6051 (2009).

12. *Web of Science (accessed 08/2022)* Web Page.

13. Seok, S. I., Gratzel, M. & Park, N. G. Methodologies toward Highly Efficient Perovskite Solar Cells. *Small* **14,** e1704177 (2018).

14. Tao, L. *et al.* Stability of mixed-halide wide bandgap perovskite solar cells: Strategies and progress. *Journal of Energy Chemistry* **61,** 395–415 (2021).

15. Brandt, R. E. *et al.* Searching for "Defect-Tolerant" Photovoltaic Materials: Combined Theoretical and Experimental Screening. *Chemistry of Materials* **29,** 4667–4674 (2017).

16. Kim, G.-W. & Petrozza, A. Defect Tolerance and Intolerance in Metal-Halide Perovskites. *Advanced Energy Materials* **10,** 2001959 (2020).

17. Tao, S. *et al.* Absolute energy level positions in tin- and lead-based halide perovskites. *Nature Communications* **10,** 2560 (2019).

18. Yin, W.-J., Shi, T. & Yan, Y. Unusual defect physics in $CH_3NH_3PbI_3$ perovskite solar cell absorber. *Applied Physics Letters* **104,** 063903 (2014).

19. Umari, P., Mosconi, E. & De Angelis, F. Relativistic GW calculations on $CH_3NH_3PbI_3$ and $CH_3NH_3SnI_3$ Perovskites for Solar Cell Applications. *Scientific Reports* **4,** 4467 (2015).

20. Musiienko, A. *et al.* Deciphering the effect of traps on electronic charge transport properties of methylammonium lead tribromide perovskite. *Science Advances* **6,** eabb6393 (2020).

21. Musiienko, A. *et al.* Defects in Hybrid Perovskites: The Secret of Efficient Charge Transport. *Advanced Functional Materials* **31,** 2104467 (2021).

22. Park, N.-G. Perovskite solar cells: an emerging photovoltaic technology. *Materials Today* **18,** 65–72 (2015).

23. Meloni, S., Palermo, G., Ashari-Astani, N., Grätzel, M. & Rothlisberger, U. Valence and conduction band tuning in halide perovskites for solar cell applications. *Journal of Materials Chemistry A* **4,** 15997–16002 (2016).

24. Prasanna, R. *et al.* Band Gap Tuning via Lattice Contraction and Octahedral Tilting in Perovskite Materials for Photovoltaics. *Journal of the American Chemical Society* **139,** 11117–11124 (2017).

25. Li, Z. *et al.* Stabilizing Perovskite Structures by Tuning Tolerance Factor: Formation of Formamidinium and Cesium Lead Iodide Solid-State Alloys. *Chemistry of Materials* **28,** 284–292 (2015).

26. Goldschmidt, V. M. Die Gesetze der Krystallochemie. *Die Naturwissenschaften* **14,** 477–485 (1926).

27. Bae, S. R., Heo, D. Y. & Kim, S. Y. Recent progress of perovskite devices fabricated using thermal evaporation method: Perspective and outlook. *Materials Today Advances* **14,** 100232 (2022).

28. Ávila, J., Momblona, C., Boix, P. P., Sessolo, M. & Bolink, H. J. Vapor-Deposited Perovskites: The Route to High-Performance Solar Cell Production? *Joule* **1,** 431–442 (2017).

29. Jeon, N. J. *et al.* Solvent engineering for high-performance inorganic-organic hybrid perovskite solar cells. *Nature Mater* **13,** 897–903 (2014).

30. Zeng, L. *et al.* Controlling the crystallization dynamics of photovoltaic perovskite layers on larger-area coatings. *Energy and Environmental Science* **13,** 4666–4690 (2020).

31. Dubey, A. *et al.* A strategic review on processing routes towards highly efficient perovskite solar cells. *Journal of Materials Chemistry A* **6,** 2406–2431 (2018).

32. Hao, F. *et al.* Solvent-Mediated Crystallization of $CH_3NH_3SnI_3$ Films for Heterojunction Depleted Perovskite Solar Cells. *Journal of the American Chemical Society* **137,** 11445–11452 (2015).

33. Radicchi, E., Mosconi, E., Elisei, F., Nunzi, F. & De Angelis, F. Understanding the Solution Chemistry of Lead Halide Perovskites Precursors. *ACS Applied Energy Materials* **2,** 3400–3409 (2019).

34. Xi, J., Yuan, J., Yan, X., Binks, D. & Tian, J. Gradient Annealing of Halide Perovskite Films for Improved Performance of Solar Cells. *ACS Applied Energy Materials* **3,** 8130–8134 (2020).

35. Hao, L. *et al.* A temperature gradient-induced directional growth of a perovskite film. *Journal of Materials Chemistry A* **8,** 17019–17024 (2020).

36. Conings, B. *et al.* A Universal Deposition Protocol for Planar Heterojunction Solar Cells with High Efficiency Based on Hybrid Lead Halide Perovskite Families. *Adv Mater* **28,** 10701–10709 (2016).

37. Babayigit, A., D'Haen, J., Boyen, H.-G. & Conings, B. Gas Quenching for Perovskite Thin Film Deposition. *Joule* **2,** 1205–1209 (2018).

38. Li, X. *et al.* A vacuum flash assisted solution process for high-efficiency large-area perovskite solar cells. *Science* **353,** 58–62 (2016).

39. Sánchez, S. & Hagfeldt, A. in *Perovskite Solar Cells* 33–89 (2021). ISBN: 9783527825790.

40. Sanchez, S., Hua, X., Phung, N., Steiner, U. & Abate, A. Flash Infrared Annealing for Antisolvent-Free Highly Efficient Perovskite Solar Cells. *Advanced Energy Materials* **8,** 1702915 (2018).

41. Radicchi, E., Mosconi, E., Elisei, F., Nunzi, F. & De Angelis, F. Understanding the Solution Chemistry of Lead Halide Perovskites Precursors. *ACS Applied Energy Materials* **2,** 3400–3409 (2019).

42. Jung, M., Ji, S. G., Kim, G. & Seok, S. I. Perovskite precursor solution chemistry: from fundamentals to photovoltaic applications. *Chemical Society Reviews* **48,** 2011–2038 (2019).

43. Valencia, A. M., Shargaieva, O., Schier, R., Unger, E. & Cocchi, C. Optical Fingerprints of Polynuclear Complexes in Lead Halide Perovskite Precursor Solutions. *The Journal of Physical Chemistry Letters* **12,** 2299–2305 (2021).

44. Flatken, M. A. *et al.* Role of the Alkali Metal Cation in the Early Stages of Crystallization of Halide Perovskites. *Chemistry of Materials* **34,** 1121–1131 (2022).

45. Radicchi, E., Mosconi, E., Elisei, F., Nunzi, F. & De Angelis, F. Understanding the Solution Chemistry of Lead Halide Perovskites Precursors. *ACS Applied Energy Materials* **2,** 3400–3409 (2019).

46. Flatken, M. A. *et al.* Small-angle scattering to reveal the colloidal nature of halide perovskite precursor solutions. *Journal of Materials Chemistry A* **9,** 13477–13482 (2021).

47. Hamill, J. C. *et al.* Sulfur-Donor Solvents Strongly Coordinate Pb^{2+} in Hybrid Organic–Inorganic Perovskite Precursor Solutions. *The Journal of Physical Chemistry C* **124,** 14496–14502 (2020).

48. Hamill, J. C., Sorli, J. C., Pelczer, I., Schwartz, J. & Loo, Y.-L. Acid-Catalyzed Reactions Activate DMSO as a Reagent in Perovskite Precursor Inks. *Chemistry of Materials* **31,** 2114–2120 (2019).

49. Chao, L. *et al.* Solvent Engineering of the Precursor Solution toward Large-Area Production of Perovskite Solar Cells. *Advanced Materials* **33,** 2005410 (2021).

50. Zhou, Y. *et al.* Manipulating Crystallization of Organolead Mixed-Halide Thin Films in Antisolvent Baths for Wide-Bandgap Perovskite Solar Cells. *ACS Applied Materials & Interfaces* **8,** 2232–2237 (2016).

51. Ahlawat, P. *et al.* Atomistic Mechanism of the Nucleation of Methylammonium Lead Iodide Perovskite from Solution. *Chemistry of Materials* **32,** 529–536 (2020).

52. Bi, C. *et al.* Non-wetting surface-driven high-aspect-ratio crystalline grain growth for efficient hybrid perovskite solar cells. *Nature Commun* **6,** 7747 (2015).

53. Wafee, S., Liu, B. H. & Leu, C.-C. Lewis bases: promising additives for enhanced performance of perovskite solar cells. *Materials Today Energy* **22,** 100847 (2021).

54. Xu, C. *et al.* Manipulation of Perovskite Crystallization Kinetics via Lewis Base Additives. *Advanced Functional Materials* **31,** 2009425 (2021).

55. Lee, J.-W. *et al.* A Bifunctional Lewis Base Additive for Microscopic Homogeneity in Perovskite Solar Cells. *Chem* **3,** 290–302 (2017).

56. Christians, J. A., Miranda Herrera, P. A. & Kamat, P. V. Transformation of the Excited State and Photovoltaic Efficiency of $CH_3NH_3PbI_3$ Perovskite upon Controlled Exposure to Humidified Air. *Journal of the American Chemical Society* **137,** 1530–1538 (2015).

57. Yang, J., Siempelkamp, B. D., Liu, D. & Kelly, T. L. Investigation of $CH_3NH_3PbI_3$ Degradation Rates and Mechanisms in Controlled Humidity Environments Using in Situ Techniques. *ACS Nano* **9,** 1955–1963 (2015).

58. Yang, J. *et al.* Oxygen- and Water-Induced Energetics Degradation in Organometal Halide Perovskites. *ACS Appl Mater Interfaces* **10,** 16225–16230 (2018).

59. Wei, W. & Hu, Y. H. Catalytic role of H_2O in degradation of inorganic-organic perovskite ($CH_3NH_3PbI_3$) in air. *International Journal of Energy Research* **41,** 1063–1069 (2017).

60. Kim, N. K. *et al.* Investigation of Thermally Induced Degradation in $CH_3NH_3PbI_3$ Perovskite Solar Cells using In-situ Synchrotron Radiation Analysis. *Scientific Reports* **7,** 4645 (2017).

61. Boyd, C. C., Cheacharoen, R., Leijtens, T. & Mcgehee, M. D. Understanding Degradation Mechanisms and Improving Stability of Perovskite Photovoltaics. *Chemical Reviews* **119,** 3418–3451 (2019).

62. Frost, J. M. *et al.* Atomistic Origins of High-Performance in Hybrid Halide Perovskite Solar Cells. *Nano Letters* **14,** 2584–2590 (2014).

63. Wang, D., Wright, M., Elumalai, N. K. & Uddin, A. Stability of perovskite solar cells. *Solar Energy Materials and Solar Cells* **147,** 255–275 (2016).

64. Dipta, S. S. & Uddin, A. Stability Issues of Perovskite Solar Cells: A Critical Review. *Energy Technology* **9,** 2100560 (2021).

65. Kato, Y. *et al.* Silver Iodide Formation in Methyl Ammonium Lead Iodide Perovskite Solar Cells with Silver Top Electrodes. *Advanced Materials Interfaces* **2** (2015).

66. Cheacharoen, R. *et al.* Design and understanding of encapsulated perovskite solar cells to withstand temperature cycling. *Energy and Environmental Science* **11,** 144–150 (2018).

67. Juarez-Perez, E. J., Hawash, Z., Raga, S. R., Ono, L. K. & Qi, Y. Thermal degradation of $CH_3NH_3PbI_3$ perovskite into NH_3 and CH_3I gases observed by coupled thermogravimetry–mass spectrometry analysis. *Energy and Environmental Science* **9,** 3406–3410 (2016).

68. Conings, B. *et al.* Intrinsic Thermal Instability of Methylammonium Lead Trihalide Perovskite. *Advanced Energy Materials* **5** (2015).

69. Wei, J. *et al.* Mechanisms and Suppression of Photoinduced Degradation in Perovskite Solar Cells. *Advanced Energy Materials* **11,** 2002326 (2021).

70. Zu, F.-S. *et al.* Impact of White Light Illumination on the Electronic and Chemical Structures of Mixed Halide and Single Crystal Perovskites. *Advanced Optical Materials* **5,** 1700139 (2017).

71. Hong, Q.-M., Xu, R.-P., Jin, T.-Y., Tang, J.-X. & Li, Y.-Q. Unraveling the light-induced degradation mechanism of $CH_3NH_3PbI_3$ perovskite films. *Organic Electronics* **67,** 19–25 (2019).

72. Wang, S., Jiang, Y., Juarez-Perez, E. J., Ono, L. K. & Qi, Y. Accelerated degradation of methylammonium lead iodide perovskites induced by exposure to iodine vapour. *Nature Energy* **2,** 16195 (2016).

73. Hoke, E. T. *et al.* Reversible photo-induced trap formation in mixed-halide hybrid perovskites for photovoltaics. *Chemical Science* **6,** 613–617 (2015).

74. Knight, A. J. & Herz, L. M. Preventing phase segregation in mixed-halide perovskites: a perspective. *Energy and Environmental Science* **13,** 2024–2046 (2020).

75. Datta, K. *et al.* Effect of Light-Induced Halide Segregation on the Performance of Mixed-Halide Perovskite Solar Cells. *ACS Applied Energy Materials* **4,** 6650–6658 (2021).

76. Li, Z. *et al.* Beyond the Phase Segregation: Probing the Irreversible Phase Reconstruction of Mixed-Halide Perovskites. *Advanced Science* **9,** 2103948 (2022).

77. Baranowski, M. & Plochocka, P. Excitons in Metal-Halide Perovskites. *Advanced Energy Materials* **10,** 1903659 (2020).

78. Wagemann, H.-G. & Eschrich, H. in *Photovoltaik* 43–62 (Vieweg+Teubner, 2010).

79. Wagemann, H.-G. & Eschrich, H. in *Photovoltaik* 167–182 (Vieweg+Teubner, 2010).

80. Peña-Camargo, F. *et al.* Revealing the doping density in perovskite solar cells and its impact on device performance. *Applied Physics Reviews* **9,** 021409 (2022).

81. Sandberg, O. J. *et al.* On the Question of the Need for a Built-In Potential in Perovskite Solar Cells. *Advanced Materials Interfaces* **7,** 2000041 (2020).

82. Nelson, J. *The Physics of Solar Cells* ISBN: 9781848168237 (Imperial College Press, 2003).

83. Würfel, P. & Würfel, U. *Physics of Solar Cells: From Basic Principles to Advanced Concepts* (Wiley, 2016).

84. Shockley, W. & Queisser, H. J. Detailed Balance Limit of Efficiency of p-n Junction Solar Cells. *Journal of Applied Physics* **32,** 510–519 (1961).

85. Caprioglio, P. *et al.* On the Relation between the Open-Circuit Voltage and Quasi-Fermi Level Splitting in Efficient Perovskite Solar Cells. *Advanced Energy Materials* **9** (2019).

86. Tress, W. *et al.* Understanding the rate-dependent J–V hysteresis, slow time component, and aging in $CH_3NH_3PbI_3$ perovskite solar cells: the role of a compensated electric field. *Energy and Environmental Science* **8,** 995–1004 (2015).

87. Futscher, M. H. *et al.* Quantification of ion migration in $CH_3NH_3PbI_3$ perovskite solar cells by transient capacitance measurements. *Materials Horizons* **6,** 1497–1503 (2019).

88. Shao, Y. *et al.* Grain boundary dominated ion migration in polycrystalline organic–inorganic halide perovskite films. *Energy and Environmental Science* **9,** 1752–1759 (2016).

89. Miyano, K., Yanagida, M., Tripathi, N. & Shirai, Y. Hysteresis, Stability, and Ion Migration in Lead Halide Perovskite Photovoltaics. *Journal of Physical Chemical Letters* **7,** 2240–5 (2016).

90. Park, N.-G. Organometal Perovskite Light Absorbers Toward a 20% Efficiency Low-Cost Solid-State Mesoscopic Solar Cell. *The Journal of Physical Chemistry Letters* **4,** 2423–2429 (2013).

91. Thiesbrummel, J. *et al.* Universal Current Losses in Perovskite Solar Cells Due to Mobile Ions. *Advanced Energy Materials* **11,** 2101447 (2021).

92. Chen, B., Yang, M., Priya, S. & Zhu, K. Origin of JV Hysteresis in Perovskite Solar Cells. *The Journal of Physical Chemistry Letters* **7,** 905–917 (2016).

93. Jacobs, D. A. *et al.* Hysteresis phenomena in perovskite solar cells: the many and varied effects of ionic accumulation. *Physical Chemistry Chemical Physics* **19,** 3094–3103 (2017).

94. Xiao, Z. *et al.* Giant switchable photovoltaic effect in organometal trihalide perovskite devices. *Nature Materials* **14,** 193–198 (2015).

95. Hernández-Balaguera, E. *et al.* Unraveling the Key Relationship Between Perovskite Capacitive Memory, Long Timescale Cooperative Relaxation Phenomena, and Anomalous J–V Hysteresis. *Solar RRL* **5,** 2000707 (2021).

96. Wali, Q. *et al.* Fundamentals of Hysteresis in Perovskite Solar Cells: From Structure-Property Relationship to Neoteric Breakthroughs. *The Chemical Record* **22** (2022).

97. Berruet, M. *et al.* Physical Model for the Current–Voltage Hysteresis and Impedance of Halide Perovskite Memristors. *ACS Energy Letters* **7,** 1214–1222 (2022).

98. Wang, Z. *et al.* Efficient ambient-air-stable solar cells with 2D–3D heterostructured butylammonium-caesium-formamidinium lead halide perovskites. *Nature Energy* **2** (2017).

99. Köhler, A. & Bässler, H. in *Electronic Processes in Organic Semiconductors* 1–86 (Wiley-VCH, 2015). ISBN: 9783527685172.

100. Rockett, A. in *The Materials Science of Semiconductors* 395–453 (Springer US, 2008).

101. Pope, M., Swenberg, C. & Swenberg, P. *Electronic Processes in Organic Crystals and Polymers* ISBN: 9780195129632 (Oxford University Press, 1999).

102. Brütting, W. in *Physics of Organic Semiconductors* 1–14 (Wiley-VCH, 2006). ISBN: 9783527606634.

103. Kietzke, T. Recent Advances in Organic Solar Cells. *Advances in OptoElectronics* **2007,** 1–15 (2007).

104. Von Hauff, E., Dyakonov, V. & Parisi, J. Study of field effect mobility in PCBM films and P3HT:PCBM blends. *Solar Energy Materials and Solar Cells* **87,** 149–156 (2005).

105. Mikhnenko, O. V., Blom, P. W. M. & Nguyen, T.-Q. Exciton diffusion in organic semiconductors. *Energy and Environmental Science* **8,** 1867–1888 (2015).

106. Hoppe, H. & Sariciftci, N. S. in *Photoresponsive Polymers II* 1–86 (Springer Berlin Heidelberg, 2007). ISBN: 9783540694540.

107. Zhu, L., Wei, Z. & Yi, Y. Exciton Binding Energies in Organic Photovoltaic Materials: A Theoretical Perspective. *The Journal of Physical Chemistry C* **126,** 14–21 (2022).

108. Benanti, T. L. & Venkataraman, D. Organic Solar Cells: An Overview Focusing on Active Layer Morphology. *Photosynthesis Research* **87,** 73–81 (2006).

109. NREL. *Best Research-Cell Efficiency Chart (accessed 06/22)* Web Page.

110. Armin, A. *et al.* A History and Perspective of Non-Fullerene Electron Acceptors for Organic Solar Cells. *Advanced Energy Materials* **11,** 2003570 (2021).

111. Zhu, L. *et al.* Single-junction organic solar cells with over 19% efficiency enabled by a refined double-fibril network morphology. *Nature Materials* **21,** 656–663. ISSN: 1476-1122 (2022).

112. Li, H.-W. *et al.* On the Study of Exciton Binding Energy with Direct Charge Generation in Photovoltaic Polymers. *Advanced Electronic Materials* **2,** 1600200 (2016).

113. Zhu, Y. *et al.* Exciton Binding Energy of Non-Fullerene Electron Acceptors. *Advanced Energy and Sustainability Research* **3,** 2100184 (2022).

114. Yan, J. *et al.* Identifying structure–absorption relationships and predicting absorption strength of non-fullerene acceptors for organic photovoltaics. *Energy and Environmental Science* **15,** 2958–2973 (2022).

115. Zhu, L. *et al.* Single-junction organic solar cells with over 19% efficiency enabled by a refined double-fibril network morphology. *Nature Materials* **21,** 656–663 (2022).

116. Yu, R. *et al.* Improved Charge Transport and Reduced Nonradiative Energy Loss Enable Over 16% Efficiency in Ternary Polymer Solar Cells. *Advanced Materials* **31,** 1902302 (2019).

117. Gasparini, N. *et al.* Exploiting Ternary Blends for Improved Photostability in High-Efficiency Organic Solar Cells. *ACS Energy Letters* **5,** 1371–1379 (2020).

118. Zhu, Y. *et al.* Rational Strategy to Stabilize an Unstable High-Efficiency Binary Nonfullerene Organic Solar Cells with a Third Component. *Advanced Energy Materials* **9,** 1900376 (2019).

119. Markvart, T. Shockley: Queisser detailed balance limit after 60 years. *Wiley Interdisciplinary Reviews: Energy and Environment,* e430 (2022).

120. Shockley, W. & Queisser, H. J. Detailed Balance Limit of Efficiency of p-n Junction Solar Cells. *Journal of Applied Physics* **32,** 510–519 (1961).

121. Tanimura, H., Kanasaki, J., Tanimura, K., Sjakste, J. & Vast, N. Ultrafast relaxation dynamics of highly excited hot electrons in silicon. *Physical Review B* **100** (2019).

122. Lissau, J. S. & Madsen, M. in *Emerging Strategies to Reduce Transmission and Thermalization Losses in Solar Cells* 1–6 (Springer International Publishing, 2022). ISBN: 9783030703585.

123. Kaiser, W. & Garrett, C. G. B. Two-Photon Excitation in CaF_2Eu^{2+}. *Physical Review Letters* **7,** 229–231 (1961).

124. Tiedje, T., Yablonovitch, E., Cody, G. & Brooks, B. Limiting efficiency of silicon solar cells. *IEEE Transactions on Electron Devices* **31,** 711–716 (1984).

125. Andreani, L. C., Bozzola, A., Kowalczewski, P., Liscidini, M. & Redorici, L. Silicon solar cells: toward the efficiency limits. *Advances in Physics: X* **4,** 1548305 (2019).

126. Green, M. Limits on the open-circuit voltage and efficiency of silicon solar cells imposed by intrinsic Auger processes. *IEEE Transactions on Electron Devices* **31,** 671–678 (1984).

127. Ojo, A. A. & Dharmadasa, I. M. Progress in development of graded bandgap thin film solar cells with electroplated materials. *Journal of Materials Science: Materials in Electronics* **28,** 6359–6365 (2017).

128. Trupke, T., Green, M. A. & Würfel, P. Improving solar cell efficiencies by down-conversion of high-energy photons. *Journal of Applied Physics* **92,** 1668–1674 (2002).

129. Sasaki, Y., Yanai, N. & Kimizuka, N. in *Emerging Strategies to Reduce Transmission and Thermalization Losses in Solar Cells* 29–48 (Springer International Publishing, 2022). ISBN: 9783030703585.

130. Li, H. & Zhang, W. Perovskite Tandem Solar Cells: From Fundamentals to Commercial Deployment. *Chemical Reviews* **120,** 9835–9950 (2020).

131. Vos, A. D. Detailed balance limit of the efficiency of tandem solar cells. *Journal of Physics D: Applied Physics* **13,** 839–846 (1980).

132. Wang, Z., Song, Z., Yan, Y., Liu, S. & Yang, D. Perovskite - a Perfect Top Cell for Tandem Devices to Break the S-Q Limit. *Advanced Science* **6,** 1801704 (2019).

133. Jiang, Y. *et al.* High-Mobility In_2O_3:H Electrodes for Four-Terminal Perovskite/$CuInSe_2$ Tandem Solar Cells. *ACS Nano* **14,** 7502–7512 (2020).

134. Moradbeigi, M. & Razaghi, M. Investigation of optical and electrical properties of novel 4T all perovskite tandem solar cell. *Scientific Reports* **12** (2022).

135. Kim, S. *et al.* Over 30% efficiency bifacial 4-terminal perovskite-heterojunction silicon tandem solar cells with spectral albedo. *Scientific Reports* **11** (2021).

136. Coletti, G. *et al.* Bifacial Four-Terminal Perovskite/Silicon Tandem Solar Cells and Modules. *ACS Energy Letters* **5,** 1676–1680 (2020).

137. Yu, G. *et al.* Optical management of spacer layer of high-performance four-terminal perovskite/silicon tandem solar cells. *Solar Energy* **228,** 226–234 (2021).

138. Bittkau, K., Kirchartz, T. & Rau, U. Optical design of spectrally selective interlayers for perovskite/silicon heterojunction tandem solar cells. *Optics Express* **26,** A750–A760 (2018).

139. Köhnen, E. *et al.* Highly efficient monolithic perovskite silicon tandem solar cells: analyzing the influence of current mismatch on device performance. *Sustainable Energy & Fuels* **3,** 1995–2005 (2019).

140. Becker, T. *et al.* All-Oxide MoO_x/SnO_x Charge Recombination Interconnects for Inverted Organic Tandem Solar Cells. *Advanced Energy Materials* **8,** 1702533 (2018).

141. Datta, K. *et al.* Monolithic All-Perovskite Tandem Solar Cells with Minimized Optical and Energetic Losses. *Advanced Materials* **34,** 2110053 (2022).

142. Brinkmann, K. O. *Metalloxidbasierte Ladungsextraktionsschichten für Perowskit-Solarzellen* Thesis (2016).

143. Jung, H. S. & Park, N. G. Perovskite solar cells: from materials to devices. *Small* **11,** 10–25 (2015).

144. Taylor, A. D. *et al.* A general approach to high-efficiency perovskite solar cells by any antisolvent. *Nature Communications* **12** (2021).

145. Castro-Méndez, A.-F., Hidalgo, J. & Correa-Baena, J.-P. The Role of Grain Boundaries in Perovskite Solar Cells. *Advanced Energy Materials* **9,** 1901489 (2019).

146. Huang, Z., Hu, X., Liu, C., Tan, L. & Chen, Y. Nucleation and Crystallization Control via Polyurethane to Enhance the Bendability of Perovskite Solar Cells with Excellent Device Performance. *Advanced Functional Materials* **27,** 1703061 (2017).

147. Xu, C., Liu, Z. & Lee, E.-C. Crystallization management for high-performance perovskite solar cells by introducing an antisolvent into the perovskite precursor. *Journal of Materials Chemistry C* **8,** 15860–15867 (2020).

148. Snyder, L. Classification off the Solvent Properties of Common Liquids. *Journal of Chromatographic Science* **16,** 223–234 (1978).

149. Clever, H. L. & Snead, C. C. Thermodynamics of Liquid Surfaces: The Surface Tension of Dimethyl Sulfoxide and Some Dimethyl Sulfoxide-Acetone Mixtures. *The Journal of Physical Chemistry* **67,** 918–920 (1963).

150. Gidey, A. T., Assayehegn, E. & Kim, J. Y. Hydrophilic Surface-Driven Crystalline Grain Growth of Perovskites on Metal Oxides. *ACS Applied Energy Materials* **4,** 6923–6932 (2021).

151. Chen, Z. *et al.* Thin single crystal perovskite solar cells to harvest below-bandgap light absorption. *Nature Communications* **8** (2017).

152. Ünlü, F. *Green Inks and Lead-free Compositions in Perovskite and Allied Materials for Photovoltaic Applications* Thesis (2022).

153. Brinkmann, K. O. *et al.* Extremely Robust Gas-Quenching Deposition of Halide Perovskites on Top of Hydrophobic Hole Transport Materials for Inverted (p–i–n) Solar Cells by Targeting the Precursor Wetting Issue. *ACS Applied Materials and Interfaces* **11,** 40172–40179 (2019).

154. Lee, J.-W. *et al.* A Bifunctional Lewis Base Additive for Microscopic Homogeneity in Perovskite Solar Cells. *Chem* **3,** 290–302 (2017).

155. Wafee, S., Liu, B. H. & Leu, C.-C. Lewis bases: promising additives for enhanced performance of perovskite solar cells. *Materials Today Energy* **22,** 100847 (2021).

156. Wang, R. *et al.* Caffeine Improves the Performance and Thermal Stability of Perovskite Solar Cells. *Joule* **3,** 1464–1477 (2019).

157. Katayama, M., Shinoda, M., Ozutsumi, K., Funahashi, S. & Inada, Y. Reevaluation of Donor Number Using Titration Calorimetry. *Analytical Sciences* **28,** 103 (2012).

158. Gutmann, V. Solvent effects on the reactivities of organometallic compounds. *Coordination Chemistry Reviews* **18,** 225–255 (1976).

159. Roiland, C. *et al.* Multinuclear NMR as a tool for studying local order and dynamics in $CH_3NH_3PbX_3$ (X = Cl, Br, I) hybrid perovskites. *Physical Chemistry Chemical Physics* **18,** 27133–27142 (2016).

160. Macomber, R. S. An introduction to NMR titration for studying rapid reversible complexation. *Journal of Chemical Education* **69,** 375 (1992).

161. Shargaieva, O., Kuske, L., Rappich, J., Unger, E. & Nickel, N. H. Building Blocks of Hybrid Perovskites: A Photoluminescence Study of Lead-Iodide Solution Species. *ChemPhysChem* **21,** 2327–2333 (2020).

162. LeBel, R. G. & Goring, D. A. I. Density, Viscosity, Refractive Index, and Hygroscopicity of Mixtures of Water and Dimethyl Sulfoxide. *Journal of Chemical & Engineering Data* **7,** 100–101 (1962).

163. Bernal-García, J. M., Guzmán-López, A., Cabrales-Torres, A., Estrada-Baltazar, A. & Iglesias-Silva, G. A. Densities and Viscosities of (N,N-Dimethylformamide + Water) at Atmospheric Pressure from (283.15 to 353.15) K. *Journal of Chemical & Engineering Data* **53,** 1024–1027 (2008).

164. Noel, N. K. *et al.* Unveiling the Influence of pH on the Crystallization of Hybrid Perovskites, Delivering Low Voltage Loss Photovoltaics. *Joule* **1,** 328–343 (2017).

165. Ouyang, J., Chu, C.-W., Chen, F.-C., Xu, Q. & Yang, Y. High-Conductivity Poly(3,4-ethylenedioxythiophene):Poly(styrene sulfonate) Film and Its Application in Polymer Optoelectronic Devices. *Advanced Functional Materials* **15,** 203–208 (2005).

166. Voroshazi, E. *et al.* Influence of cathode oxidation via the hole extraction layer in polymer:fullerene solar cells. *Organic Electronics* **12,** 736–744 (2011).

167. Jin Bae, E., Hun Kang, Y., Jang, K.-S. & Yun Cho, S. Enhancement of Thermoelectric Properties of PEDOT:PSS and Tellurium-PEDOT:PSS Hybrid Composites by Simple Chemical Treatment. *Scientific Reports* **6,** 18805 (2016).

168. Yu, Z., Xia, Y., Du, D. & Ouyang, J. PEDOT:PSS Films with Metallic Conductivity through a Treatment with Common Organic Solutions of Organic Salts and Their Application as a Transparent Electrode of Polymer Solar Cells. *ACS Appl Mater Interfaces* **8,** 11629–38 (2016).

169. Rajagopal, A., Yao, K. & Jen, A. K. Toward Perovskite Solar Cell Commercialization: A Perspective and Research Roadmap Based on Interfacial Engineering. *Adv Mater* **30,** e1800455 (2018).

170. Xia, Y., Yan, G. & Lin, J. Review on Tailoring PEDOT:PSS Layer for Improved Device Stability of Perovskite Solar Cells. *Nanomaterials* **11,** 3119 (2021).

171. Zhou, X. *et al.* Synergistic effects of multiple functional ionic liquid-treated PEDOT:PSS and less-ion-defects S-acetylthiocholine chloride-passivated perovskite surface enabling stable and hysteresis-free inverted perovskite solar cells with conversion efficiency over 20%. *Nano Energy* **63,** 103866 (2019).

172. Wolff, C. M. *et al.* Reduced Interface-Mediated Recombination for High Open-Circuit Voltages in $CH_3NH_3PbI_3$ Solar Cells. *Advanced Materials* **29** (2017).

173. Stolterfoht, M. *et al.* Approaching the fill factor Shockley–Queisser limit in stable, dopant-free triple cation perovskite solar cells. *Energy and Environmental Science* **10,** 1530–1539 (2017).

174. Degani, M. *et al.* 23.7% Efficient inverted perovskite solar cells by dual interfacial modification. *Science Advances* **7,** eabj7930.

175. Xu, X. *et al.* Ultraviolet-ozone surface modification for non-wetting hole transport materials based inverted planar perovskite solar cells with efficiency exceeding 18%. *Journal of Power Sources* **360,** 157–165 (2017).

176. You, J. *et al.* The fabrication of homogeneous perovskite films on non-wetting interfaces enabled by physical modification. *Journal of Energy Chemistry* **38,** 192–198 (2019).

177. Deng, Y. *et al.* Surfactant-controlled ink drying enables high-speed deposition of perovskite films for efficient photovoltaic modules. *Nature Energy* **3,** 560–566 (2018).

178. Rohrschneider, L. Solvent characterization by gas-liquid partition coefficients of selected solutes. *Analytical Chemistry* **45,** 1241–1247 (1973).

179. Snyder, L. R. Classification of the solvent properties of common liquids. *Journal of Chromatography A* **92,** 223–230 (1974).

180. Snyder, L. R. *Introduction to Modern Liquid Chromatography* (2009).

181. Clever, H. L. & Snead, C. C. Thermodynamics of Liquid Surfaces: The Surface Tension of Dimethyl Sulfoxide and Some Dimethyl Sulfoxide-Acetone Mixtures. *The Journal of Physical Chemistry* **67,** 918–920 (1963).

182. Shen, J. *et al.* Liquid Phase Exfoliation of Two-Dimensional Materials by Directly Probing and Matching Surface Tension Components. *Nano Letters* **15,** 5449–5454 (2015).

183. Płowaś, I., Świergiel, J. & Jadżyn, J. Relative Static Permittivity of Dimethyl Sulfoxide + Water Mixtures. *Journal of Chemical & Engineering Data* **58** (2013).

184. Griffin, W. C. Calculation of HLB values of non-ionic surfactants. *Journal of the Society of Cosmetic Chemistry* **5,** 249–256 (1954).

185. Griffin, W. C. Classification of Surface-Active Agents by "HLB.". *Journal of Cosmetical Science* **1,** 311–326 (1949).

186. GESTIS. *Stoffdatenbank (accessed 03/22)* Web Page.

187. Jouyban, A., Soltanpour, S. & Chan, H.-K. A simple relationship between dielectric constant of mixed solvents with solvent composition and temperature. *International Journal of Pharmaceutics* **269,** 353–360 (2004).

188. Scherrer, P. Bestimmung Der Grösse Und Der Inneren Struktur von Kolloidteilchen Mittels Röntgestrahlen. *Nachrichten von der Gesellschaft der Wissenschaften zu Göttingen, Mathematisch-Physikalische Klasse,* 98–100 (1918).

189. Miranda, M. A. R. & Sasaki, J. M. The limit of application of the Scherrer equation. *Acta Crystallographica Section A* **74,** 54–65 (2018).

190. Jenny, P., Roekaerts, D. & Beishuizen, N. Modeling of turbulent dilute spray combustion. *Progress in Energy and Combustion Science* **38,** 846–887 (2012).

191. Lin, S. P. & Reitz, R. D. Dropt and Spray Formation from a Liquid Jet. *Annual Review of Fluid Mechanics* **30,** 85–105 (1998).

192. Brinkmann, K. *et al.* Suppressed decomposition of organometal halide perovskites by impermeable electron-extraction layers in inverted solar cells. *Nature Communications* **8,** 13938 (2017).

193. Green, M. A. *et al.* Solar cell efficiency tables (Version 58). *Progress in Photovoltaics: Research and Applications* **29,** 657–667 (2021).

194. Tiep, N. H., Ku, Z. & Fan, H. J. Recent Advances in Improving the Stability of Perovskite Solar Cells. *Advanced Energy Materials* **6,** 1501420 (2016).

195. Leijtens, T. *et al.* Stability of Metal Halide Perovskite Solar Cells. *Advanced Energy Materials* **5,** 1500963 (2015).

196. Roose, B., Dey, K., Chiang, Y. H., Friend, R. H. & Stranks, S. D. Critical Assessment of the Use of Excess Lead Iodide in Lead Halide Perovskite Solar Cells. *Journal of Physical Chemical Letters* **11,** 6505–6512 (2020).

197. Niu, G. *et al.* Study on the stability of $CH_3NH_3PbI_3$ films and the effect of post-modification by aluminum oxide in all-solid-state hybrid solar cells. *Journal of Material Chemistry A* **2,** 705–710 (2014).

198. Manshor, N. A. *et al.* Humidity versus photo-stability of metal halide perovskite films in a polymer matrix. *Phys Chem Chem Phys* **18,** 21629–39 (2016).

199. Divitini, G. *et al.* In situ observation of heat-induced degradation of perovskite solar cells. *Nature Energy* **1** (2016).

200. Kim, A. *et al.* Fully solution-processed transparent electrodes based on silver nanowire composites for perovskite solar cells. *Nanoscale* **8,** 6308–16 (2016).

201. You, J. *et al.* Improved air stability of perovskite solar cells via solution-processed metal oxide transport layers. *Nature Nanotechnol* **11,** 75–81 (2016).

202. Chen, W. *et al.* Efficient and stable large-area perovskite solar cells with inorganic charge extraction layers. *Science* **350,** 944–948 (2015).

203. Hirvikorpi, T., Vähä-Nissi, M., Nikkola, J., Harlin, A. & Karppinen, M. Thin Al_2O_3 barrier coatings onto temperature-sensitive packaging materials by atomic layer deposition. *Surface and Coatings Technology* **205,** 5088–5092 (2011).

204. Kaltenbrunner, M. *et al.* Flexible high power-per-weight perovskite solar cells with chromium oxide–metal contacts for improved stability in air. *Nature Materials* **14,** 1032–1039 (2015).

205. Guerrero, A. *et al.* Interfacial Degradation of Planar Lead Halide Perovskite Solar Cells. *ACS Nano* **10,** 218–224 (2016).

206. Bush, K. A. *et al.* Thermal and Environmental Stability of Semi-Transparent Perovskite Solar Cells for Tandems Enabled by a Solution-Processed Nanoparticle Buffer Layer and Sputtered ITO Electrode. *Advanced Materials* **28,** 3937–43 (2016).

207. Kim, I. S. & Martinson, A. B. F. Stabilizing hybrid perovskites against moisture and temperature via non-hydrolytic atomic layer deposited overlayers. *Journal of Materials Chemistry A* **3,** 20092–20096 (2015).

208. Koushik, D. *et al.* High-efficiency humidity-stable planar perovskite solar cells based on atomic layer architecture. *Energy and Environmental Science* **10,** 91–100 (2017).

209. Behrendt, A. *et al.* Highly robust transparent and conductive gas diffusion barriers based on tin oxide. *Adv Mater* **27,** 5961–5967 (2015).

210. Trost, S. *et al.* Tin Oxide (SnO_x) as Universal "Light-Soaking" Free Electron Extraction Material for Organic Solar Cells. *Advanced Energy Materials* **5** (2015).

211. Zardetto, V. *et al.* Atomic layer deposition for perovskite solar cells: research status, opportunities and challenges. *Sustainable Energy & Fuels* **1,** 30–55 (2017).

212. Trost, S. *et al.* Overcoming the "Light-Soaking" Issue in Inverted Organic Solar Cells by the Use of Al:ZnO Electron Extraction Layers. *Advanced Energy Materials* **3,** 1437–1444 (2013).

213. Snaith, H. J. *et al.* Anomalous Hysteresis in Perovskite Solar Cells. *Journal of Physical Chemical Letters* **5,** 1511–5 (2014).

214. Unger, E. L. *et al.* Hysteresis and transient behavior in current–voltage measurements of hybrid-perovskite absorber solar cells. *Energy and Environmental Science* **7,** 3690–3698 (2014).

215. Calado, P. *et al.* Evidence for ion migration in hybrid perovskite solar cells with minimal hysteresis. *Nature Commun* **7,** 13831 (2016).

216. Deng, Y., Dong, Q., Bi, C., Yuan, Y. & Huang, J. Air-Stable, Efficient Mixed-Cation Perovskite Solar Cells with Cu Electrode by Scalable Fabrication of Active Layer. *Advanced Energy Materials* **6,** 1600372 (2016).

217. Han, Y. *et al.* Degradation observations of encapsulated planar $CH_3NH_3PbI_3$ perovskite solar cells at high temperatures and humidity. *Journal of Materials Chemistry A* **3,** 8139–8147 (2015).

218. Knez, M., Nielsch, K. & Niinistö, L. Synthesis and Surface Engineering of Complex Nanostructures by Atomic Layer Deposition. *Advanced Materials* **19,** 3425–3438 (2007).

219. Wilson, C. A., Grubbs, R. K. & George, S. M. Nucleation and Growth during Al_2O_3 Atomic Layer Deposition on Polymers. *Chemistry of Materials* **17,** 5625–5634 (2005).

220. Batzill, M. & Diebold, U. The surface and materials science of tin oxide. *Progress in Surface Science* **79,** 47–154 (2005).

221. Trost, S. *et al.* Avoiding Photoinduced Shunts in Organic Solar Cells by the Use of Tin Oxide (SnO_x) as Electron Extraction Material Instead of ZnO. *Advanced Energy Materials* **6,** 1600347 (2016).

222. Semancik, S. & Cox, D. F. Fundamental characterization of clean and gas-dosed tin oxide. *Sensors and Actuators* **12,** 101–106 (1987).

223. Emara, J. *et al.* Impact of Film Stoichiometry on the Ionization Energy and Electronic Structure of $CH_3NH_3PbI_3$ Perovskites. *Advanced Materials* **28,** 553–559 (2016).

224. Misra, R. K. *et al.* Temperature- and Component-Dependent Degradation of Perovskite Photovoltaic Materials under Concentrated Sunlight. *The Journal of Physical Chemistry Letters* **6,** 326–330 (2015).

225. Nie, W. *et al.* Light-activated photocurrent degradation and self-healing in perovskite solar cells. *Nature Commun* **7,** 11574 (2016).

226. Hoffmann, L. *et al.* Spatial Atmospheric Pressure Atomic Layer Deposition of Tin Oxide as an Impermeable Electron Extraction Layer for Perovskite Solar Cells with Enhanced Thermal Stability. *ACS Applied Materials and Interfaces* **10,** 6006–6013 (2018).

227. Levy, D. H., Freeman, D., Nelson, S. F., Cowdery-Corvan, P. J. & Irving, L. M. Stable ZnO thin film transistors by fast open air atomic layer deposition. *Applied Physics Letters* **92,** 192101 (2008).

228. Hoffmann, L. *et al.* Atmospheric pressure plasma enhanced spatial atomic layer deposition of SnO_x as conductive gas diffusion barrier. *Journal of Vacuum Science & Technology A* **36,** 01A112 (2018).

229. Hoffmann, L. *et al.* Gas Diffusion Barriers Prepared by Spatial Atmospheric Pressure Plasma Enhanced ALD. *ACS Applied Materials & Interfaces* **9,** 4171–4176 (2017).

230. Klumbies, H. *et al.* Thickness dependent barrier performance of permeation barriers made from atomic layer deposited alumina for organic devices. *Organic Electronics* **17,** 138–143 (2015).

231. Leterrier, Y. Durability of nanosized oxygen-barrier coatings on polymers. *Progress in Materials Science* **48,** 1–55 (2003).

232. Fahlteich, J., Fahland, M., Schönberger, W. & Schiller, N. Permeation barrier properties of thin oxide films on flexible polymer substrates. *Thin Solid Films* **517,** 3075–3080 (2009).

233. Sobrinho, A. S. d. S., Czeremuszkin, G., Latrèche, M. & Wertheimer, M. R. Defect-permeation correlation for ultrathin transparent barrier coatings on polymers. *Journal of Vacuum Science & Technology A* **18,** 149–157 (2000).

234. Meyer, J., Schmidt, H., Kowalsky, W., Riedl, T. & Kahn, A. The origin of low water vapor transmission rates through Al_2O_3/ZrO_2 nanolaminate gas-diffusion barriers grown by atomic layer deposition. *Applied Physics Letters* **96,** 243308 (2010).

235. Poodt, P. *et al.* On the kinetics of spatial atomic layer deposition. *Journal of Vacuum Science & Technology A: Vacuum, Surfaces, and Films* **31,** 01A108 (2013).

236. Elam, J. W. *et al.* Atomic layer deposition of tin oxide films using tetrakis(dimethylamino) tin. *Journal of Vacuum Science & Technology A* **26,** 244–252 (2008).

237. Bush, K. A. *et al.* 23.6%-efficient monolithic perovskite/silicon tandem solar cells with improved stability. *Nature Energy* **2** (2017).

238. Zhao, J. *et al.* Self-Encapsulating Thermostable and Air-Resilient Semitransparent Perovskite Solar Cells. *Advanced Energy Materials* **7,** 1602599 (2017).

239. Gahlmann, T. *et al.* Impermeable Charge Transport Layers Enable Aqueous Processing on Top of Perovskite Solar Cells. *Advanced Energy Materials* **10,** 1903897 (2020).

240. Higuchi, M., Uekusa, S., Nakano, R. & Yokogawa, K. Postdeposition Annealing Influence on Sputtered Indium Tin Oxide Film Characteristics. *Japanese Journal of Applied Physics* **33,** 302–306 (1994).

241. Wu, W.-F. & Chiou, B.-S. Effect of annealing on electrical and optical properties of RF magnetron sputtered indium tin oxide films. *Applied Surface Science* **68,** 497–504 (1993).

242. Jain, V. K. & Kulshreshtha, A. P. Indium-Tin-Oxide transparent conducting coatings on silicon solar cells and their "figure of merit". *Solar Energy Materials* **4,** 151–158 (1981).

243. Zilberberg, K. & Riedl, T. Metal-nanostructures – a modern and powerful platform to create transparent electrodes for thin-film photovoltaics. *Journal of Materials Chemistry A* **4,** 14481–14508 (2016).

244. Lee, C.-C., Chen, S.-H. & Jaing, C.-c. Optical monitoring of silver-based transparent heat mirrors. *Applied Optics* **35,** 5698–5703 (1996).

245. Köstlin, H. & Frank, G. Optimization of transparent heat mirrors based on a thin silver film between antireflection films. *Thin Solid Films* **89,** 287–293 (1982).

246. Della Gaspera, E. *et al.* Ultra-thin high efficiency semitransparent perovskite solar cells. *Nano Energy* **13,** 249–257 (2015).

247. Yang, Y. *et al.* Multilayer Transparent Top Electrode for Solution Processed Perovskite/Cu(In,Ga)(Se,S)$_2$ Four Terminal Tandem Solar Cells. *ACS Nano* **9,** 7714–7721 (2015).

248. Kim, H., Kim, H.-S., Ha, J., Park, N.-G. & Yoo, S. Empowering Semi-Transparent Solar Cells with Thermal-Mirror Functionality. *Advanced Energy Materials* **6,** 1502466 (2016).

249. Haacke, G. New figure of merit for transparent conductors. *Journal of Applied Physics* **47,** 4086–4089 (1976).

250. Winkler, T. *et al.* Efficient large area semitransparent organic solar cells based on highly transparent and conductive ZTO/Ag/ZTO multilayer top electrodes. *Organic Electronics* **12,** 1612–1618 (2011).

251. Zilberberg, K. *et al.* Highly Robust Indium-Free Transparent Conductive Electrodes Based on Composites of Silver Nanowires and Conductive Metal Oxides. *Advanced Functional Materials* **24,** 1671–1678 (2014).

252. Nie, W. *et al.* High-efficiency solution-processed perovskite solar cells with millimeter-scale grains. *Science* **347,** 522–525 (2015).

253. Domanski, K. *et al.* Not All That Glitters Is Gold: Metal-Migration-Induced Degradation in Perovskite Solar Cells. *ACS Nano* **10,** 6306–14 (2016).

254. Jeangros, Q. *et al.* In Situ TEM Analysis of Organic–Inorganic Metal-Halide Perovskite Solar Cells under Electrical Bias. *Nano Letters* **16,** 7013–7018 (2016).

255. Yang, J., Siempelkamp, B. D., Mosconi, E., De Angelis, F. & Kelly, T. L. Origin of the Thermal Instability in $CH_3NH_3PbI_3$ Thin Films Deposited on ZnO. *Chemistry of Materials* **27,** 4229–4236 (2015).

256. Matsumoto, F., Vorpahl, S. M., Banks, J. Q., Sengupta, E. & Ginger, D. S. Photodecomposition and Morphology Evolution of Organometal Halide Perovskite Solar Cells. *The Journal of Physical Chemistry C* **119,** 20810–20816 (2015).

257. Lee, Y. I. *et al.* A Low-Temperature Thin-Film Encapsulation for Enhanced Stability of a Highly Efficient Perovskite Solar Cell. *Advanced Energy Materials* **8** (2018).

258. Lv, Y. *et al.* Low-Temperature Atomic Layer Deposition of Metal Oxide Layers for Perovskite Solar Cells with High Efficiency and Stability under Harsh Environmental Conditions. *ACS Applied Materials & Interfaces* **10,** 23928–23937 (2018).

259. Kim, I. S. *et al.* Liquid Water- and Heat-Resistant Hybrid Perovskite Photovoltaics via an Inverted ALD Oxide Electron Extraction Layer Design. *Nano Letters* **16,** 7786–7790 (2016).

260. Meyer, J. *et al.* Transition Metal Oxides for Organic Electronics: Energetics, Device Physics and Applications. *Advanced Materials* **24,** 5408–5427 (2012).

261. Shim, J. W. *et al.* Polyvinylpyrrolidone-modified indium tin oxide as an electron-collecting electrode for inverted polymer solar cells. *Applied Physics Letters* **101,** 073303 (2012).

262. Trost, S. *et al.* Plasmonically sensitized metal-oxide electron extraction layers for organic solar cells. *Scientific Reports* **5,** 7765 (2015).

263. Cheng, J. *et al.* Plasmon-induced hot electron transfer in AgNW@TiO_2@AuNPs nanostructures. *Scientific Reports* **8,** 14136 (2018).

264. Peña-Camargo, F. *et al.* Halide Segregation versus Interfacial Recombination in Bromide-Rich Wide-Gap Perovskite Solar Cells. *ACS Energy Letters* **5,** 2728–2736 (2020).

265. Brinkmann, K. O. *et al.* Perovskite–organic tandem solar cells with indium oxide interconnect. *Nature* **604,** 280–286 (2022).

266. Brinkmann, K. O. *et al.* The Optical Origin of Near-Unity External Quantum Efficiencies in Perovskite Solar Cells. *Solar RRL* **5,** 2100371 (2021).

267. Prasanna, R. *et al.* Band Gap Tuning via Lattice Contraction and Octahedral Tilting in Perovskite Materials for Photovoltaics. *Journal of the American Chemical Society* **139,** 11117–11124 (2017).

268. Zhou, Y. *et al.* Composition-Tuned Wide Bandgap Perovskites: From Grain Engineering to Stability and Performance Improvement. *Advanced Functional Materials* **28** (2018).

269. Meloni, S., Palermo, G., Ashari-Astani, N., Grätzel, M. & Rothlisberger, U. Valence and conduction band tuning in halide perovskites for solar cell applications. *Journal of Materials Chemistry A* **4,** 15997–16002 (2016).

270. Lin, R. *et al.* All-perovskite tandem solar cells with improved grain surface passivation. *Nature* **603,** 73–78 (2022).

271. Al-Ashouri, A. *et al.* Monolithic perovskite/silicon tandem solar cell with 29% efficiency by enhanced hole extraction. *Science* **370,** 1300–1309 (2020).

272. Al-Ashouri, A. *et al.* Conformal monolayer contacts with lossless interfaces for perovskite single junction and monolithic tandem solar cells. *Energy and Environmental Science* **12,** 3356–3369 (2019).

273. Slotcavage, D. J., Karunadasa, H. I. & McGehee, M. D. Light-Induced Phase Segregation in Halide-Perovskite Absorbers. *ACS Energy Letters* **1,** 1199–1205 (2016).

274. Unger, E. L. *et al.* Roadmap and roadblocks for the band gap tunability of metal halide perovskites. *Journal of Materials Chemistry A* **5,** 11401–11409 (2017).

275. Rau, U. Reciprocity relation between photovoltaic quantum efficiency and electroluminescent emission of solar cells. *Physical Review B* **76,** 085303 (2007).

276. Caprioglio, P. *et al.* Nano-emitting Heterostructures Violate Optical Reciprocity and Enable Efficient Photoluminescence in Halide-Segregated Methylammonium-Free Wide Bandgap Perovskites. *ACS Energy Letters* **6,** 419–428 (2021).

277. Belisle, R. A. *et al.* Impact of Surfaces on Photoinduced Halide Segregation in Mixed-Halide Perovskites. *ACS Energy Letters* **3,** 2694–2700 (2018).

278. Park, B.-w. *et al.* Understanding how excess lead iodide precursor improves halide perovskite solar cell performance. *Nature Communications* **9,** 3301 (2018).

279. Duong, T. *et al.* High Efficiency Perovskite-Silicon Tandem Solar Cells: Effect of Surface Coating versus Bulk Incorporation of 2D Perovskite. *Advanced Energy Materials* **10** (2020).

280. Jiang, Q. *et al.* Surface passivation of perovskite film for efficient solar cells. *Nature Photonics* **13,** 460–466 (2019).

281. Ruddlesden, S. N. & Popper, P. The compound $Sr_3Ti_2O_7$ and its structure. *Acta Crystallographica* **11,** 54–55 (1958).

282. Rau, U., Blank, B., Müller, T. C. M. & Kirchartz, T. Efficiency Potential of Photovoltaic Materials and Devices Unveiled by Detailed-Balance Analysis. *Physical Review Applied* **7,** 044016 (2017).

283. Wu, C. G., Chiang, C. H. & Chang, S. H. A perovskite cell with a record-high-V(oc) of 1.61 V based on solvent annealed $CH_3NH_3PbBr_3$/ICBA active layer. *Nanoscale* **8,** 4077–85 (2016).

284. Eperon, G. E. *et al.* Perovskite-perovskite tandem photovoltaics with optimized band gaps. *Science* **354,** 861–865 (2016).

285. Longo, G. *et al.* Fully Vacuum-Processed Wide Band Gap Mixed-Halide Perovskite Solar Cells. *ACS Energy Letters* **3,** 214–219 (2018).

286. Rajagopal, A., Stoddard, R. J., Jo, S. B., Hillhouse, H. W. & Jen, A. K.-Y. Overcoming the Photovoltage Plateau in Large Bandgap Perovskite Photovoltaics. *Nano Letters* **18,** 3985–3993 (2018).

287. Braly, I. L., Stoddard, R. J., Rajagopal, A., Jen, A. K.-Y.-. & Hillhouse, H. W. Photoluminescence and Photoconductivity to Assess Maximum Open-Circuit Voltage and Carrier Transport in Hybrid Perovskites and Other Photovoltaic Materials. *The Journal of Physical Chemistry Letters* **9,** 3779–3792 (2018).

288. Rajagopal, A. *et al.* Highly Efficient Perovskite–Perovskite Tandem Solar Cells Reaching 80% of the Theoretical Limit in Photovoltage. *Advanced Materials* **29,** 1702140 (2017).

289. Wang, L. *et al.* Potassium-Induced Phase Stability Enables Stable and Efficient Wide-Bandgap Perovskite Solar Cells. *Solar RRL* **4,** 2000098 (2020).

290. Lin, Q., Armin, A., Nagiri, R. C. R., Burn, P. L. & Meredith, P. Electro-optics of perovskite solar cells. *Nature Photonics* **9,** 106–112 (2015).

291. Yang, B. *et al.* Perovskite Solar Cells with Near 100% Internal Quantum Efficiency Based on Large Single Crystalline Grains and Vertical Bulk Heterojunctions. *Journal of the American Chemical Society* **137,** 9210–9213 (2015).

292. Lin, R. *et al.* Monolithic all-perovskite tandem solar cells with 24.8% efficiency exploiting comproportionation to suppress Sn(ii) oxidation in precursor ink. *Nature Energy* **4,** 864–873 (2019).

293. Gharibzadeh, S. *et al.* 2D/3D Heterostructure for Semitransparent Perovskite Solar Cells with Engineered Bandgap Enables Efficiencies Exceeding 25% in Four-Terminal Tandems with Silicon and CIGS. *Advanced Functional Materials* **30,** 1909919 (2020).

294. Kim, G. *et al.* Impact of strain relaxation on performance of α-formamidinium lead iodide perovskite solar cells. *Science* **370,** 108–112 (2020).

295. Duong, T. *et al.* Rubidium Multication Perovskite with Optimized Bandgap for Perovskite-Silicon Tandem with over 26% Efficiency. *Advanced Energy Materials* **7,** 1700228 (2017).

296. Chen, B. *et al.* Enhanced optical path and electron diffusion length enable high-efficiency perovskite tandems. *Nature Communications* **11,** 1257 (2020).

297. Wang, R. *et al.* Constructive molecular configurations for surface-defect passivation of perovskite photovoltaics. *Science* **366,** 1509–1513 (2019).

298. Moghadamzadeh, S. *et al.* Triple-cation low-bandgap perovskite thin-films for high-efficiency four-terminal all-perovskite tandem solar cells. *Journal of Materials Chemistry A* **8,** 24608–24619 (2020).

299. Jeong, J. *et al.* Pseudo-halide anion engineering for α-$FAPbI_3$ perovskite solar cells. *Nature* **592,** 381–385 (2021).

300. Kakavelakis, G. *et al.* Efficient and Highly Air Stable Planar Inverted Perovskite Solar Cells with Reduced Graphene Oxide Doped PCBM Electron Transporting Layer. *Advanced Energy Materials* **7,** 1602120 (2017).

301. Zhao, X. *et al.* Extending the Photovoltaic Response of Perovskite Solar Cells into the Near-Infrared with a Narrow-Bandgap Organic Semiconductor. *Advanced Materials* **31,** 1904494 (2019).

302. Mali, S. S., Patil, J. V., Arandiyan, H. & Hong, C. K. Reduced methylammonium triple-cation $Rb_{0.05}(FAPbI_3)_{0.95}(MAPbBr_3)_{0.05}$ perovskite solar cells based on a TiO_2/SnO_2 bilayer electron transport layer approaching a stabilized 21% efficiency: the role of antisolvents. *Journal of Materials Chemistry A* **7,** 17516–17528 (2019).

303. Jeong, M. *et al.* Stable perovskite solar cells with efficiency exceeding 24.8% and 0.3-V voltage loss. *Science* **369,** 1615–1620 (2020).

304. Li, J. *et al.* Vapor Exchange Deposition of an Air-Stable Lead Iodide Adduct on 19% Efficient 1.8 cm^2 Perovskite Solar Cells. *ACS Applied Energy Materials* **2,** 2506–2514 (2019).

305. Agbaoye, R. O., Akinlami, J. O., Afolabi, T. A. & Adebayo, G. A. Unraveling the Stable Phase, High Absorption Coefficient, Optical and Mechanical Properties of Hybrid Perovskite $CH_3NH_3Pb_xMg_{1-x}I_3$: Density Functional Approach. *Journal of Inorganic and Organometallic Polymers and Materials* **30,** 299–309 (2020).

306. Tablero Crespo, C. Absorption coefficients data of lead iodine perovskites using 14 different organic cations. *Data in Brief* **27,** 104636 (2019).

307. Chen, C.-W. *et al.* Optical properties of organometal halide perovskite thin films and general device structure design rules for perovskite single and tandem solar cells. *Journal of Materials Chemistry A* **3,** 9152–9159 (2015).

308. Leijtens, T., Bush, K. A., Prasanna, R. & McGehee, M. D. Opportunities and challenges for tandem solar cells using metal halide perovskite semiconductors. *Nature Energy* **3,** 828–838 (2018).

309. Han, Q. *et al.* High-performance perovskite/$Cu(In,Ga)Se_2$ monolithic tandem solar cells. *Science* **361,** 904–908 (2018).

310. Hou, Y. *et al.* Efficient tandem solar cells with solution-processed perovskite on textured crystalline silicon. *Science* **367,** 1135–1140 (2020).

311. Palmstrom, A. F. *et al.* Enabling Flexible All-Perovskite Tandem Solar Cells. *Joule* **3,** 2193–2204 (2019).

312. Lin, R. *et al.* All-perovskite tandem solar cells with improved grain surface passivation. *Nature* **603,** 73–78 (2022).

313. Zhao, D. *et al.* Efficient two-terminal all-perovskite tandem solar cells enabled by high-quality low-bandgap absorber layers. *Nature Energy* **3,** 1093–1100 (2018).

314. Hao, F., Stoumpos, C. C., Chang, R. P. H. & Kanatzidis, M. G. Anomalous Band Gap Behavior in Mixed Sn and Pb Perovskites Enables Broadening of Absorption Spectrum in Solar Cells. *Journal of the American Chemical Society* **136,** 8094–8099 (2014).

315. Al-Ashouri, A. *et al.* Conformal monolayer contacts with lossless interfaces for perovskite single junction and monolithic tandem solar cells. *Energy and Environmental Science* **12,** 3356–3369 (2019).

316. Green, M. A. *et al.* Solar cell efficiency tables (version 56). *Progress in Photovoltaics: Research and Applications* **28,** 629–638 (2020).

317. Yu, G., Gao, J., Hummelen, J. C., Wudl, F. & Heeger, A. J. Polymer Photovoltaic Cells: Enhanced Efficiencies via a Network of Internal Donor-Acceptor Heterojunctions. *Science* **270,** 1789–1791 (1995).

318. Zhao, J. *et al.* Efficient organic solar cells processed from hydrocarbon solvents. *Nature Energy* **1,** 15027 (2016).

319. Yan, C. *et al.* Non-fullerene acceptors for organic solar cells. *Nature Reviews Materials* **3,** 18003 (2018).

320. Liu, Q. *et al.* 18% Efficiency organic solar cells. *Science Bulletin* **65,** 272–275 (2020).

321. Cheng, P., Li, G., Zhan, X. & Yang, Y. Next-generation organic photovoltaics based on non-fullerene acceptors. *Nature Photonics* **12,** 131–142 (2018).

322. Armin, A. *et al.* A History and Perspective of Non-Fullerene Electron Acceptors for Organic Solar Cells. *Advanced Energy Materials* **11,** 2003570 (2021).

323. Liu, J. *et al.* Fast charge separation in a non-fullerene organic solar cell with a small driving force. *Nature Energy* **1,** 16089 (2016).

324. Qian, D. *et al.* Design rules for minimizing voltage losses in high-efficiency organic solar cells. *Nature Materials* **17,** 703–709 (2018).

325. Chen, X. *et al.* Efficient and Reproducible Monolithic Perovskite/Organic Tandem Solar Cells with Low-Loss Interconnecting Layers. *Joule* **4,** 1594–1606 (2020).

326. Li, C., Wang, Y. & Choy, W. C. H. Efficient Interconnection in Perovskite Tandem Solar Cells. *Small Methods* **4,** 2000093 (2020).

327. Yuan, J. *et al.* Single-Junction Organic Solar Cell with over 15% Efficiency Using Fused-Ring Acceptor with Electron-Deficient Core. *Joule* **3,** 1140–1151 (2019).

328. Yu, R. *et al.* Improved Charge Transport and Reduced Nonradiative Energy Loss Enable Over 16% Efficiency in Ternary Polymer Solar Cells. *Advanced Materials* **31,** 1902302 (2019).

329. Du, X. *et al.* Unraveling the Microstructure-Related Device Stability for Polymer Solar Cells Based on Nonfullerene Small-Molecular Acceptors. *Advanced Materials* **32,** 1908305 (2020).

330. Crowell, C. R. The Richardson constant for thermionic emission in Schottky barrier diodes. *Solid-State Electronics* **8,** 395–399 (1965).

331. Nagasawa, M., Shionoya, S. & Makishima, S. Electron Effective Mass of SnO_2. *Journal of the Physical Society of Japan* **20,** 1093–1093 (1965).

332. Werner, J. H. & Güttler, H. H. Barrier inhomogeneities at Schottky contacts. *Journal of Applied Physics* **69,** 1522–1533 (1991).

333. Chand, S. & Kumar, J. Effects of barrier height distribution on the behavior of a Schottky diode. *Journal of Applied Physics* **82,** 5005–5010 (1997).

334. Gu, S. *et al.* Tin and Mixed Lead–Tin Halide Perovskite Solar Cells: Progress and their Application in Tandem Solar Cells. *Advanced Materials* **32,** 1907392 (2020).

335. Hagleitner, D. R. *et al.* Bulk and surface characterization of In_2O_3(001) single crystals. *Physical Review B* **85,** 115441 (2012).

336. Lany, S. *et al.* Surface Origin of High Conductivities in Undoped In_2O_3 Thin Films. *Physical Review Letters* **108,** 016802 (2012).

337. Shiga, M. *et al.* Sparse modeling of EELS and EDX spectral imaging data by nonnegative matrix factorization. *Ultramicroscopy* **170,** 43–59 (2016).

338. Zhang, S. & Scheu, C. Evaluation of EELS spectrum imaging data by spectral components and factors from multivariate analysis. *Microscopy* **67,** i133–i141 (2018).

339. Bellingham, J. R., Phillips, W. A. & Adkins, C. J. Intrinsic performance limits in transparent conducting oxides. *Journal of Materials Science Letters* **11,** 263–265 (1992).

340. Timmreck, R. *et al.* Characterization of tandem organic solar cells. *Nature Photonics* **9,** 478–479 (2015).